AIRBORNE REMOTE SENSING OF ESTUARINE INTERTIDAL

RADIONUCLIDE CONCENTRATIONS

By

Michael Patrick Rainey

Submitted to

The Faculty of Natural Sciences, University of Stirling, August 1999

for the degree of

Doctor of Philosophy

This research was undertaken at the Department of Environmental

Science, University of Stirling, Stirling.

ABSTRACT

The ability to map industrial discharges through remote sensing provides a powerful tool in environmental monitoring. Radionuclide effluents have been discharged, under authorization, into the Irish Sea from BNFL (British Nuclear Fuels Plc.) sites at Sellafield and Springfields since 1952. The quantitative mapping of this anthropogenic radioactivity in estuarine intertidal zones is crucial for absolute interpretations of radionuclide transport. The spatial resolutions of traditional approaches *e.g.* point sampling and airborne gamma surveys are insufficient to support geomorphic interpretations of the fate of radionuclides in estuaries.

The research presented in this thesis develops the use of airborne remote sensing to derive high-resolution synoptic data on the distribution of anthropogenic radionuclides in the intertidal areas of the Ribble Estuary, Lancashire, UK. From multidate surface sediment samples a significant relationship was identified between the Sellafield-derived ^{137}Cs & ^{241}Am and clay content (r^2=0.93 & 0.84 respectively). Detailed *in situ*, and laboratory, reflectance (0.4-2.5µm) experiments demonstrated that significant relationships exist between Airborne Thematic Mapper (ATM) simulated reflectance and intertidal sediment grain-size. The spectral influence of moisture on the reflectance characteristics of the intertidal area is also evident. This had substantial implications for the timing of airborne image acquisition.

Low-tide Daedalus ATM imagery (Natural Environmental Research Council) was collected of the Ribble Estuary on May 30th 1997. Preprocessing and linear unmixing of the imagery allowed accurate sub-pixel determinations of sediment clay content distributions (r^2=0.81). Subsequently, the established relationships between ^{137}Cs & ^{241}Am and sediment grain-size enabled the radionuclide activity distributions across the entire intertidal area (92km^2) to be mapped at a geomorphic scale (1.75m). The accuracy of these maps was assessed by comparison with *in situ* samples and the results of previous radiological studies within the estuary. Finally, detailed conclusions are made regarding radionuclide sinks and sources, and surface activity redistribution within the Ribble Estuary environment.

ACKNOWLEDGEMENTS

SUBJECT INDEX

FIGURE INDEX

xi

TABLE INDEX

PLATE INDEX

TABLE OF ACRONYMS

AIS-2	Airborne Imaging Spectrometer
ANN	Artificial Neural Networks
ASD	Analytical Spectral Devices Inc.
ATM	Airborne Thematic Mapper
AVHRR	Advanced Very High Resolution Radiometer
AVIRIS	Airborne Visible and Infrared Imaging Spectrometer
BIL	Binary Interleaved
BNFL	British Nuclear Fuels Plc.
BSQ	Binary Sequential
CASI	Compact Airborne Spectrographic Imager
DAIS	Digital Airborne Imaging Spectrometer
DGPS	Differential Geographic Positioning System
DN	Digital Number
EA	Environment Agency
ENVI	Environment for Visualising Images
EPFS	Equipment Pool for Field Spectrometry
ERS-1	European Resources Satellite-1
GER	Geophysical and Environmental Research Corporation
HMIP	Her Majesty's Inspectorate of Pollution
IAEA	International Atomic Energy Agency
IFOV	Instantaneous Field of View
IRIS	Infra Red Intelligent Spectroradiometer
LIDAR	LIght Detection and Ranging
LOI	Loss on Ignition
MAFF	Ministry of Agriculture, Fisheries and Food
MLC	Maximum Likelihood Classification
MNF	Minimum Noise Fraction
MSS	Multispectral Scanner
NERC	Natural Environmental Research Council
NOAA	National Oceanic and Atmospheric administration
NVC	National Vegetation Classification
PCA	Principal Component Analysis

RMS	Root Mean Square
SAR	Synthetic Aperture Radar
SIRIS	Single Field of View Infra Red Intelligent Spectroradiometer
SPOT	Satellite Pour l'Observation de la Terre
SURRC	Scottish Universities Research and Reactor Centre
SSC	Suspended Sediment Concentration
TM	Thematic Mapper

1. INTRODUCTION

1.1   RESEARCH IN CONTEXT

Estuaries are critical interfaces between the marine and terrestrial environment. Within estuaries, intertidal areas form an important component of the ecological framework and represent substantial sources and sinks of environmental contaminants discharged into the aquatic environment. Consequently, there is a growing interest by regulatory and industrial bodies into monitoring these contaminants. Of particular interest is an understanding of the geomorphological characteristics of intertidal regions, their interaction with contaminants, the potential ecological consequences and the impact on sea-to-land transfer.

Whilst environmental systems tend to be inherently spatially heterogeneous, the estuarine, and specifically the intertidal, environments are even more complicated because of their considerable temporal instability. To characterise this heterogeneity through isolated point samples is commonly time-consuming, expensive and spatially inaccurate. Consequently, remote sensing would appear to offer a solution by providing inexpensive synoptic views that can be analysed to extract spatially representative information about the environment of interest. Nevertheless, this valuable tool is often neglected by environmental scientists due to preconceptions regarding its ability to identify and quantify features in the landscape.

Of particular interest to this study is the fate of radionuclides in estuarine intertidal environments of the Irish Sea, which often represent sinks and sources of anthropogenic

1

radioactivity from authorised BNFL (British Nuclear Fuels Plc.) Sellafield discharges (Aston and Stanners, 1982; Assinder *et al.*, 1985; Tyler *et al.*, 1995; Brown, 1997). Traditional radioactivity monitoring techniques (*e.g.* point sampling) are inappropriate for accurate quantification of surface radionuclide distributions on an estuary-wide scale. Equally, airborne and hovercraft-based radiometrics lack the appropriate spatial resolution required for mechanistic interpretations of activity distributions. Consequently, this study explores the applicability of airborne remote sensing for quantitative investigations of surface radionuclide distributions in estuaries.

The Ribble Estuary was selected for the development and validation of a remote intertidal radionuclide monitoring technique. This decision was primarily based on the compact morphology of the estuary, the accessible nature of the intertidal areas and the unique array of radionuclides present in the estuarine sediments. In addition, the surface activities of Sellafield-derived radionuclides in the Ribble Estuary have been shown by a number of studies to have a strong association with sediment grain-size (Assinder *et al.*, 1997; Brown, 1997). Preliminary reflectance studies have shown that intertidal sediments of contrasting grain-size can be distinguished spectrally (Tyler *et al.*, 1995; Bryant *et al.*, 1996). From these preliminary investigations it was determined that remote sensing may be used to map the surface radionuclide distributions in the Ribble Estuary. Consequently, through a series of detailed *in situ* and laboratory investigations, coupled with the acquisition of low-tide imagery, this study examines the capacity of airborne remote sensing for monitoring Sellafield-derived radionuclides in the surface intertidal sediments of the Ribble Estuary.

1.2 CONVENTIONAL MEASUREMENT OF ESTUARINE RADIOACTIVITY

Enhanced radioactivity levels, as a result of nuclear weapon testing fallout and authorised discharges, are a common feature of both our terrestrial and marine environments. Attempts to measure these activities through point sampling can lead to a misrepresentation of their spatial distribution. Nevertheless, point sampling is the most common technique used to monitor the spatial distribution of radionuclides in an estuarine environment (*e.g.* Aston and Stanners, 1982; Assinder *et al.*, 1997; Brown, 1997). This involves the interpolation between a limited number of sample sites identified as being representative of the intertidal radionuclide distribution. Primarily the distances between the sample points determine the spatial accuracy of the subsequent characterisation. However, financial constraints and intertidal accessibility often pre-set the number of sample points and, consequently, the distance between them. Brown (1997) attempted to quantify the spatial distribution of the surface intertidal radionuclides in the Ribble Estuary through point sampling. However, during this study only six sites within the estuary were sampled and, consequently, many of the subsequent conclusions regarding radionuclide redistribution and estuarine trends were potentially biased by the spatially incomplete dataset.

Airborne gamma surveying is an established alternative to point sampling when monitoring estuarine radionuclide distributions. This technique is well suited to large-scale environmental surveys for baseline monitoring and emergency response (Sanderson *et al.*, 1995). In September 1992, airborne gamma surveying was used to monitor the activities of the saltmarshes and exposed intertidal sediment in the Ribble Estuary (Sanderson *et al.*, 1993). However, the coarse spatial resolution (200 - 400m)

limits the ability of this technique to identify radionuclide sources and sinks in the intertidal environment at a scale for process-based interpretations. Consequently, this inhibits the definition of radionuclide distribution processes at geomorphological scales, which is crucial to the understanding of sea to land transfer of radionuclides. This technique is also unsuitable for providing information about the distribution of low-energy gamma emitters (*e.g.* ^{241}Am, ^{234}Th) and radionuclides that emit no gamma ray (*e.g.* ^{99}Tc). In addition, this technique is both expensive (*e.g.* helicopter and manpower costs) and time-consuming (*e.g.* multiple flight lines necessary due to narrow swath-width), which makes it inappropriate for extensive investigations. To summarise, it is apparent that a need exists in environmental radioactivity research for a relatively fast, inexpensive, high-resolution synoptic tool, which is capable of monitoring Sellafield-derived radionuclides.

1.3   THESIS AIMS AND CONTRIBUTIONS

The primary objective of this study is to develop and validate an airborne remote sensing technique for monitoring radionuclide distributions in surface intertidal sediments. This study also examines a range of subject areas including environmental radioactivity, sediment reflectance and image analysis and classification.

In Chapter 2, the general morphological, sedimentological, faunal and floral characteristics of estuarine environments are reviewed. In particular, this includes the characteristics of the Ribble Estuary as defined by previous studies. The source, transport and distribution of a suite of radionuclides that are present in the Ribble Estuary are also reviewed in this chapter. In addition, previous *in situ* and image

4

investigations of intertidal environments are discussed. Lastly, comparisons are made between the various image processing, analysis and classification techniques that are available. Chapter 3 provides descriptions of the principal techniques used in the reflectance, sedimentological, radiological and image investigations of this project. This includes a brief outline of the decisions behind the selection of the image analysis techniques.

The thesis objective is realised through the remaining chapters. Chapter 4 describes a detailed investigation of the spectral characteristics of Ribble Estuary intertidal sediment. This includes a range of laboratory and *in situ* reflectance studies into the influence of grain-size and moisture on the reflectance of sediment. The implications of the results on the subsequent collection and analysis of airborne imagery are also outlined.

The Daedalus 1268 Airborne Thematic Mapper (ATM) imagery of the Ribble Estuary provided by the Natural Environment Research Council (NERC) is described in Chapter 5. The image preparation procedure, which includes radiometric, geometric and atmospheric correction, is detailed. The subsequent analysis and classification of the ATM imagery of the exposed intertidal areas is outlined and this includes the validation and calibration procedures used to define the accuracy of the overall methodology. In Chapter 6, the clay distribution images of the Ribble Estuary, described in the previous chapter, are converted into maps of surface Sellafield-derived radionuclide activities. The relationships between sediment grain-size and radioactivity that are used in the conversion are detailed and reviewed. The accuracy of the subsequent activity images is examined and the radionuclide distribution as described by the imagery is summarised.

Lastly, chapter 6 considers the various controls on the radionuclide sources and sinks that have been identified in the Ribble Estuary.

In the final chapter, the implications and contributions of this study are analysed and discussed. The findings described in each chapter are compared with each other and placed into the context of previous research. The success of this project to map intertidal sediments and, consequently, to monitor surface intertidal activities in the Ribble Estuary is discussed. A range of potential adjustments to the methodology is suggested and future applications of this study are outlined. This includes the identification of other estuaries that may be mapped through a similar methodology. Finally, the main conclusions of this study are summarised.

1.4   SUMMARY

It is acknowledged that Sellafield-derived radionuclides have a complex distribution within the surface sediments of estuarine intertidal areas. Conventional point surveying methods and aerial gamma surveys lack the spatial resolution to accurately quantify surface activity distributions, which is necessary for process-based investigations. Consequently, there is a requirement for a high spatial resolution, synoptic technique that can accurately identify the radionuclide contents of the surface sediment.

The objective of this project is to develop a valid airborne remote sensing technique for high-resolution monitoring of surface intertidal radionuclides in estuarine environments. The technique will be based on relationships between sediment reflectance, grain-size and radionuclide content. These relationships are to be identified and defined within the

Ribble Estuary study area and this is expected to lead to the successful creation of surface activity images from remotely sensed data. In doing so, this will validate an innovative, cost-effective and accurate tool for mapping surface distributions of anthropogenic radionuclides.

2. ESTUARIES, RADIONUCLIDES AND REMOTE SENSING

2.1   INTRODUCTION

This project brings together three very diverse fields of research namely environmental radioactivity, estuarine sedimentology and optical remote sensing. Since there have been no previous attempts to map radionuclides using conventional airborne remote sensing, this chapter looks in detail at a range of related remote sensing studies. The project study area, the Ribble Estuary, is also introduced and its importance as a sink for BNFL Sellafield and Springfields derived radionuclides is examined.

2.2   ESTUARINE ENVIRONMENTS

2.2.1   Estuaries

Estuaries are geologically young, dynamically evolving landforms, which act as important and well-used interfaces between the human population and coastal and marine activities. An estuary is defined as an inlet of the sea reaching into a river valley as far as the upper limit of tidal rise, usually being divisible into three sectors: (a) a marine or lower estuary, in free connection with the open sea; (b) a middle estuary, subject to strong salt and freshwater mixing; and (c) an upper or fluvial estuary, characterised by freshwater but subject to daily tidal action (Fairbridge, 1980). They may belong to one of three broad classes, salt-wedge, partially-mixed, or well-mixed, depending on the extent to which the freshwater river discharge mixes with the tidal saltwater (Bowden, 1980). Partially mixed estuaries, such as the Ribble Estuary (Burton, 1994; in Brown, 1997), have a significant vertical density gradient. Due to

tidal currents, vertical mixing extends throughout the depth, resulting in a gradual increase in salinity from the surface to the bottom. In addition, turbulence, caused by friction at the estuary bed creating shear stress, enhances the mixing at the saltwater/freshwater interface. A two-layered flow structure exists, with the seaward flowing water in the upper layer and the landward flowing water in the lower layer. A surface of no motion exists between the layers, slightly above the mid-depth line. Bowden (1980) estimates that the flow in both layers is typically an order of magnitude greater than the river discharge, while the oscillatory tidal currents may be two orders of magnitude greater.

2.2.2 Estuarine Sedimentation

Conditions for sediment deposition are more favourable in estuaries than in most other marine environments due to the shelter offered against both strong waves and offshore currents, allowing fine particles time to settle. Postma (1980) suggests there are three main mechanisms for near-shore sediment accumulation, 1) wave transport of coarse material *e.g.* sand and pebbles, 2) tidal transport of fine-grained sand and silt and 3) estuarine circulation which enables silt and mud deposition. In partially-mixed estuaries, such as the Ribble, the landward bottom flow moves both fluviatile and marine suspended sediment to the head of the tidal intrusion where a turbidity maximum develops. The high concentration of suspended sediments combined with the turbulence at this point encourages settling.

The process of suspended sediment settling is augmented in two ways, biological aggregation and flocculation (Postma, 1980). The ingestion and subsequent excretion of small clay particles by organisms results in faecal pellets, which have a greater settling

9

velocity. Flocculation is the process whereby molecular attractive forces of clay particles cause clay floccules to form. This is only possible in saltwater where interaction between free cations neutralises the negative charges of the particles that would normally cause clays to repel. If the water is agitated the particles collide more often, resulting in faster floccule growth. Floccules settle much faster than individual grains, promoting estuarine trapping of fine sediments.

2.2.3 Estuarine Tidal Flats

Tidal flats develop wherever wave energy is relatively low and usually have very low gradients (1:1000). Although dominantly mudflats, tidal flats often include large sand and silt domains and are commonly dissected by tidal channels, with saltmarshes predominantly located on the landward side. The low tidal areas are submerged and, consequently, under the influence of currents for a longer period of time, resulting in the fine sediments remaining in suspension and only bedload sediment i.e. coarse sand, being deposited. Mud flats, which form in the landward intertidal areas, are only submerged at high tide i.e. when current speeds fall to zero. During this period of slack water the fine sediments, still in suspension, are able to settle. The aggregates of clay, silt and organic material, formed by flocculation and biological activity, combine to form cohesive fine sediment beds. The shear strength and bulk density of these sediments increases rapidly with depth, due to moisture loss and compaction. Unlike the coarser tidal flats, with relatively uniform shear strength, the ability of tidal currents to resuspend mudflat sediments decreases with sediment depth (Mehta, 1989). Where soft mud occurs it is generally homogenous and indicates that sedimentation is rapid.

When mudflat sedimentation is relatively slow the sediment is better oxygenated and, consequently, supports a greater species diversity, with macrofauna being more abundant (Dyer, 1998). In contrast, where sedimentation is rapid, the biology tends to be poor with a predominance of worms. Similarly, the distribution of sediment particle sizes in tidal flats has a strong influence on macrobenthos density. This is illustrated in a study of The Wash estuary, which associated changes in sediment characteristics, due to reclamation, to changes in bird feeding (Goss-Custard and Yates, 1992). The number of observed Dunlin and Redshank were positively correlated to mud distribution and the number of Oystercatchers and Bar-tailed Godwit were negatively correlated. In conclusion, a map of estuarine sediment distribution could be used to infer the distribution of various bird population feeding areas.

Microphytobenthos, such as cyanobacteria and diatoms, are a common feature on the soft substrates of estuarine tidal flats (Dyer, 1998). Cyanobacteria (blue-green algae) are a large and varied group of bacteria that possess chlorophyll a, enabling them to carry out photosynthesis in the presence of light and air. An example species common on intertidal flats, is *Chlorella scopulorum*, which liberates its extracellular nitrogen as peptides and free amino acids. Where cyanobacteria are in abundance at the mudflat surface, they are visible to the eye and have a characteristic colour, which may vary from green, blue-green, or olive-green to various shades of red to purple or black. Although colour may be used to indicate the presence of cyanobacteria, final identification is not possible in the field. The Nature Conservancy Council's report on Aquatic Estuarine Communities (1991) found that reduced salinity mudflats usually had a green covering which they identified as 'blue-green algae and diatoms'. Diatoms are especially related to cyanobacteria, and may be recognised by the characteristic brown patches of coloration they produce and the slight

mounds on which they form (Dyer, 1998). These are generally abundant everywhere in estuaries except at levels approaching the high-water mark where conditions of drainage are such that the sediments may dry out. Generally cyanobacteria penetrate only the top 5mm of the sediment, however diatoms are motile and may migrate to depths of 18cm (McLusky, 1989). Cyanobacteria and diatoms play an important role in the accretion of saltmarshes by stabilising the sand and mud and building up humus. This was demonstrated by Sutherland *et al.* (1998) in a series of laboratory and field studies to determine the effect of biofilms on sediment erodibility. From comparisons of biotic and abiotic sediment, it was found that the diatom, *Nitzschia curvilineata*, increases the erosion threshold of sediment (*i.e.* makes the sediment more stable).

2.2.4 Sediment Class Definitions

Within this study a number of terms are used with reference to estuarine sediment types with particular clay (<2μm), silt (>2μm and <63μm), and sand (>63μm) components. To avoid later confusion, these terms are defined within the context of this study.

The term 'mud' refers to fine intertidal sediment, which is dominated by the silt fraction and has a high proportion of clay (>6%) in comparison to other intertidal sediment types. The term 'silt' refers to intertidal sediments with large silt and sand components, the clay component is typically less than 6%. The term 'sand' refers to sediment that is primarily made up of the sand fraction and has less than 1% clay. In addition, the terms 'endmember mud' and 'pure mud' are used in later discussions and these refer to a silty sediment with very high relative clay content (*c.*12%). The terms 'endmember sand' and 'pure sand' are also used and these refer to sediment with a very low clay content (*c.* 0.5%).

12

2.3   RIBBLE ESTUARY

2.3.1 Location and Dimensions

The Ribble Estuary, Lancashire joins the Irish Sea at Lytham St. Annes (Figure 2.1). It is 85km due south of Sellafield, with Blackpool and Southport close to the estuary mouth. The estuary is macrotidal, experiencing diurnal tides of 4 meters and the normal tidal limit reaches above Preston Docks (Brown, 1997). The upper estuary is narrowly constrained between two banks, whilst the mouth is large and wide. The dimensions of the estuary and its intertidal zone are detailed in Table 2.1 (Buck, 1993).

Table 2.1 Ribble Estuary Dimensions (Buck, 1993)

Total area (ha)	Intertidal area (ha)	Shore length (km)	Channel length (km)	Mean tidal range (m)
11,920	10,670	107.5	28.4	7.9

2.3.2 Catchment Geology

The River Ribble rises in the Yorkshire Dales and travels 80 miles through Settle, Clitheroe, Ribchester and Preston before reaching the Irish Sea. The solid geology at the source is predominantly Carboniferous limestones with overlying Permian sandstones and mudstones (HMIPa, 1994). Further south the river crosses the Craven faults where the geology is a mix of Dinantian limestones, Carboniferous grits and Namurian shales. Near the tidal limit, the river passes over sandstone of the Sherwood Sandstone Group and, finally, Singleton Mudstones of the Mercia Mudstone Group. The Ribble River tributaries to the north cross a similar geology, however the southern tributaries cross a distinct suite of rock types, which include Westphalian coal measures. This unit is of particular importance due to its natural uranium and thorium content (HMIPa, 1994; Brown, 1997).

13
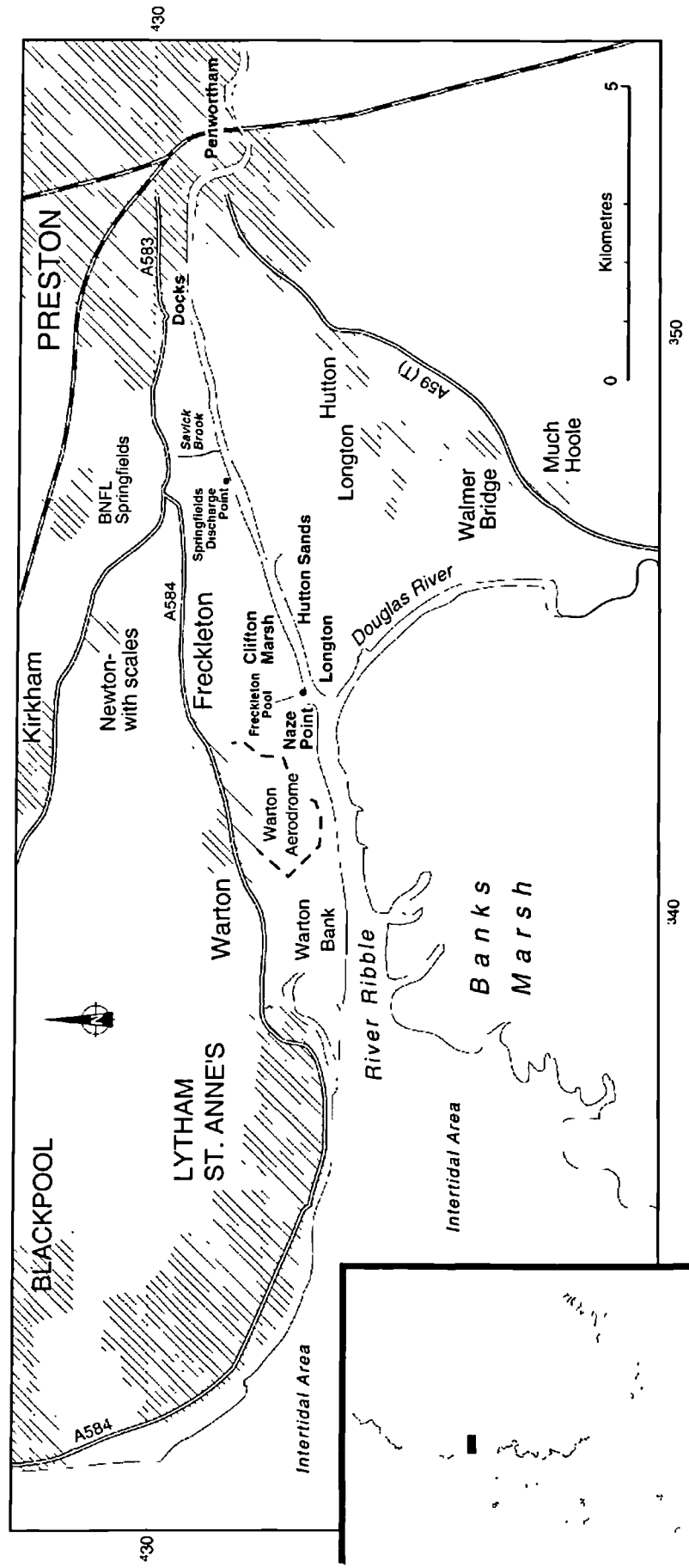
Figure 2.1 Map of the Ribble Estuary

14

Successive Pleistocene glaciations result in most of the River Ribble catchment having a covering of glacial boulder clay. In the main channel and 1km either side, recent alluvium cover can be observed, which is evidence for substantial channel movement in the past. At the source of many of the tributaries, glacial sands and gravels are located. Boulder clay, peat, marine and estuarine fluvial deposits and blown sand cover the sandstones and mudstones at the mouth of the estuary (HMIPa, 1994).

2.3.3 Estuarine Sediment Mineralogy

The fluvio-glacial deposits on the floor of the Irish Sea are the dominant source of sediment to the Ribble Estuary, although the input of fine sediments are thought to be mainly alluvial in origin (Brown, 1997). In 1994, detailed mineralogical investigations of the intertidal sediments within the estuary were carried out by Brown (1997). Whole-rock mineralogical analysis of twelve intertidal mud samples determined that all the samples were dominantly quartz with associate plagioclase, orthoclase, calcite, dolomite, chlorite/kaolinite and mica. Clay mineralogical analysis determined that illite was the dominant clay mineral, with smectite, kaolinite and chlorite present as minor components. Throughout the estuary, variability in the mineralogical composition of the sediments was found to be low. Brown (1997) suggests this is due to the sediments having the same source and subsequent homogenisation through reworking and mixing.

Bryant *et al.* (1996) sampled a selection of sites (A-I) at Warton Bank and established that the fine-grained sediment is composed of illite, smectite with associated kaolinite and chlorite and the coarse-grained sediment is composed of quartz with associated aragonite, plagioclase, calcite, dolomite and orthoclase (Figure 2.2). Halite is occasionally present as an efflorescent deposit on the polygonated dry muds.

15
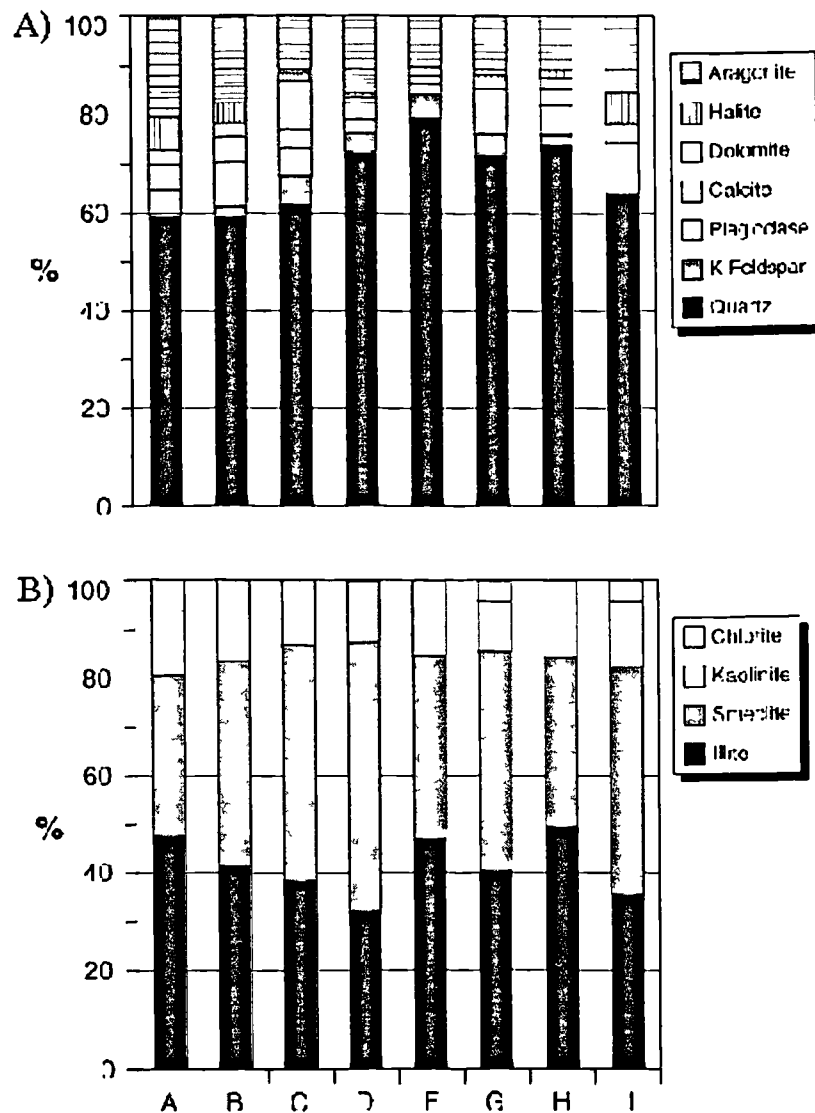
Figure 2.2 A) Whole Sample Mineralogy and B) Clay Mineralogy of Intertidal Sediment Collected from Warton Bank Sample Sites, A to I (Bryant *et al.*, 1996)

2.3.4 Sediment Dynamics

At three sites along the Ribble Estuary, measurements of vertical velocity and salinity distributions carried out by Burton *et al.* (1995) revealed strong stratification during the ebb tide and little stratification on the flood tide. Vertical shear-induced dispersion dominated during the ebb tide and turbulent dispersion was observed as the most important mixing component during the flood tide. This results in significantly more dispersion on the ebb tide as opposed to the flood tide. Burton *et al.* (1995) also stated

16

that tidal 'pumping' caused by tidal asymmetry and vertical density effects led to upstream storage of mud. Lyons (1997), who also recognised upstream sediment transport to be a product of tidal 'pumping', added that the freshwater induced currents were the dominant control of downstream transport. Lyons (1997) stated that whilst tidal 'pumping' was dominant during a spring tide, it was significantly reduced during a neap tide. This results in no net transport during the neap tide and an overall net increase in estuarine sediment.

Although it is accepted that there is a net influx of sediment into the Ribble Estuary, this sediment is not uniformly distributed. A survey, carried out between 1991 and 1993, found that areas such as Freckleton Pool, Savick Brook and the upper Ribble main channel (*e.g.* Penwortham Park) act as sinks for the fine grained sediment during spring tides (Mudge *et al.*, 1997b). Suspended sediment settles out at the tidal limits during periods of low-river flow resulting in rapid sediment accumulation. Subsequent high-river flow remobilizes and deposits this sediment further down the estuary. High tides may then remobilize the sediment and return it to the tidal heights. This is described as an oscillatory movement, attributed to the length of the estuary and its restriction to a narrow channel near Preston (Mudge *et al.*, 1997b). There is no evidence for any significant loss of sediment during a normal tidal cycle, and it has been established that most of the sediment comes from outside the estuary.

Based on radiocaesium profiles, Mamas *et al.* (1995) estimated the sedimentation rates, from 1982 onwards, of the intertidal sediments along the Ribble Estuary (Table 2.2). However, although these results are useful, they provide no information about the cycle of sediment erosion and deposition. In contrast to the earlier study, Brown (1997)

examined the short-term erosion and accretion within the estuary. Sediment traps were positioned at six equally distanced points between Lytham and Penwortham and sampled monthly over an eighteen-month period (Figure 2.3). The subsequent results suggest that the mouth of the estuary is undergoing a net loss of sediment whilst the inner estuary is rapidly infilling (Table 2.3). Brown suggests this process may be augmented by the cessation of dredging in the early 1980's.

Table 2.2 Estimated Sedimentation Rates in the Ribble Estuary (Mamas *et al.*, 1995)

Location	Contemporary Sedimentation	Average Sedimentation
Lytham	No Data	~ 100mm/y
Naze	15-20mm/y	~ 40-45mm/y
Preston Docks	~ 20-25mm/y	~ 40-45mm/y
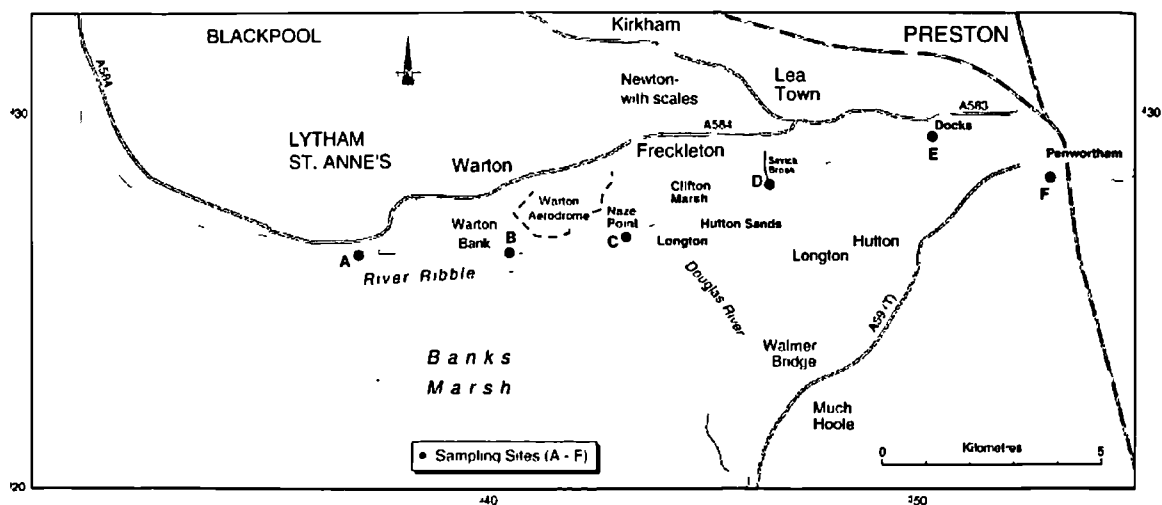
Figure 2.3 Location of the Sites Sampled by Brown (1997) on a Monthly Basis

Table 2.3 Annual Sediment Accumulation/Erosion for Sample Sites in the Ribble Estuary (Brown, 1997)

Sampling Site	Annual Accretion (cm)	Status
Lytham	-7.1	Erosional
Warton	-3.3	Erosional – neutral
Naze	+29.3	Accretional
Clifton	+4.1	Neutral
Docks·	+11.8	Accretional

18

2.3.5 Estuarine Flora and Fauna

Behind the intertidal flats of the Ribble Estuary, stretch extensive saltmarshes including one of the largest areas of unbroken saltmarsh in Britain (Buck, 1993). The unimproved nature of these areas means a variety of saltmarsh plants are preserved. In addition, the nationally rare dune plant *Epipactis dunensis* is found on dunes adjacent to the estuary.

The Ribble Estuary contains a diverse fauna including the natterjack toad, the sand lizard, grey seals, a range of invertebrates and a large bird population. The estuary supports ten internationally important populations and ten nationally important wintering populations of waterfowl. The Ribble is also the main centre in England for pink-footed geese (Buck, 1993). Within the estuarine intertidal flats however, a general lack of burrowing organisms was observed by Mamas *et al.* (1995).

2.3.6 Human Influences and Activities

In the late 19th and early 20th Century extensive engineering work was carried out to improve navigation in the estuary, which resulted in a relatively straight, narrow channel. Training walls were constructed facing the main channel position and consequently these allowed mudflats and saltmarsh regions to form. Since the early 1980s dredging of the estuary ceased, resulting in extensive siltation of the channel (HMIPa, 1994).

At present there are a large number of human activities based in the Ribble Estuary. Leisure pursuits include sailing in the main channel, trail-biking, horse-riding and various forms of racing on the sand dunes and sandflats in the south of the estuary. Industrial activities, although limited in the estuary, include gas exploration, commercial

19

sand extraction, and various forms of fishing and shellfish collection. Of the surrounding saltmarsh, approximately 98% is commercially grazed and *Salicornia* picking occurs on 10ha (Buck, 1993).

2.4 RADIONUCLIDES

2.4.1 Sources of Radionuclides in the Irish Sea

Sellafield

A wide range of contaminants are discharged under licence into the Irish Sea, including an array of fission products and actinides, from the nuclear fuel reprocessing plant BNFL Sellafield, which is the largest nuclear complex in the U.K. (McDonald and Jones, 1997). Sellafield has discharged radioactive waste since 1952, under authorisation from EA and MAFF, through a pipeline that extends 2.1km from the low-water mark and ends 20m below the surface of the water. The quantities of radionuclides discharged have changed markedly with time, with peak discharges of ^{241}Am in 1974 and of ^{137}Cs in 1975 (Figure 2.4). Tritium dominates all marine discharges from Sellafield, however it is one of the least radiologically significant radionuclides per unit discharge. Of the discharged radionuclides, ^{238}Pu, ^{239,240}Pu, ^{241}Pu, ^{241}Am, ^{134}Cs and ^{137}Cs are of primary interest due to the large quantities released into the sea, their relatively long half-lives, their biological affinity and radiotoxicity.

Springfields

Another source of radionuclides to the Irish Sea, and more importantly to the Ribble Estuary, is BNFL Springfields (Figure 2.1), which manufactures fuel and fuel products for nuclear power stations in the UK and abroad. Most of the work involves the

purification of uranium ore concentrates with a smaller input of recycled uranium from Sellafield (HMIPa, 1994). The main radionuclides present in the liquid effluent produced are ^{234}Th, ^{232}Th and ^{230}Th and significant quantities of daughter nuclides (McCartney *et al.*, 1992). This effluent is continuously discharged (Figure 2.5), under authorisation by EA, through a pipe to a location 20km from the mouth and 11km downstream from the normal tidal limit of the Ribble Estuary (Figure 2.1).
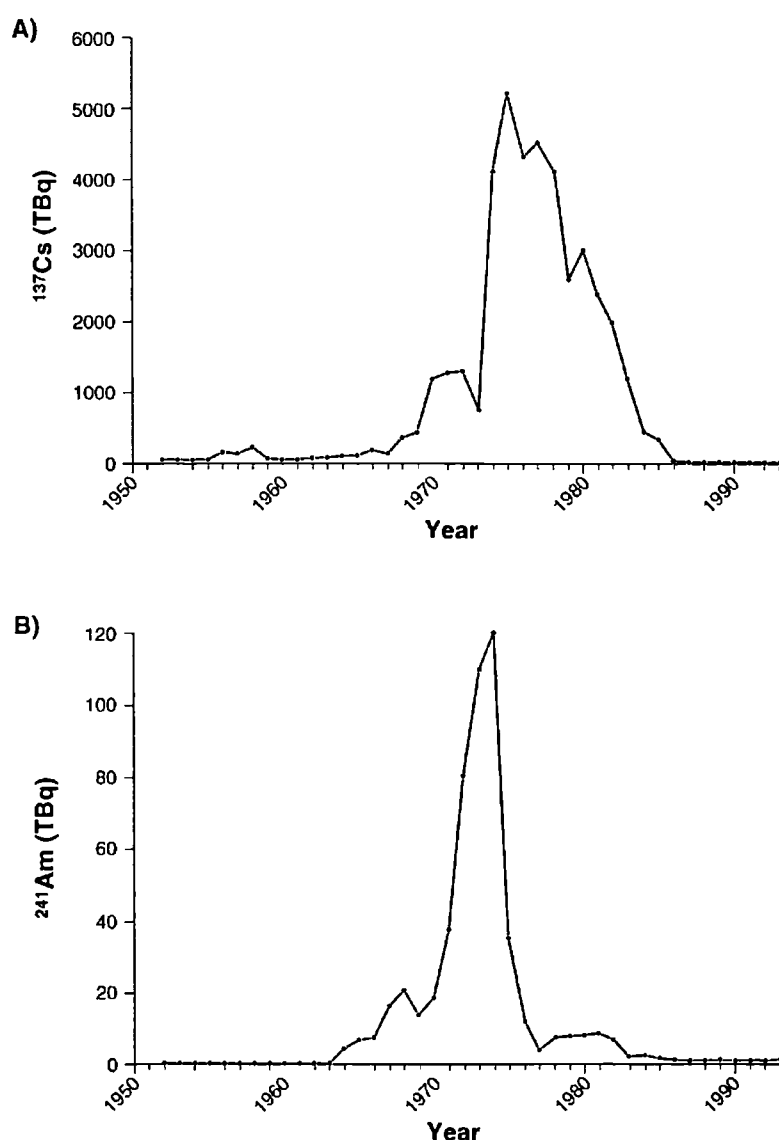
Figure 2.4 Discharges of a)^{137}Cs and b) ^{241}Am in Liquid Waste from Sellafield, 1952-1993 (Hunt, 1997)
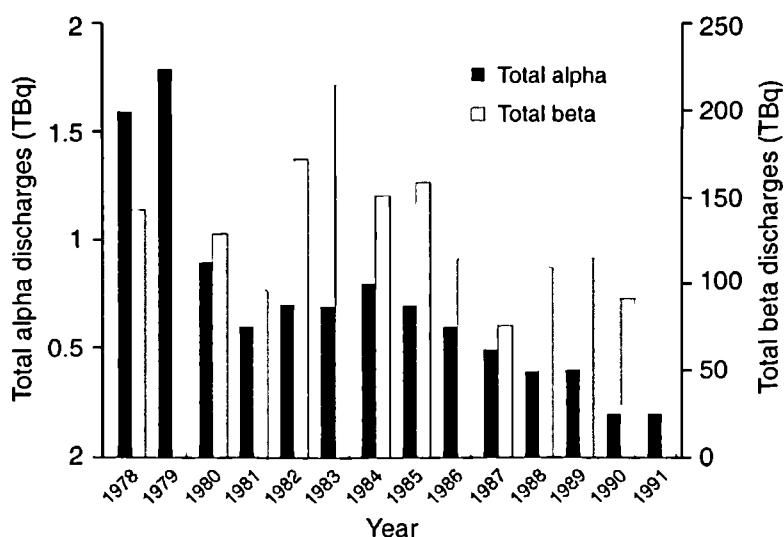
Figure 2.5 Annual Discharges from BNFL Springfields into the Ribble Estuary (HMIPa, 1994)

2.4.2 Geochemical Behaviour of Anthropogenic Radionuclides

A large suite of radionuclides is present in the intertidal sediments of the Ribble Estuary. Sellafield-derived anthropogenic radionuclides such as ^{137}Cs, ^{134}Cs, ^{241}Pu and ^{241}Am are the most common, though Springfields-derived technically enhanced (^{234}Th and ^{234}Pa) and natural (^{232}Th, ^{238}U and ^{40}K) radionuclides are also present. To understand the distribution of these radionuclides within intertidal sediments of estuaries, an awareness of their geochemical behaviour is necessary. The Sellafield-derived radionuclides, ^{137}Cs and ^{241}Am, are of primary interest to this project and are described in detail.

Radiocaesium

Radiocaesium exhibits straightforward chemical behaviour as a metal from Group I, existing only in a single oxidation state. The isotope, ^{137}Cs, is a fission product discharged by Sellafield, with a half-life of 30 years. Caesium behaves 'conservatively' meaning the bulk of its inventory is transported in solution with only a small fraction being adsorbed to sediment particulate. The ^{137}Cs distribution coefficient (K_d = Activity

per unit mass solid/Activity per unit volume liquid) is relatively low, around 3×10^3 in coastal waters (IAEA, 1985).

Caesium is preferentially adsorbed on clay minerals, specifically illitic clay minerals as a result of their small hydrated radii (Hird and Rimmer, 1995). Usually large strongly hydrated ions are adsorbed in preference to Cs^+ ions on the external and expanded internal surfaces of the clay minerals. These ions are however physically unable to adsorb on the interlayer surfaces close to collapsed central regions of individual illite crystals called 'wedge zones'. Weakly hydrated ions such as Cs^+ can adsorb on these specific sites, neutralising the charge on the internal surfaces of the clay. This can result in further inter-layer collapse leading to fixation of the caesium ions. The predominant association of caesium with clay has been recognised in a number of environments including freshwater sediment (Francis and Brinkley, 1976; Pardue *et al.*, 1989,), Cumbrian soils (Livens and Baxter, 1988), intertidal sediments (Jones *et* al., 1984; Assinder *et al.*, 1997; Clifton *et al.*, 1997) and saltmarsh sediments (Assinder *et al.*, 1997; Brown, 1997).

However, the caesium radionuclides in the Irish Sea water are in disequilibrium with the older sediment bound radionuclides, due to significantly reduced contemporary Sellafield discharges. Consequently, remobilization of 'fixed' caesium radionuclides from clay minerals is an important process (Hunt and Kershaw, 1990; Cook *et al.*, 1997). This occurs within the interlayer sites of the illite crystals, where caesium exchanges with NH_4^+, and is released into the water phase. Hunt and Kershaw (1990) estimated that 600TBq of ^{137}Cs was released by this process between the period 1983 and 1988 in the Sellafield offshore vicinity.

Plutonium and Americium

Plutonium (Pu) and Americium (Am) are part of a group of artificial elements called actinides, which have atomic numbers of 93 and above. ^{239,240}Pu exists in the seawater of the Irish Sea in a number of oxidation states, with more than 90% in the oxidised forms (V and VI) and Pu (V) predominating (McDonald and Jones, 1997). Pu isotopes have variable half-lives (^{239}Pu, 24110yrs; ^{240}Pu, 6537yrs; ^{241}Pu, 14.4yrs) and the IAEA recommended mean K_d value in coastal waters is 1 x 10^5. ^{241}Am has a half-life of 432.2 years, it usually exists in the (III) oxidation state and in coastal waters its mean K_d value is 2 x 10^6 (IAEA, 1985).

Plutonium and americium behave 'non-conservatively' following discharge by Sellafield into the Irish Sea, with the bulk of the inventory rapidly associating with suspended and bed sediments. Pu and Am adsorption is dependent purely on the availability of reaction surfaces and an equilibrium state (K_d) between the dissolved and the particulate-associated phases is generally reached quickly in a marine environment (McKay and Pattenden, 1993). However, a significantly larger proportion of adsorbed Pu is in equilibrium with the surrounding seawater, than adsorbed Am. McKay and Pattenden (1993) suggest this difference is due to different adsorption mechanisms rather than the adsorption substrates. The Am inventory in deposited sediments can be augmented if ^{241}Pu, which can decay by beta emission to produce ^{241}Am, is also present. This can complicate the distribution of ^{241}Am in the environment because ^{241}Pu has different chemical properties and is therefore subject to different transfer mechanisms.

Natural radionuclides

Thorium and uranium are common natural radionuclides found in the Irish Sea. In the Ribble Estuary these radionuclides (specifically ^{234}U, ^{238}U, ^{228}Th, ^{230}Th, ^{232}Th, ^{234}Th and ^{234m}Pa) are present at enhanced levels due to the release of significant quantities of these nuclides by BNFL Springfields. For example, in Ribble sediments the ^{238}U concentration ranges from 3-111 Bq kg^{-1} (Assinder *et al.*, 1997), compared to 3.6-22 Bq kg^{-1} for the fine-grained sediments of a range of other UK coastal sites (McDonald *et al.*, 1991).

Thorium is relatively insoluble in most natural waters and as a result is entirely transported in particulate form. Consequently, the spatial variation of ^{228}Th, ^{230}Th, and ^{232}Th activity concentrations in intertidal sediment is generally related to the grain-size distribution (Assinder *et al.*, 1997). Thorium has a mean K_d value of 5×10^6 (IAEA, 1985), indicating its particle reactive nature. Unlike the other isotopes there is a poor relationship between ^{234}Th (and consequently ^{234m}Pa by decay) and sediment grain-size in the Ribble Estuary because of short half lives and discharge trends.

Uranium normally exists as three isotopes with mass numbers 234, 235 and 238. U has a mean K_d value of 5×10^2 and hence behaves 'conservatively' with the bulk of its inventory transported in solution. In the Ribble Estuary the ^{234}U and ^{238}U activity concentrations increase with increasing proportion of grains less than 63μm (Assinder *et al.*, 1997).

2.4.3 Radionuclide Behaviour in the Irish Sea

The Irish Sea is a semi-enclosed body of water, with a surface area of 1×10^5 km and a mean depth of 60m. It is effectively divided into two regions to the east and west of the Isle of Man. The western part consists of a deep channel (>100m), whereas depths in the eastern Irish Sea seldom exceed 50m. There is a net transfer of water northwards through the North Channel, resulting in a mean water residence time of about 18 months (Bowden, 1955; in McKay and Pattenden, 1993). The dynamics of the Irish Sea are dominated by tides that are propagated in the Atlantic with large variations in amplitude. Around the Sellafield area, these tides tend to oscillate, flowing south-east parallel to the coast during weak tides and north-west during storms. In general, the bottom sediments of the Irish Sea consist largely of sand and gravel, with areas of mud and sandy-mud close to the Sellafield discharge point and between the Isle of Man and Ireland (Wright *et al.*, 1971; in McKay and Pattenden, 1993).

The 'conservative' behaviour of caesium means that after discharge from Sellafield it predominantly remains in solution, with approximately 10% attached to the Irish Sea sediments (MacKenzie *et al.*, 1994). In contrast, almost all the Am and most of the Pu is taken up immediately by the sediments close to the discharge point. The result is a concentration of waste radionuclides in a deposit of silt and mud offshore from Sellafield. MacKenzie *et al.* (1987, 1994) concluded that the dominant transfer mechanism of caesium and actinides to intertidal areas of the NE Irish Sea is redistribution of the contaminated sediment near Sellafield (Figure 2.6). The study also concluded that, due to predepositional mixing of the accumulating intertidal sediments, it is impossible to decipher the temporal variations in individual releases. This is based on the maximum radionuclide concentrations observed in the intertidal sediment

occurring several years after the maximum discharges and the lag times varying for each radionuclide. In agreement with this study, Brown (1997) implied from observed vertical distributions of Sellafield-derived radionuclides in the Ribble Estuary saltmarshes that the transport mechanism included the mixing of recent and historical contamination before deposition. Cook *et al.* (1997) confirmed that particle associated transport dominated in the north-eastern Irish Sea, but stated that this is not the case in the North Channel area.
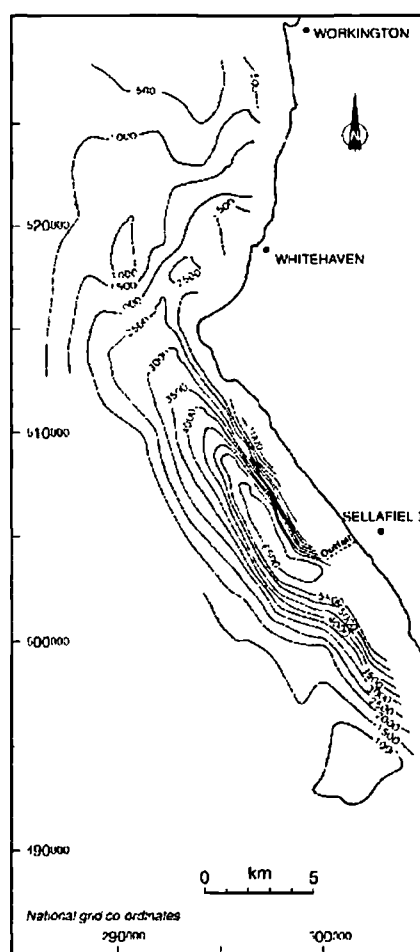
Figure 2.6 Distribution of ^{137}Cs (Bq kg^{-1}) in Seabed Sediments in the Eastern Irish Sea for the year 1982 (Jones *et al.*, 1988)

At present the Sellafield discharges are approximately two orders of magnitude less than those in the mid-1970s. This results in relatively low contemporary concentrations of

27

radionuclides in the seawater, which leads to dissolution of the radionuclides from the sediment. As stated earlier, there is no evidence that caesium and the actinides are irreversibly bound to the sediments. MacKenzie *et al.*, (1994) calculated that dissolution reduced the concentration of ^{137}Cs and the actinides in depositing intertidal sediments of the Solway Coast by half over 3-4 years and 4 -7 years respectively. Based on seawater samples from the north-east Irish Sea, Cook *et al.* (1997) estimated halving times of 350 years for ^{239}Pu and ^{241}Pu and 7-12 years for caesium. Both of these studies demonstrate that caesium is affected more significantly than the actinides by redissolution. In 1992, a core was collected from the mud/silt area offshore from Sellafield and examined by McDonald *et al.* (1993). In addition to demonstrating that these sediments were well mixed, it found that ^{137}Cs redissolution was significant to a depth of 25cm. McDonald *et al.* (1993) concluded that due to the low magnitude of contemporary discharges, redissolution of historical deposits represents a significant source of radionuclides to the intertidal areas of the Irish Sea.

2.4.4 Radionuclides and Estuaries

In many estuaries, the distribution of radionuclides in the surface sediments of intertidal environments has been directly correlated to sediment grain-size. Stanners and Aston (1981) examined the distribution of ^{137}Cs in the sediments at 30 sites along the Cumbria and Lancashire coasts. This study confirmed the sediment/radioactivity relationship and estimated lag times of up to 6 years between radionuclide discharge and coastal deposition. Assinder *et al.* (1985) studied the Esk Estuary, NW England, and concluded that its physical characteristics and proximity to Sellafield controlled the behaviour of the radionuclides. The particulate activities were high and a major part of this total activity was made from reworked earlier deposits. The study also concluded that the

total water activity for radionuclides with low K_d values (*e.g.* Caesium) had a distribution similar to salinity, whilst 'non-conservative' radionuclides, such as Pu, followed the pattern of suspended sediment. Aston and Stanners (1982) confirmed the influence of grain-size on the geographic distribution of ^{137}Cs in surface sediments of the Ravenglass Estuary, NW England. This conclusion was used to account for the increase in radionuclide activities up the estuary of the River Irt from the sea. Lastly, Clifton *et al.* (1997) examined the relationships between particle-size, radionuclide content and magnetic properties of the intertidal sediment from a range of environments in the Eastern Irish Sea. The results confirmed that concentrations of ^{137}Cs and ^{241}Am are highly influenced by the abundance of intertidal sediment less than 32μm. Highly significant correlations were also observed between magnetic remanence and ^{137}Cs. This is due to the dependence of magnetic remanence on grain-size and this study underlined its potential as a grain-size proxy. A poorer correlation between remanence and ^{241}Am activities was evident.

The Ribble Estuary

The Ribble Estuary in particular has been subject to a range of studies by BNFL, MAFF (Ministry of Agriculture, Fisheries and Food), EA (Environment Agency) and University based groups, and many of these have produced maps of the distribution of radionuclides.

An extensive survey of the intertidal surface sediments by Assinder *et al.* (1997), established that the spatial distribution ^{137}Cs, ^{238}Pu, ^{239}Pu, ^{240}Pu and ^{241}Am is related to grain-size distribution. The origin of these radionuclides was determined from ^{238}Pu/^{239,240}Pu and ^{137}Cs/^{241}Am activity concentration ratios as being Sellafield. Brown

(1997) investigated further the relationship between ^{241}Am and ^{137}Cs concentrations and the specific surface area of the intertidal sediments. This study found that although both relationships were significant, specific surface area could not however account for all the activity variation. Brown suggests a range of sources of deviation including: *1)* Some samples may have been exposed to historically contaminated sediment; *2)* High river discharges or tidal changes may have introduced sediment with low ^{137}Cs and ^{241}Am concentrations to the sample areas; *3)* ^{137}Cs adsorbed on internal surfaces of sediments is independent of specific surface area.

Assinder *et al.* (1997) confirmed that the Springfields-derived radionuclides (^{234}U, ^{238}U, ^{228}Th, ^{230}Th, ^{232}Th,) are also significantly related to sediment grain-size. It was established that these radionuclides tend to concentrate in the fine-grained sediments of the upstream areas. A poor relationship, however, was found between ^{234}Th (and consequently ^{134m}Pa) and grain-size. Tyler *et al.* (1995) also found very little regional association between the ^{234}Th activities and the sediment size fractions and concluded that this radionuclide was controlled by localised mixing of discharge effluent with suspended sediments and depositional pathway mechanisms. This is supported by McCartney *et al.* (1992) who collected surface sediment samples along a transect past the mouth of the estuary and analysed them for thorium isotopes. The results of the study suggest that the various thorium isotopes were not being transported out of the estuary, unlike the more soluble ^{226}Ra. Similarly, Brown (1997) concluded from a study of the Ribble Estuary saltmarshes that the Springfields-derived ^{234}Th is rapidly transported from source-to-sink, with little or no mixing with contamination discharged years earlier.

30

From examinations of the radionuclide distributions in the intertidal surface sediments, Assinder *et al.* (1997) concluded that there was no evidence for any long-term change in the activity concentrations, although temporal changes at each site were recognised. The highest activities were measured in the fine-grained sediment adjacent to Penwortham Park and Savick Brook (Figure 2.1). Brown (1997) demonstrated that the surface activities of these areas were temporally very variable. For example at Penwortham in October 1994 the ^{137}Cs activity measured was 729 Bq kg^{-1} and at the same site in February 1995 the activity was only 4.2 Bq kg^{-1}. Brown (1997) also concluded that no well-defined longitudinal trend in specific activities was observed in the estuary. It was suggested that this is a product of the embankments and training walls that exist in the Ribble. In addition, cores collected during this study, in the intertidal sediments of the Ribble Estuary, show that ^{137}Cs and ^{241}Am also have complex vertical distributions, with peak activities occurring at various depths (Table 2.4).

The redistribution of radionuclides and, consequently, dose rates, in the Ribble Estuary is strongly linked to the fine-grained sediment dynamics within the estuary. From analysis of the changes in $^{234}Th/^{137}Cs$ and $^{234}Th/^{239,240}Pu$, Mudge *et al.* (1997b) concluded that Savick Brook (Figure 2.1) is a major contributor of contaminated sediment to other parts of the estuaries. During low-river flow, this area acts as a sink for fine-grained sediment, which is then washed to the outer estuary during high tide. Most of this sediment does not reach the Irish Sea; instead it is transported back up the estuary. Consequently, the contaminated sediment from Savick Brook is redistributed across the whole of the estuary.

Table 2.4 ^{137}Cs and ^{241}Am Surface and Peak Specific Activities, for a Range of Ribble Estuary Intertidal Cores (Brown, 1997)

Core	Surface ^{137}Cs (Bq kg^{-1})	Sub-surface ^{137}Cs Peak (Bq kg^{-1})*	Surface ^{241}Am (Bq kg^{-1})	Sub-surface ^{241}Am Peak (Bq kg^{-1})
Long03	579 ± 8	3350 ± 27 (42)	192 ± 9	499 ± 13
Banks03	442 ± 6	4421 ± 24 (35)	144 ± 7	833 ± 18
War03	574 ± 26	3834 ± 154 (23)	196 ± 28	762 ± 60
War04	205 ± 9	957 ± 42 (33)	85 ± 8	259 ± 31
War05	530 ± 24	3548 ± 138 (32)	235 ± 24	967 ± 51
Clifton	836 ± 16	3301 ± 27 (97)	232 ± 31	610 ± 23
Lytham	368 ± 3	1355 ± 17 (39)	100 ± 4	274 ± 16

* Specific depth (cm) of ^{137}Cs activity peak is shown in brackets in column 3.

Mudge *et al.* (1997a) measured the beta dose and gamma air kerma rates of the Ribble Estuary, and calculated the effective doses to people who frequent the estuary. The gamma air kerma rates were relatively constant during the four visits. Large variations only occurred at areas of rapid accretion or erosion such as Savick Brook. The maximum rate recorded was 192 nGyh^{-1} (where Gy=Gray) at Longton Marsh (Figure 1), and 64% of this was derived from Sellafield discharges. The beta dose rates varied both spatially and temporally due to proximity to, and large variations in, Springfields discharges. A maximum dose rate of 19.4 μSvh^{-1} (where Sv=Sievert) was recorded at Savick Brook, when fine-grained sediments were deposited on a recent tide contaminated with fresh Springfields discharges. The study estimated that groups such as anglers and wildfowlers received maximum doses of 20.8 μSv and 36.2 μSv respectively. Higher dose rates were estimated for dog-walkers and bird-watchers (59.5 μSv) along the main channel and on Lytham Marshes (73.3 μSv). Whilst these dose rates are thought to be relatively minimal, they are however substantial enough to need continual review. From saltmarsh cores, Brown (1997) confirmed that ^{137}Cs is the most significant contributor to the gamma air kerma rate for the saltmarsh environment. The

Springfields-derived ^{234}Pa and ^{234}Th were also identified as potentially important components of the gamma air kerma rate during certain conditions. A clearer representation of the spatial variation of gamma dose rates across the Ribble Estuary was provided by an aerial gamma survey by Sanderson *et al* (1993) in 1992 (Section 2.6.2). The resultant maps supported the results of many of the ground-based surveys of this area.

Based on a limited number of cores, Brown (1997) also made estimates of the ^{137}Cs inventories for intertidal regions covered by distinct sediment facies within the Ribble Estuary (Table 2.5). The radionuclide distribution with depth within the large intertidal regions was calculated from isolated cores. However, no individual inventory estimates were made for the saltmarsh creek networks present, which have unique radionuclide distributions with depth. Consequently, this affected the accuracy of the final inventory estimates. If a reliable map of intertidal surface sediment grain-size or activity had been available, this would have allowed areas that have dissimilar distributions with depth (*e.g.* creeks) to be identified and estimated separately.

Table 2.5 ^{137}Cs Inventories for Sediment Facies in the Ribble Estuary (Brown, 1997)

Facies Type	Area (Km^2)	^{137}Cs Total Inventory (kBq)
Channel Margin - Coarse	4.5	0.363×10^9
Channel Margin - Fine	2.2	1.835×10^9
Channel Margin - Upper Estuary	1.1	0.917×10^9

2.5 REFLECTANCE SPECTRORADIOMETRY

Remote sensing is basically the transfer of radiant energy, either emitted or reflected, from a surface to a sensor. A marked increase in the number of satellite and airborne sensors, since the early seventies, has produced a demand for *in situ* data. Reflectance spectroradiometry represents the most important type of field measurement, providing an insight into the physical relationship between the electromagnetic spectrum and surface properties. This relationship can be incorporated into a model, validated with spectral measurements of known surfaces, which can be used to determine the unknown characteristics of a surface from measured spectral reflectances (Asrar, 1989). In addition, reflectance data can be used for atmospheric correction of imagery and to examine the potential of particular spectral bands for a specific task.

2.5.1 Reflectance Measurement

Reflection is the process by which electromagnetic flux, incident on a stationary surface, leaves that surface from the incident side without a change in frequency. Reflectance is the fraction of the incident flux that is reflected *i.e.* the ratio of reflected to incident flux. The bidirectional reflectance distribution function, BRDF, is a fundamental parameter when describing the reflectance of a surface (Nicodemus, 1982). However, the BRDF can never be measured directly because truly infinitesimal elements of solid angle do not include measurable amounts of radiant flux (Nicodemus *et al.*, 1977). To overcome this, the reflectance factor is used, which is an integration of this quantity over finite solid angles of incidence and exitance (Asrar, 1989). A reflectance factor is defined as the ratio of the radiant flux actually reflected by a sample surface to that which would be reflected into the same reflected beam geometry by an ideal perfectly diffuse

34

(Lambertian) standard surface irradiated in exactly the same way as the sample (Robinson and Biehl, 1979). The term reflectance factor, which is also called the bidirectional reflectance factor, is most often used to describe the field-measured reflectance.

Reflectance factors are often calculated to allow comparison within multitemporal datasets. Robinson and Biehl (1979) created a field calibration method for the reflectance factor which is designed to obtain a property of the scene that is nearly independent of the irradiance and the atmospheric conditions at the time of measurement. The procedure contains the response, V_s, of the instrument viewing the subject and the response, V_r, of the instrument viewing a level reference surface, and produces an approximation of the bidirectional reflectance factor of the subject (2.1).

$$R_s(\theta i,\phi_r;\theta_r,\phi_r) \equiv \frac{V_s}{V_r} R_r(\theta_i,\phi_i;\theta_r,\phi_r) \qquad\qquad 2.1$$

Where, $R_r(\theta_i,\phi_i;\theta_r,\phi_r)$ - Bidirectional reflectance factor of the reference surface
ϕ_r - Azimuth angles of reflection
ϕ_i - Azimuth angles of incidence
θ_r - Zenith angle of reflection
θ_i - Zenith angle of incidence

This calibration process contains some basic assumptions: *1)* the incident radiation is dominated by its directional component (*i.e.* clear sky), *2)* the instrument responds linearly to entrant flux, *3)* the viewing angle and illumination conditions are the same for the reference material and the sample surface, and *4)* the reflectance properties of the reference material are known (Asrar, 1979). In reality, perfect Lambertian surfaces cannot be achieved by reference surfaces in the field, instead reference materials *e.g.* barium sulphate ($BaSO_4$) are calibrated beforehand to accommodate for loss of radiance.

In addition, the instruments used to measure surface reflectance must be calibrated to allow comparison of data collected from two different instruments.

2.5.2 Sediment Reflectance Properties

Successful data extraction from airborne imagery of the Ribble Estuary intertidal sediments is dependent on detailed knowledge of the *in situ* spectral properties of the various surfaces. The reflectance of an intertidal surface is not solely determined by its grain-size, rather it is a combination of the effect of this and other variables such as surface water, moisture content, cyanobacteria and iron-oxide content. There has been very little research directed into the reflectance characteristics of estuarine intertidal sediment. Consequently, studies into the reflectance properties of soils and the effect of grain-size on reflectance of other materials are very relevant to this project.

A series of reflectance investigations has been performed on the intertidal sediments of the Ribble Estuary as part of a feasibility study for this project (Tyler *et al.*, 1995; Bryant *et al.*, 1996). This included the examination of laboratory spectra for a range of dried, ground and homogenised intertidal sediment samples from the Ribble Estuary. The spectral response of these sediments was found to be largely controlled by their grain-size, organic content and bulk mineralogy. It was possible to distinguish samples with high sand and a low LOI (Loss On Ignition) value from samples with a low sand and a high LOI value. In other words, a strong positive correlation between sand content and reflectance and a strong negative correlation between clay content and reflectance was identified. Although the field spectra showed that sediment size fractions could be correlated to reflectance, where surfaces were dominated by halite efflorescence the correlation was greatly reduced. These studies concluded that the *in*

36

situ surface conditions were a major influence on the relationship between reflectance and sediment grain-size.

A more recent study by Thompson *et al.* (1998) used ground radiometry to establish the ability of a Compact Airborne Spectrographic Imager (CASI) to differentiate various intertidal surfaces on the East Coast of England. However, the primary aim of this study was not to examine the spectral difference of the intertidal sediments, rather to spectrally discriminate between different classes of intertidal vegetation. Bare sediment surfaces were split into only two classes – sand and mud. In addition, no consideration was taken of the effect of moisture on the ability to distinguish these sediment types. Consequently, although this study found that sand and mud could be differentiated using a limited spectral range (400-900nm) it does not provide a major insight into the relationship between reflectance and sediment grain-size.

Leu (1977) examined the relationship that exists between the mean grain-size of intertidal sediment (beach sand) and spectral reflectance. In this study, the grain-size determinations were performed using standard sieving techniques, the presence of iron stains was determined on a visual basis and the spectral measurements ranged from 0.35 to 2.5μm. Leu (1977) concluded that for the iron-stained samples channel 1 (0.43-0.47μm) was positively correlated to grain-size while channel 4 (0.51-0.53μm) was negatively correlated to grain-size. However, for the non-stained samples, he failed to find any correlation. Leu (1977) then went on to suggest a model which includes the effects of moisture and iron-staining to explain his results. Although these results are of interest, this study only looked at a limited range of sediment grain-sizes, making it very difficult to make any direct comparisons with the variable estuarine environment.

37

Reflectance studies of soils offer a close analogy to the characteristics of intertidal sediments. The most complete reference material is that by Irons *et al.* (1989) who reviewed a wide range of publications on soil reflectance spectra. This review describes the spectral characteristics of a range of soil properties and also recognises how various characteristic reflectance features can overlap each other (Table 2.6). For example, absorption due to ferrous iron in the middle infrared wavelengths can be strong enough to mask the water absorption at $1.4\mu m$.

The visible and near-infrared characteristics of a range of minerals have been defined during many laboratory reflectance studies (Hook, 1990; Marsh, 1993; Ramasamy *et al.*, 1993; Drake, 1995; Price, 1995). The most complete study was by Hunt and Salisbury (1970, 1971) who constructed a detailed library of the spectral features of carbonate and silicate minerals. Although of interest, data of this nature are difficult to apply within this project for a number of reasons: *1)* the low spectral resolution of ATM data, *2)* the complex mineral mixtures of intertidal sediments hinders identification of specific absorption features, *3)* the high moisture content of sediments lowers the overall reflectance therefore masking many distinctive absorption features.

2.5.3 Microphytobentos Reflectance Properties

Microphytobenthos presence on the intertidal areas of the Ribble Estuary (Section 2.2.3) demands that the project is aware of its spectral characteristics. However there are very few previous studies that have looked directly at the spectral effect of intertidal microphytobenthos. The most substantial study was that by Thomson *et al.* (1998) who used a Spectron SE590 spectroradiometer to compare the abilities of different CASI bandsets for discrimination of different classes of intertidal vegetation. It was found

38

that ten different intertidal surfaces could be distinguished. Areas of bare intertidal sand

were found to be distinguishable from sandy areas with a diatom covering; similarly,

bare mudflats were distinguishable from mudflats with an algal covering. In addition

the study found that the effectiveness of the various bandsets differed very little,

although it was important to ensure that key parts of the spectrum were covered

including blue and red chlorophyll absorption troughs and the red edge.

Table 2.6 Soil Reflectance Spectra Characteristics (Irons *et al.*, 1989)

Moisture Content	General decrease in soil reflectance with increasing moisture. Prominent absorption bands at 1.4 and 1.9μm. Weaker absorption bands at 0.97, 1.2 and 1.77μm.
Iron and Iron Oxide Content	General steep decrease in reflectance towards the blue and ultraviolet parts of the spectrum. Main absorption bands at 0.7, 0.87 and 1.0μm. Weaker absorption bands between 0.4 and 0.55μm. Additional absorption in the middle infrared can be attributed to ferrous iron.
Organic Matter Content	General decrease over entire shortwave region as organic content increases. >5% - Concave shape between 0.5 and 1.3μm. <5% - Convex shape between 0.5 and 1.3μm. Reflectance spectra vary depending on the type of decomposition (sapric or hemic).
Mineralogy (examples)	Quartz - High reflectance throughout the shortwave region (no absorption features if no impurities). Kaolinite - A wide absorption feature near 0.9μm. Layer silicates - Hydroxyl bands near 1.4 and 2.2μm. Gypsum absorption features at 1.8 and 2.3μm.
Particle Size	General increase in reflectance and decrease in the contrasts of absorption features as particle size decreases. Clayey soils sometimes appear darker, related to either the mineralogy or the tendency of clay particles to aggregate.
Surface Conditions (*e.g.* roughness, moisture content, presence of plant residue)	In general reflectance is greater from a smooth soil rather than a rough one. A crusted soil has a higher spectral reflectance (between 0.43 and 0.73μm) than a soil with the crust broken.

Information regarding the spectral characteristics of microphytobenthos can also be gleaned from a range of other studies. For example, an earlier study of intertidal seaweed along the coast of Brittany, France, identified the spectral absorption peaks produced by chlorophyll a, which is abundant in cyanobacteria, in the visible blue and red parts of the spectrum (Bajjouk *et al.*, 1996). Pinker and Karnelli (1995) examined the spectral response of cyanobacteria crusts in a semi-arid environment and concluded that its visible/infrared reflectance was lower than the sand dune spectra, except below 0.55μm. Similarly O'Neill (1994) studied microphytic crusts, which contain cyanobacteria, in semi-arid Australia and found the crusts had a lower overall reflectance (0.4 - 2.5 μm) in comparison to a clean surface. A chlorophyll absorption feature was also obvious at 0.625μm, which deepened if the soils were wet, due to increased photosynthesis. Karnelli and Tsoar (1995) also identified this absorption feature in reflectance spectra of cyanobacteria crusts on desert-dune sand along the Israel-Egypt border. These identified absorption characteristics are potentially a useful source of information for the identification of microphytobenthos cover in the intertidal regions of remotely sensed imagery.

2.6   REMOTE SENSING, IMAGE INTERPRETATION AND ANALYSIS

2.6.1   Remote Sensing

Remote sensing is potentially a fast, cost-effective and accurate way of gaining detailed synoptic information about an environment. Conventional ground surveys collect a range of samples within an area and the accuracy of any subsequent spatial representations is limited by the need to extrapolate between the sample sites. Without additional information, it is also difficult to ascertain how spatially representative point

samples are (Tyler *et al.,* 1996). Remote sensing provides direct information from each image pixel of an area and in the case of the aerial imagery used in this project that is equivalent to a sample in every 1.75m square. The data from a small number of sample points can be placed into a spatial context using remote sensing, providing cheaper and higher spatial resolution data than a detailed conventional survey.

Individual studies tend to have distinct objectives and, consequently, each requires a suitable platform and image type. Although relatively inexpensive, the coarse spatial and spectral resolution of satellite imagery often makes it unsuitable for detailed environmental studies (Table 2.7). Similarly, the temporal inflexibility of this data makes it impractical for any project requiring imagery of an area at a specific time or date. In contrast, the only constraint on airborne imagery is the need for cloud-free conditions and these data generally have a much finer spatial and spectral resolution making it ideal for monitoring small-scale environmental changes. The increased cost and the difficulty of geometric and radiometric calibration are the main disadvantages of airborne data.

2.6.2 Airborne Gamma Ray Spectrometry

Airborne gamma ray spectrometry is a unique remote sensing technique, which was originally developed as a large scale survey tool in uranium exploration and geological mapping (Sanderson *et al.,* 1995). Later developments in the hardware and methodology enabled it to be used for resolving and mapping different components of the radiation environment. Consequently airborne gamma ray surveying has become a significant tool for mapping natural, anthropogenic and technologically-enhanced natural radiation sources in the environment.

Table 2.7 A Summary of the Main Satellite Remote Sensing Platforms and Sensors

Satellite Name	Spectral Bandwidths	Spatial Resolution	Temporal Resolution
SPOT (Satellite Pour l'Observation de la Terre)	Multispectral Mode		26 Day
	1. 0.5 - 0.59	20m	
	2. 0.61-0.68	20m	
	3. 0.79-0.89	20m	
	Panchromatic Mode		
	1. 0.51 - 0.73	10m	
Landsat 1 2 3	1. 0.5 - 0.6	80m	18 Day
MSS (Multispectral Scanner)	2. 0.6 - 0.7	80m	
	3. 0.7 - 0.8	80m	
	4. 0.8 - 1.1	80m	
Landsat 4, 5	1. 0.45 - 0.52	30m	16 Day
TM (Thematic Mapper)	2. 0.52 - 0.60	30m	
	3. 0.63 - 0.69	30m	
	4. 0.76 - 0.90	30m	
	5. 1.55 - 1.75	30m	
	6. 2.1 - 2.35	30m	
	7. 10.4 - 12.5	120m	
AVHRR (Advanced Very High Resolution Radiometer)	1. 0.58 - 0.68	1.1km	12 hour
	2. 0.72 - 1.10	1.1km	
	3. 3.55 - 3.93	1.1km	
	4. 10.5 - 11.5	1.1km	

During an airborne gamma ray survey a spectrometer is elevated above the ground by a helicopter or a fixed-wing aircraft (Sanderson *et al.*, 1995). Normally a detector measuring ^{137}Cs at aerial survey altitudes of between 50m and 100m has a field of view of 130m and 195m respectively. The spectrometer used by the Scottish Universities Research and Reactor Centre (SURRC) is comprised of a standard 16 litre NaI detector coupled to an aerial radiometrics rack containing instrumentation power supplies, pulse height and multi-channel analyser and data-logging computer.

As part of a programme of baseline mapping for nuclear sites, a short aerial gamma ray survey was conducted in the vicinity of Springfields from the 1st to the 5th September 1992 (Sanderson *et al.*, 1993). The main objective was to define the existing radiation

background from aerial survey heights to enable future changes to be determined through repeat surveys. The survey area was a 20 x 12 km rectangular box centred about the Ribble Estuary, with a single flight line up the River Ribble through Preston. The maps produced provide a broad indication of the distribution and sources of environmental radioactivity in the Ribble at the time of the survey. These maps also support the conclusions of many ground-based surveys *e.g.* that ^{137}Cs on the saltmarshes is the dominant source of external gamma radiation (Brown, 1997). The Springfields contribution to radiation associated with the estuarine system, the sediments, the tide-washed pastures, the saltmarshes and the riverbanks was found to be minor in comparison with the Sellafield-derived signal. Nevertheless, with the equipment configuration flown in 1992, this technique was unable to map the distribution of low-energy gamma emitting radionuclides (*e.g.* ^{241}Am) in the Ribble Estuary. In addition, the tendency of baseline surveying to broaden large features and underestimate small-scale features affected the spatial accuracy of the results. For example the survey failed to identify a substantial signal any further than 1km east of Savick Brook due to the narrow morphology of the mudbanks in these regions.

The main advantage of aerial gamma ray spectrometry is its ability to produce large-scale spatially representative environmental surveys for baseline mapping and emergency response techniques. The mobility of the observational platform, combined with the spatial response of the detector, make this possible. Data can also be recorded at a rate that is at least two orders of magnitude greater than ground based estimates (Sanderson *et al.,* 1995). This method can be applied to remote locations, and the nature of these measurements minimises exposure of survey teams to contamination from radiation hazards. The above advantages are also true for monitoring radionuclide

surface distribution through Daedalus ATM data. In contrast, however, ATM data has a much greater spatial resolution (*e.g* 1.75m from 700m altitude) than aerial gamma surveys, which have an effective resolution of approximately 200-400m. Consequently, the manipulation of ATM data can potentially provide more spatially detailed maps of the surface radionuclide distribution in intertidal sediments. However, it is worth noting that ATM data, unlike aerial gamma surveys, is generally only collected during cloudfree conditions and has no depth penetration capabilities.

2.6.3 Remote Sensing of Estuaries

Marine Studies

In contrast to this project, the majority of estuarine remote sensing studies are interested in the estuarine waters rather than the surrounding deposited sediments. The hydrodynamics, specifically the freshwater/seawater interactions, of many estuaries have been examined in detail. There is also significant interest in the distribution of suspended sediment (Hudson *et al.*, 1994), salinity (Lavery *et al.*, 1993; Khorram, 1982), temperature and chlorophyll (Nieke *et al.*, 1995) within these waters.

The Tay Estuary in Dundee is a good example of an estuary that has undergone a range of both satellite and airborne remote sensing studies, with very different objectives. An early study by Cracknell *et al.* (1982) used Landsat 2 imagery to map the distribution of the sandbanks and the location of an estuarine front. The study concluded that although satellite data could be used to monitor broad changes in the estuary morphology, it was unable to quantify accurately depths beyond 3 or 4m. The combination of infrequent satellite imagery and frequent cloud cover was also found to be an inhibiting factor. Ferrier and Anderson (1996, 1997) avoided this constraint by using airborne remote

sensing when studying effluent dispersal and mixing processes in the Tay Estuary.

Three data sources were included: *1)* Daedalus ATM imagery, *2)* digitised black-and-white and colour-infrared aerial photographs, and *3)* ground spectroradiometers. The remotely sensed results correlated well with ground data and were incorporated into a modified simulation model of the flushing capacity of the Tay Estuary. The main limiting factor was the inability to extract reliable information from the imagery about the mixing processes below the surface. Nevertheless, this is a good example of airborne remote sensing providing a unique and invaluable source of data to estuarine studies.

A common application of remote sensing in estuarine environments is mapping the distribution of suspended sediment concentrations. For example, Hudson *et al.* (1994) developed an algorithm, with the aid of laboratory spectra, for mapping the suspended sediment concentrations (SSC) in the Humber Estuary using CASI imagery. In the subsequent results, the structures in the water were found to correlate well with the bathymetry of the area *i.e.* high SSC values coincided with shoals and low values were situated over channels. A similar study by Collins and Pattiaratchi (1984) used ATM imagery to study SSC distribution in the Swansea Bay area. Although this study failed to provide very detailed information about the SSCs in the Bay, localised flow patterns were identified from the classified imagery using the suspended material as a tracer. The Plymouth Sound Research Project also used ATM imagery to map the suspended sediment distributions present in the bay (Fitzpatrick, 1990). The imagery was collected and processed by NERC, before being combined to form a composite image of the Plymouth Sound, which was calibrated using *in situ* measurements.

The main advantages of using airborne remote sensing in these marine studies are that: *1)* multiple flights can be carried out at various tidal states and phases, *2)* near-synoptic coverage is obtained, *3)* in comparison to satellite-based instruments the spatial and spectral resolution is much greater and *4)* in comparison to conventional field sampling programs the information is obtained relatively cheaply (Collins and Pattiaratchi, 1984).

Coastal Ecological Studies

Remote sensing has long been recognised as an important tool in ecological studies of wetlands. For example, Anderson (1973) produced 1:2,400 and 1:6,000 scale maps of the major plant species in the New Jersey wetlands along the marine coastal zone using colour and colour-IR aerial photography. More recent studies have taken advantage of the various satellite datatypes and image processing technologies now available. In response to a need for non-destructive methods for evaluating the San Pablo Bay, California, wetlands, Zhang *et al.* (1997) used reflectance spectroradiometry at three locations. Preliminary analysis of *in situ* samples and reflectance spectra (collected using an ASD (Analytical Spectral Devices Inc.) Spectroradiometer II (350-1060nm)) established that a significant relationship exists between vegetation indices, based on Landsat Thematic Mapper (TM) bandwidths, and plant biomass. This was confirmed by a TM scene of the area displayed as a grey-scale vegetation index image in which the spatial patterns were consistent with patterns of biomass abundance. However this study concluded that vegetation indices could not be used to differentiate between plant species.

In Britain, two important studies by Donoghue *et al.* (1987, 1994) of the estuarine saltmarsh vegetation in The Wash, England, successfully outlined the potential of

satellite remote sensing for wetland species differentiation. Using Landsat TM imagery, the major NVC (National Vegetation Classification) plant communities in the saltmarshes were successfully mapped. In the 1994 study, two methods of vegetation classification, Maximum Likelihood Classifier (MLC) and Linear Mixture Modelling, were compared. The former revealed considerable information about plant species distribution within the saltmarsh, while the latter, was more suitable for identifying partial vegetation cover in the pioneer zone. Consequently the study concluded that the best results were obtained when both strategies were used in conjunction. Although vegetation and intertidal sediment were successfully distinguished no attempt was made to differentiate between the sediment types.

Remote sensing has also been used as a tool in numerous ecological studies of the littoral zone. In the past, black-and-white, colour and colour-infrared photographs have been utilised to map accurately the benthic algae present on intertidal sediments (Steffensen and McGregor, 1976). More recent studies have used a wide range of platforms and datatypes to map intertidal flora. For example, Bajjouk *et al.* (1996) used the fine, programmable bands of CASI to classify and map the seaweed and algae cover on the intertidal sediments along a stretch of the Brittany coastline. The study began by characterising the major reflectance features of the various algae under various moisture conditions. From the results the CASI bandwidths were selected for easy discrimination of littoral algae and seaweed from the imagery. Preliminary results showed that green, red and brown algae could be identified and that it may be possible to distinguish between two species of brown algae.

Intertidal Sediment Studies

Whilst many ground-based reflectance studies have recognised the correlation between reflectance and grain-size (Section 2.5.2), only a few have attempted to use remote sensing to map sediment facies. In all cases, these studies used satellite, rather than aerial, data and this severely affected the accuracy of the results produced.

The extensive nature of the intertidal flats in the Danish Wadden Sea means conventional sampling and mapping techniques are either too expensive or time-consuming. Numerous studies have consequently attempted to map this region using various remote sensing datatypes. The earliest studies combined *in situ* reflectance data and Landsat -1, -2, -3 MSS data (Table 2.7) to map parts of the intertidal zone (Folving, 1984; Bartholdy and Folving, 1986). From examinations of a range of reflectance spectra, no direct correlation was evident between sediment grain-size parameters and spectral response. This is probably due to the limited spectral range (400 - 800μm) examined by each study. Nevertheless, all the studies were able to distinguish broadly between the sand and mud areas, and further sediment sub-classes were identified through morphology and location. Bartholdy and Folving (1986) concluded that it was impossible to create detailed grain-sized maps from Landsat MSS imagery. The poor spatial, spectral and radiometric resolution of this datatype, combined with the complex nature of the tidal flats, were identified as the main limiting factors. It is also worth noting that Folving (1984) recognised the overwhelming influence of water on the ability to map tidal flats through remote sensing. Consequently, it was predicted that in future studies the best result would be obtained by using scenes recorded during the beginning of the flood when the sediments would be at their driest.

Recognising the limitations of the earlier studies, Doerffer and Murphy (1989) attempted to map the Wadden Sea area using Landsat TM data (Table 2.7) and a sub-pixel classification technique. Through an unsupervised classification, the study first identified the non-intertidal areas in the TM subscene and masked them out. The resultant image then underwent factor analysis to identify the main factors or sources underlying the combined spectral variation in the seven TM channels. Three independent factors (topography, water and temperature) were identified as being responsible for 82% of the spectral variance in the TM bands. Doerffer and Murphy (1989) consequently concluded that factor analysis could be used to map the distribution of the factors that control sediment surface characteristics. Although this method does not directly map the sediment types, it can identify the broad distribution of sediment facies and any temporal change. As with the earlier studies, the presence or absence of water cover was recognised as a problem that must be overcome before a definitive classification is possible.

One of the more recent studies of the Wadden Sea intertidal area was carried out by Jacobsen and Neilson (1990), who examined a $20km^2$ region using a single SPOT scene (Table 2.7). This limited study attempted to use the spectral diversity within the imagery to recognise the main ecological units present and an intertidal zonation, based on moisture and sediment characteristics. However, the only significant conclusion of this study is that remote sensing could potentially be used to support and interpret intertidal ground truth data.

Although the above Wadden Sea studies are of significant interest, the later work by Yates et al. (1993) in The Wash, England has the most relevant implications for this

49

project. Using two low-tide Landsat 5 TM data sets, one collected during a neap tide and the other collected at a spring tide, Yates *et al.* (1993) attempted to map the distribution of intertidal surface sediments in the estuary. Three methods were used to classify the data: *1)* maximum likelihood classification, *2)* multiple regression and *3)* linear mixture modelling. The first classifies each pixel, whilst the last two attempt to quantify the amount of each sediment type within each pixel. Mixture modelling achieved both the best and poorest accuracy in classifying the muddy (93.7%) and the sandy (20.8%) sediments respectively. Yates *et al.* (1993) suggest that this is because mixture modelling was used on the neap tide data, which increases the chances of an extensive muddy veneer. The greatest source of error however is the reliance of this study on a negative relationship between infrared reflectance and percentage sand, to differentiate the sediments. This relationship only exists where the sandy areas have a film of water that absorbs the infrared reflectance and, consequently, the well-drained sandy areas were poorly classified by this technique. The difficulty of obtaining cloudfree satellite imagery of intertidal areas at a particular tidal state is also highlighted by this study. This suggests that the temporal resolution of the Landsat TM data is unsuitable for mapping the intertidal sediments of an estuary.

Finally, a study by Populas *et al.* (1995) compared the ability of SPOT, ERS-1 SAR and aerial images to rank the shoreline of the Loire Estuary, France, in terms of its ecological sensitivity to pollution. Included in the area of interest of this study were the extensive tidal flats, and consequently attempts were made to classify them in terms of grain-size. A minimum distance classification was applied to the SPOT imagery, however the results correlated poorly with the grain-size variation of the area. The colour aerial photographs were mosaiced together, but the presence of a thin film of

50

water on the tidal flats meant they were too highly influenced by illumination conditions and therefore of little use. However, a reasonably accurate map of sediment grain-size was produced from the SAR imagery. The basis of this was an assumption that two physical factors, moisture and grain-size, influenced the backscatter cross-section in the tidal flat area. An 'intertidal only' subset of the imagery was then density-sliced into five classes and the results were compared with sites of known grain-size. Populas *et al.* (1995) concluded that radar images outperform visible imagery when mapping intertidal sediment characteristics. However the present low temporal and spatial resolution (28m) of ERS-1 SAR data makes it impractical for detailed mapping of intertidal sediment. For example during a five month period in 1992 only one of the six ERS-1 Synthetic Aperture Radar (SAR) images of this study area coincided with low-tide conditions. Similarly, during a five-month period in 1990, only one of the seven available SPOT images of the Loire Estuary coincided with both a low-tide and cloud-free conditions. As before, this study underlines the difficulty of using satellite data to monitor an intertidal environment.

2.6.4 Atmospheric Correction Techniques

The atmosphere affects both satellite and aerial imagery, causing the signal amplitude and the spectral characteristics of the returning signal from the earth's surface to change. Sunlight may be reflected directly to the sensor and atmospheric molecules, aerosols and clouds may attenuate the solar energy reflected from the earth's surface. The atmospheric constituents vary, and so their effect on the imagery can change both temporally and spatially. Successful atmospheric correction removes this effect, ensuring that any subsequent image classification is based purely on the spectral characteristics of the surface components. The importance of atmospheric correction to

remotely sensed data is widely recognised and for this reason there is a wide range of papers detailing the various correction algorithms available. These techniques vary greatly in complexity and prerequisite information; for example, some require *in situ* radio-sonde data, whilst others use only the remotely sensed data. Consequently, the first stage in atmospheric correction is the selection of a suitable technique based on the data available.

Some correction techniques include complex computer models that predict spectral radiance for various viewing geometries and atmospheric conditions. The inverse 5S model, for example, has often been used to calculate ground reflectance from sensor reflectance by taking into account the effects of gaseous absorption and scattering by molecules and aerosols (Singh, 1994; Zagolski *et al.,* 1995; Milovich *et al.,* 1995). This code was originally developed to estimate the reflectance at sensor level of an observed pixel from the ground reflectance. To perform the computations the user has to specify a range of input parameters *e.g.* aerosol characteristics, spectral band of observation, sensor reflectance, geometrical conditions and an atmospheric model (Tanre *et al.,* 1990). These may come from a range of sources, including pre-calculated look-up tables, existing meteorological data sets (*e.g.* from the British Atmospheric Data Centre), *in situ* measurements or data calculated directly from the imagery. For example, when atmospherically correcting a series of AVIRIS (Airborne Visible and InfraRed Imaging Spectrometer) images, Zagolski *et al.* (1995) combined *in situ* measurements taken with a radio-sonde at the time of image acquisition, with measurements made directly from the image. The aerosol optical thickness is the most common characteristic measured directly from the imagery, and this is possible due to the presence of dark points in selected bandwidths (Gilabert *et al.,* 1994). Fast

atmospheric correction techniques commonly use neither *in situ* data nor data calculated from the imagery, and instead obtain all the necessary radiation parameters from look-up tables (Fraser *et al.*, 1992). In the same way as the complexity of the various models varies, the accuracy of the results also varies, and in most cases the latter is related to the quality of the atmospheric input parameters. A common source of error is where the adjacency effect, *i.e.* the effect of the neighbouring pixels on the apparent reflectance of a pixel, is not taken into account (Milovich, 1995). To summarise, the major disadvantage of these techniques is their dependency on information other than the digital image data.

The second type of correction extracts all the necessary information about the atmospheric conditions, at the time of collection, from the imagery itself. The most common of these techniques is dark target subtraction, which is based on the assumption that there are at least a few pixels within the image which should be black, but instead have a non-zero value. This value is assumed to be a product of atmospheric haze and consequently an image may be haze corrected by subtracting the dark-pixel digital number (DN) from all the image pixel values. A potential problem is when the dark-pixel values selected do not conform to a realistic relative atmospheric scattering model, causing some or all of the spectral bands to be overcorrected. Chavez (1988) overcame this by selecting only DN values that conformed to a realistic relative scattering model so that the haze values were wavelength dependent and correlated with each other. When selecting suitable dark pixels in any scene it is important that the radiance associated with such pixels is not being contributed to by neighbouring pixels. In using the dark subtraction technique Gonima (1993) reduced the problem of adjacency effects by selecting only pure areas greater than 3 by 3 pixels. Less common atmospheric

53

correction techniques which extract the necessary information directly from the imagery include Flat Field Correction, Least Upper Bound Residual and the Log Residual (Roberts *et al.*, 1985).

Uniquely, the empirical line or regression atmospheric correction method is independent of any atmospheric input parameters obtained from either lookup tables or directly from the imagery. This technique uses natural or man-made targets in the imagery, which are of known reflectance, to develop linear relationships between the digital radiance data and the actual surface reflectance. In an attempt to correct Airborne Imaging Spectrometer (AIS-2) data Conel *et al.* (1987) compared this technique against the log residual and radiative transfer modelling techniques. The empirical line method performed well, returning predicted surface reflectance values within a few percent of the actual observed values. However problems were encountered when compensating for both water and CO_2 effects at various places in the spectrum. Nevertheless, in the context of the Ribble Estuary study, the level of accuracy achieved by the empirical line method would be sufficient for the atmospheric correction of the ATM imagery. Van den Bosch *et al.* (1991) compared the empirical line technique against the Lowtran 7 method (with radio-sonde data) for the atmospheric correction of a radiometrically corrected AVIRIS scene. In this regression method three targets (one of which was a corrugated metal roof) were used. The Lowtran spectra were found to be sensitive to errors in moisture content, though this was possibly related to radio-sonde errors. In contrast, the regression method had the advantage of not being reliant on the radio-sonde accuracy. Ferrier (1995) attempted to evaluate the empirical line method by comparisons against three methods of radiative transfer modelling. However, in this study the ground survey targets could only be identified in the AVIRIS image to an

accuracy of approximately two pixels, which introduced large errors into the results of the empirical line method. Consequently, the radiative transfer techniques out-performed the regression method, emphasising the need for very accurate ground target locations.

Finally, there is a number of techniques specifically created for atmospheric correction of thermal infrared imagery, which is essential prior to any accurate estimation of land or sea-surface temperatures. The split-window technique is the most common means of atmospherically correcting the two thermal bands of AVHRR data (Harris and Mason, 1992; Kalluri and Dubayah, 1995). This method is based on the principle that the two atmospheric windows centred on 10.5 and 11.5μm absorb radiance differently. Consequently, the surface temperatures are calculated using a linear function of the difference in brightness temperature of the two channels. The single thermal band of the Landsat TM sensor, however, prevents the use of the various split-window algorithms. In this case, alternative algorithms based on radiative transfer models, with atmospheric profiles obtained from temporally coincident radiosondes, are generally used (Hurtado *et al.*, 1996).

2.6.5 Image Classification

Classification is the process by which the main surface types present within an image may be differentiated and mapped. There is a range of classification techniques available and these are broadly referred to as either 'hard' or 'soft'. Hard classifiers such as Parallelpiped, Minimum Distance and Maximum Likelihood Classification (MLC) produce one classified image, with each pixel in a single class. However the MLC is a unique 'hard' classifier as it may be softened by taking the *posteriori*

probabilities into account. Linear Mixture Modelling, C-means classification, Multiple Regression and Artificial Neural Networks (ANN) are examples of 'soft' or 'fuzzy' classification techniques that map the sub-pixel proportions of each surface, producing a series of grey-scale abundance images. The ability of these techniques to classify imagery of different environments has been compared in numerous studies.

Cross et al. (1991) compared the abilities of MLC and mixture modelling to map forest cover in two locations using AVHRR data. The results of both classifications were compared with a classified TM image of the same area and it was clear that both classifications underestimated forest cover. Where the underestimation was greatest, the mixture modelling performed significantly better than the MLC technique achieving a r^2 correlation coefficient of 0.8 with the TM proportion maps. Haguenin et al. (1997) compared a subpixel classification technique with a series of traditional classification methods including isodata clustering, MLC and minimum distance. The aim of the study was to classify Bald Cypress and Tupelo Gum wetland in Landsat TM imagery of Georgia and S. Carolina. The subpixel process yielded significantly better results, due mainly to the inability of the hard classifiers to identify Cypress which was heavily mixed with other tree species.

As detailed in Section 2.6.3 Yates et al. (1993) found that both the mixture modelling and regression analysis classification procedures more accurately classified the muddy sediments of The Wash intertidal zone than the MLC technique. Mixture modelling has also been demonstrated to outperform significantly the MLC, Parallelepiped and k-nearest neighbour classification techniques when mapping surface geologic cover of TM data (Van der Meer, 1997). In this instance, spectral unmixing had the advantage of

requiring no ground knowledge because it used the spectral characteristics of ground cover classes derived from laboratory reflectance studies. When mapping the vegetation communities of saltmarshes in The Wash estuary, Donoghue *et al.* (1994) demonstrated that linear mixture modelling could provide more accurate results than the traditional MLC technique. A level of 90% agreement was achieved between the 1984 NCC survey and the mixture model of a 1991 Landsat image. In summary, soft classifiers, *e.g.* mixture modelling, have outperformed traditional 'hard' classifiers in a range of environmental remote sensing studies. This is primarily due to the failure of 'hard' classifiers to recognise units that grade into each other or have sub-pixel boundaries.

The capabilities of the various sub-pixel classifiers that are available have been compared in a range of studies of different environments. For example, Atkinson *et al.* (1997) compared the ability of three of the most commonly used soft classifiers (ANN, mixture modelling and fuzzy c-means classification) to map land cover units in AVHRR data. Classified SPOT images were used to derive the known 'sub-pixel' proportions of each land cover class. The ANN technique achieved a significantly greater mapping accuracy than the others did, but as Atkinson *et al.* (1997) state this superiority is balanced against the requirement of an expansive set of training data. Of the remaining techniques, supervised fuzzy c-means classification was found to be slightly more accurate than mixture modelling. Bastin (1997) also concluded that the fuzzy c-means classifier outperformed mixture modelling, when mapping four land cover classes from MSS imagery simulated from TM data. Although the linear mixture modelling performed well, problems with similar class signatures lowered the overall accuracy. This is probably a function of the low dimensionality of the MSS data, which limits the number of surface units identifiable by mixture modelling (Settle and Drake, 1993).

57

This may also explain the poor performance of mixture modelling when unmixing AVHRR data (Atkinson *et al.*, 1997). Consequently, the dimensionality constraint is an important consideration before the selection of mixture modelling as an image classifier (Section 3.6.2).

Linear Mixture Modelling

Based on a careful selection procedure (Section 3.6.1), linear mixture modelling was chosen as the most suitable classifier for mapping the distribution of the Ribble Estuary surface intertidal grain-sizes. To gain a deeper understanding of this relatively new technique, a selection of previous studies have been reviewed.

A common problem when unmixing a remotely sensed scene is the presence of one or more non-linear components *i.e.* a surface or surfaces with a non-linear spectral relationship with the other components. Most images will have at least one such component *e.g.* surface moisture, shade or vegetation cover. In theory, linear mixture modelling is unsuitable for classifying such scenes; however in practice, where linear mixing is the dominant process, this technique can produce valid results (Bryant, 1996). Nevertheless, a common mistake made by many studies is not in the unmixing of the imagery but in the later interpretation of the results. For example, Bierwirth (1990) unmixed NS001 scanner data of a geological test site in North Queensland, Australia to produce proportion maps for four mineral types (clay, haematite, goethite and quartz). Green and dry vegetation were also included as individual endmembers in the unmixing process. However these are non-linear components, since any individual photon must pass through the vegetation before being reflected by the underlying mineralogy to the sensor. Consequently, in order to remove this non-linear spectral influence, Bierwirth

(1990) rescaled the resultant mineral mixture maps, forcing the pixel values to be purely a function of the minerals present. However, the validity of this correction procedure is questionable as it inherently assumes that the non-linear component has some linear spectral relationship with the other components. A more appropriate solution is to calibrate the abundance imagery for the linear components using sites of known cover mixtures. The problem of non-linear components is of particular importance to intertidal remote sensing studies, where water and microphytobenthos are unlikely to mix linearly (Donoghue *et al.*, 1994).

The dimensionality constraint of linear unmixing has been identified as a potential source of error when classifying highly correlated datasets (Bastin, 1997; Atkinson *et al.*, 1997). Of the many studies that have recognised this constraint, few have attempted to overcome it. One potential technique for doing so is the use of the Spectral Angle Mapper (SAM) to extract the most important components constituting the bulk of the spectral variability. Van der Meer (1995) used this technique to reduce the number of endmembers from a theoretical twelve to five pure ones before unmixing a TM scene of Southern Spain. As a result, the low dimensionality of the TM dataset did not constrain the ability to unmix the pure endmembers in the imagery. A similar technique is partial unmixing, where the number of pre-defined endmembers is one greater than the number of spectrally defined target materials (Boardman *et al.*, 1995). The extra endmember represents the composite of all the other surface components *i.e.* 'everything else'. Boardman *et al.* (1995) applied this technique to carbonate mapping from an AVIRIS scene of the North Grapevine Mountains. The target units were calcite and dolomite, and a background composite endmember represented the rest of the spectral variation. The technique successfully demonstrated how the complexity of the unmixing can be

59

driven by the number of targets, and not by the number of surface components in the scene. This also shows how a few key endmembers can be unmixed from a highly correlated dataset. Finally, a more fundamental solution to the problem of data dimensionality is to select a datatype with potentially more dimensions *e.g.* AVIRIS or ATM.

2.7   SUMMARY

Within this chapter a general review of estuaries, radioactivity and remote sensing has been completed. This includes an introduction to the study area, the Ribble Estuary, and its morphological and sedimentological characteristics. From this detailed critique a number of fundamental conclusions have been drawn that are particularly significant to this project:

- The Ribble Estuary is a dynamic environment, which forms an important interface between human activity and the Irish Sea.

- The Ribble Estuary is acting as a sink for fine-grained marine sediment and, consequently, Sellafield-derived radionuclides.

- From conventional sampling programmes and aerial gamma surveys it is not possible to map the surface distribution of these radionuclides on a morphological scale.

- It may be possible to map the surface intertidal sediments of the Ribble Estuary through airborne remote sensing based on relationships between reflectance (0.4 - 2.5μm) and grain-size.

- The surface distribution of the Sellafield-derived radionuclides may subsequently be inferred on a morphological scale through the strong associations between sediment grain-size and activities.

- Due to the gradual sediment facies boundaries in the intertidal environment, a 'soft' image classification technique (*e.g.* linear unmixing) is likely to provide the most accurate sediment distribution maps.

The next chapter, Chapter 3, outlines the main *in-situ*, laboratory and image analysis techniques used in this project.

3. *IN-SITU*, LABORATORY AND IMAGE ANALYSIS TECHNIQUES

3.1 INTRODUCTION

Mapping radionuclide distributions in surface intertidal sediments through airborne remote sensing requires the implementation and development of a range of diverse techniques to bridge the gap between sediment radioactivity and airborne imagery. These techniques can be broken into a number of distinct groups.

1. Conventional analysis methods used to define the physical characteristics of surface intertidal sediments.

2. Techniques used to define the radionuclide content of surface sediments and hence to characterise the radionuclide/sediment grain-size associations.

3. Reflectance spectroradiometry techniques used to define the spectral (350–2500nm) characteristics of intertidal sediments.

4. Techniques used in the collection and pre-processing of the Daedalus AADS 1268 Airborne Thematic Mapper (ATM) imagery.

5. Image analysis methods used to extract the grain-size characteristics of the surface sediments from the ATM imagery, upon which the subsequent surface radionuclide distribution maps are based.

In this chapter, each of the major techniques used in this project is described. Where applicable the theory behind the methods and the software used to implement the techniques are outlined. Equally, the rationale behind the selection of certain techniques over other available methods is explained.

3.2 SEDIMENT SAMPLE COLLECTION AND ANALYSIS

3.2.1 Introduction

Airborne remote sensing of an estuarine environment provides spectral information of the surface intertidal sediments only; no information about the underlying sediments can be extracted directly from the imagery. To provide comparable field information about the sediment, surface scrapings (<1cm) were collected during both the *in situ* spectral investigations and the acquisition of Ribble Estuary airborne imagery. In this section, the sampling strategy and the subsequent sediment analysis and preparation is outlined.

3.2.2 Sampling Strategy

To investigate the sediment variability, sampling was carried out along measured transects perpendicular and parallel to the main channel during the *in situ* investigations. Repeat samples were also collected within a series of $2m^2$ square grids between the saltmarsh edge and the main channel. A differential geographic positioning system (DGPS) was used to define the locations of these samples.

During the 1995 and 1997 image acquisition, surface samples were collected, at a number of representative locations within the estuary, along transects perpendicular to the main channel. The start and finish of each transect were defined using a DGPS system and care was taken not to disturb the sampling areas. In 1997, white plastic markers ($1m^2$), which are visible in the imagery, were also laid out at the beginning and end of the transects. The sample sites were evenly spaced along each transect using a tape measure and the sample locations were marked with stakes (Plate 3.1 & Plate 3.2).

Sampling was repeated after a period of exposure to investigate the variation in sediment moisture over time.

Plate 3.1   Example Sample Transect at Warton Bank During the 1997 Image Acquisition. Sampling was Carried Out to the Right of the Markers in the Photograph.

Plate 3.2   Example Sample Transect at Lytham St. Annes During the 1997 Image Acquisition. Sampling was Carried Out to the Right of the Markers in the Photograph.

3.2.3 Sediment Sampling Technique

Surface sediment scrapings (<1cm) were collected using trowels and double sealed in labelled plastic bags. A substantial amount of moisture was inadvertently lost in the transfer from the intertidal surface to the plastic bags. During sampling the surface moisture conditions, cyanobacteria cover, nature of rippling and percentage mud draping were observed and/or photographed. The samples were stored for a short period of time (< 2 weeks) before laboratory analysis. A selection of bulk surface sediments was also collected for use in laboratory reflectance experiments.

3.2.4 Sediment Moisture Analysis

As a potential aid to the interpretation of the airborne imagery the moisture content of the collected sediments was determined. In the laboratory each sample was homogenised, sub-sampled, placed in a pre-weighed tray, weighed and dried in a fan-assisted oven at 50-90° until completely dry. The dried sample was then re-weighed and the percentage moisture content was calculated.

3.2.5 Grain-size Analysis

The grain-size of each fresh sub-sample was measured using the Malvern Longbed particle-sizer at Westlakes Scientific Consulting Ltd., which can measure sediments within the grain-size range 0.05μm-900μm. In the particle-sizer, each sample is exposed to a laser beam producing a light scatter pattern, which is related to the particle size distribution of the sample. The % clay (<2μm), % silt (2μm-63μm) and % sand (>63μm) volumes were subsequently calculated from the instrument output. Specific surface area and distribution parameters such as kurtosis and skewness can also be calculated from this output.

3.2.6 Sample Preparation for Gamma Ray Analysis

A number of the dried sediment samples produced by the moisture assessment technique were selected for gamma ray analysis. Each sample was removed from its drying tray and ground to a fine dust using a pestle and mortar. The sample was then placed into 500g tubs and homogenised using a rotator. A sub-sample of each sediment was then sieved through a 1mm sieve before being placed into an oven for half an hour at 45-50°C. A pre-weighed petri dish was then packed with the sediment, sealed and re-weighed, allowing the sample weight to be calculated. The samples sealed in the petri dishes were then ready for gamma ray analysis.

3.3   GAMMA RAY SPECTROMETRY

3.3.1   Introduction

The Sellafield-derived anthropogenic radionuclides, ^{241}Am and ^{137}Cs, are readily detectable through laboratory based gamma ray spectrometry. Gamma rays are electromagnetic radiation emitted from the nucleus of an unstable atom following β-emission, electron-capture, positron emission, α-particle emission or isometric decay. These rays are emitted, with well-defined energies characteristic of specific nuclei, as a result of the transition between nuclear states. Assuming a sediment sample has more than one radionuclide present, a spectrum of monoenergetic photons is emitted. This spectrum is converted into a combination of lines and continuous components by the detector, from which the energies and intensities of the original photons can be determined. The radionuclides present may then be identified from the raw photon data.

All the intertidal sediment samples collected during the 1995 image acquisition and a selection of the intertidal samples collected during the 1997 image collection underwent gamma spectrometry analysis (Table 3.1). The objective of this work was to establish the relationship between the grain-size and the ^{241}Am and ^{137}Cs content of the intertidal sediments of the Ribble Estuary. The spatial and temporal stability of the relationships was also assessed.

Table 3.1 Inventory of the 1995 and 1997 Surface Sediment Samples Selected for Gamma Ray Spectrometry

Sample Site	1995	1997
Longton	34	
Savick Brook	8	
Penwortham	2	
Warton Bank	32	14
Lytham St. Annes		6
Docks		7

3.3.2 Spectral Analysis

Any measurement of absolute emission rates of gamma rays (i.e. not relative to a similar source of known activity) requires knowledge of the detector efficiency (Knoll, 1989). As it is very difficult to determine precisely the efficiency of a detector, combined with the fact that this efficiency may change with time, it is necessary to perform periodic detector efficiency calibrations. This is done using multiple sources or single sources sequentially, which have been calibrated by some other means.

The gamma detector used in this study is owned by Westlakes Scientific Consulting Ltd. and is a 30% efficient P-type germanium detector, which was calibrated prior to the counting of the samples. Each sealed small petri dish containing the prepared sample was placed on top of the detector for a period of 13000 to 60000 seconds i.e. until an

adequate spectra could be collected. The raw spectra were collected using the EG&G Ortec 92X Spectrum Master.

3.3.3 Quantitative Analysis

The Jim Fitzgerald Gamma Analysis Software (FitzPeaks 1.7) was used to analyse the spectral data produced by the detector. For each sample, the relevant spectral file, the detector calibration file, the details of the sample and the counting time were entered into the software. A Peak Search was then performed by the software to locate the peaks in the spectrum, which were subsequently measured. The environmental background was then subtracted and quantitative analysis was performed to determine the isotopes present and their activity.

3.4 REFLECTANCE SPECTRA COLLECTION AND PROCESSING

3.4.1 Introduction

Reflectance spectrometry is the quantitative measurement of a material's reflectance in the field or in the laboratory. There are three sources of light in the field, i.e. direct illumination, diffuse illumination and scatter from surroundings, each with different spectral characteristics. When spectra are collected in cloud-free summer conditions, direct solar illumination is the dominant source of reflectance. In the laboratory, the use of artificial light allows the illumination conditions and the sample geometry to be controlled. The true or absolute reflectance of a material can be determined by calibrating the raw spectrum using the spectral response of a reference sample (Section 2.5.1). This assumes the target and reference materials are collected under the same

illumination conditions and allows the spectral nature of different surfaces to be compared.

In this project, reflectance spectroradiometry was used to characterise spectrally the various surfaces found within the intertidal zone of the Ribble Estuary. This information was subsequently used as an aid in the acquisition, analysis and interpretation of the Ribble imagery. The techniques used to collect and process the raw spectra are described in detail in this section.

3.4.2 Spectra Collection

In 1995, coincident with image acquisition, the GER IRIS (Infra Red Intelligent Spectroradiometer) Mk IV spectroradiometer (NERC Equipment Pool for Field Spectroradiometry (EPFS)) was used to collect bi-directional reflectance spectra of the intertidal sediments (Plate 3.3). This instrument is a dual-beam field spectroradiometer that can simultaneously collect a measurement of a target and reference panel.

In 1996 and 1997, the high-performance single-beam ASD FieldSpec Portable Spectrometer (NERC EPFS) was used in a series of field (Plate 3.4) and laboratory (Plate 3.5) investigations. This instrument measures between the visible and short-wave infrared (350-2500nm) and allows rapid collection of replicate spectra that can be viewed in real-time on the LCD screen. The 1.2m cable and the 8° field of view allow mobility, flexibility and accurate selection of target surfaces. Unlike the previous instrument, this spectroradiometer does not simultaneously collect a reference spectrum with each target spectra. Consequently, a reference spectrum is collected using a

calibrated reference panel (NERC: Spectralon Panel 1011) immediately after each set of

replicate target spectra.
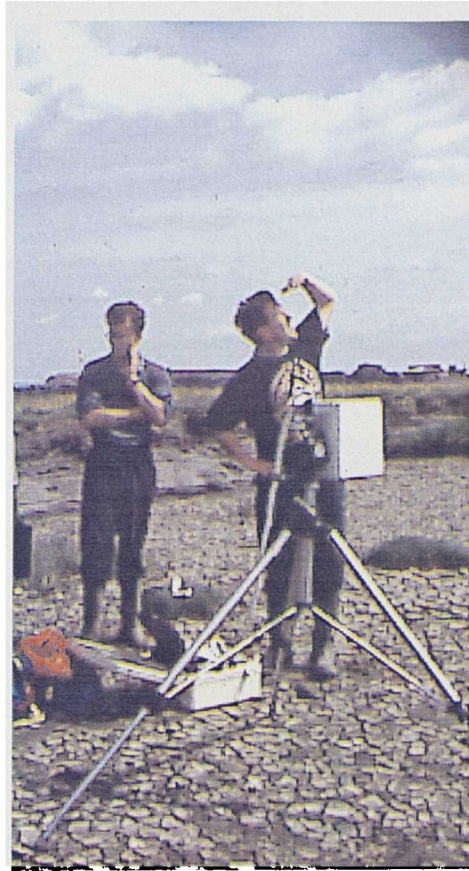
Plate 3.3 GER IRIS Mk IV Spectroradiometer
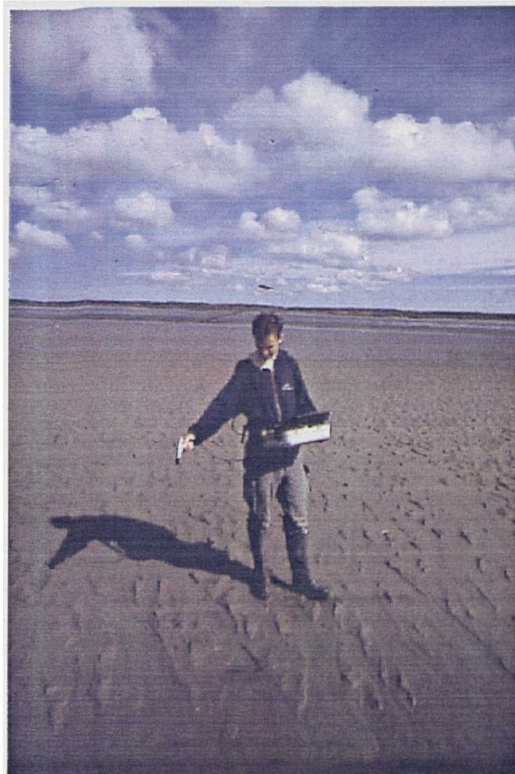
Plate 3.4 ASD Spectroradiometer used During *In Situ* Measurements
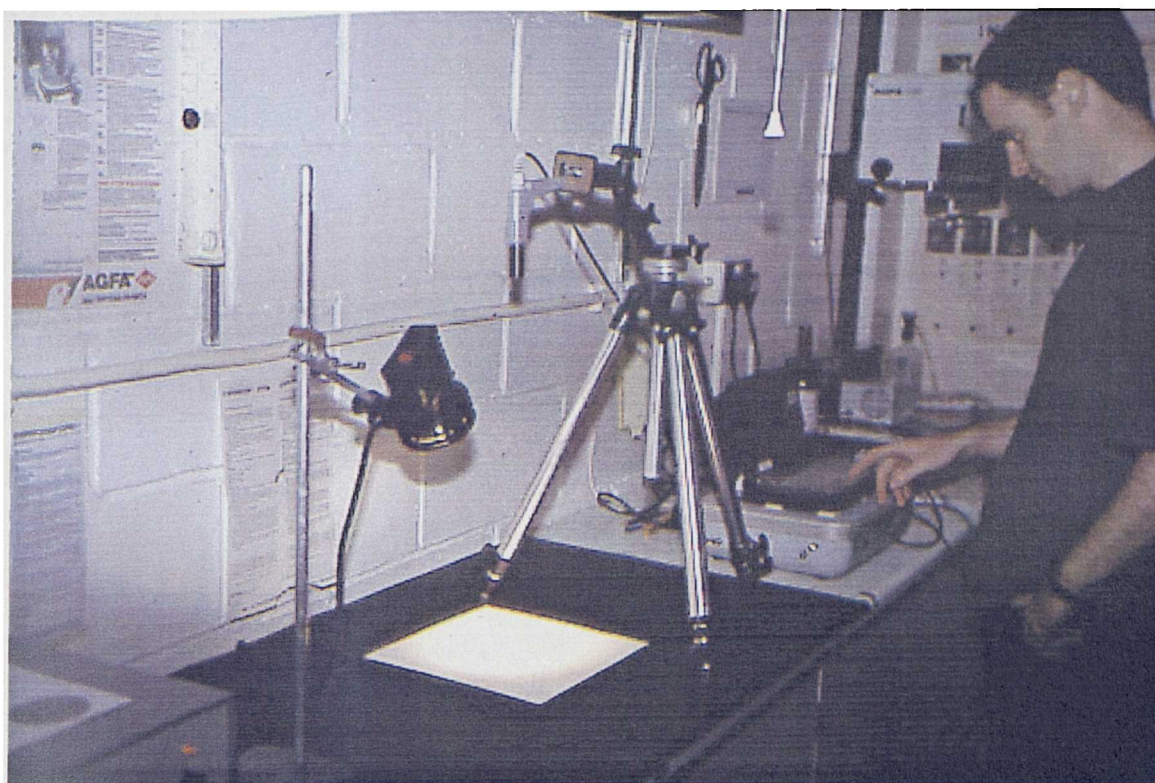
Plate 3.5 ASD Spectroradiometer used During Laboratory Investigations. The Surrounding Black Cardboard Side-panels Normally Present were Removed to Enable this Photograph to be Taken.

3.4.3 Conversion to Absolute Reflectance

Absolute reflectance is calculated by ratioing the collected target and reference spectra, and subsequently applying a correction using the associated reference panel calibration file (NERC EPFS). This calibration technique partially compensates for variations in the solar zenith angle during the *in situ* reflectance spectra acquisition; no further corrections were made.

The REFSPEC software provided by NERC EPFS was used to convert each of the replicate target spectra into absolute reflectance. Through a command line that contains the input spectrum file, the associated reference spectrum file, an ASCII-format panel calibration file and the output filename, REFSPEC produces an output text file

(Appendix 1). This file contains the absolute reflectance values of the target surface between 350 and 2500nm at a 1nm resolution.

3.4.4 Averaging and Atmospheric Correction

To produce a single representative spectrum for each target surface, an average spectra was created from the set of replicate absolute reflectance files. The windows most severely affected by the atmosphere *i.e.* between 1353-1408nm, 1803-1969nm and 2483-2500nm, were removed from each of the *in situ* representative spectra.

3.4.5 ATM Bandwidth Deconvolution

To aid in the analysis and interpretation of the ATM imagery, the averaged laboratory and *in situ* spectra were deconvolved into ATM bandwidths. Each spectrum was multiplied by filter function values files, provided by NERC EPFS, and subsequently normalised to get representative ATM bandwidth values (Appendix 2).

3.5   AIRBORNE IMAGERY COLLECTION AND PROCESSING

3.5.1   Introduction

Airborne imagery was collected of the Ribble Estuary during 1995 and 1997 in coincidence with detailed *in situ* fieldwork. In 1995, the objective was to acquire imagery of the whole estuary including a high proportion of the surrounding saltmarsh areas (Figure 3.1). At this preliminary stage of the project, the saltmarsh areas were regions of potential interest. In 1997, the project concentrated on collecting high spatial resolution imagery of the intertidal sediments exposed at low tide (Figure 3.2). In this section the remote sensing platform and the imaging sensors used to collect the Ribble

imagery are described. Also, the 1995 and 1997 image collection strategies and the subsequent data pre-processing techniques are outlined.
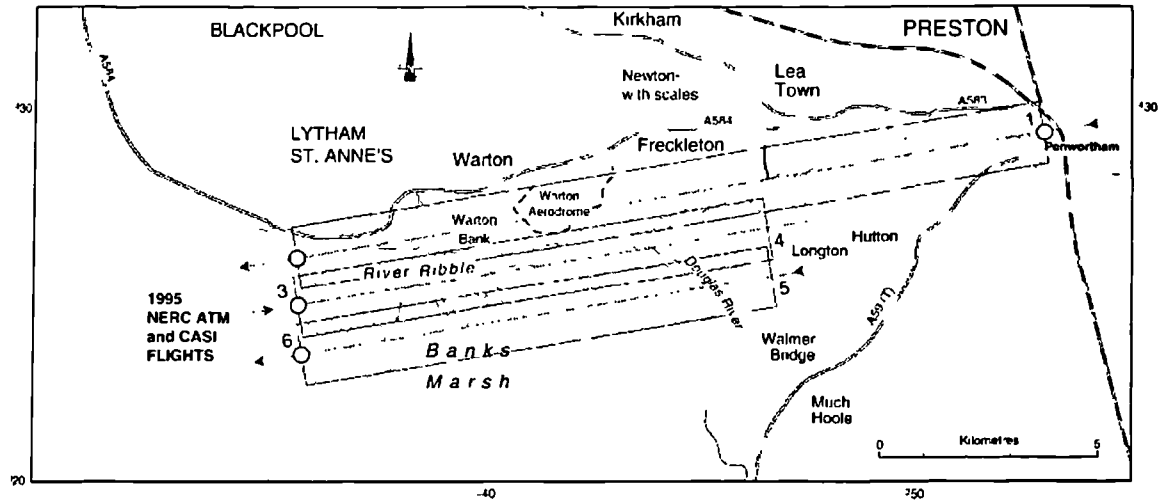
Figure 3.1 Outline of the 1995 Image Acquisition Strategy
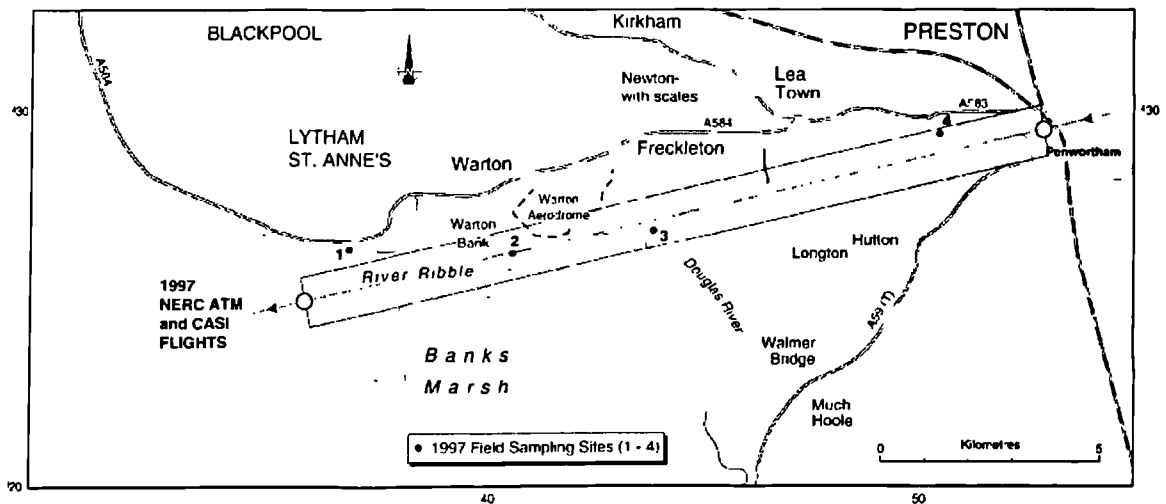
Figure 3.2 Outline of the 1997 Image Acquisition Strategy and the Locations of the 1997 Sample Points

3.5.2 Remote Sensing Platform and Sensors

The NERC Piper PA31 350 Chieftain aircraft was the platform used to collect imagery of the Ribble Estuary in 1995 and 1997 (Figure 3.3). Onboard the aircraft, a Daedalus

1268 Airborne Thematic Mapper, a Compact Airborne Spectrographic Imager (CASI)

and a Wild RC-10 Survey camera were installed. The ATM multispectral scanner

(Figure 3.4) is a passive sensor designed to collect and record radiation from the earth's

surface. The radiation is separated into 11 spectral bands, which simulate the satellite-

borne LANDSAT Thematic Mapper and range from the visible blue to the thermal

infrared (Table 3.2). Channels 1 to 5 are in the visible, 6 to 8 are in the near-infrared, 9

and 10 are in the short wave infrared, and lastly band 11 is a thermal infrared band. The

IFOV is 2.5m and the swathwidth is 1.5km at 1000m altitude (Figure 3.5). CASI is a

pushbroom imaging spectrograph designed for acquisition of visible and near-infrared

multispectral imagery from aircraft. The spectral range of the instrument is 430 to

870nm and the across-track field of view is 34.2°. Before data acquisition, the centre

wavelength and bandwidth can be defined for up to nineteen non-overlapping spectral

bands. The Wild RC-10 camera, which has a 6-inch lens and a navigation sight, was

used to collect vertical colour stereoscopic photographs in coincidence with the ATM

image collection.
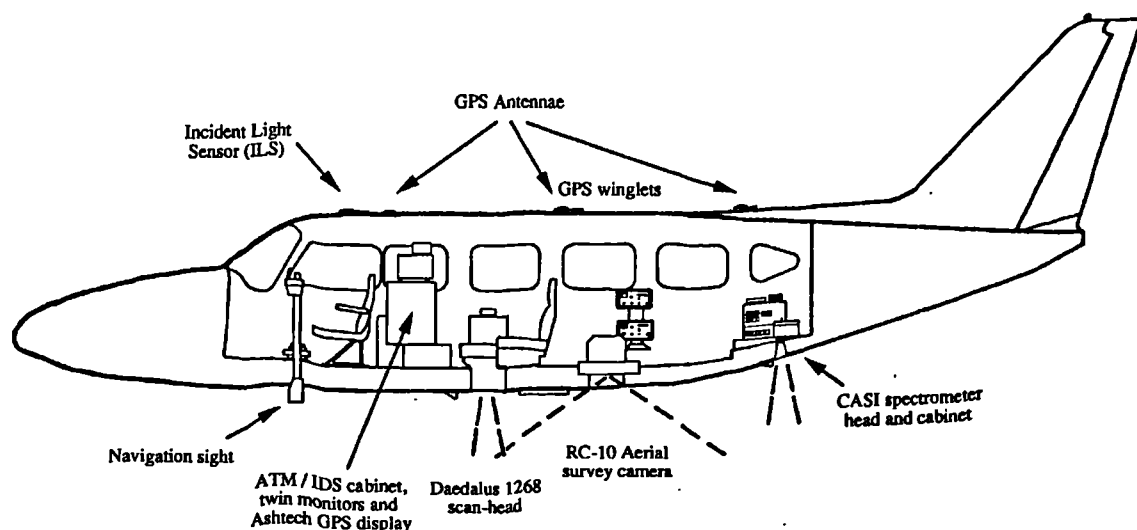
Figure 3.3 NERC Piper PA31 350 Chieftain Aircraft (Wilson, 1995)
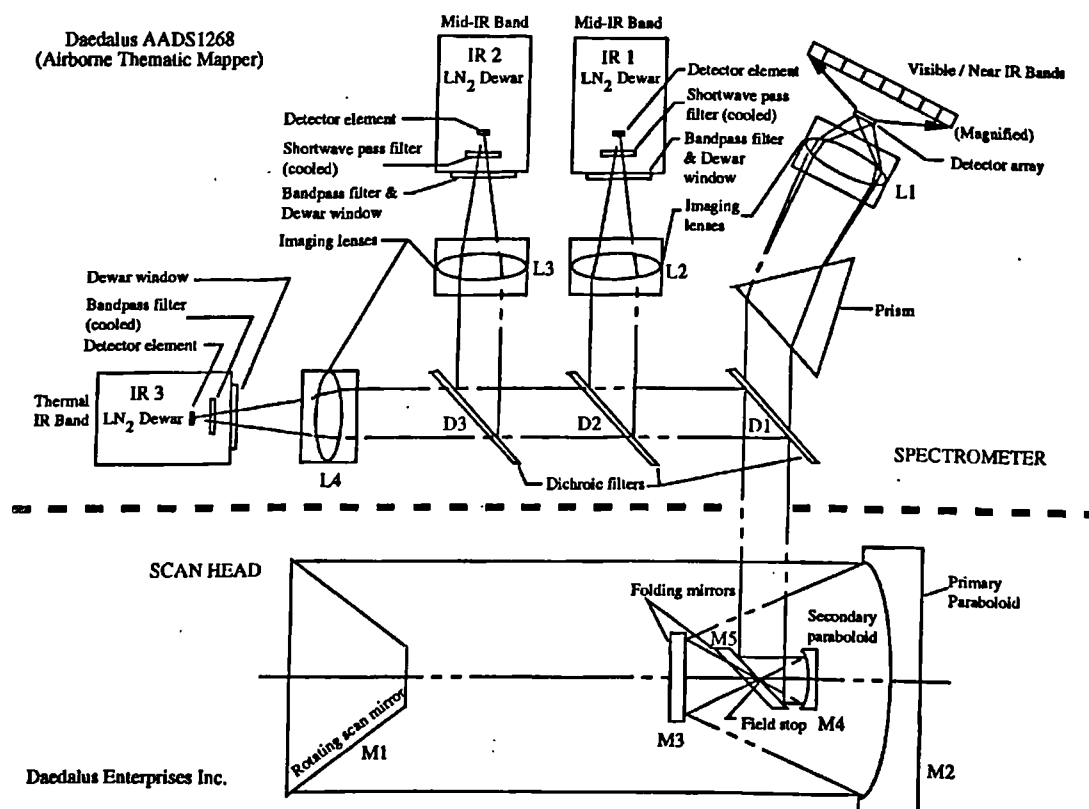
Figure 3.4 Daedalus ATM Multispectral Scanner (Wilson, 1995)

Table 3.2 Daedalus ATM Multispectral Scanner Bandwidths (Wilson, 1995)

ATM Band	ATM Bandwidth (nm)	Landsat TM Band
Band 1	420 - 450	
Band 2	450 - 520	1
Band 3	520 - 600	2
Band 4	605 - 625	
Band 5	630 - 690	3
Band 6	695 - 750	
Band 7	760 - 900	4
Band 8	910 - 1050	
Band 9	1550 - 1750	5
Band 10	2080 - 2350	7
Band 11	8500 - 13000	6
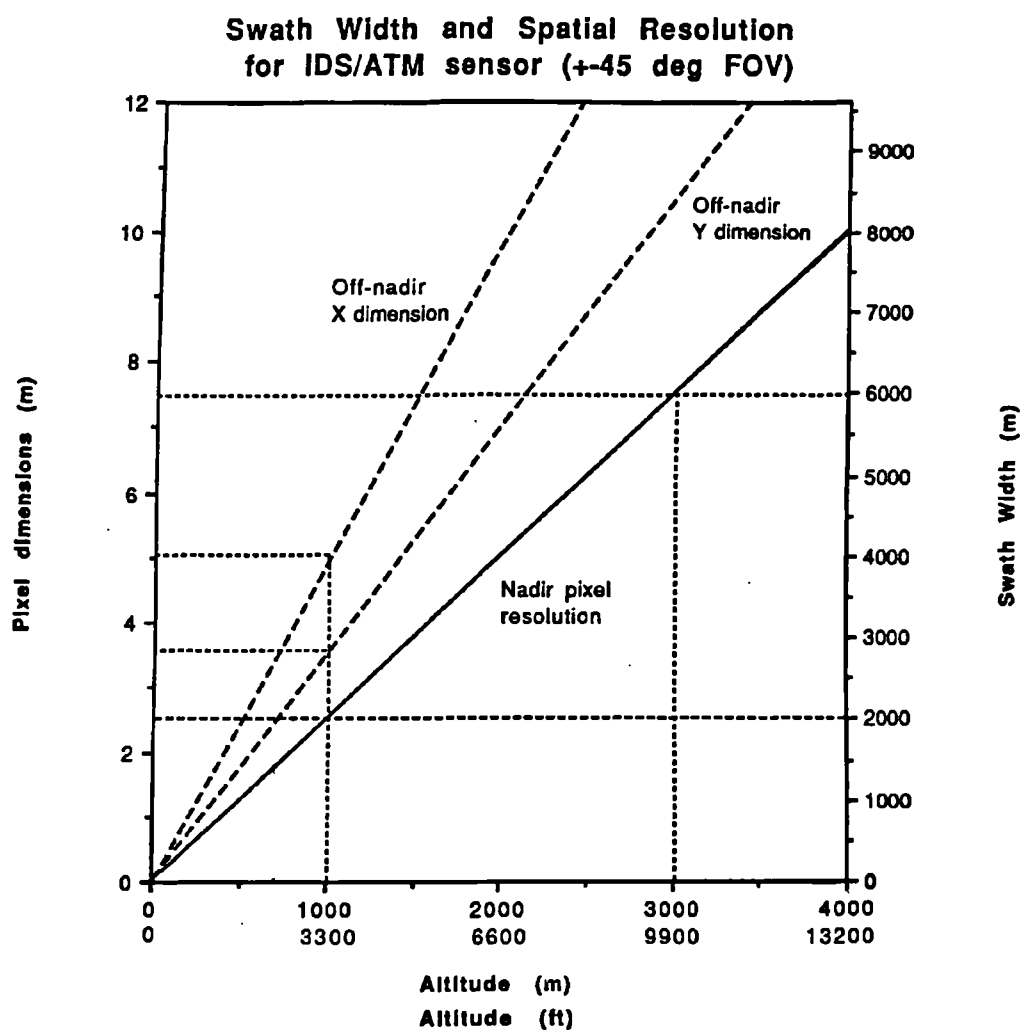
Figure 3.5 Relationship between IFOV, Altitude and Spatial Resolution for the Daedalus ATM Scanner (Wilson, 1995)

3.5.3 Flight Strategy

In 1995, ATM imagery was collected during two sets of three parallel flights; the first set was collected during low-tide conditions and the second during high-tide conditions. A complete coverage of the Ribble Estuary intertidal sediments is contained within the combined first and second low-tide lines of imagery (Figure 3.1). The first line of imagery (a214011b.hdf) includes the Lytham St Annes and Penwortham areas, and the second line (a214021b.hdf) contains the well-exposed Warton Bank and Longton areas. The third low tide image contains only the saltmarsh-dominated area of Banks Marsh

and consequently is not used in this project. The low-tide ATM imagery was collected at an altitude of 1000m, which resulted in a spatial resolution of 2.5m at nadir. Colour, stereoscopic aerial photographs and CASI imagery were collected in coincidence with the ATM imagery.

In 1997, a single flight path was chosen which closely followed the main estuary channel and included the majority of the Ribble Estuary intertidal area (Figure 3.2). One and a half hours after the intertidal areas were exposed, five lines of ATM imagery were collected along this path over a 3.25 hour period. All the flight lines were collected at 700m (1.75m spatial resolution), excluding the second flight line, which was collected at 1500m. The Lytham St. Annes region was found to be missing from the low-altitude flight lines, although this area was included within the flight plan submitted with the NERC flight application. Colour, stereoscopic aerial photographs and CASI imagery were also collected with the ATM imagery.

3.5.4 Data Processing

For both the 1995 and the 1997 datasets, colour aerial photographs were the first products received from NERC and these were followed later by the radiometrically corrected ATM and CASI imagery. The radiometric correction procedure converts the raw data into geophysical radiance units ($\mu W.cm^{-2}.sr^{-1}.nm^{-1}$) using appropriate radiometric calibration coefficients. The floating numbers produced are then scaled by multiplying by 1000, to retain precision, and converted to 16-bit data for storage (Wilson *et al.*, 1996).

Along with the radiometrically-corrected imagery, NERC provides the end-user with software (GCORR and EXHDF) that facilitates geometric correction of the imagery. The GCORR software combines scanner image data and post processed navigation information stored in the header of each raw image to produce a map projection referenced rectilinear image, corrected for aircraft position, altitude and ground surface separation. The pixel size in meters was calculated from the altitude, as in Figure 3.5 (Wilson *et al.* handbook). GCORR is operated using a single command line containing the input filename, the output HDF filename and the output pixel size (Appendix 3). Although GCORR does all image processing in rectilinear co-ordinates, a conversion from Lat/Long/Height to UK National Grid map projection co-ordinates is included. The EXHDF software is subsequently used to convert the geocorrected HDF files, produced by GCORR, into either BIL or BSQ format, allowing the files to be imported into an image-processing package. This correction procedure was applied to the ATM data only, as the CASI data was determined to be unsuitable for mapping intertidal sediment grain-size due to the limited spectral range of the instrument.

Based on NERC guidelines it was expected that the 1997 processed imagery would be received from NERC shortly after data acquisition. Unfortunately, due to a series of difficulties the final processed data was not received until fifteen months after image acquisition. Due to the dependency of this project on the 1997 dataset to validate the image analysis and classification methodology, this delay severely affected the structure and progress of this project.

3.6 INFORMATION EXTRACTION

3.6.1 Selection of Information Extraction Technique

The success of any remote sensing project is fundamentally determined by the ability to extract the required information from the imagery. As outlined in Section 2.6.5, a wide variety of image analysis and classification techniques exist for this purpose. The performance of these techniques is predominantly dependent on the data type, the environment within the imagery and the image content to be extracted. The examination of previous remote sensing studies provides an insight into the weaknesses and strengths of these various analysis techniques. Consequently, a suitable image analysis methodology may be constructed for a particular project based on the results of previous similar studies.

The estuarine intertidal zone is a unique environment subject to a range of surface conditions, with gradational boundaries between the various grain-size domains. Any attempt to map the grain-size distribution within this region through ATM imagery requires a very specific approach. 'Soft' classifiers allow the intertidal sediment grain-size to be mapped on a sub-pixel basis producing individual distribution maps for each cover type. Alternatively, 'hard' classifiers define each pixel as an individual cover type, making no attempt to account for the possible significant sediment variation within each pixel. As a result of this, 'soft' classification techniques have significantly outperformed the conventional 'hard' classifiers in a range of previous intertidal remote sensing studies (Cross *et al.*, 1991; Yates *et al.*, 1993; Donoghue *et al.*, 1994; Haguenin *et al.*, 1997; Van der Meer, 1997). Consequently, it is determined that a 'soft'

classification technique is required to identify and map successfully the grain-size variability contained within the intertidal areas of the ATM imagery.

The selection of a 'soft' classification approach was only the first step, the next stage was to chose the most suitable of the available techniques. The three techniques considered were artificial neural networks, linear mixture modelling and fuzzy c-means classification. This decision was based on the performance of the various techniques in similar environments, the availability of the software and the amount of training data required (Section 2.6.5). It was determined that the ANN technique was too reliant on an extensive training set to be used in this project (Atkinson *et al.*, 1997). The software necessary to use the fuzzy c-means classifier was not available to this project. In contrast to the above, linear mixture modelling is readily available as a module within the image processing package ENVI (Environment for Visualising Images) and it does not require an extensive training set to be effective. In studies where this technique was considerably outperformed by other 'soft' classifiers it is suggested that the dimensionality constraint of the technique was ignored (Bastin, 1997; Atkinson *et al.*, 1997). Consequently, it is expected that if this technique is used within the dimensionality guidelines it will provide results at least comparable to those of the other 'soft' techniques. In conclusion, linear mixture modelling was selected to analyse the ATM imagery of this project due to its performance in certain previous studies, its availability and its independence of an extensive training set.

3.6.2 Linear Mixture Modelling

Linear mixture modelling is an image classification technique which is based on the assumption that each observed pixel reflectance is a linear product of the spectral

signatures of the surface components present, multiplied by their relative amounts. This inherently assumes that there is no significant amount of multiple scattering between the different cover types; each photon that reaches the sensor has interacted with just one cover type (Settle and Drake, 1993). This will only occur when the components are distributed as discrete patches that are smaller than the resolution of the sensor (Singer and McCord, 1979). Each component is also assumed to have an individual, characteristic signature.

Boardman (1989) outlined a very straightforward linear mixture model, which is based on a linear relationship between the observed spectrum and a library of pure spectra representative of each ground component. The abundance of the various components within an image pixel can consequently be calculated by inverting this linear relationship (3.1).

$$A \times X = B$$
$$\Rightarrow X = A^{-1} \times B$$

3.1

Where, A - an M by N endmember library matrix
X - an N by 1 unknown abundance vector
B - an M by 1 observed data vector
M - the total number of bands
N - the number of mixing endmembers

Boardman (1989) states that the calculation should be done in an overdetermined way i.e. there should be more spectral bands than ground components. Settle and Drake (1993) refined this by stating that the number of identifiable surface types should be less than or equal to one greater than the number of spectral dimensions within the dataset (3.2).

$$c \leq n + 1$$

3.2

Where, c - the number of surface components
n - the number of spectral dimensions

This recognises that some spectral bands may have very similar image information and, therefore, the total number of bands is a poor determinant of the number of surface components that may be identified. Consequently, the spectral dimensionality of a dataset, as may be defined by a Minimum Noise Fraction Transform (MNF) for example, is thought to be a better determinant.

Finally, linear mixture models can be designed in such a way that the output is either 'constrained' or 'unconstrained' depending on the application requirements. A 'constrained' model ensures that the surface fractions (f) present in each pixel are non-negative and add up to unity (3.3).

$$f_1 + f_2 + f_3 + \ldots f_c = 1 \qquad\qquad \textbf{3.3}$$

An 'unconstrained' model does not force the output through any rules, instead it accepts the model output although some of the results may be unrealistic *e.g.* the total of the fractions may be greater than unity.

3.6.3 Image Analysis Methodology

Introduction

As stated above, linear mixture modelling was selected as the basis of the image analysis and classification methodology of this project. Included in this methodology are a number of other techniques, which improve the quality of the data and compliment the linear unmixing of the imagery. The entire range of image processing techniques used in this project is available in the ENVI package. This system is capable of visualising and analysing a wide range of satellite and airborne remote sensing data. In

this section, the image analysis and classification methodology and the relevant software are introduced.

Minimum Noise Fraction Transform

Daedalus ATM imagery has inherently a very variable signal to noise ratio depending on the bandwidth. Although most bands have a high signal to noise ratio, band 1 for example has such a low ratio that it provides little or no information. Any classification based on the ATM imagery will unavoidably include this intrinsic sensor noise, resulting in a less accurate product. Consequently, the first objective of the analysis methodology was to use a technique that would reduce the sensor noise within the dataset whilst not removing any of the image information.

Principal component analysis (PCA) is a standard data compression and enhancement tool in most remote sensing studies. However, this technique does not always produce images of decreasing image quality with increasing band number. Consequently, Green *et al.* (1988) designed the MNF transform, which is essentially an improved principal component transformation, consisting of two cascaded principal component transformations. These transforms compress the image information into component bands of increasing noise fraction (decreasing signal/noise ratio) with increasing band number. The first transformation decorrelates and rescales the noise in the data and the second is a standard principal component transformation of the data. This results in the data being divided into coherent portions with large eigenvalues and noise-dominated portions with near-unity eigenvalues. The noisiest bands may then be filtered or removed, before the components are transformed back to the original co-ordinate system. Alternatively, as in this project, the MNF bands can be used directly as the

basis for image classification. In removing or filtering the components with high noise some image information is inevitably lost, however this loss is generally much less than if a smoothing filter was applied directly to the raw untransformed data. In addition, the number of coherent MNF bands produced by a transformation is also a reasonable representation of the dimensionality of an image dataset. The MNF transform relies on the high between band correlation that exists in many remote sensing datatypes including ATM.

The MNF transform software used in this project is part of the Transforms module in ENVI and it is a modification of the work by Green *et al.* (1988). When applied to a ten band ATM image, the Forward Transform option produces ten MNF bands and an eigenvalue plot that shows the distribution of image information across the ten MNF bands. The noise statistics used in this transformation may be estimated from previously calculated noise statistics, from a 'dark' image associated with the dataset or, as in this project, directly from the input data. An inverse MNF transform option is also available in ENVI, which can be used to transform the selected coherent MNF bands back into the original image space.

Endmember Selection

As a preliminary to linear unmixing, it is necessary to know the number of spectrally distinct surface components present in the imagery, their identity, and the pure pixels representative of these components. By placing various combinations of the coherent MNF bands in 2-D scatterplots it may be possible to fulfil these requirements. Firstly, the number of spectrally distinct components or endmembers equals the number of significant extremes found in the scatterplots (Smith *et al.*, 1985; Cross *et al.*, 1991). Secondly, the

'pure' pixels, which are assumed to represent 100% of each component, are located at the tips of each extreme in feature space and consequently they can then be detected in image space. Lastly, the 'pure' pixels in image space may be subsequently identified either from *in situ* knowledge or libraries of ground spectra.

Within ENVI a 2-D scatterplot tool is available which allows various combinations of the coherent MNF bands to be selected and displayed together. The pixel distribution within the scatterplot can be density sliced, allowing the major spectral endmembers to be determined. The extreme of each endmember in feature space can then be selected as a region of interest and this results in all the image pixels being automatically highlighted. The spectral endmembers represented by these pixels can then be identified.

Linear Mixture Modelling

The Boardman (1989) linear mixture model, described in Section 3.6.2, was written in IDL to form the basis of the SIPS (Special Image Processing System) unmixing program (Kruse *et al.*, 1993). This is basically the same program as used in ENVI's linear unmixing module and, like the SIPS program, ENVI offers the option of fully constrained, partially constrained or unconstrained unmixing.

The linear unmixing procedure is based on a selection of endmember spectra. In ENVI, these spectra may be derived from the endmember 'pure' pixels that were identified in the scatterplots or alternatively from imported spectral libraries. The unmixing of an image produces a series of grey-scale images, each representing the calculated abundance distribution of a particular endmember. The term abundance refers to the relative surface extent of each cover type. A root-mean-square (RMS) error image is also produced which

highlights the areas of high unmixing error. Linear unmixing is an iterative procedure, which continues until the abundance images are an accurate representation of the ground component distributions in the imagery. When the results are found to be inadequate the endmember spectra selection is refined and the linear unmixing is repeated with the new spectra. Similarly, the 'constrained' and 'unconstrained' linear unmixing options can be experimented with to improve the overall results.

3.7 SUMMARY

Within this chapter, the main techniques used to *1)* determine the physical characteristics of the intertidal sediments, *2)* quantify radionuclide activity concentrations, *3)* spectrally characterise the sediments and *4)* collect and process the airborne imagery have been outlined. The procedure behind the selection of Linear Mixture Modelling instead of alternative image classification techniques has been explained. Finally, the analysis procedure used to classify the ATM imagery of the Ribble Estuary was defined. Where applicable, this included an outline of the fundamental theory behind the techniques and the software used to implement them.

The next chapter, Chapter 4, looks in detail at the *in-situ* and laboratory spectral characteristics of intertidal sediment and the subsequent implications for aerial remote sensing of this environment.

4. *IN SITU* AND LABORATORY-BASED REFLECTANCE SPECTRORADIOMETRY: CHARACTERISATION OF INTERTIDAL SEDIMENTS

4.1 INTRODUCTION

Spectral characterisation of intertidal sediments across a range of microenvironments is fundamental prior to the collection and analysis of airborne imagery. Recent remote sensing studies of intertidal zones have classified the sediments present based on their appearance within the imagery, without any detailed *in situ* knowledge of the surface reflectance (Folving, 1984, Bartholdy and Folving, 1986, Doerffer and Murphy, 1989, Jacobsen and Neilson, 1990, Yates *et al.* 1993, and Populas *et al.* 1995). Although this approach has the advantage of being relatively inexpensive and quick, the accuracy of the results is influenced by variations in the atmosphere between the surface and the sensor. This project has taken the opposite approach *i.e.* bottom-up; the spectral nature of the sediments is investigated using high-resolution *in situ* reflectance spectroradiometry, before any attempt is made to differentiate them in the imagery.

The reflectance (0.4 - 2.5μm) of intertidal sediment is controlled by a range of properties such as grain-size, moisture content, organic content, cyanobacteria, iron-oxide content, and mineralogy (Asrar, 1989). To determine grain-size, it is therefore necessary to recognise how this sediment characteristic influences the reflectance spectrum and how this is affected by other sediment properties, primarily surface and interstitial moisture.

In situ spectroradiometric investigations at Warton Bank in 1994 using the GER SIRIS (Single Field of View Infra Red Intelligent Spectroradiometer) identified a strong negative relationship between the clay content of the sediments and reflectance within the 0.4 - 2.5µm range (Tyler *et al.*, 1995; Bryant *et al.* 1996). Outlined in this chapter are the results of further *in situ* and laboratory experiments carried out to define this relationship, and to quantify the influence of interstitial and surface moisture conditions on the association (Rainey *et al.*, In Press). The implication of the results on the timing of airborne remote sensing campaigns is also discussed.

4.2   *IN SITU* CHARACTERISATION OF INTERTIDAL SEDIMENTS

4.2.1   Objective

The primary objectives of the *in situ* investigations were, *1)* to define accurately the relationship between reflectance (0.4 - 2.5 µm) and sediment grain-size, *2)* to identify the spectral effects, if any, of topography, moisture and other surface characteristics on sediment reflectivity, *3)* to examine the seasonal variability of the sediment/reflectance relationship and *4)* to identify the most useful ATM bandwidths for sediment mapping.

4.2.2   Areas of Investigation

Two sites of contrasting location, scale, sediment type and topography were selected for spectral examination. Warton Bank is representative of the narrow, sloped intertidal area, typical of the middle and inner reaches of the Ribble Estuary (Plate 3.1) and Lytham St. Annes is an example of the relatively flat large intertidal expanses of the outer estuary (Plate 3.2). Warton Bank contains a range of sediment types including muds, silts and sands whilst, Lytham St. Annes is dominated by fine sediment.

4.2.3 Method

Field Studies

In situ reflectance spectroradiometry was carried out on the intertidal sediments of the

Ribble Estuary during intensive field studies in 1995, 1996 and 1997 (Table 4.1). The

GER IRIS Mk IV spectroradiometer (loaned from NERC EPFS) was used in the 1995

study to collect bi-directional reflectance spectra of the intertidal sediments (Plate 3.3).

During the 1996 and 1997 field investigations the ASD spectroradiometer (loaned from

NERC EPFS) was used to collect reflectance spectra of the intertidal surface (Plate 3.4).

The instrument's superior spectral collection and storage capabilities, combined with its

portability and real-time spectra viewing capabilities, enabled a more detailed spectral

investigation of the intertidal environment. Technical details of both the above

spectroradiometers, their output and how these files were processed is provided in

Section 3.4.2.

Table 4.1 A Summary of the *In Situ* Spectroradiometric Experiments Carried Out in the Ribble Estuary

Date	Location	Spectroradiometer	Transect Name	No. Of Sites
August 1995	Warton	IRIS	Transect A	7
			Transect B	7
June 1996	Warton	ASD	Transect A	30
			Transect B	18
			Transect C	15
			Transect D	15
	Lytham	ASD	Transect A	5
February 1997	Warton	ASD	Transect A	24
			Transect B	20
			Transect C	17
	Lytham	ASD	Transect A	28
			Transect B	22

1995 Field Study

In August 1995, the GER IRIS spectroradiometer was used to collect spectra along two transects from the saltmarsh edge to the main channel at Warton Bank (Figure 4.1). At each sample site, five repeat spectra and a sediment sample were collected simultaneously. The intertidal area appeared relatively dry after being exposed to summer drying conditions for a few hours before sampling.
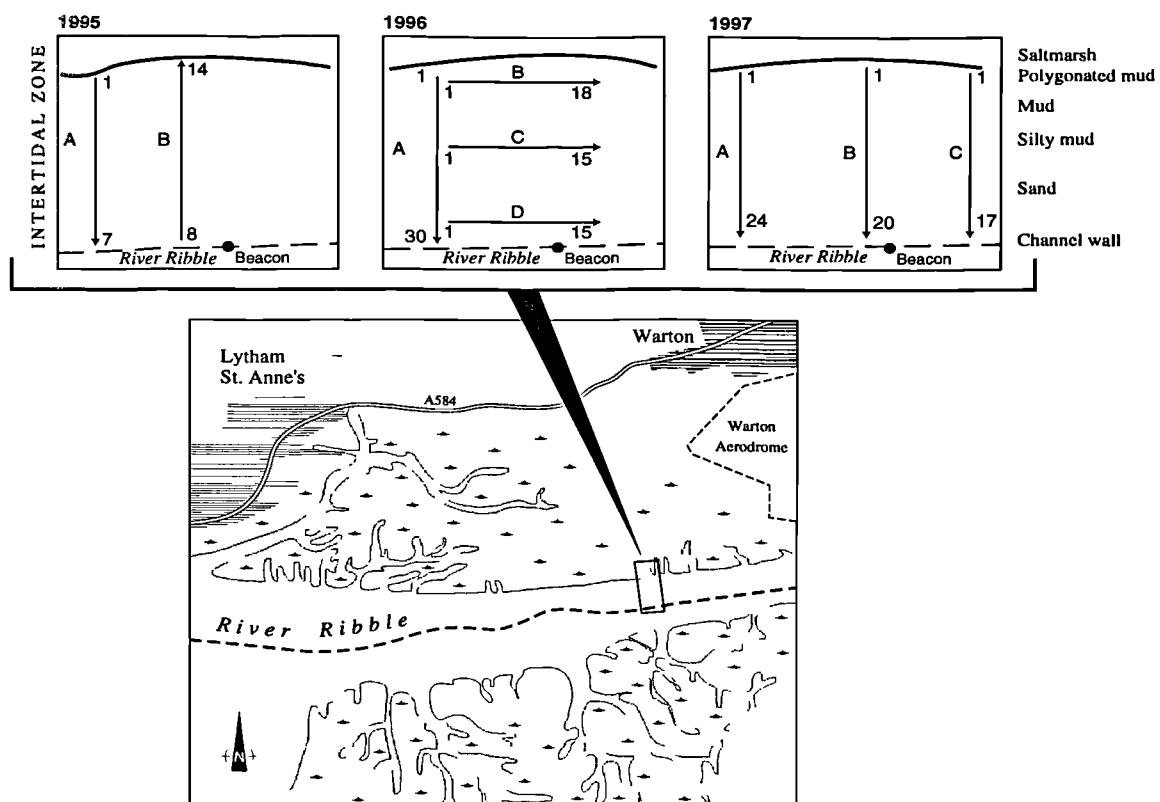
Figure 4.1 Outline of the Sampling Transects for the 1995, 1996 and 1997 Fieldwork at Warton Bank

1996 Study

In June 1996, sets of ten repeat reflectance spectra, with associated reference spectra and sediment samples, were collected using the ASD spectroradiometer along transect A_{96}, perpendicular to the channel, and along three parallel transects, B_{96}, C_{96} and D_{96} (Figure 4.1). Transect A_{96} was first sampled between 09:30 and 10:30, before tidal inundation.

At 15:30, immediately after sediment re-exposure, sampling was repeated along transect A_{96}, and transects B_{96}, C_{96} and D_{96} were subsequently measured out and sampled (Plate 4.3). Sampling along transect B_{96} was partially repeated following a short period of exposure. A preliminary investigation was also undertaken at Lytham St. Annes, where reflectance spectra with associated sediment samples were collected along a short transect perpendicular to the channel.

1997 Study

In February, fieldwork was carried out to characterise the direct effect of moisture and exposure on the reflectance of intertidal sediment. At Warton Bank reflectance spectra and samples were collected using the ASD spectroradiometer along three transects (A_{97}, B_{97} and C_{97}) perpendicular to the main channel (Figure 4.1). Sampling along transect A_{97} was partially repeated after a period of exposure. However, the intertidal area appeared to remain very wet throughout this study, as drying conditions were minimal. At Lytham St. Annes, similar sampling was carried out along two transects perpendicular to the main channel. After a period of exposure, every second site along transect A_{lyth97} was re-sampled.

4.2.4 Results

Spectral Variability

Analysis of the three spectral datasets concluded that along approximately 80% of the transects examined, the simulated ATM bands 9 and 10 had significantly greater coefficients of variance (%CV) in comparison to the other bands, indicating that they may be more responsive to changes in sediment conditions. The 1996 results confirmed that the spectral variation within these bandwidths was greater along transects

perpendicular to the main channel (*i.e.* the direction of maximum change in sediment grain-size) than along the parallel transects (Table 4.2).

Table 4.2 Spectral Variation Along the Perpendicular (A_{96}) and Parallel (B_{96}, C_{96} and D_{96}) Transects Sampled During the 1996 Study

Transect	Orientation to Main Channel	CV% (ATM9)	CV% (ATM10)
Transect A (Dry)	Perpendicular	35.6	51.8
Transect A (Wet)	Perpendicular	38.4	55.4
Transect B (Wet)	Parallel	12.1	19.0
Transect C (Wet)	Parallel	28.1	32.7
Transect D (Wet)	Parallel	19.0	26.2

Reflectance and Percentage Clay/Sand

The 1995 spectral investigation identified a significant positive relationship between intertidal percentage sand content and almost all the simulated ATM bandwidths (Table 4.3). A similar, although negative, relationship existed between the majority of the ATM bandwidths and percentage clay content. The strongest and most significant relationships existed between percentage sand and ATM bands 9 ($r^2=0.51$) and 10 ($r^2=0.61$). Comparable associations between ATM band 9 and percentage sand ($p<0.01$) were also observed in 1996 along the perpendicular transect A_{96} before tidal inundation and along transect B_{96} after a period of exposure (Table 4.4).

Influence of Interstitial and Surface Moisture on the Sediment/Reflectance Relationship

The relationship between ATM reflectance and sediment grain-size properties was found to be very different along transects with high interstitial moisture contents. In 1996, when the sediments were saturated immediately after tidal inundation, the previous positive relationship between band 9 and percentage sand along A_{96} was

Table 4.3 Pearson Correlation and Level of Significance for ATM Band Associations With Percentage Sand Content of Intertidal Sediment

ATM Bandwidth	Pearson Correlation with % Sand (significant to)	Pearson Correlation with % Clay (significant to)
ATM 1	0.53 (NS)	- 0.4 (NS)
ATM 2	0.56 (< 0.05)	- 0.45 (NS)
ATM 3	0.66 (< 0.02)	- 0.54 (<0.05)
ATM 4	0.66 (< 0.01)	- 0.54 (<0.05)
ATM 5	0.65 (< 0.02)	- 0.54 (<0.05)
ATM 6	0.61 (0.02)	- 0.50 (NS)
ATM 7	0.45 (NS)	- 0.34 (NS)
ATM 8	0.49 (NS)	- 0.38 (NS)
ATM 9	0.78 (< 0.01)	- 0.68 (<0.01)
ATM 10	0.72 (< 0.01)	- 0.62 (<0.02)

Table 4.4 Correlations between ATM Bands 9 and 10 and Percentage Sand along Warton Bank Transects

Date	Transect (Conditions)	Orientation to Main Channel	ATM9/%Sand Pearson Correlation (significant to)	ATM10/%Sand Pearson Correlation (significant to)
1995	A+B (Dry)	Perpendicular	0.78 (<0.01)	0.72 (<0.01)
1996	A (Dry)	Perpendicular	0.52 (<0.01)	0.45 (<0.01)
	A (Wet)	Perpendicular	- 0.60 (<0.01)	- 0.61 (<0.01)
	B (Wet)	Parallel	0.38 (NS)	0.48 (<0.05)
	B (Dry)	Parallel	0.88 (<0.01)	0.85 (<0.02)

replaced by a significant negative relationship (p<0.01) as shown in Table 4.4 and Figure 4.2. This suggests that when intertidal sediments are completely saturated the sands have a significantly lower reflectance than the mud, which is the reverse of what was observed before. This negative relationship was better described (r^2 changed from 0.36 to 0.67) when percentage moisture was included in the multiple regression equation (4.1).

$$ATM9 = 0.302 - 0.00182 * [sand(\%)] - 0.00265 * [water(\%)] \qquad (4.1)$$

This equation suggests that in this case the effect of moisture on the spectral response of the sediment is greater than the influence of percentage sand concentration. The remaining noise in the relationship may be associated with surface moisture.

A | TOPOGRAPHY
Mud → Silt → Sand

Metres

Po l l
Wdt-r

% Cla/	8 91	5 46	0 7?
% Silt	75 90	59 9.	1 1c
% Sand	15 19	14 55	98 15

0   1 0m
Saltmarsh   Channe Wal

B 30 BEFORE HIGH TIDE

Dry po yo natet mud

% ATM9 REFLECTANCE

'nderl)inq trend

Po l of walr r

Saltmarsh   Channel Wall

C 30 AFTER HIGH TIDE

% ATM9 REFLECTANCE

Underlyinq trend

Saltmarsh   Channel Wa l
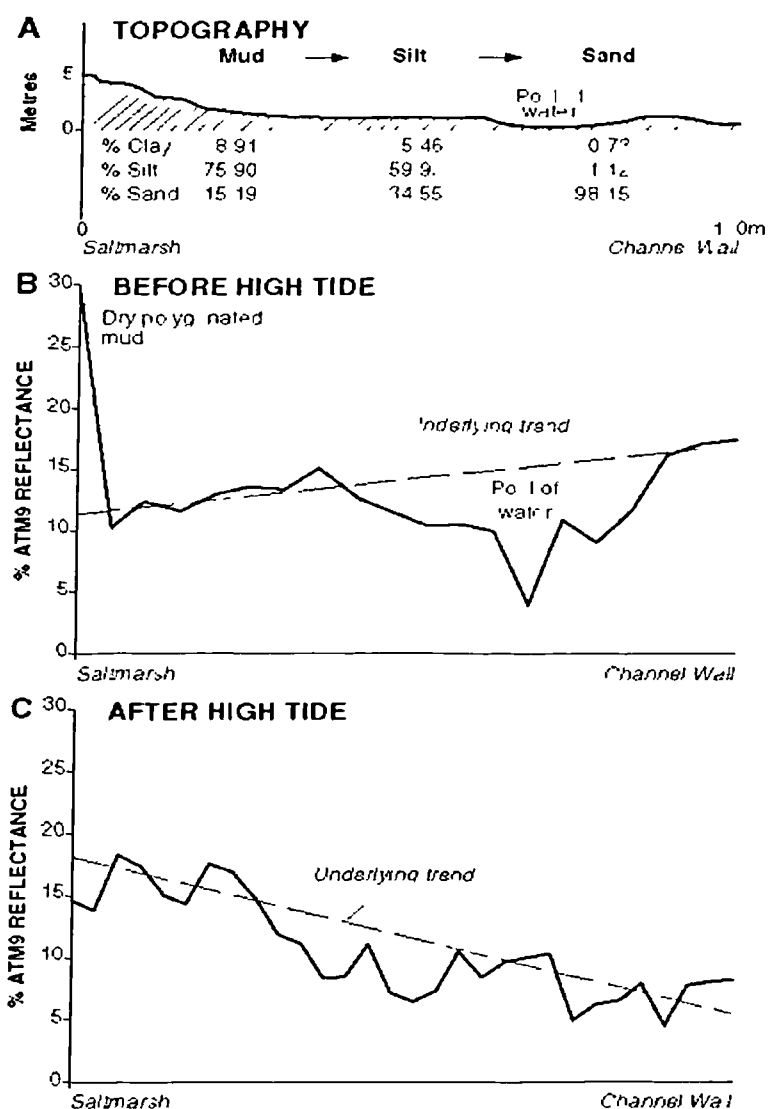
Figure 4.2 Transect A at Warton Bank Sampled in 1996 Demonstrating a)Topography, b)Reflectance Before High Tide and c)Reflectance Immediately After High Tide

Within sediments which were exposed for short periods of time to drying conditions, and consequently with relatively high interstitial moisture contents, only weak relationships, if any, were observed between ATM bands 9 and 10 and percentage sand or clay. For example no significant relationship between sediment grain-size and ATM

94

bands 9 and 10 reflectance were observed along transects parallel to the main channel sampled shortly after tidal inundation at Warton Bank in 1996. Similarly, after a short period of exposure at Warton Bank in 1997, no significant relationship was observed along transect A_{97} (Figure 4.1). Along transect B_{97} a negative though insignificant relationship was observed between ATM band 10 and percentage sand (r=-0.407). Within transect C_{97} a negative though insignificant relationship existed between band 9 and percentage clay (r=-0.431), and an insignificant positive relationship existed between band 9 and percentage sand (r=0.441). Similar observations were made at Lytham St. Annes in 1997, between band 10 and percentage sand along one of the perpendicular transects (r=0.376), confirming that this is not a site-specific effect. The inclusion of moisture in the regression equations did not improve the relationship along either of the Lytham St. Annes transects.

Surface water, in the form of small pools and saltmarsh creeks, was found along some of the transects sampled. As expected, these pools significantly attenuated the overall sediment reflectance, masking the relationship between sediment grain-size and reflectance. Consequently, the spectral variability within the sediment domains containing pools and/or creeks, was predominantly a function of surface water. For example along transect A at Warton Bank sampled before tidal inundation in 1996, a large pool of water dramatically lowered the sediment reflectance, increasing the spectral variability (%CV = 37.5) within the sand-dominated sediment domain (Figure 4.2).

4.2.5 Principal Component Analysis

Principal component analysis (PCA) was applied to all the simulated ATM bands of the *in situ* spectra collected during three years of study. This technique produces an optimal presentation of multivariate data by projecting the raw data into the space defined by the eigenvectors of the data variance-covariance matrix (Smith *et al.*, 1985). As can be seen in the eigenvalue plot (Figure 4.3) approximately 87% of the variance is contained in the first two principal components (PC). On the basis of this, a scatterplot was generated of PC 1 against PC 2, and the distribution of the spectra in feature space was analysed (Figure 4.4).
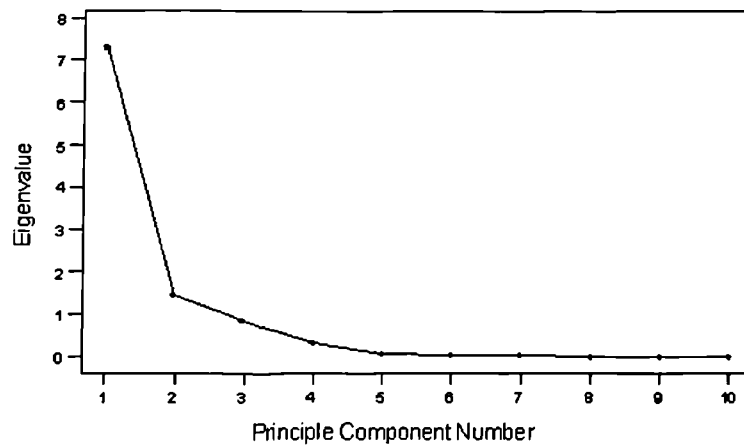
Figure 4.3 Eigenvalue Plot Produced From PCA of *In Situ* Spectra
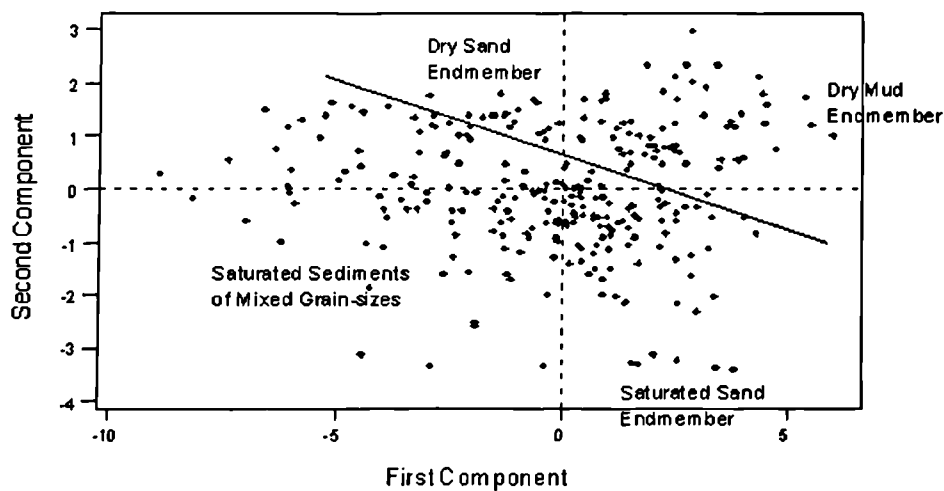
Figure 4.4 Scatterplot of PC 1 Against PC 2, Produced From PCA of the *In Situ* Spectra, With the Location of the Main Endmembers Labelled

96

Reflectance spectra of pure sand and mud areas, which were exposed for a long period of time to rapid drying conditions, were found to have very distinct locations in feature space (Figure 4.4.). The dry mud and sand spectra are principally separated along the PC 1 axis, which contains 73% of the total statistical variance (Figure 4.4.), consequently this suggests these surfaces are spectrally very different. This is underlined when the endmember dry sand and dry mud spectra are examined individually as in Figure 4.5.
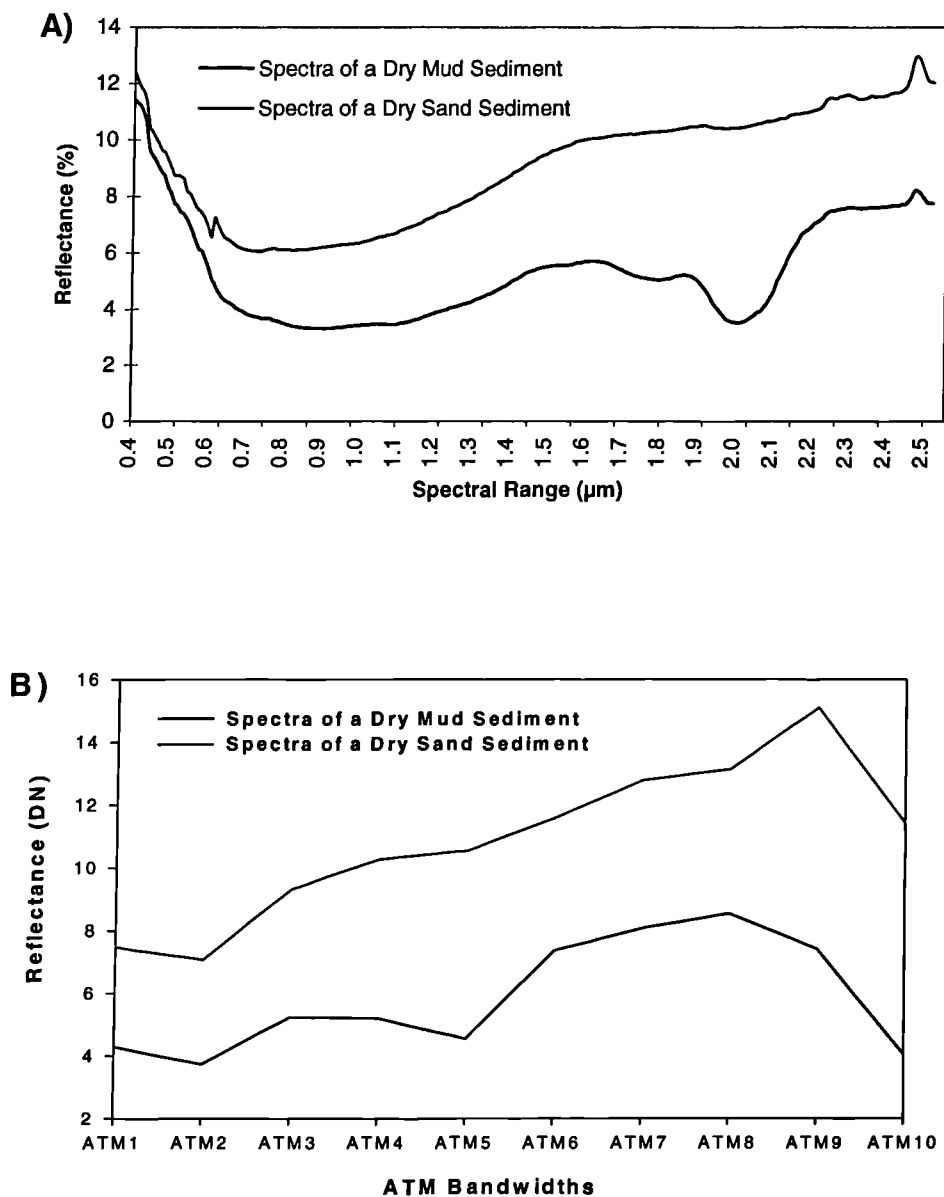
Figure 4.5 Example A)Raw Endmember Spectra and B) ATM Simulated Endmember Spectra, Representing a Dry Mud and a Dry Sand Sample Identified Through PCA

It is also evident from the scatterplot that the distribution of high moisture sediment spectra in feature space is not determined by their grain-size. Although some of the wet sand spectra are clustered, the rest of the high moisture sediment spectra, including the remaining wet sand spectra, are randomly distributed. The high moisture sediment spectra are predominantly located below the line in Figure 4.4. Consequently, it is suggested that in the scatterplot of *in situ* spectra variations in sediment type appear to expressed along PC 1, whilst moisture variations are expressed along the vertical PC 2 axis.

4.2.6 Discussion

It has been proven that a strong positive relationship exists between percentage sand and ATM reflectance along transects which have been exposed to rapid drying conditions for a long period of time (*i.e.* >2 hours). Since this association is not seen in sediments with high moisture contents, it can be concluded that it is the loss of interstitial moisture that enables the grain size/reflectance relationship to exist. Nearly all the ATM bands have an association with percentage sand, although it is strongest for bands 9 and 10.

The influence of interstitial moisture on sediment reflectance is also most evident in bands 9 and 10. The 1996 results have demonstrated that no constant relationship exists between ATM bands 9/10 and sediment grain-size when the intertidal area has high moisture contents. Similarly the 1997 results show that under these conditions the grain-size/reflectance relationships are more often insignificant. The only strong relationship observed between bands 9/10 and percentage sand during these conditions was a negative one along the perpendicular transect at Warton Bank (A_{96}), sampled as the tide retreated in 1996. It is suggested that this is due to the mud having a relatively higher reflectance in bands 9/10 than the coarser sediment for a short period of time

immediately after intertidal exposure, when all the sediments are saturated. Lastly, the variation in spectral reflectance for sediments with high moisture contents is notably controlled by the amount of interstitial and surface moisture present. This can vary nearly as much within sediment domains as across them *e.g.* Table 4.2.

The PCA results demonstrate that dry intertidal sediments may be spectrally differentiated on the basis of grain-size. In contrast, the location of saturated sediment spectra in feature space is obviously not determined by this characteristic. The advantage of this analysis technique is that it uses all ten simulated ATM bands. In the 1995 results, seven of the ten ATM bands had a significant association with the percentage sand of the intertidal sediments. Consequently, although the strongest relationship existed for bands 9 and 10, it is evident from the PCA results that the most efficient use is made of ATM data when all ten multispectral bands are combined to differentiate the sediment grain-sizes.

The topography of an intertidal area is an important determinant for the relationship between reflectance and sediment grain-size. Although it is not immediately evident in these results, it is accepted that sloped intertidal areas such as Warton Bank initially lose their surface moisture more quickly than flat areas like Lytham St. Annes. Consequently the spectral effect of moisture on the reflectance/grain-size relationship is relatively less, allowing them to be more accurately mapped. Also, where small topographical depressions exist, pools of surface water develop and, as demonstrated in the 1996 and 1997 results, these dramatically attenuate sediment reflectance, masking any relationship with grain-size. It is suggested that both large and small-scale intertidal

topographical features have important consequences on the ability to spectrally differentiate sediments of different grain-size from the airborne imagery.

Finally, the seasonal variability of the sediment/reflectance relationship is also apparent in this study. The best relationships observed were at Warton Bank in August 1995 after the sediments had been exposed for a long period of time to strong summer drying conditions. However, at both Lytham St. Anne's and Warton Bank no strong relationship existed along the sampled transects before or after exposure in February 1997, due to the weak winter drying conditions insufficiently reducing the sediment interstitial moisture content. Similarly the extent of the pools of surface water did not noticeably alter during the 1997 field studies. It can be concluded from this that seasonality is a significant factor in the ability to differentiate sediments spectrally.

4.3 LABORATORY CHARACTERISATION OF SEDIMENT REFLECTANCE

4.3.1 Objective

Laboratory experiments allow the spectral characteristics of intertidal sediments to be examined in detail under controlled conditions. The experiments in this project had three aims: *1)* to identify the main spectral differences between sediments of different grain-size, *2)* to examine the spectral effect of moisture content on these reflectance characteristics, and *3)* to investigate the spectral distinctiveness of intertidal sediments of various grain-sizes through PCA analysis. Experiment 2 was undertaken, following preliminary analysis of the results of Experiment 1, to gain a detailed understanding of the spectral nature of the individual sediment size fractions (Rainey *et al.*, In Press).

4.3.2 Method

Both reflectance experiments were carried out in a darkroom, with photographic tape and black card used to prevent light scatter from the instrumental and background surfaces. The source of illumination was a halogen lamp mounted on a stand and an ASD spectroradiometer was used to collect reflectance spectra (Plate 3.5).

In Experiment 1, bulk sediment samples of known grain-size (Table 4.5) from the Ribble Estuary were used to fill three shallow black containers to a depth of 2cm. Each sample was saturated, weighed and 10 repeat reflectance spectra and a reference spectrum were collected. The samples were then placed in a fan-assisted drying oven (100°C), and at regular intervals were re-weighed and a set of spectra collected. This continued until each sample weight stabilised *i.e.* the sample was dry.

Table 4.5 Characteristics of the 1996 Laboratory Sediment Samples

	Sample A	Sample B	Sample C
Mean Grain-size (μm)	186.63	135.73	44.97
% Sand	97.72	86.26	28.11
% Silt	1.55	12.13	65.18
% Clay	0.73	1.61	6.71

In Experiment 2, bulk sediment samples from the Ribble Estuary were wet-sieved and washed to produce three samples of grain-size <63μm, 63-125μm and 125-215μm respectively. These samples were used to examine the reflectance of specific size fractions under varying moisture conditions. The Experiment 1 procedure outlined above was repeated using the sieved samples.

4.3.3 Results

Spectral Variability

The coefficient of variance was greatest in ATM bandwidths 9 and 10 for each sediment sample, especially the fine-grained samples, suggesting these bands are more sensitive to moisture variations (Table 4.6). This may have been predicted from the proximity of these ATM bandwidths to strong water absorption features visible within the reflectance spectra. Due to this, and the significance of these bandwidths in the *in situ* results, the spectral effect of moisture on bands 9 and 10 is described in detail.

Table 4.6 Coefficient of Variance for Each ATM Band, and the Correlation Coefficients (r) and Coefficients of Determination (R^2) between Reflectance and Loss of Moisture for the Sand Sample of Laboratory Experiment 1

ATM Band	Coefficient of variance	Pearson Correlation (Significance level)	R-squared value
Band 1	29.89	- 0.94 (<0.01)	0.89
Band 2	30.38	- 0.93 (<0.01)	0.87
Band 3	28.95	- 0.94 (<0.01)	0.89
Band 4	28.88	- 0.95 (<0.01)	0.90
Band 5	29.31	- 0.95 (<0.01)	0.90
Band 6	29.57	- 0.95 (<0.01)	0.91
Band 7	29.67	- 0.95 (<0.01)	0.91
Band 8	29.83	- 0.95 (<0.01)	0.92
Band 9	37.87	- 0.97 (<0.01)	0.96
Band 10	52.44	- 0.96 (<0.01)	0.93

Spectral Response to Drying of Ribble Intertidal Sediments

The reflectance of Sample A (Experiment 1) in all ATM bandwidths approximates a positive linear relationship with loss of moisture (Figures 4.6A). The strongest relationships exist between bands 9 and 10 and percentage moisture (Table 4.7). Although there is an indication of an additional influence, the association between band 9 and percentage moisture for Sample B is approximated as being linear (Figure 4.6B). In contrast, the reflectance of Sample C (mud) has a non-linear relationship with drying,

demonstrating two distinct spectral stages during the loss of moisture (Figure 4.6C). The

ATM band 9 value initially remains reasonably constant during the loss of the first 75% of

moisture, however following this, reflectance increases rapidly from 10 DN to 34 DN. At

absolute dryness the maximum band 9 values for Samples A and B are substantially

greater than for Sample C (mud), however at saturation the difference is negligible.

Maximum spectral contrast between Sample A and Sample C, in ATM band 9, exists

when the sediments are at 25% saturation. The spectral contrast between Sample A and

Sample B does not vary substantially with loss of moisture.
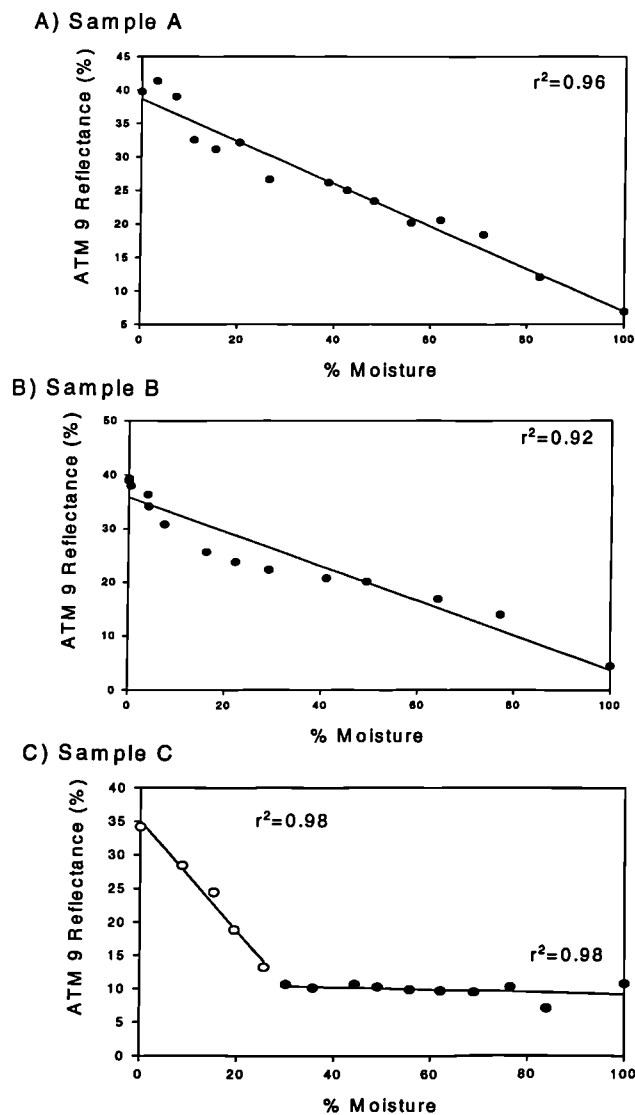
Figure 4.6 Relationship between ATM Band 9 Reflectance and Percentage Moisture for typical a) Sand, b) Silt and c) Mud Samples from the Ribble Estuary

Table 4.7 Spectral Ranges and Relationship between Reflectance and Moisture Loss of Laboratory Experiment 1 Samples

Sample Name	ATM 9 Spectral Range (DN)	Pearson Correlation (Level of Significance)	ATM 9 Reflectance v Drying Regression (r^2)
Sample A	7 – 41	-0.97 (<0.01)	0.96
Sample B	4- 39	-0.95 (<0.01)	0.92
Sample C	7 –34	-0.76 (<0.01)	0.59

Spectral Response to Drying of Individual Sediment Size Fractions

The results of Experiment 2 provide detailed information regarding the spectral effect of moisture on the individual size fractions (Table 4.8). Sample 1 (125-215 μm) and Sample 2 (63-125 μm) have a similar positive linear response in all the ATM bandwidths with loss of moisture (Figure 4.7A and 4.7B). In contrast, Sample 3 (<63μm) has at least three distinct spectral stages during drying (Figure 4.7C). In ATM band 9 for example, reflectance increases from 2.5 DN to 15 DN (moisture 100% - 95%), before decreasing from 15 DN to 9 DN (moisture 95% - 50%) and lastly, in stage 3, reflectance increases rapidly from 9 DN to 32.5 DN (moisture 50% - 0%). Detailed spectral changes below 40% moisture were not obtained due to the prolonged drying times required by Sample 3, coupled with time constraints. However the general trend is in agreement with the final stage of drying for Sample C of Experiment 1 (Figure 4.7C). The spectral contrast between the two coarse samples in band 9 did not change significantly with drying.

Table 4.8 Spectral Ranges and Relationships between Reflectance and Moisture Loss of Laboratory Experiment 2 Samples

Sample (Grain-size Range)	ATM 9 Spectral Range (DN)	Pearson Correlation (level of Significance)	ATM 9 Reflectance v Drying Regression (r^2)
Sample 1 (215-125μm)	0.49 - 50.38	-0.98 (<0.01)	0.97
Sample 2 (125-63μm)	0.77 - 39.36	-0.97 (<0.01)	0.96
Sample 3 (<63μm)	2.5 - 32.5	-0.62 (<0.01)	0.39
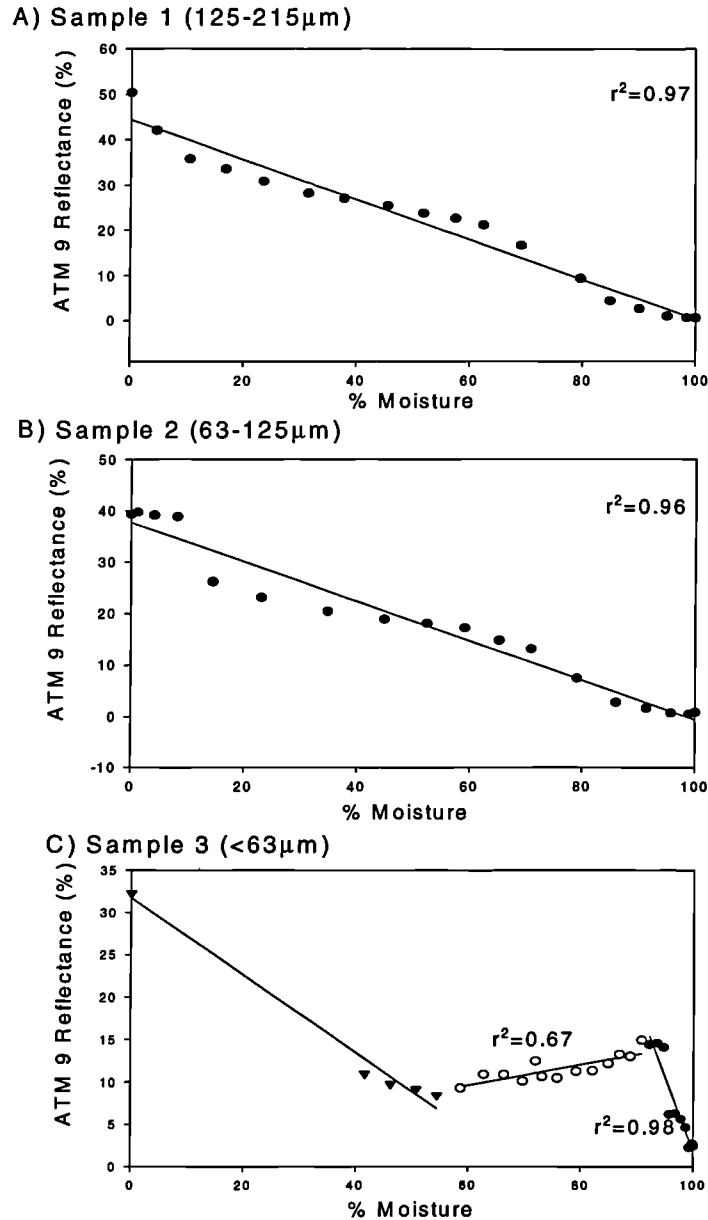
Figure 4.7 Relationship between ATM Band 9 Reflectance and Percentage Moisture for Three Sediment Size Fractions, a)215-125μm, b)125-63μm and c)<63μm

4.3.4 Principal Component Analysis

Principal component analysis was applied to the simulated ATM bands of the laboratory spectra collected during Experiment 1. Approximately 99.6 % of the variance is contained in the first two principal components as shown in Figure 4.8. On this basis, a scatterplot

was generated of PC 1 against PC 2 (Figure 4.9), and the distribution of the laboratory spectra in feature space was analysed.
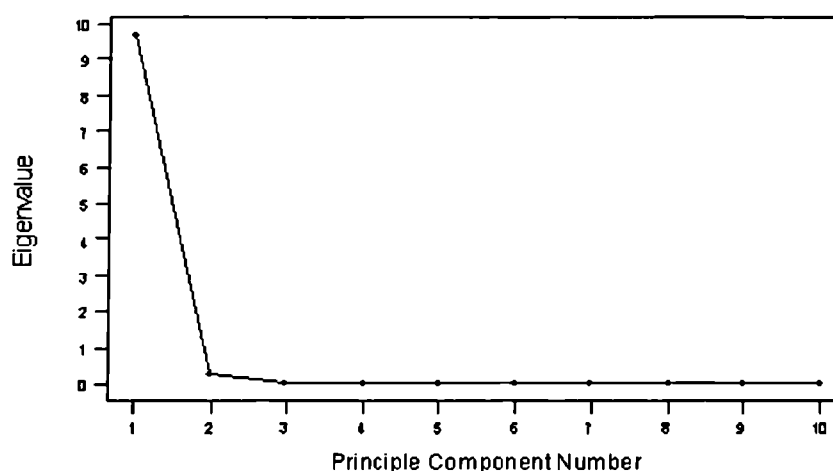
Figure 4.8 Eigenvalue Plot Produced from PCA of Laboratory Spectra
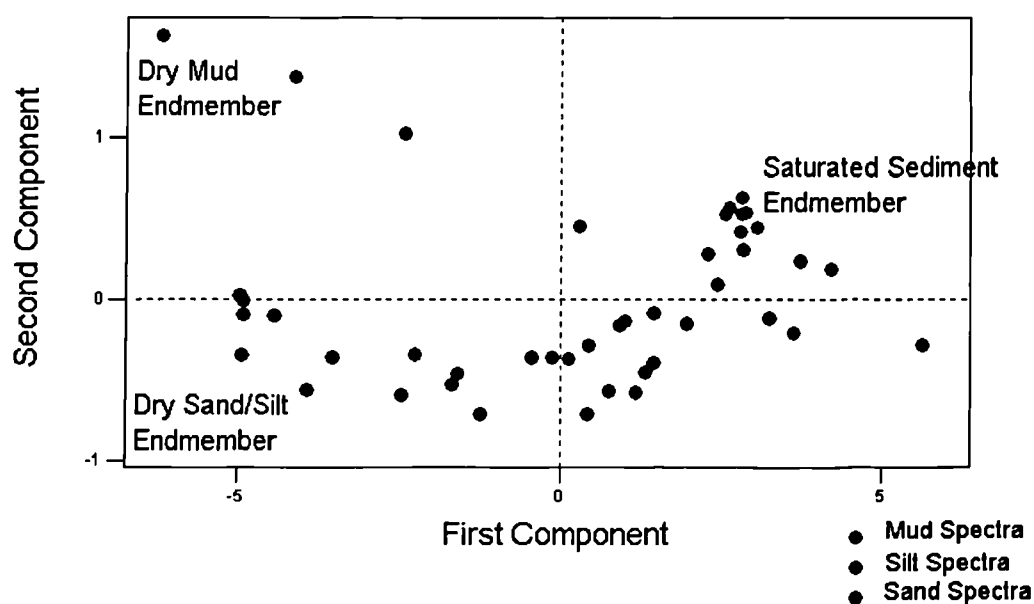
Figure 4.9 Scatterplot of PC 1 against PC 2, Produced from the PCA of the Laboratory Spectra, with the Locations of the Main Endmembers Labelled

It is evident from the scatterplot that the spectral effect of sediment grain-size becomes more obvious with loss of moisture. The spectra of the sand, silt and mud samples when they were saturated are all relatively closely located in feature space. As the

106

sediments lose moisture, the position of their spectra gradually moves towards the left of the scatterplot *i.e.* from positive to negative along PC 1, which contains 96.8% of the variance. The spectral contrast between the mud sample and the coarser samples also increases as the sediments get drier. When the sediments are absolutely dry, the mud sample has a distinct location relative to the coarse samples in feature space. In contrast, the silt and the sand samples maintain similar positions in the scatterplots with loss of moisture.

4.3.5 Discussion

These experiments clearly demonstrate that moisture is a substantial determinant of intertidal sediment reflectance and, consequently, a significant factor in differentiating sediments of contrasting grain-size. The effect of moisture is not waveband dependent as it has been observed in all the ATM bands. When the sediments are saturated the spectral contrast between sediments of contrasting grain-size is minimal. As the mud sediment (Sample C) loses moisture it initially remains spectrally stable before a rapid increase in reflectance. In contrast, the coarser sediments have a single approximately linear increase in reflectance with loss of moisture. Consequently, the fundamental finding from these laboratory experiments is that sediments of contrasting grain-size have contrasting reflectance responses during drying. This can be used to estimate the conditions when the maximum spectral contrast exists between sediments of different grain-size.

The mud sample (Experiment 1) has a relatively constant reflectance during the loss of the initial 75% of moisture, which is in complete contrast to the spectral response of the silt and sand samples. As an explanation, it is suggested that the $<63\mu m$ component, which

107

is largest in the mud sample (Sample C), acts as a control on the reflectance response. In Experiment 2, the reflectance of the <63μm sample lowers significantly as the moisture levels change from 90% to 40%. It is proposed that this spectral effect is limiting the reflectance response of the mud sample in Experiment 1 during the early stages of drying. The sand (Sample A) and silt (Sample B) samples have insignificant quantities of the <63μm component (Table 4.5), and hence their spectral response to drying is not noticeably constrained.

In both experiments, the relationship between drying and reflectance for the two coarser sediments is characterised by a sinuous line rather than a straight one (Figure 4.6 & 4.7). There is no obvious explanation for this behaviour although there are a few possibilities. Firstly, this could be a spectral effect of residual fine sediment attached to the coarser grains as it dries, although this is unlikely as the coarse sediment of Experiment 2 was thoroughly washed. Secondly, the sinuosity could be caused by slightly different drying times *i.e.* length of time in the oven, resulting in different rates of moisture loss and distribution in the sample. Thirdly, and most probably, this pattern could be caused by the sediment naturally losing moisture at different rates *e.g.* surface moisture would evaporate relatively quickly in comparison to interstitial moisture. Lastly, a more simple explanation is that the reflectance of coarse sediment may inherently not respond in a perfectly linear fashion to moisture loss.

In these laboratory experiments, the spectral contrast between the fine and coarse samples increased steadily until the final stages of moisture loss. This is clearly demonstrated in the results of the PC analysis of the laboratory spectra. The maximum spectral contrast between the samples existed when the mud sample (Experiment 1) had

lost 75% of its moisture *i.e.* before it responded spectrally. During both experiments, the coarser samples lost their moisture more rapidly than the mud sample, suggesting mud has greater water retention capabilities. Consequently, in the field when the sediments are under similar drying conditions, it is expected that their variable moisture loss capabilities will substantially enhance the spectral contrast described above.

In both Figure 4.5 and the PCA scatterplot, it is evident that the spectral contrast between the silt and sand samples doesn't increase significantly with drying. This is mainly due to both sediment types having a linear response to moisture loss. It is possible to suggest from this that mud will be the intertidal sediment type easiest identified from the remote sensing imagery. This is important, as this sediment type contains the highest percentage clay and consequently the highest levels of radioactivity.

It is worth noting that when all the sediment samples of Experiment 1 were saturated, although the spectral difference was not statistically significant, the mud sample had a higher reflectance in ATM bands 6 to 10. This suggests that in the field when the sediments are sufficiently saturated a negative relationship may be identifiable between ATM band 9 and percentage sand content. The identification of such a relationship is dependent on the sensitivity of the ATM instrument to small-scale spectral differences. Nevertheless, it may explain the negative relationship observed along the saturated transect (A_{96}) at Warton Bank in 1996.

Finally, as stated earlier, the primary cause of the spectral contrast that may exist between fine and coarse intertidal sediments exposed to drying conditions is their differing spectral response to moisture loss. However, this does not explain the intrinsic

relationship between particle size and reflectance, as may be observed between the fine and coarse sediment samples when they have reached absolute dryness in the laboratory experiments (Figure 4.6 & 4.7). Consequently, although it is beyond the primary objectives of this project, a number of potential physical explanations of this relationship are suggested:

1) The larger number of mineral faces present in fine sediment, due to the increased surface area of the particles, may promote more internal reflection and less direct reflection.

2) Quartz, which increases in abundance with grain-size, may naturally be a stronger reflector than the softer minerals (*e.g.* smectite) that are more common in finer sediments.

2) It may be that the lattice structure of clays, which are more abundant in fine sediment, causes these minerals to be a poor reflector of radiant energy.

Although these theories are unsupported, this does highlight an area of potentially interesting and valuable future research.

4.4   IMPLICATIONS FOR AERIAL REMOTE SENSING

From the 1995 results, it is concluded that a strong positive relationship exists between the percentage sand content and ATM reflectance of intertidal sediments, which have had lengthy exposure to summer drying conditions. This relationship is strongest for bands 9 and 10, although the greatest spectral variance exists in all ten bands combined as observed in the PCA analysis results. The later 1996 and 1997 experiments demonstrated that in general either no relationship or only a weak negative or positive association exists between ATM band 9 and percentage sand content of sediments

110

which have not been exposed to drying conditions or have been exposed only to weak-drying winter conditions.

The laboratory experiments demonstrate that muds and sands become more spectrally distinct as the moisture content decreases from 100% to 25%. From the field investigations it is known that approaching 99% of the intertidal sediments have at least 25% moisture content, even during the driest conditions. This implies that the spectral contrast between the sediment domains of an intertidal environment increases the longer the sediments are exposed to drying conditions. Consequently, the accuracy of any intertidal sediment classification based on an ATM image is dependent on the timing of the data collection *i.e.* relative to the sediment exposure time to rapid drying conditions. This conclusion was applied to the timing of the 1997 collection of airborne imagery. On the 30th May 1997, four lines of imagery were collected after the sediments were exposed for a long period of time to rapid drying conditions.

4.5 SUMMARY

It is possible to distinguish spectrally between different sediments in an intertidal environment that has been exposed to drying conditions. The *in situ* and laboratory experiments have shown that no reliable relationship exists between grain-size and reflectance when the sediments have high moisture contents. The level of spectral contrast between the sediments is clearly related to the length of time since inundation and the seasonal drying effects. The relationship between topography and variations in interstitial and surface moisture has been shown to be an essential consideration in the analysis and interpretation of intertidal imagery. The spectral uniqueness of fine

sediments, as observed in the laboratory experiments, suggests that these sediments can be mapped more accurately than coarser sediments. It is also evident that the combined spectral variance of all the ATM bands may be more useful for sediment classification than individual bands, even though the relationship to sediment grain-size is slightly stronger in some bandwidths. These preliminary investigations ensured that the data collected in 1997 was collected during ideal conditions, guaranteeing the best possible subsequent map of the intertidal surface sediments.

The results of these experiments dictated the timing and planning of the 1997 flights and the subsequent classification of the imagery. In the next chapter, the value of this preliminary reflectance spectroradiometry and detailed flight planning is demonstrated.

5. ANALYSIS OF AIRBORNE THEMATIC MAPPER IMAGERY

5.1 INTRODUCTION

As stated earlier, the primary aim of this project is to map accurately the Sellafield-derived radionuclides present in the surface intertidal sediments of the Ribble Estuary. Production of these activity maps is dependent on the accurate mapping of intertidal sediment grain-size distribution from ATM imagery. This chapter details how *in situ* spectral knowledge of the Ribble intertidal sediments, an array of image analysis techniques and a large image dataset may be combined to provide representative maps of intertidal sediment distribution.

5.2 GROUND TRUTH AND ATM IMAGE DATASET

5.2.1 Ground Truth Data

The image dataset contains ATM imagery, collected in 1995 and 1997, of the entire Ribble Estuary (Figure 3.1 and 3.2). The 1995 imagery includes two suitable low-tide images that were used as the basis for much of the preliminary image-based spectral investigations of the Ribble Estuary. However, validation of the sediment distribution maps produced from this imagery was impeded, due to the corruption of the GPS files containing the 1995 sample site locations.

A total of 125 sediment samples were collected from four intertidal locations within the Ribble Estuary during the acquisition of the 1997 imagery. Three of the sample areas appear within the 1997 imagery i.e. Warton Bank, Longton and the Docks (Figure 3.2).

The locations of the individual sample sites were defined using *in situ* orientation measurements, differential GPS and marker boards that were visible in the imagery (Section 3.2.2). The results of the subsequent sediment analysis enabled the grain-size distribution maps produced from the 1997 imagery to be validated. Consequently, the majority of the sediment and activity maps of the Ribble Estuary produced by this study are based on 1997 images.

In 1996, ten samples were collected from each of three $2m^2$ quadrats situated between the saltmarsh edge and the main channel at Warton Bank. These samples were used to estimate the amount of error introduced to the ground truth results by sampling and analytical error.

5.2.2 Image Dataset

The 1997 dataset contains five lines of ATM imagery of the Ribble Estuary collected during a neap tide on May 30th (Table 5.1), when the intertidal area was completely exposed (from approximately 09:54 to 15:54). Based on the *in situ* and laboratory reflectance measurements it was expected that the imagery collected after the longest period of exposure would provide the best results (Section 4.4). Consequently, the last or 'dry' 1997 image was used to produce a grain-size distribution map for the entire intertidal area of the Ribble Estuary (Figure 5.1). A subset of the first or 'wet' 1997 image was also analysed to examine the influence of interstitial moisture on the ability to create grain-size maps from ATM imagery.

Figure 5.1 Colour Composite (Bands 4, 3, 2) of the Raw 'Dry' 1997 Image of the Ribble Estuary, Collected on May 30th During Low Tide

115

Table 5.1 1997 Image Acquisition Times

Flight Line	Start Time	Finish Time
a150011b.hdf - 'Wet'	11:31:19	11:36:28
a150021b.hdf	12:37:09	12:43:25
a150031b.hdf	12:54:31	13:00:33
a150041b.hdf	13:25:17	13:30:50
a150051b.hdf - 'Dry'	14:40:06	14:45:52

The Lytham St. Annes region where detailed sampling and *in situ* spectral work was carried out in 1996 and 1997 (Table 4.1) is outside the image area of the 1997 dataset (Figure 3.2). Consequently, a subset of the first of the low-tide 1995 images (a214011b.hdf), containing the Lytham St Annes intertidal area, was selected for analysis to complete the coverage of the intertidal area. This subset was validated using 1997 sample sites, on the assumption that the overall sediment size distribution in this area was stable from 1995 to 1997.

5.3   IMAGE PREPARATION

5.3.1   Objective

Image preparation is the foundation to the eventual classification of the intertidal sediments within the imagery. This involves correction of the raw data and manipulation of the imagery to allow the intertidal areas, and consequently the spectral variation within them, to be analysed. Where a range of potential techniques exist, the most suitable is highlighted and described, both in theory and in operation.

5.3.2   Radiometric and Geometric Correction

Radiometric correction is an essential part of the ATM image preparation and was performed externally by NERC (Section 3.5.4). Subsequent, geometric correction

reduced any spatial errors within the raw ATM imagery and this was achieved using the GCORR software provided by NERC (Section 3.5.4).

It was found that GCORR was unable to handle large atmospherically-corrected images with sharp bends in the flight path, introducing considerable random noise into the geometrically-corrected product. Consequently, contrary to convention, atmospheric correction was undertaken after geometric correction (Appendix 3). The output HDF files produced by GCORR were reformatted to BIL format using EXHDF software provided by NERC, allowing the files to be imported into an image-processing package.

5.3.3 Atmospheric Correction

Atmospheric correction attempts to remove the spectral effects of the atmosphere, ensuring the ATM recorded radiance is as close as possible to the actual radiance reflected from the ground surface (Section 2.6.4). The 1997 imagery, upon which the majority of the grain-size distribution maps are based, was collected at low altitude during uniform cloud-free conditions. In addition, the minimum band values of the 1997 images are considerably lower than those of the 1995 images (Table 5.2). Consequently, it was assumed that the spectral influence of the atmosphere was minimal during the 1997 image acquisition.

A wide range of atmospheric correction techniques exist, from the complex computer models to the simpler corrections based directly on the imagery (Section 2.6.4). However, during the 1997 image acquisition no *in situ* reflectance or atmospheric measurements were made due to the unavailability of the necessary equipment. Consequently a simple and reliable atmospheric correction technique was required.

117

Dark target subtraction was found to fit these prerequisites and was available as an atmospheric correction module in ENVI. This is a limited atmospheric correction technique that removes scattering or haze from the imagery and requires no ground data (Section 2.6.4).

Table 5.2 Minimum Band Values, Expressed as Scaled 16-bit DN, used in the Atmospheric Correction of the ATM Imagery

ATM Band	'Dry' 1997 Image	'Wet' 1997 Image	1995 Image
Band 1	1	1	84
Band 2	2	7	3
Band 3	18	15	26
Band 4	42	5	52
Band 5	11	1	624
Band 6	3	15	431
Band 7	1	1	408
Band 8	1	5	240
Band 9	1	1	62
Band 10	1	1	33

The three selected images were atmospherically corrected in this way following geometric correction. The minimum values for each image band, excluding the thermal bands, were calculated and subsequently subtracted from the pixel values in each band (Table 5.2).

5.3.4 Image Registration

To display the latitude/longitude or Ordnance Survey details associated with each geocorrected image file in ENVI, it is necessary to edit the associated header file.

This involves defining the map projection parameter and the pixel size in the image header. The image and map co-ordinates corresponding to the 'Magic Pixel', used by

ENVI as the starting point for the map co-ordinate system, are then entered. The accuracy of the geocorrection can subsequently be assessed.

5.3.5 Image Subsetting

As stated earlier, the whole of the 'dry' 1997 image was selected for analysis and classification, based on the results of the preliminary reflectance experiments. A large subset of the 'wet' 1997 image was also selected for analysis, to investigate the importance of sediment exposure time on the ability to classify intertidal images. To complete the coverage of the Ribble Estuary intertidal flats, a subset of the first low-tide 1995 image, containing the large flat intertidal area near Lytham St. Annes, was also selected. The boundaries of these areas of interest were defined in ENVI, enabling the image subsets to be created (Table 5.3).

Table 5.3 The Pixel Dimensions of the Geocorrected Images Selected for Classification

Image	Rows (pixels)	Columns (pixels)
1997 Line 5	2853	10604
1997 Line 1 Subset	971	3421
1995 Line 1 Subset	459	535

5.3.6 Image Masking

As stated earlier, only imagery of the exposed intertidal zones of the Ribble Estuary is of interest to this project. To classify accurately the sediments within the intertidal areas, it was first necessary to minimise the spectral complexity of the image by isolating the intertidal regions from all other spectral features. Consequently, all non-intertidal areas such as the surrounding saltmarsh, the main channel and the man-made structures were masked out of the imagery. Due to sunglint caused by the low sun-angle, the intertidal area south of the main channel in the 'wet' 1997 image subset was also masked out.

119

Using aerial photographs the areas to be removed were accurately identified and selected as areas of interest in ENVI, which were combined to form a mask. The resultant masks were then permanently applied to each image, resulting in images containing intertidal areas only.

5.4 IMAGE CLASSIFICATION

5.4.1 Objective

The primary objective of this section was to produce the most accurate map of sediment distribution from the ATM imagery of the Ribble Estuary. Previous studies have shown that a 'soft' or fuzzy classification technique is likely to give a more accurate result than 'hard' classification techniques (Section 2.6.5). Of the available 'soft' techniques, Linear Mixture Modelling was considered the most suitable, primarily because: *1)* it does not require extensive training data; *2)* it has been shown to be relatively successful in unmixing satellite data of similar environments (Yates *et al.* 1993); *3)* the software is readily available as a module within ENVI (Section 3.6.1). Consequently, Linear Mixture Modelling was used as the centrepiece of the image analysis process designed to classify the ATM imagery of the Ribble Estuary (Section 3.6.3).

The methodology used to create grain-size distribution maps from ATM images of intertidal sediment has a number of discrete stages:

1) Maximisation of the signal to noise ratio, as a means of improving the final classification products.

2) Examination of each dataset in feature space and, subsequent, identification of the image spectral endmembers.

3) Classification of the imagery based on the 'pure' image pixels representing each of the spectral endmembers.

4) Calibration and validation of the abundance imagery produced by linear unmixing.

5.4.2 Minimum Noise Fraction Transform

The minimum noise fraction (MNF) transformation, described in Section 3.6.3, is a noise reduction technique designed to maximise the signal to noise ratio and hence improve the image quality (Green *et al.*, 1988). Each transformation of a ten-band ATM image produces ten MNF bands of decreasing image information, allowing bands consisting predominantly of noise to be excluded from subsequent processing and classification. The spectral dimensionality of the dataset, which is fundamental to linear spectral unmixing, may also be determined.

The first ten bands of the three masked images were separately placed through a forward MNF transform, each producing ten MNF bands of decreasing image quality with increasing component number and an accompanying eigenvalue graph. Following examination of the eigenvalues and eigenimages of each band, those containing a significant amount of coherent image information were selected as the basis for spectral endmember selection and image unmixing. To validate the noise-removal ability of this technique, the coherent MNF bands, produced from the transform of the 'dry' 1997 image, were placed through an inverse MNF transform and the resultant images were compared to the original masked imagery.

5.4.3 Linear Mixture Modelling

Linear unmixing attempts to calculate the proportion of the various surface components present in each image pixel based on the spectral characteristics of the surfaces (Section 3.6.2). The number of spectral endmembers used in linear unmixing must be less than or equal to one greater than the number of spectral dimensions in the data (Settle and Drake, 1993).

The number of coherent MNF bands produced from each image was used as an approximation of the dimensionality of each dataset and, consequently, to estimate the number of spectral endmembers that could be unmixed (Equation 3.2). The coherent MNF bands and the 2-D scatterplot tool in ENVI were then used to examine the distribution of the data in feature space and the nature of the spectral mixing. From scatterplots of various MNF band combinations, the spectral endmembers of each scene were identified. The extreme of each endmember in feature space (*c.*12-20 pixels) was subsequently highlighted and the pure representative image pixels were identified. These image pixels were then selected and a mean spectrum was calculated for each *endmember. The source of each spectral* endmember was identified from a combination of aerial photographs, *in situ* knowledge and the mean spectra plots. Scatterplots based on various sized image windows were experimented with, to determine how representative they were of the spectral variability contained within a whole line of imagery.

The endmember pixel selection procedure described above was an iterative process. Initially, pure pixels were selected to represent the dominant spectral endmembers of each scene and used to unmix the imagery. The subsequent abundance images were

then assessed using *in situ* knowledge of the area and the associated RMS error image. On this basis it was determined whether the spectral endmembers of the imagery were adequately represented by the selected endmember pixels. If this was not the case the selection of endmember pixels was refined and the spectral unmixing of the imagery was repeated. The number of iterations varied greatly (approximately between 5 and 15) depending on the nature of the spectral endmembers within the imagery. In general, the linear unmixing of an image was found to be insensitive to variations in the selection of pixels representing distinct spectral endmembers. However, where the extreme of a spectral endmember was indistinct minor variations in the selected representative pixels resulted in substantial variations in the resulting abundance imagery. As a solution to this problem, various combinations of the coherent MNF bands were plotted against each other until the extreme of the spectral endmember was better defined, making it easier to select representative pixels.

Pure pixels representing the dominant endmembers of each scene were imported into the Linear Spectral Unmixing tool in ENVI. These endmembers were used as the basis for 'unconstrained' spectral unmixing of the coherent MNF bands. This technique was chosen in preference to 'constrained' unmixing due to the potentially non-linear spectral nature of moisture in the intertidal environment. The resulting grey-scale abundance images and the associated root-mean-square error image, were subsequently examined to assess the accuracy of the unmixing and the suitability of the defined spectral endmembers.

5.4.4 Calibration

As detailed within Section 5.2, sediment samples were collected during the 1997 image acquisition to enable calibration of the subsequent sediment abundance maps. The 1997 sample sites were located in the imagery from white marker boards and sample site distance measurements (Section 3.2). Similarly, orientation measurements were used to calculate the location of the 1997 sample sites in the 1995 Lytham St. Annes image subset.

The sand, mud, water and microphytobenthos abundance of each sample site was calculated from the images produced by linear unmixing. The relationships between the sample sediment characteristics and the abundance estimates were defined by exponential equations. The equations were determined on an empirical basis to represent the 'best fit' for each relationship. A selection of the exponential equations was subsequently used to produce percentage clay maps of the Ribble Estuary. This calibration procedure was applied to the abundance imagery of the 'dry' 1997 image and the Lytham St. Annes image subset.

5.5 RESULTS

5.5.1 'Dry' 1997 Image

Image Preparation

The image preparation process successfully produced a registered image of the exposed intertidal zones present within the 'dry' 1997 image, in the correct geometric orientation (Figure 5.2). The dark subtraction technique resulted in no significant visual changes in the imagery.

MNF Transform

The MNF transform of the masked 'dry' 1997 image produced ten bands, of which the first four contained 93% of the total statistical variance in the 10-band image dataset and are represented by coherent eigenimages (Table 5.4). Band 5 was found to contain less than 2.5% of the total image information, however due to the quality of the associated eigenimage it was combined with the first four bands, and used as the basis of the endmember selection and unmixing process. The remaining incoherent bands were discarded. From the associated eigenvalues, it was determined that the image had approximately four data dimensions, suggesting that five endmembers could be successfully unmixed from the spectral dataset (Equation 3.2). As stated earlier, the coherent MNF bands produced from the 'dry' 1997 image underwent an inverse MNF transform. The image produced was subsequently compared to the original ATM image and through a visual assessment was found to have a higher signal to noise ratio, especially in ATM band 1 (Figure 5.3). This suggests that the MNF transform successfully separated the majority of the image noise into the incoherent MNF bands without removing a significant amount of image information.

Table 5.4 Eigenvalues of the MNF Bands Produced from the MNF Transform of the 'Dry' 1997 Image, the 'Wet' 1997 Image and the 1995 Image Subset

MNF Band	'Dry' 1997 Image	'Wet' 1997 Image	1995 Image Subset
Band 1	156.23	179.8	34.39
Band 2	29.64	43.7	18.75
Band 3	16.67	22.2	8.11
Band 4	10.31	9.59	5.23
Band 5	5.22	4.97	3.00
Band 6	3.36	3.23	2.42
Band 7	3.02	1.78	1.40
Band 8	1.93	1.42	1.26
Band 9	1.45	1.12	1.20
Band 10	1.13	0.916	1.15
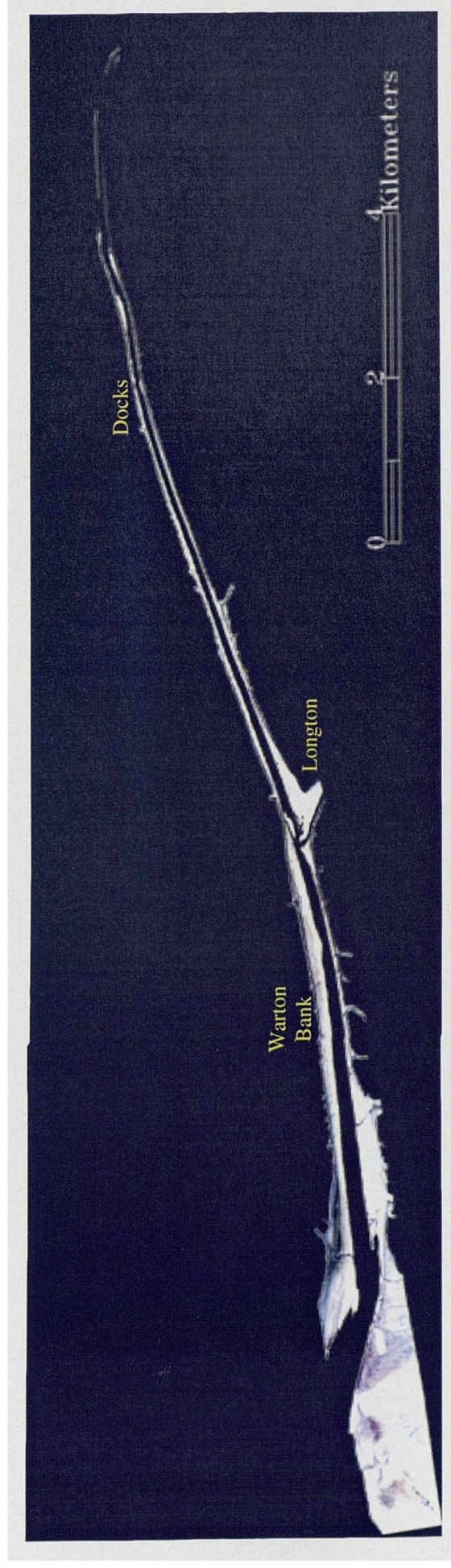
Figure 5.2 Colour Composite (Bands 4, 3, 2) of the 'Dry' 1997 Image of the Ribble Estuary, Following Geocorrection and Masking

126

Endmember Selection

The four dominant spectral endmembers of the imagery were identified from 2-D scatterplots of various combinations of the first four MNF bands (Figure 5.4). These were subsequently found to represent mud, sand, water and microphytobenthos present in the imagery. Due to software limitations, these scatterplots were based on an image window (4293 x 1250) that included the Warton, Longton and outer estuary area, rather than the whole scene. Examination of the entire image revealed that this image window was representative of the spectral variability within the intertidal area. In Scatterplot 1 (Figure 5.4a), the data are very compressed in feature space with only one obvious endmember. This endmember is more clearly identifiable in Scatterplot 2 (Figure 5.4b), and, consequently, this scatterplot was used to select representative pure sand and water image pixels. The spectral endmember of mud is masked by the microphytobenthos endmember in both Scatterplot 1 and 2, making it impossible to locate pure mud pixels in the imagery. In Scatterplot 3 (Figure 5.4c), however, mud and microphytobenthos have unique positions in feature space relative to the MNF band 4 axis, as a result this scatterplot was used to define the representative pure image pixels for these endmembers.
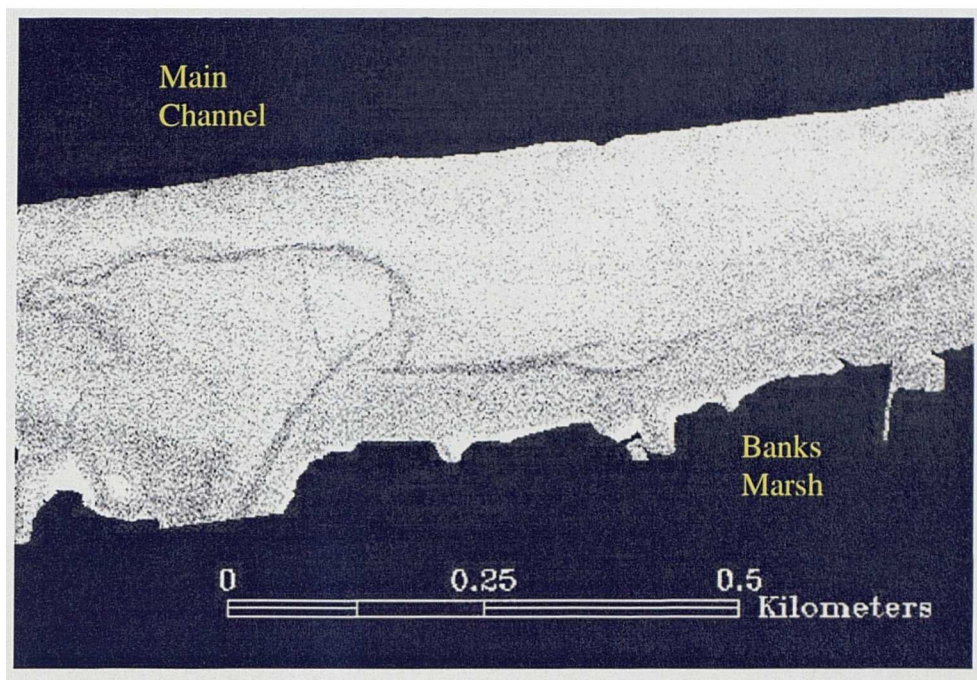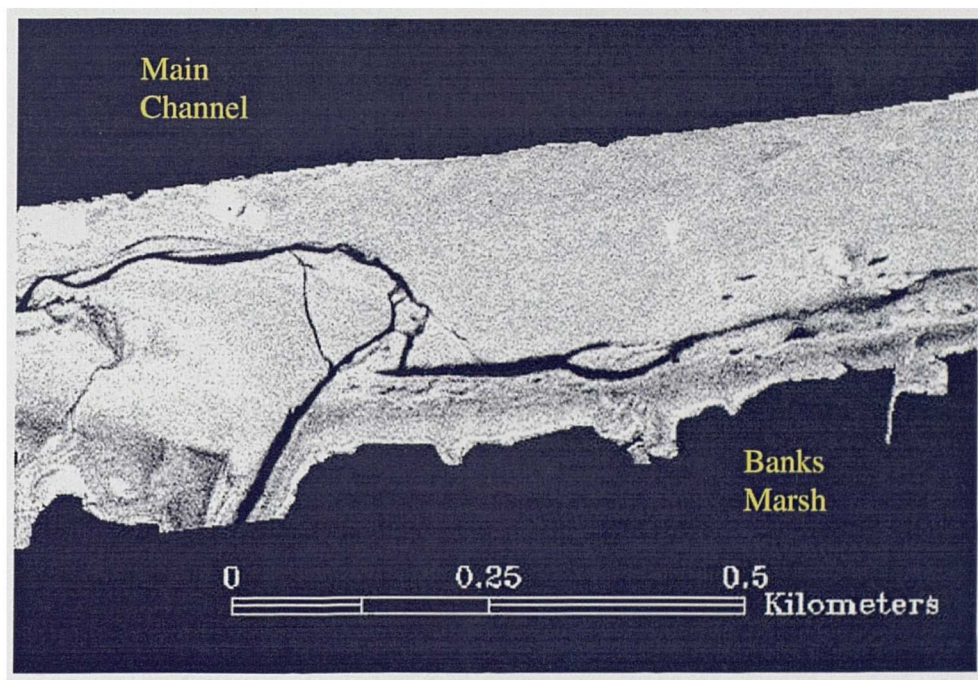
Figure 5.3 A Subset of ATM Band 1 of the 'Dry' 1997 Image A) Before and B) After
Noise Reduction by the MNF Transform
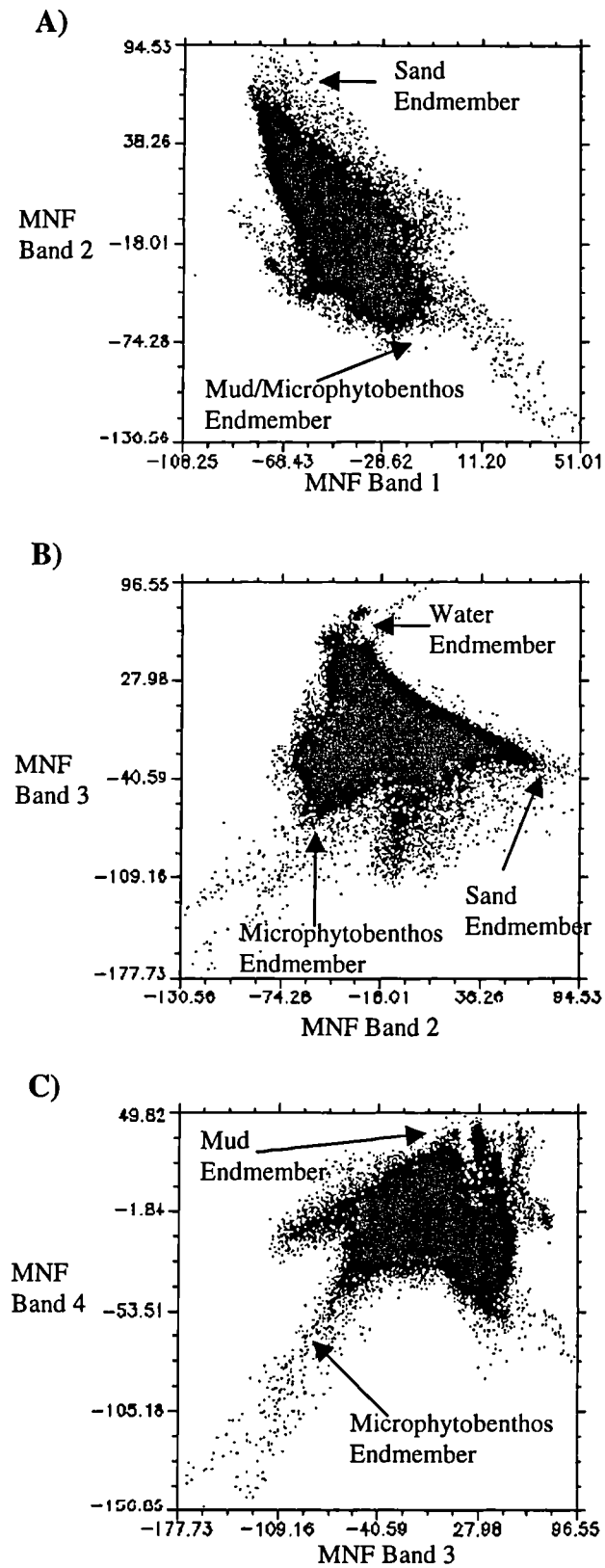
Figure 5.4 2-D Scatterplots of a) MNF Band 1 Against 2, b) MNF Band 2 Against 3 and c) MNF Band 3 Against 4, with the Dominant Spectral Endmembers of the 'Dry' 1997 Image Identified

Pure Endmember Image Pixels

The extreme of the mud spectral endmember was represented by pure image pixels that correspond to areas of polygonated mud close to the edge of the saltmarsh, near the mouth of a creek at Banks Marsh (Figure 2.1). The water endmember was represented by areas within a large creek flowing out of Banks Marsh and across the southern intertidal area. Pure sand pixels were identified on the ridge of a large sandbank west of Warton. A small area of unmasked saltmarsh vegetation at the edge of a large creek represented the extreme of the vegetation/microphytobenthos endmember from Warton Bank. The mean spectra of these representative pure pixels were found to agree in general with the *in situ* spectral knowledge of these surface types (Figure 5.5). For example in the higher bandwidths moisture has an overall low reflectance, and sand has a substantially higher overall reflectance than mud. However, in contrast to the *in situ* reflectance spectroradiometry results, the greatest spectral contrast between sand and mud appears to exist in ATM band 7. This may be a product of the imagery not being atmospherically corrected unlike the *in situ* reflectance spectra.
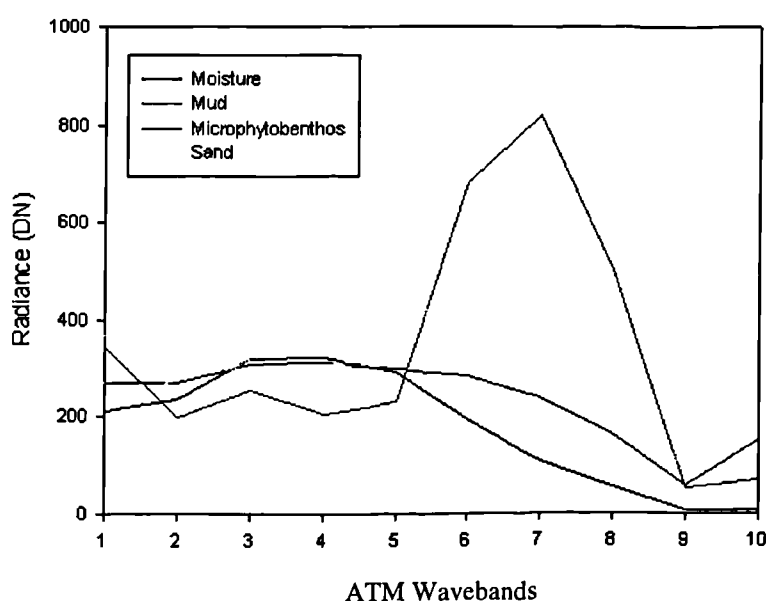
Figure 5.5 Mean Spectra of the Endmember Pixels Used to Unmix the 'Dry' 1997 Image

Intertidal Mud Distribution

The selected endmember pixels were used to linearly unmix the intertidal areas of the 'dry' 1997 image, producing sand, water, mud and microphytobenthos abundance maps, and an associated Root Mean Square (RMS) error image. The mud abundance image is an accurate representation of the mud distribution within the intertidal zones of the Ribble Estuary (Figure 5.6). This is supported by the empirical relationship (given in equation 5.1) between the image-derived mud abundance estimates and the actual clay content of the 1997 sample sites (r^2=0.79, p<0.01).

$$\%Clay = \exp[1.39 + 1.44(MudAbundance)] \qquad\qquad \textbf{5.1}$$

Although intertidal clay content cannot be determined directly from the ATM imagery, this shows that it can be indirectly calculated from the mud abundance imagery produced by spectral unmixing (Section 2.2). The above relationship is based on sample sites from three contrasting locations in the Ribble Estuary and is therefore assumed to be representative for the whole intertidal area. The associated RMS error image demonstrates that the unmixing error is relatively low within the fine-grained intertidal sediment areas (Figure 5.7). However, the spectral profiles reveal that where microphytobenthos cover is high, the mud abundance (Figure 5.8) appears to be slightly underestimated (Figure 5.9). In order to correct this, both the microphytobenthos and mud abundance estimates were combined and then compared with the sample site data. The empirical relationship between the abundance estimates and the observed clay content was improved (r^2=0.815, p<0.01), supporting the earlier suggestions that microphytobenthos attenuates the spectral characteristics of mud (5.2).

$$\%Clay = \exp[1.56 + 1.04(MudAbundance) + 0.677(MicroAbundance)] \qquad \textbf{5.2}$$

131
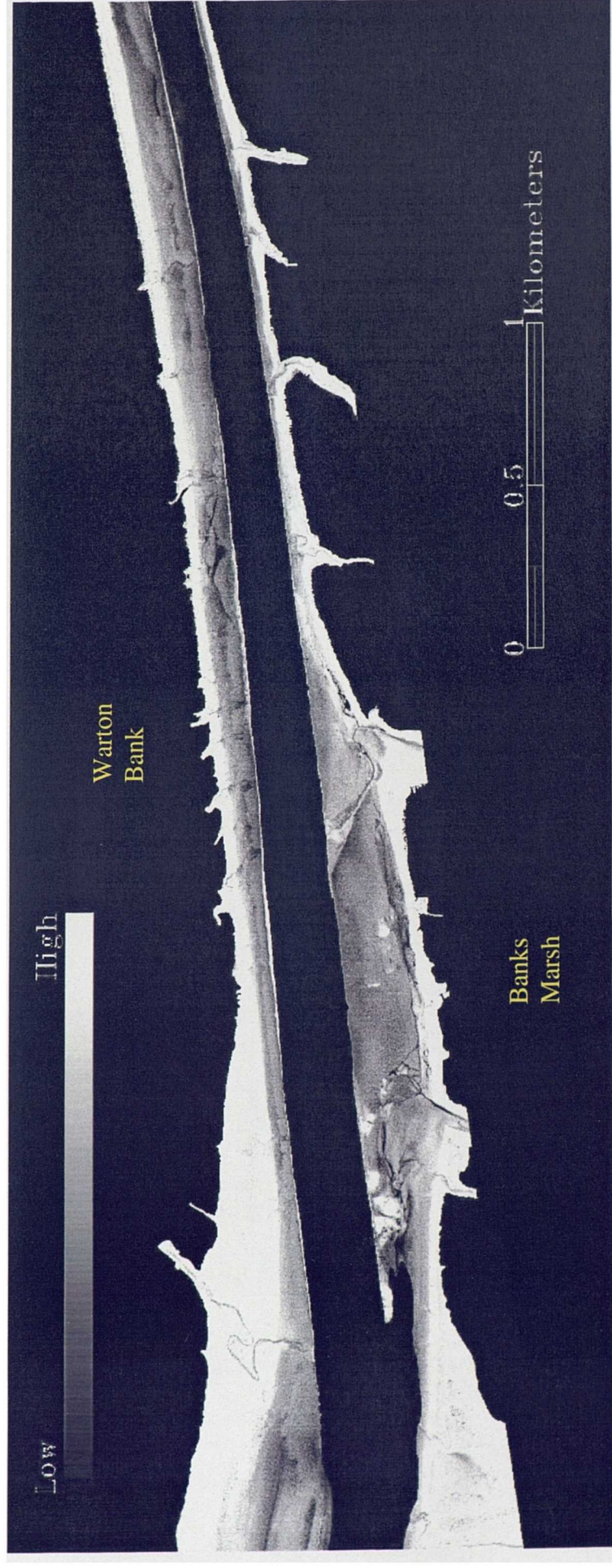
Figure 5.6 Subset of the Mud Abundance Image Produced from the 'Dry' 1997 Image

132
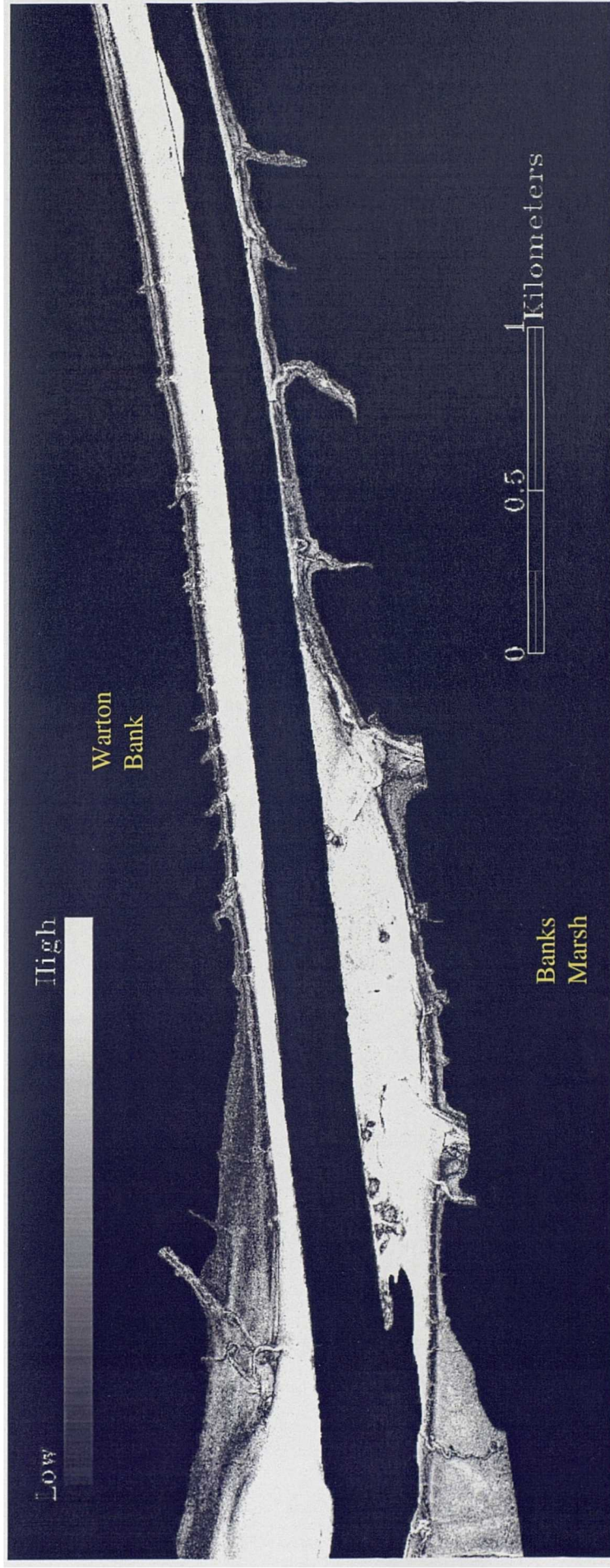
Figure 5.7 Subset of the Associated RMS Error Image Produced by the Linear Unmixing of the 'Dry' 1997 Image

133
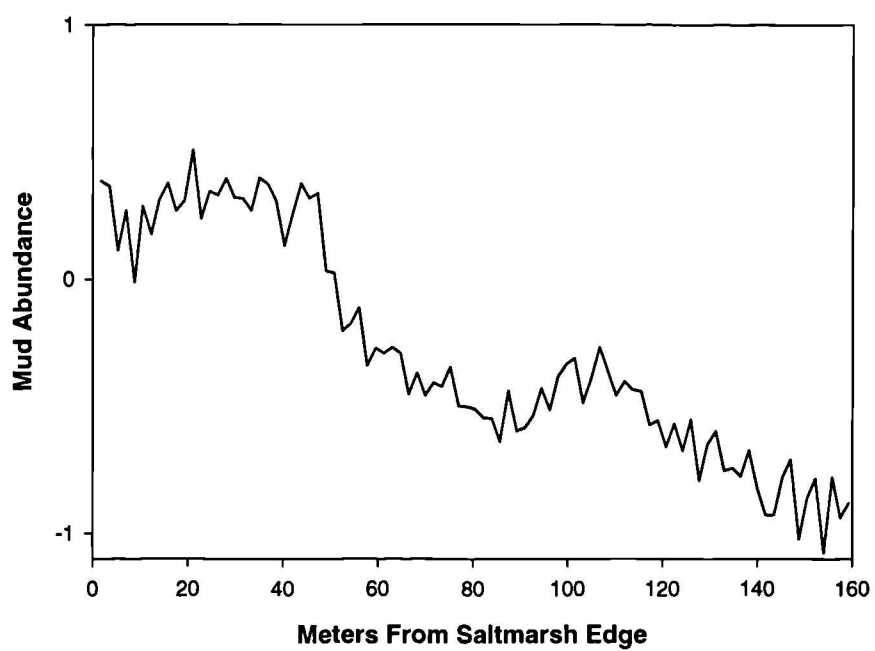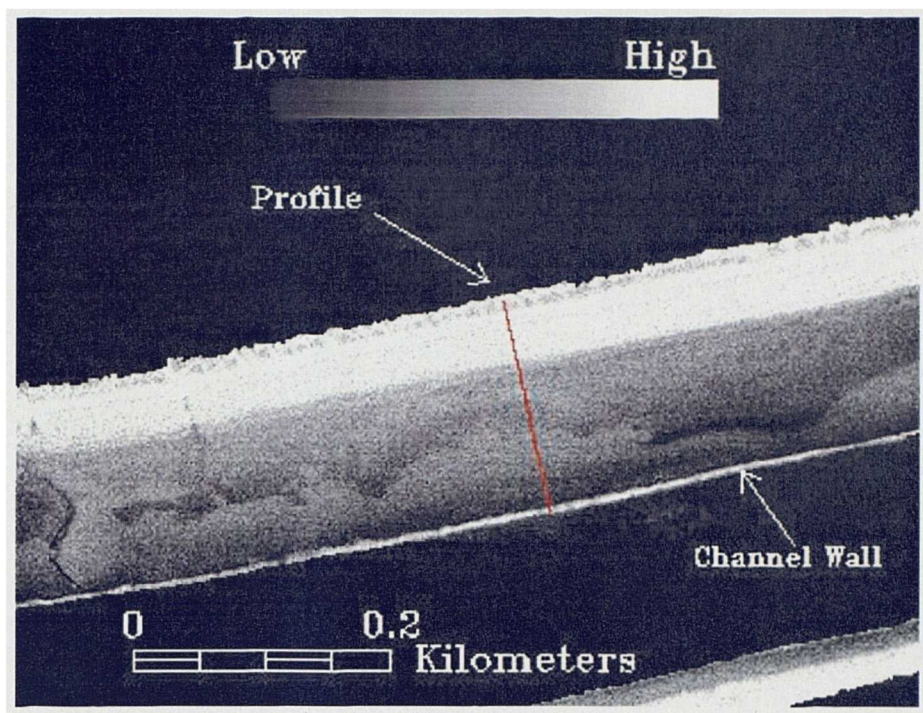
Figure 5.8 Typical Mud Abundance Profile from the Saltmarsh Edge to the Main Channel from the 'Dry' 1997 Mud Abundance Image
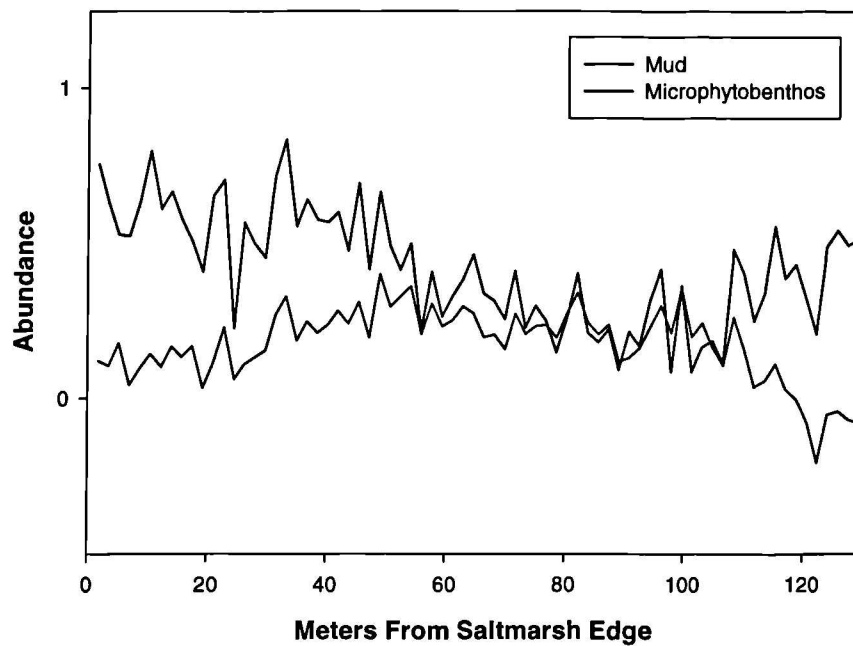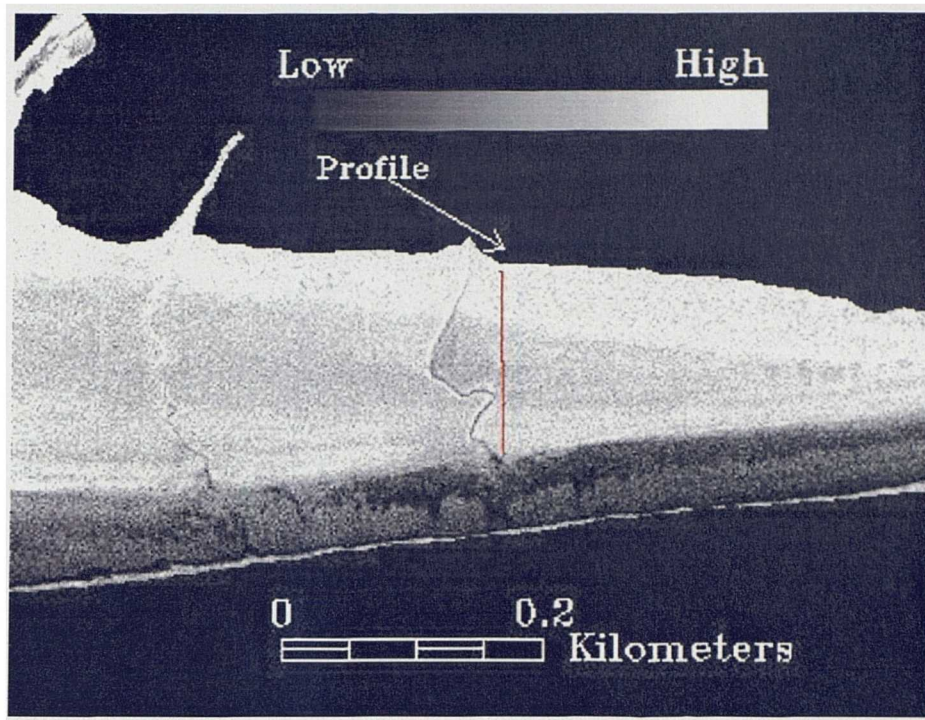
Figure 5.9 Profile of a) Microphytobenthos and b) Mud Abundance from the Saltmarsh Edge to the Main Channel Illustrating the Attenuating Effects of Microphytobenthos on the 'Dry' 1997 Mud Abundance Image

Similarly, surface water is found to mask the true spectral characteristics of the underlying mud, causing underestimation (Figure 5.10). Interstitial moisture, however, appears to only spectrally influence areas where the mud signal is very weak i.e. the actual clay levels are lower than two percent. Finally, the channel walls and the stone-topped large ridges, found in a number of locations in the Ribble Estuary e.g. Longton intertidal area, were misclassified as areas of high mud abundance, probably due to the similar spectral nature of these surface types.

Intertidal Sand Distribution

A significant, though weak, relationship was found between the sand content of the 1997 sample sites and the abundance image estimates (r^2=0.499, p<0.01). The associated RMS error image demonstrates that the unmixing error within the sand-dominated areas is approximately one order of magnitude greater than that within the mud-dominated areas of the imagery (Figure 5.7). Spectral profiles within the sand abundance image (Figure 5.11) reveal that the estimated sand increases towards the main channel from the saltmarsh, as expected from field investigations (Figure 5.12). However, the increase in sand abundance is gradual unlike the steep increase followed by a plateau observed in reality (Figure 5.13). A possible explanation for this difference is the equally steep increase in moisture abundance estimates of the sediments at the base of the sloped mudflats (Figure 5.12). Consequently, it is proposed that the greater spectral attenuation caused by the increasing interstitial moisture contents results in an underestimation of sand abundance, which smoothes the expected steep increase. To correct this, the moisture abundance image was combined with the sand abundance image, and this improved the relationship between the estimated and observed sand
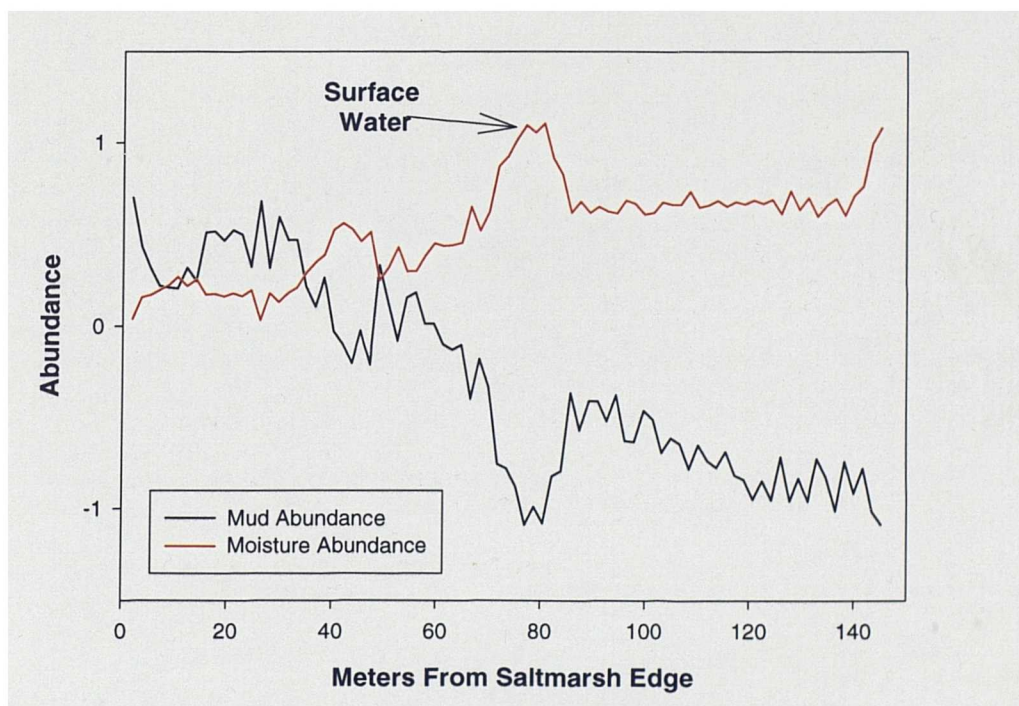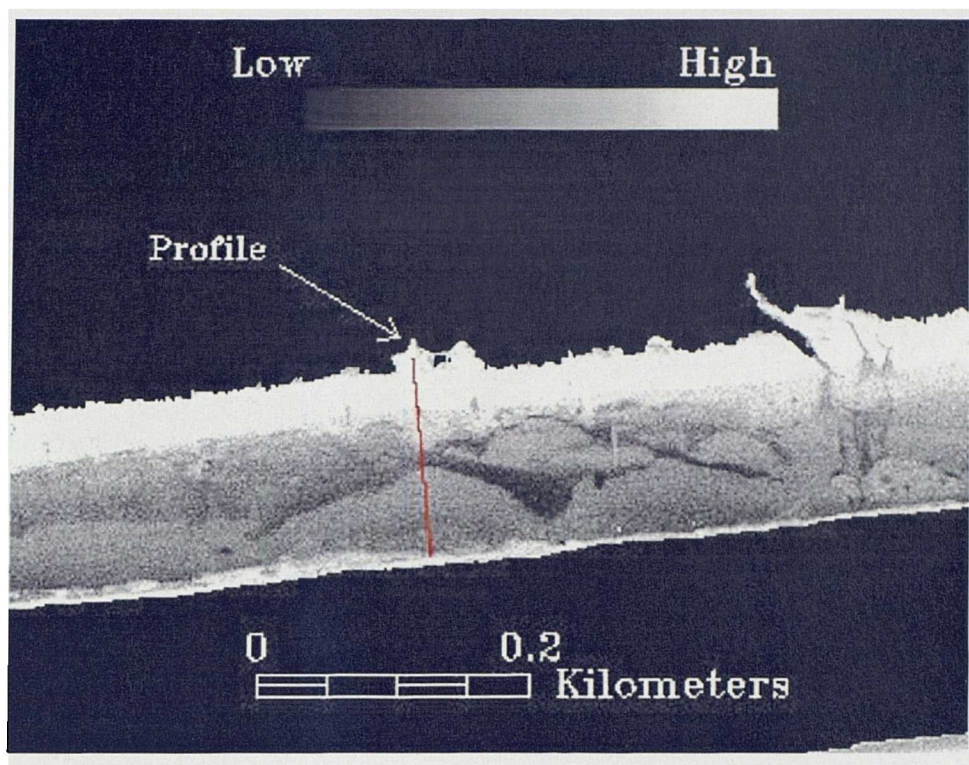
Figure 5.10 Profile of a) Mud and b) Moisture Abundance from the Saltmarsh Edge to the Main Channel, Illustrating the Attenuating Effects of Surface Moisture on the 'Dry' 1997 Mud Abundance Image
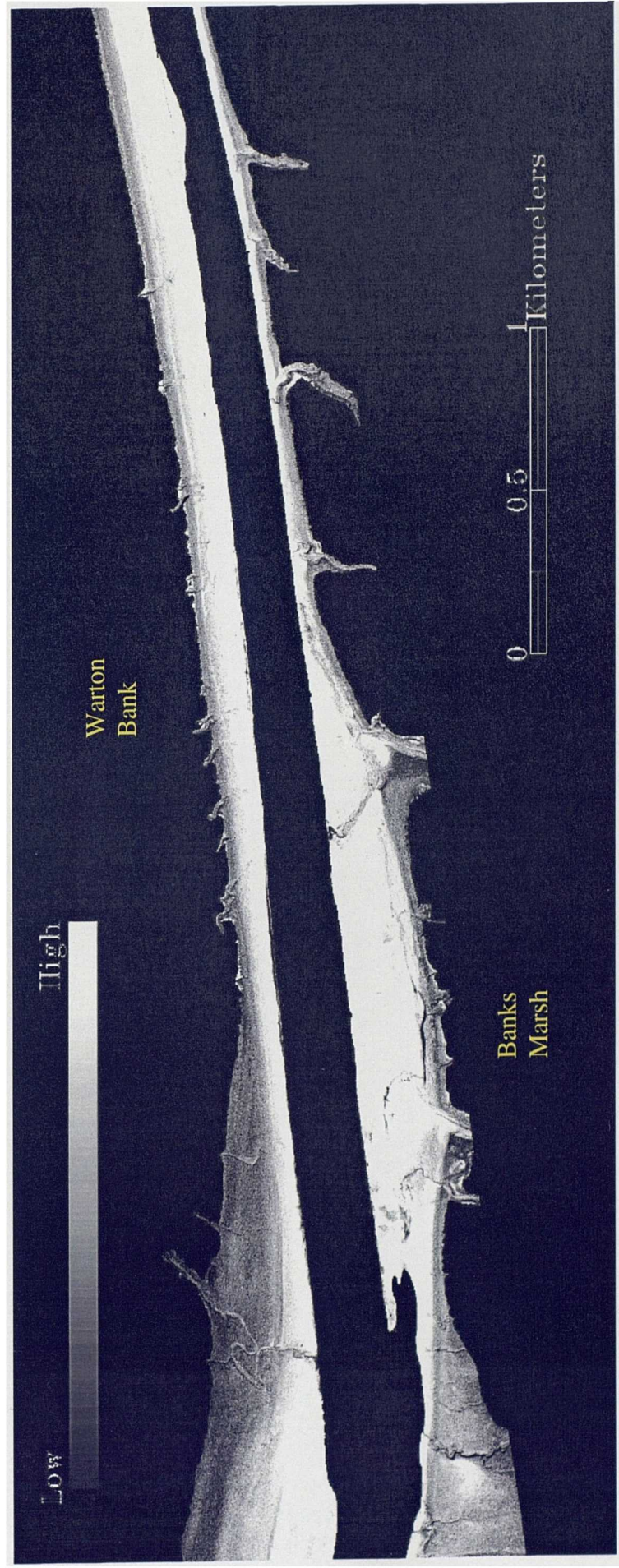
Figure 5.11 Subset of the Sand Abundance Image Produced by the Linear Unmixing of the 'Dry' 1997 Image

138
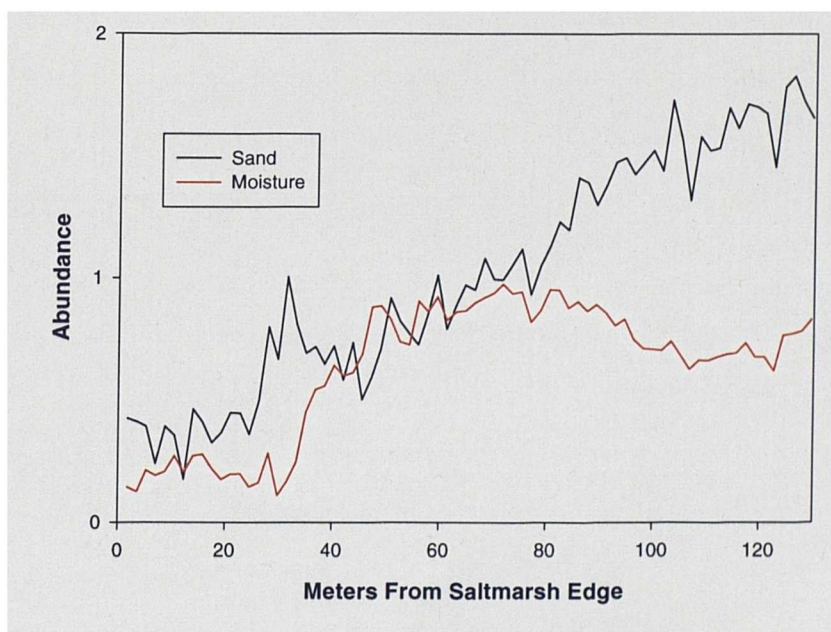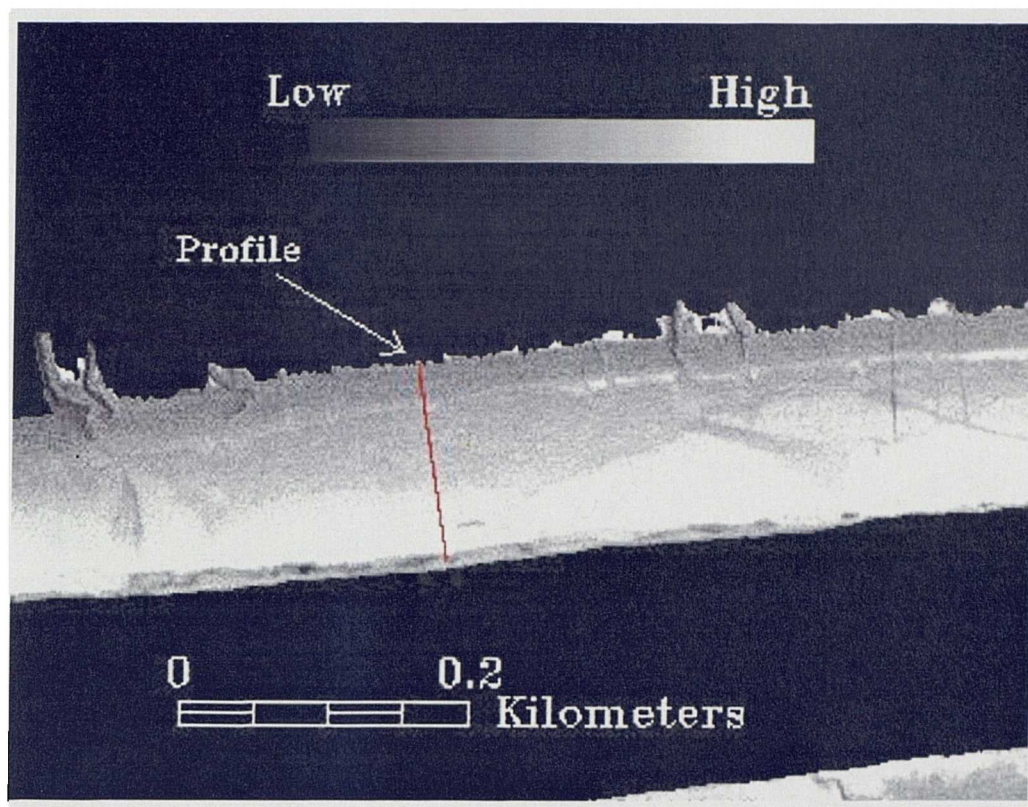
Figure 5.12 Profile of a) Sand and b) Moisture Abundance from the Saltmarsh Edge to the Main Channel, Illustrating the Attenuating Effects of Moisture on the 'Dry' 1997 Sand Abundance Image

contents significantly (r^2=0.753, p<0.01). Areas of polygonated mud close to the saltmarsh were misclassified as having high sand abundance (Figure 5.14); it is suggested that this is a product of halite efflorescence in these areas (Bryant *et al.*, 1996).
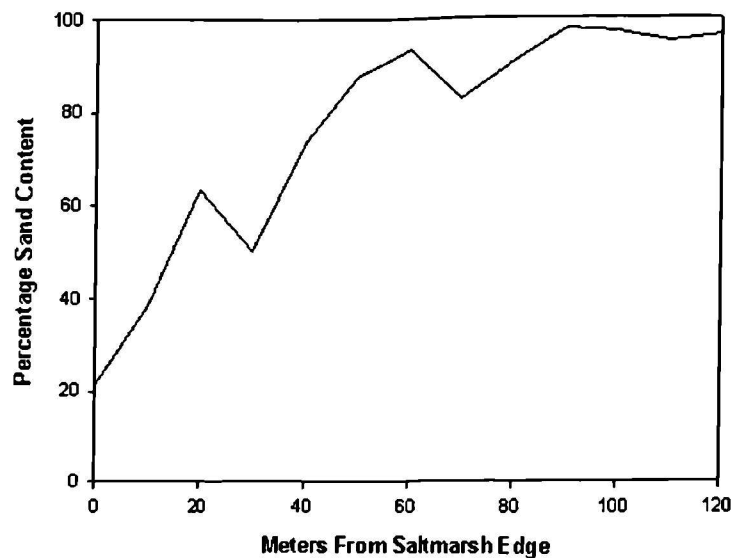
Figure 5.13 Percentage Sand Profile from the Saltmarsh Edge to the Main Channel, Calculated from 1997 *In Situ* Measurements
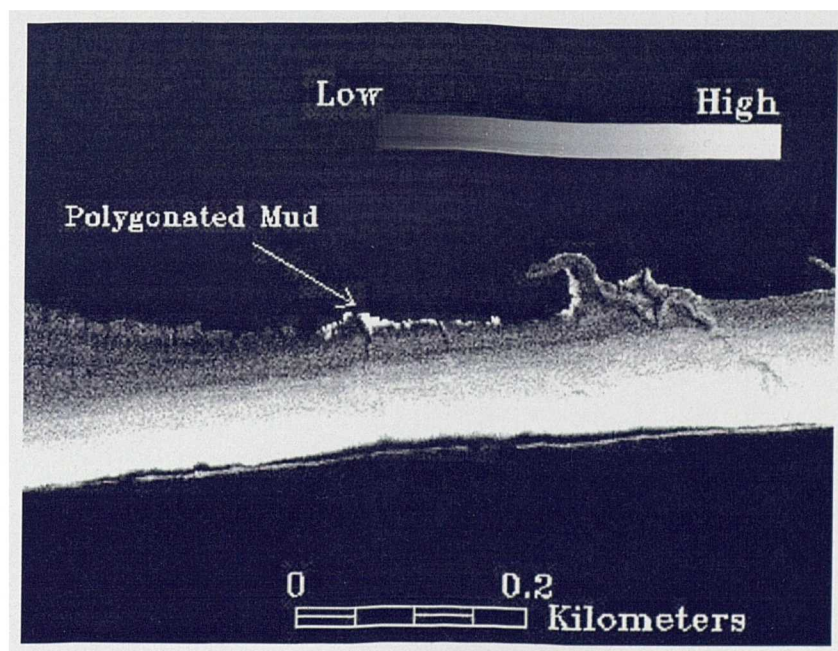
Figure 5.14 Subset of the 'Dry' 1997 Sand Abundance Image, Containing Polygonated Mud Areas, which are Misclassified as Areas of High Sand Abundance

Intertidal Moisture and Microphytobenthos Distribution

As discussed in Section 3.2.3, it was difficult to get accurate *in situ* sediment moisture estimates during the 1997 image acquisition. Consequently, this impeded the validation of the moisture abundance image (Figure 5.15A), although comparisons with aerial photographs and *in situ* observations were possible. The flat, sand-dominated intertidal areas in the imagery have higher moisture abundance estimates than the sloped mud-dominated areas close to the saltmarsh. This could be a product of topography and exposure time, or alternatively, the spectral influence of moisture may be more evident within the sand domains. The saltmarsh creeks crossing the intertidal zone are clearly defined throughout the moisture image as bright high abundance features.

The abundance of microphytobenthos was not accurately quantified in the field during the 1997 image acquisition. However the microphytobenthos abundance image produced from the 'dry' 1997 image appears to correlate closely with *in situ* observations made during image acquisition (Section 3.2.3). The extensive microphytobenthos mat near the large creek at the western end of Warton Bank is very well defined, and variations in its density are identifiable (Figure 5.15B). Equally the microphytobenthos cover, observed during sampling, on the sloped intertidal area close to the saltmarsh and on the banks of the small saltmarsh creeks is identifiable in the imagery.

A)
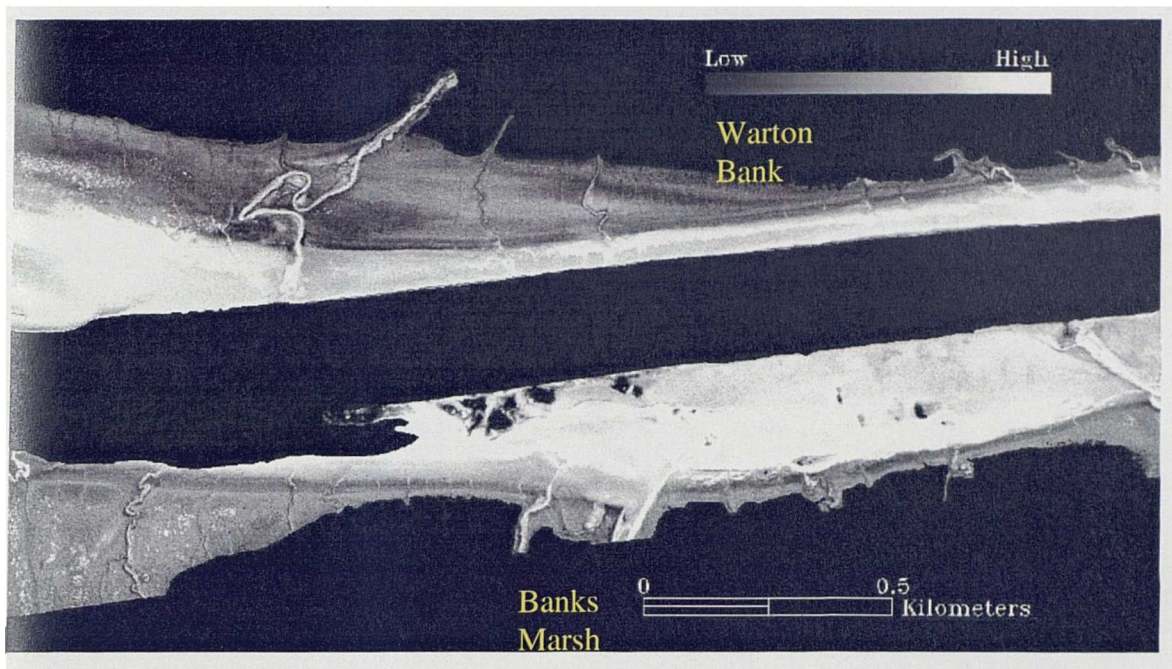
B)

Figure 5.15 Subset of the a)Moisture and b)Microphytobenthos Abundance Image Produced by the Linear Unmixing of the 'Dry' 1997 Image

142

5.5.2 'Wet' 1997 Image

Image Preparation

Image preparation produced a registered image of the northern intertidal area present within the dimensions of the 'wet' 1995 image subset, in the correct geometric orientation. As with the 'dry' line, there are no obvious visual differences between the intertidal areas of the image subset before and after atmospheric correction.

MNF Transform

Examination of the eigenvalues of the MNF bands produced by the transform of the 'wet' 1997 subset reveals that 95% of the image information is held within the first four bands of the imagery (Table 5.4). Similarly, the associated eigenimages of the first four bands are found to contain coherent image information. Although band 5 contains only 1.8 percent of the total image eigenvalues, the associated eigenimage was found to contain pertinent image information and was consequently retained. The remaining MNF bands, 6 to 10, were discarded. The eigenvalues also reveal that within the image subset there are approximately four data dimensions, and hence five spectral endmembers could be unmixed from the imagery (Equation 3.2).

Endmember Selection

The first four MNF bands were plotted against each other in a series of scatterplots, as shown in Figure 5.16. Sand, mud, water and microphytobenthos were identified, from these scatterplots, as representing the four dominant spectral endmembers of the imagery. The sand and water endmembers were clearly separable along the MNF band 3 axis in Scatterplot 2 (Figure 5.16b), and pure pixels representing each of these endmembers were selected. The mud endmember is masked by the microphytobenthos
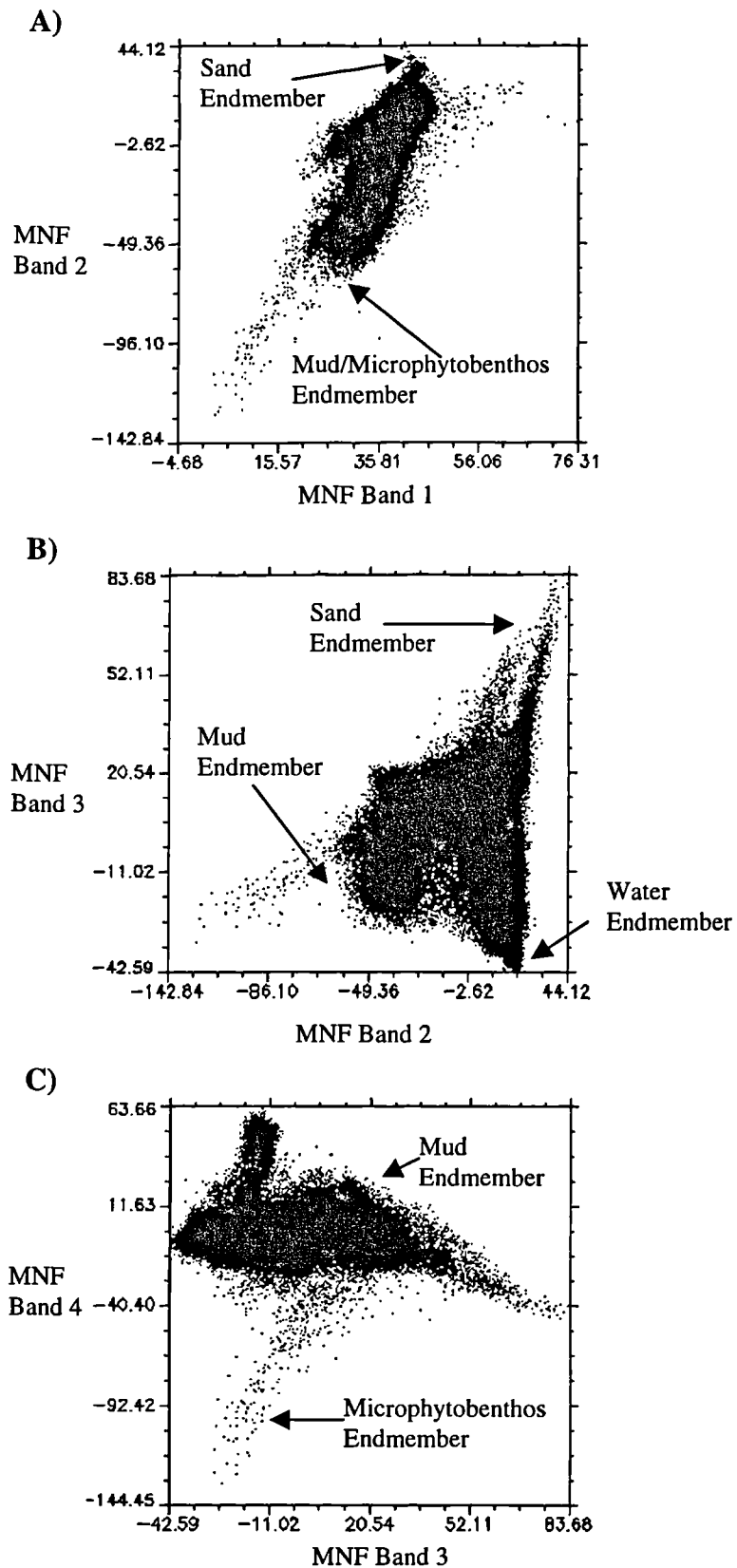
Figure 5.16 2-D Scatterplots of a) MNF Band 1 Against 2, b) MNF Band 2 Against 3 and c) MNF Band 3 Against 4, with the Dominant Spectral Endmembers of the 'Wet' 1997 Image Identified

endmember in Scatterplots 1 and 2 and, consequently, no pure pixels could be accurately identified. However, in Scatterplot 3 (Figure 5.16c) the mud and microphytobenthos endmembers were separated along the MNF band 4 axis, allowing pure pixels representing each to be selected.

Pure Endmember Image Pixels

The mud endmember was represented by image pixels from areas of polygonated mud at the edge of the saltmarsh, near the mouth of a large creek from the Warton Bank saltmarsh. The sand endmember was represented by a series of pixels along the ridge of a sandbank in the outer estuary, whilst channel water in the outer estuary was the location of the water endmember pixels. Lastly, unmasked vegetation along the edge of the Warton Bank saltmarsh formed the extreme of the microphytobenthos endmember in feature space. The mean spectra of each set of endmember pixels compare well with the mean spectra of the pixels used to unmix the 'dry' ATM image (Figure 5.17).
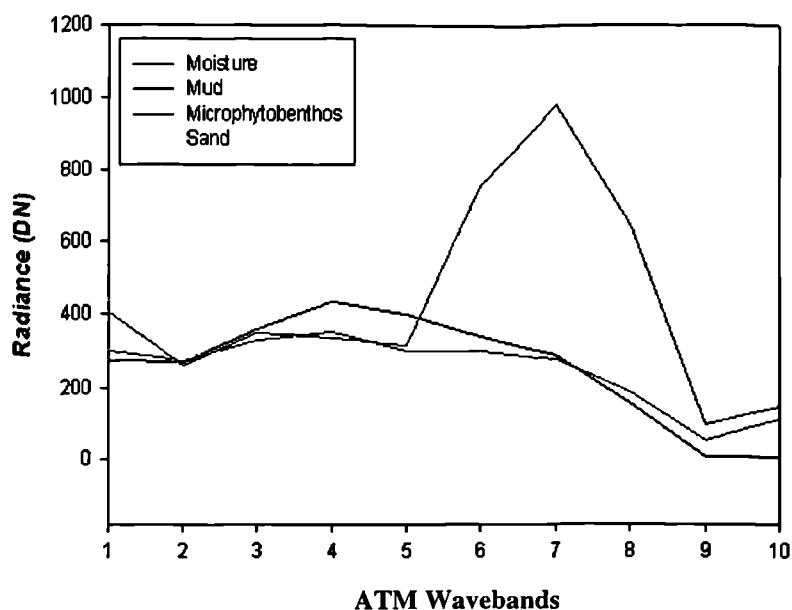
Figure 5.17 Mean Spectra of the Four Groups of Endmember Pixels, for the 'Wet' 1997 Image, Selected from the Scatterplots

Intertidal Mud Distribution

The final product, of the iterative endmember selection and spectral unmixing process was a series of abundance images for mud, sand, water and microphytobenthos, with an associated RMS error image. The mud abundance estimates have a strong empirical relationship (r^2=0.765, p<0.01) with the clay content of the sample sites measured (5.3).

$$\%Clay = \exp[-0.995 + 4.13(MudAbundance)] \qquad \textbf{5.3}$$

As with the 'dry' 1997 image results, Equation 5.3 demonstrates that the pure mud pixels used to unmix the imagery, also approximate the pixels with the greatest clay content (Section 2.3.3). Examination of the associated RMS error image revealed that the unmixing error increased in the fine-grained areas where the intertidal sediments are covered by microphytobenthos. The mud abundance values are also found to decrease significantly in the areas of high microphytobenthos abundance (Figures 5.18). Consequently, it was determined that the microphytobenthos present attenuated the spectral signal of the mud resulting in underestimation of mud abundance (Figure 5.19), as observed in the 'dry' 1997 image results. To correct for this effect, the microphytobenthos and mud abundance estimates were combined and correlated against actual clay content (Equation 5.4).

$$\%Clay = \exp[-1.02 + 3.55(MudAbundance) + 4.29(MicroAbundance)] \qquad \textbf{5.4}$$

A)
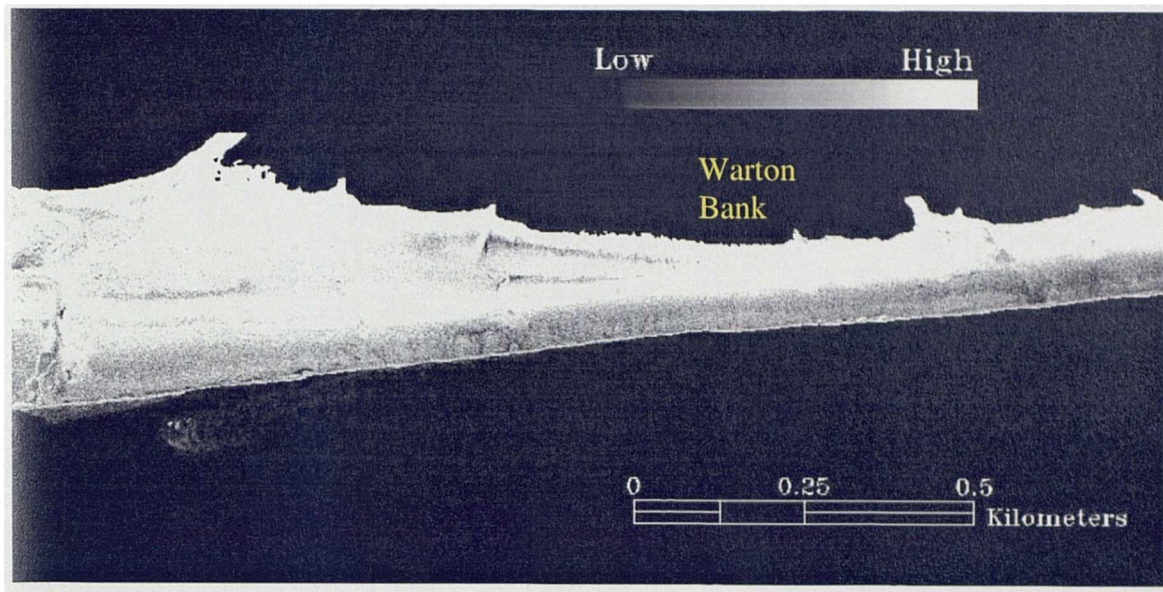
B)
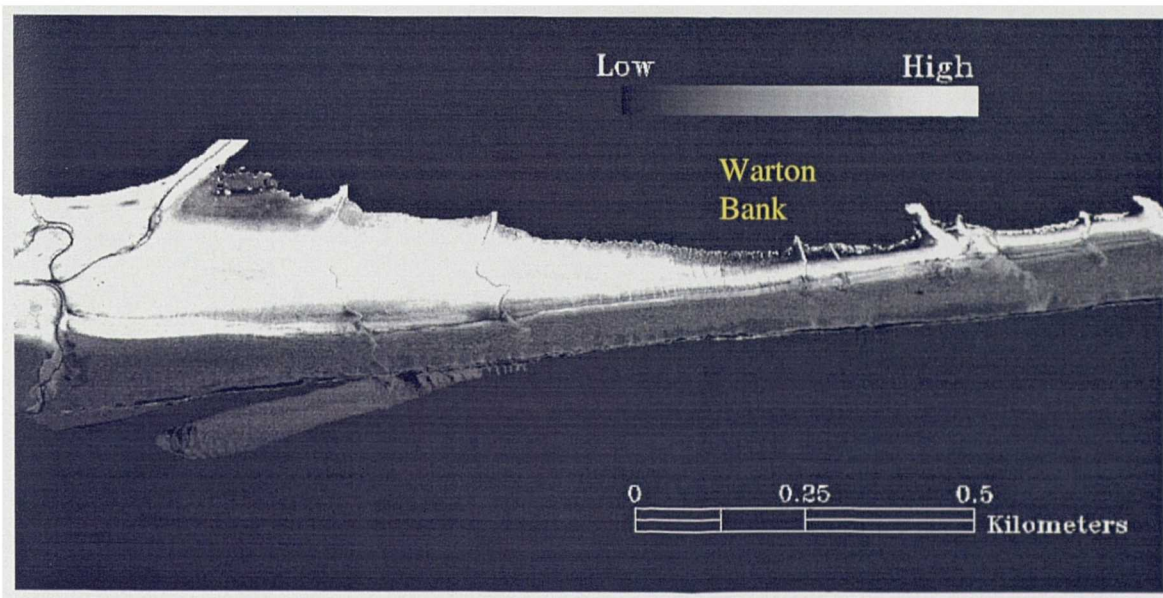
Figure 5.18 Subsets of the a)Mud and b)Microphytobenthos Abundance Images
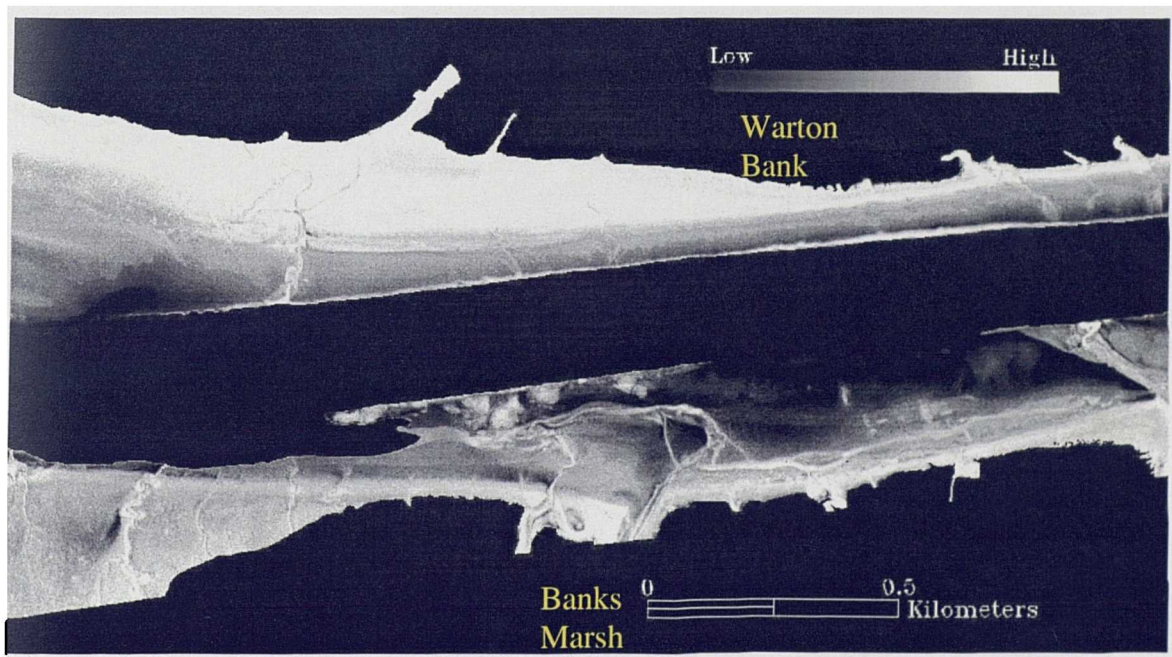Produced by the Linear Unmixing of the 'Wet' 1997 Image
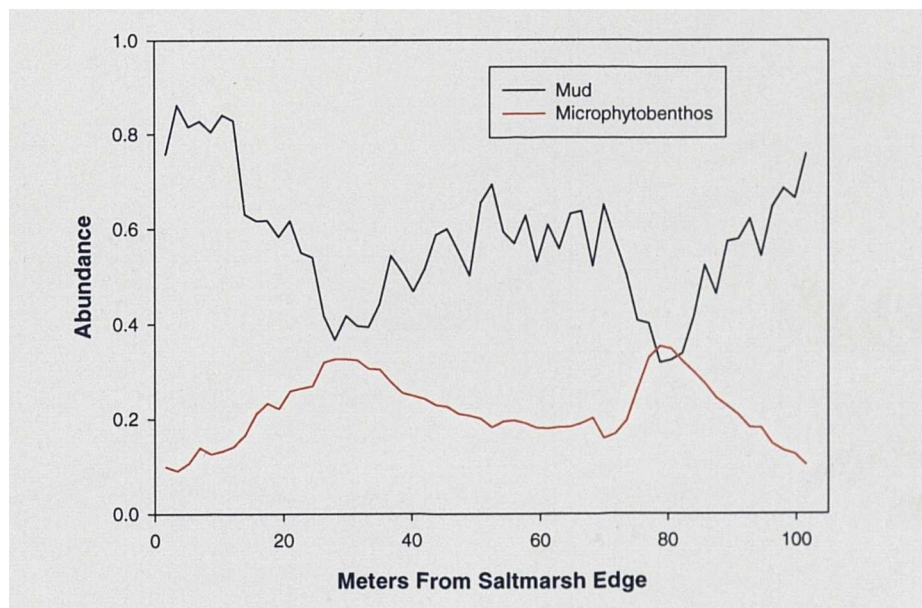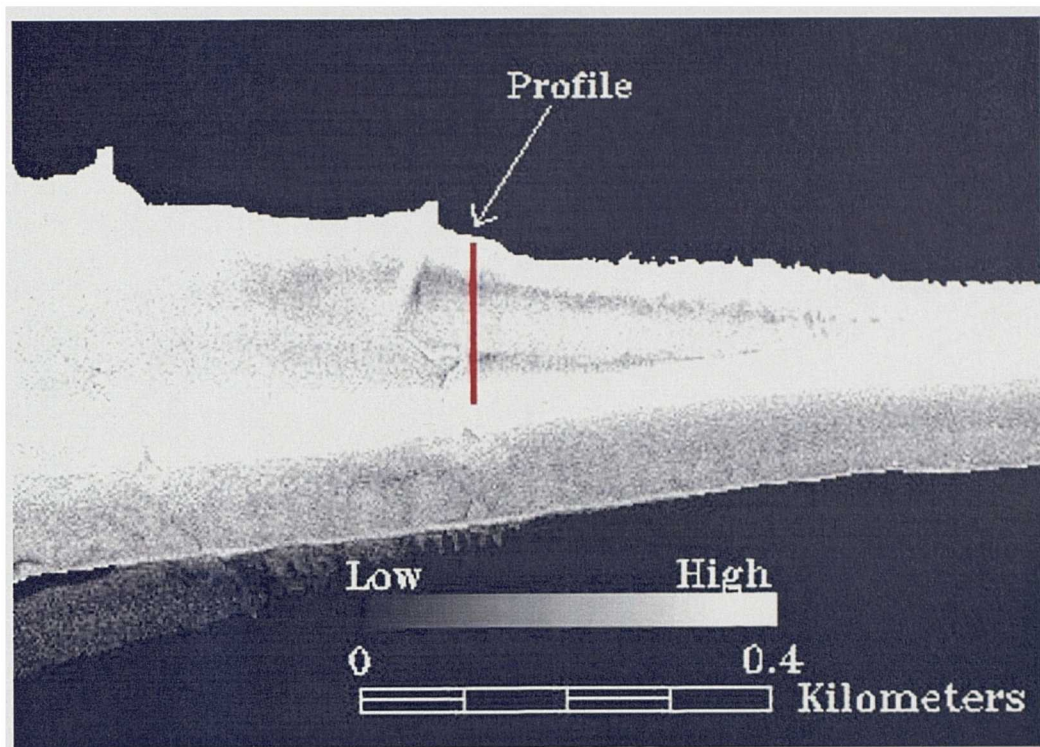
Figure 5.19 Profile of a) Microphytobenthos and b) Mud Abundance from the Saltmarsh Edge to the Main Channel, Demonstrating the Attenuating Affects of Microphytobenthos Within the 'Wet' 1997 Mud Abundance Imagery

This marginally improved the relationship between the combined estimates and actual clay content, supporting the theory that microphytobenthos partially masks the spectral signal of the mud ($r^2=0.790$, $p<0.01$). Pools of surface water were also shown to severely attenuate the spectral signal of mud causing underestimation. Finally, as in the 'dry' 1997 image results, the channel walls were misclassified as being areas of high mud abundance.

Intertidal Sand Distribution

The sand abundance estimates, produced from the subset of the 'wet' 1997 ATM image, demonstrate no significant association with the percentage sand of the *in situ* samples ($r^2=0.034$). However, examination of the sand and moisture abundance images found that sand-dominated sample sites have high water abundance values (Figure 5.20). Similarly, spectral profiles within this abundance image show that the sand abundance does not increase significantly from the saltmarsh edge to the main channel, as would otherwise be expected (Figure 5.21). Consequently, it was assumed that the high sediment moisture was attenuating the spectral signal of the sands, as in the abundance imagery of the 'dry' 1997 image. To correct for this, the sand and moisture abundance estimates were combined and the result was compared to the actual sand contents. A very strong relationship was evident ($r^2=0.793$, $p<0.01$), demonstrating that where high interstitial moisture contents exist the image analysis technique fails to unmix the spectral characteristics of sand. As observed in the 'dry' 1997 abundance imagery, polygonated mud is misclassified in the sand image as areas of high abundance.

A)
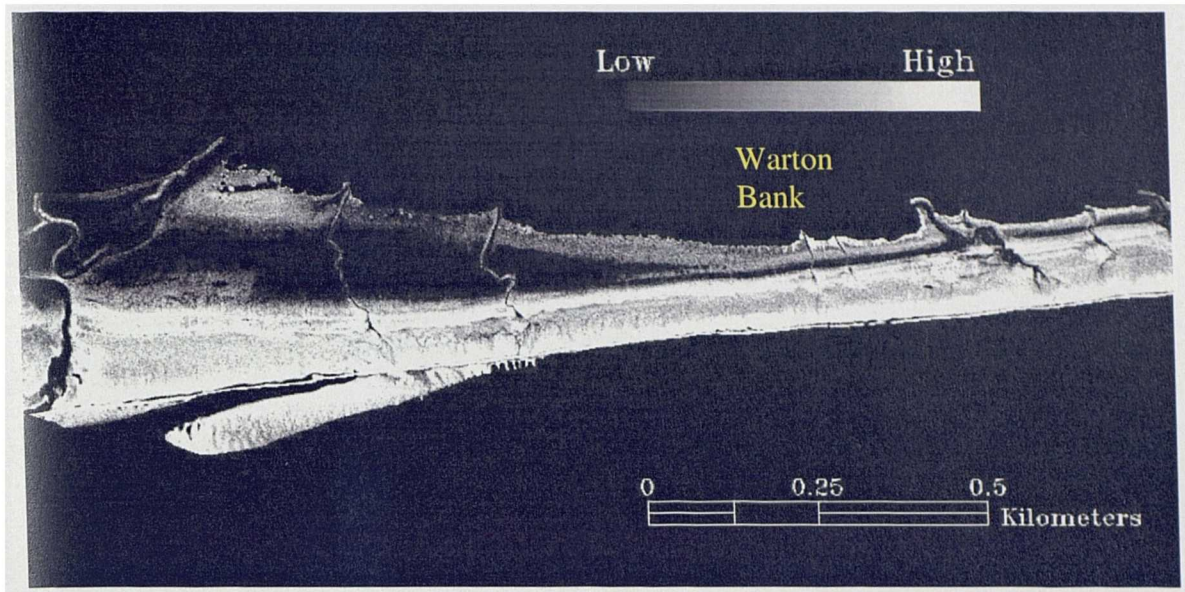
B)
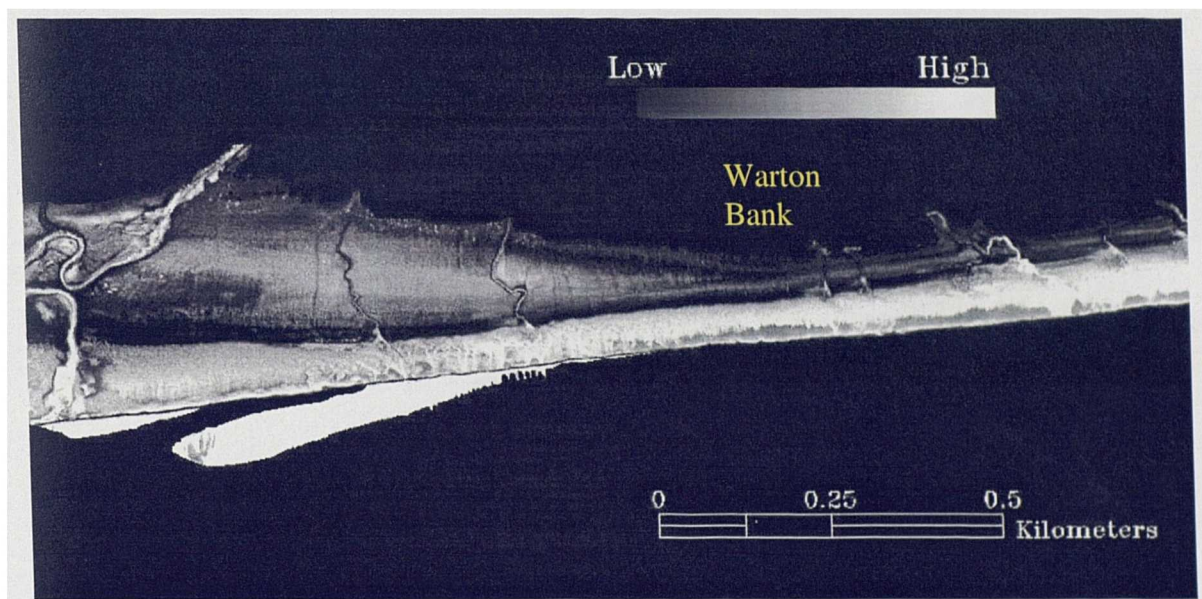
Figure 5.20 Subsets of the a)Sand and b)Moisture Abundance Images Produced by the Linear Unmixing of the 'Wet' 1997 Image
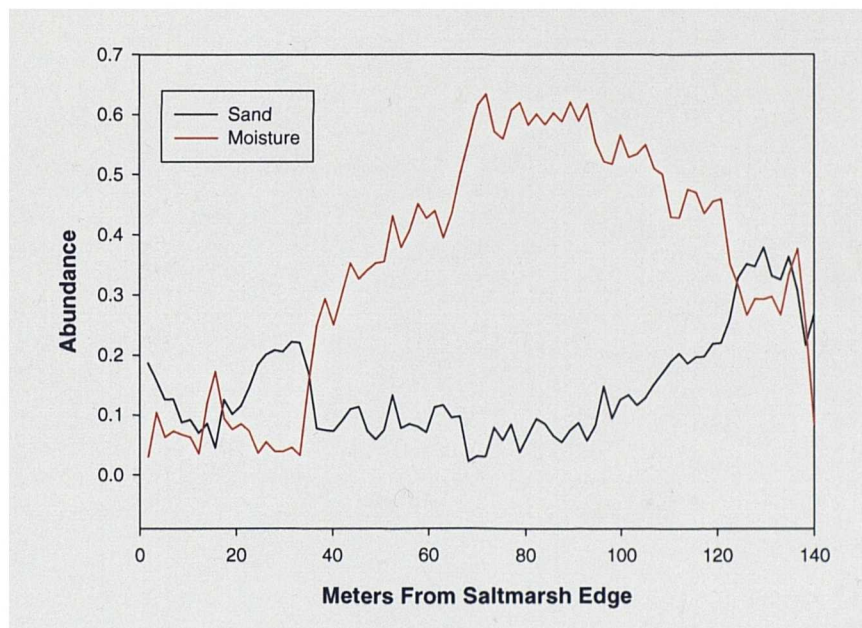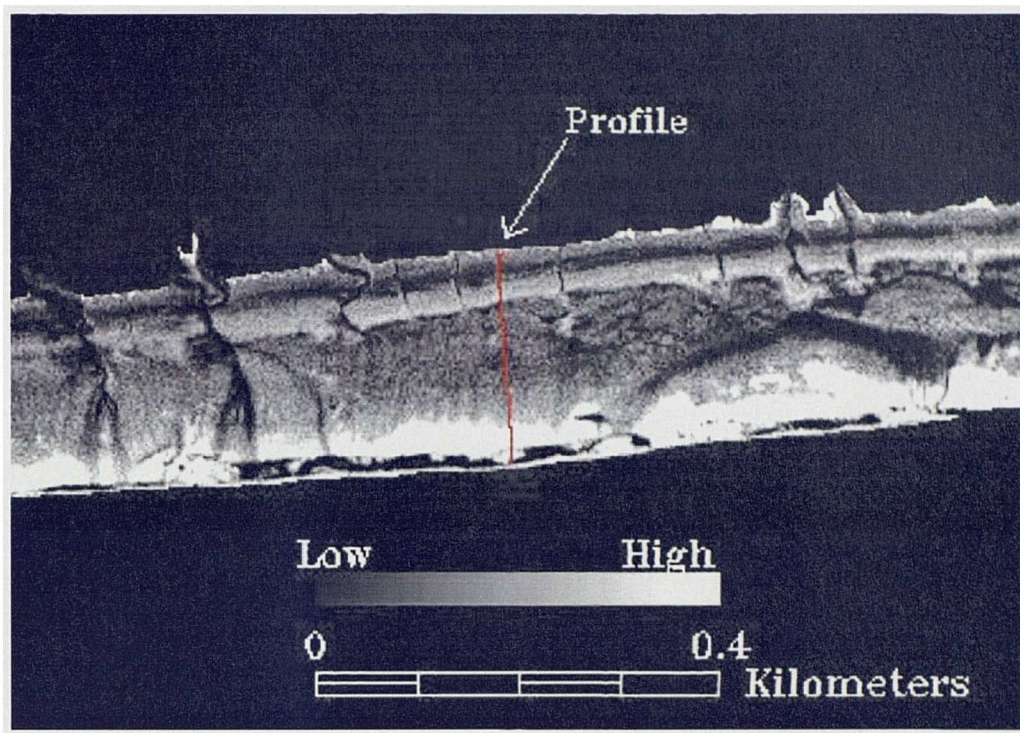
Figure 5.21 Profile of a) Sand and b) Moisture Abundance from the Saltmarsh Edge to the Main Channel, Illustrating the Attenuating Effects of Moisture on the 'Wet' 1997 Sand Abundance Image

Intertidal Moisture and Microphytobenthos Distribution

As with the 'dry' 1997 image, it was impossible to validate accurately the microphytobenthos and moisture abundance maps because no reliable ground data was collected during the flights. Based on aerial photographs and *in situ* knowledge of the area, it was concluded that the moisture abundance image was representative of the relative distribution of moisture (Figure 5.20B). For example, the distribution of the saltmarsh creeks as they cross the intertidal area is accurately defined. Known topographic lows across the intertidal area have also got higher moisture content estimates as expected.

Similarly, the microphytobenthos abundance image (Figure 5.18B) was found to correlate closely with the colour aerial photographs and *in situ* knowledge of the estuary. For example, the large microphytobenthos mat located on the western extremes of the Warton Bank intertidal area is clearly defined, as is the presence of microphytobenthos along the banks of the small saltmarsh channels.

5.5.3   1995 Lytham St. Annes Subset

Image Preparation

The result of the image preparation performed on the first 1995 low-tide image is a small registered image of the intertidal area immediately surrounding Lytham St. Annes, in the correct geometric orientation (Figure 5.22).

MNF Transform

The MNF transform performed on this image produced four coherent bands that contain 86 percent of the total eigenvalues (Table 5.4). MNF bands 5 and 6, were found to have

relatively low eigenvalues but the corresponding eigenimages contained relevant image information, consequently, only bands 7-10 were discarded from further processing. Based on the number of coherent MNF bands, the image subset was estimated to have approximately four spectral dimensions (Equation 3.2).
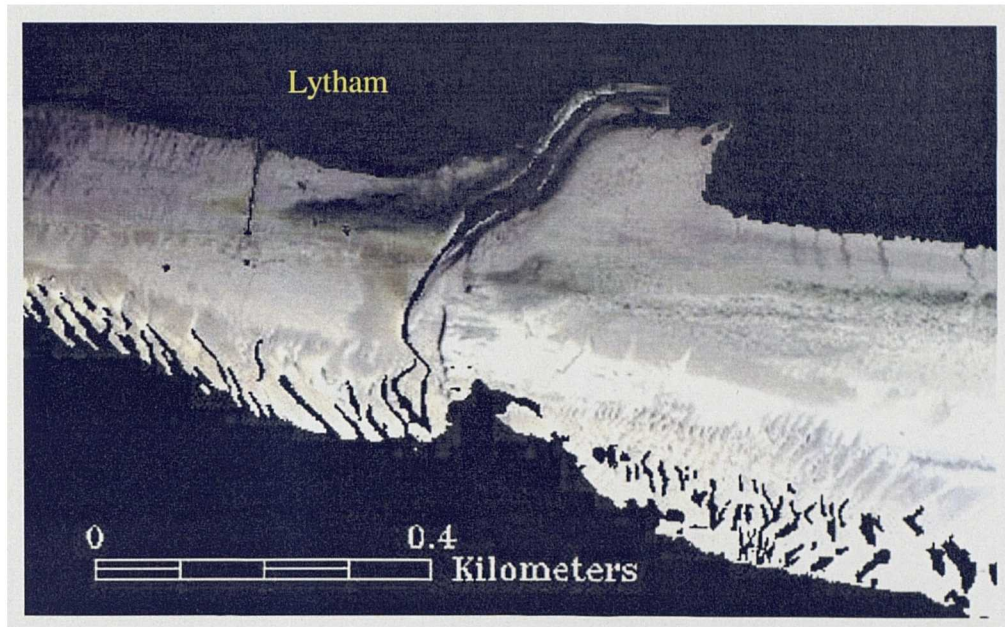
Figure 5.22 Colour Composite (Bands 4, 3, 2) of the Geocorrected and Atmospherically Corrected 1995 Lytham St Annes Image Subset After Masking

Endmember Selection

The scatterplots produced from the coherent MNF bands are considerably different from those used to define the endmembers of the 1997 imagery (Figure 5.23). This is assumed to be a function of the image subset size, which is considerably smaller than the 1997 images and, consequently, contains a limited range of sedimentology. Within Scatterplot 1 (Figure 5.23a), sand, water and microphytobenthos are the only identifiable endmembers. The sand endmember is very distinct and this was used to identify the pure sand image pixels. In Scatterplot 2 (Figure 5.23b), the mud, water and microphytobenthos endmembers are identifiable and image pixels representing the extremes of these endmembers were selected for unmixing.
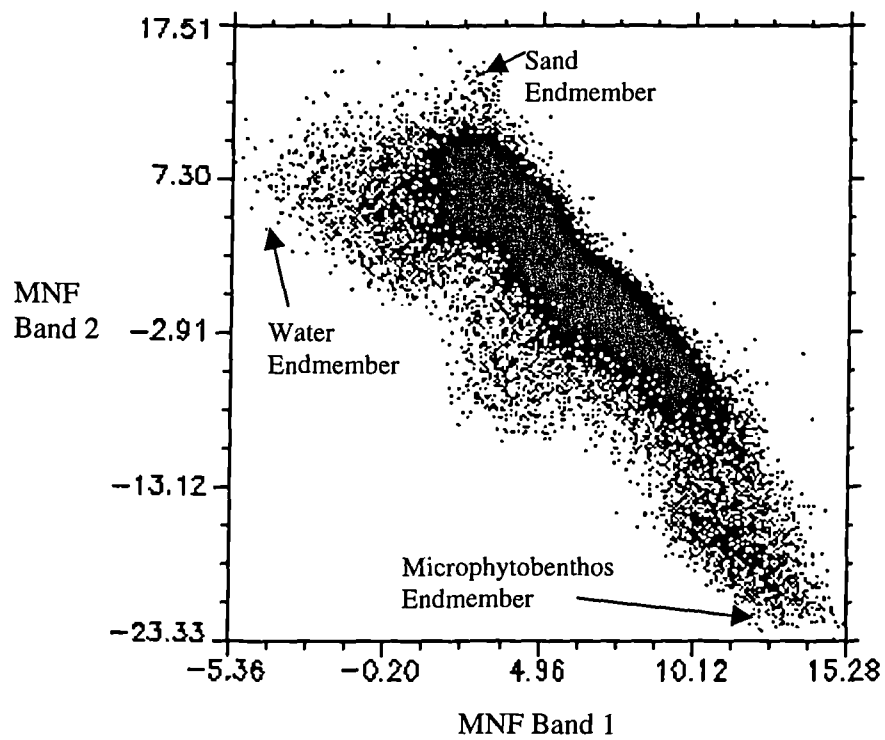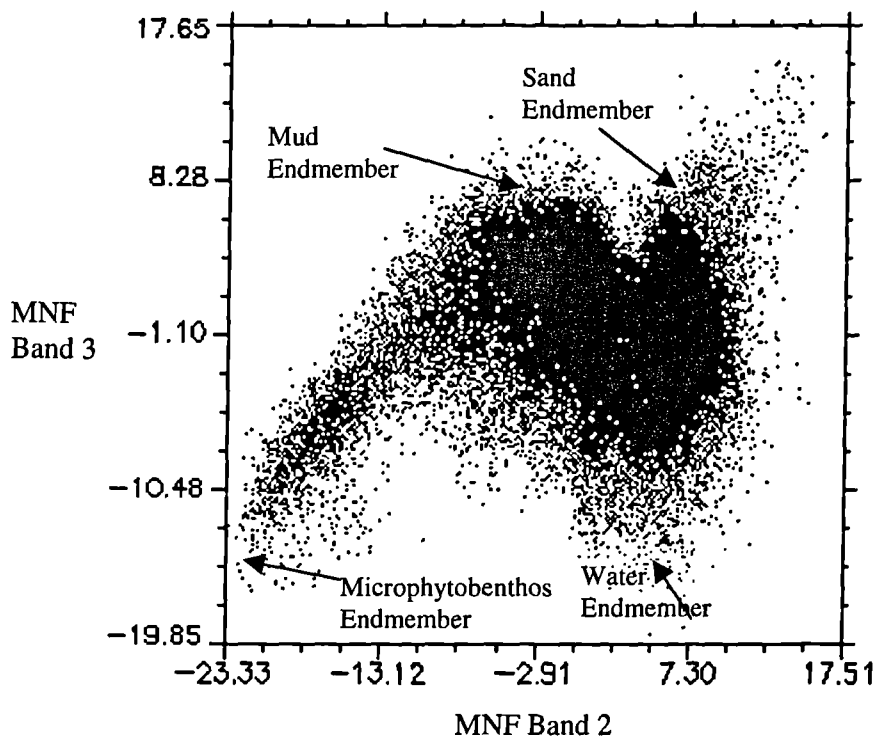
Figure 5.23 2-D Scatterplots of a) MNF Band 1 Against 2 and b) MNF Band 2 Against 3, with the Dominant Spectral Endmembers of the 1995 Image Subset Identified

Pure Endmember Image Pixels

The mud endmember is represented in the imagery by an area close to the large saltmarsh channel which crosses the intertidal area, whilst the selected sand image pixels are located on the ridges of the large sand bars close to the main channel. The microphytobenthos endmember is represented by image pixels located in the centre of the large microphytobenthos mat, west of the large saltmarsh channel. Areas of unmasked channel water close to the edge of the sandbars represent the extreme of the water endmember in Scatterplot 2. The mean spectra of these pixels are comparable to the mean endmember spectra used to unmix the 1997 imagery.

Intertidal Mud Distribution

The selected 'pure' image pixels were used to unmix linearly the MNF imagery, producing sand, mud, water and microphytobenthos abundance images with an associated RMS error image. Spectral profiles through the mud abundance image (Figure 5.24A) show there is an overall lowering in abundance towards the main channel from the saltmarsh, with a central band of high abundance (Figure 5.25). A significant moderate relationship (r^2=0.498, p<0.01) exists between the mud abundance estimates and the 1997 clay measurements made at 48 sites within the image area (Equation 5.5).

$$\% Clay = \exp[0.653 + 1.46(MudAbundance)] \qquad \textbf{5.5}$$

This relationship is very slightly improved (r^2=0.5, p<0.01), when the microphytobenthos abundance is included in the regression equation (Equation 5.3).

$\%Clay = \exp[0.589 + 1.51(MudAbundance) + 0.194(CyanAbundance)]$ **5.6**

Lastly, areas of shadow close to the main estuary, produced by the large sand mega-ripples and the low sun-angle during image collection, were misclassified as areas of high mud abundance.

A)
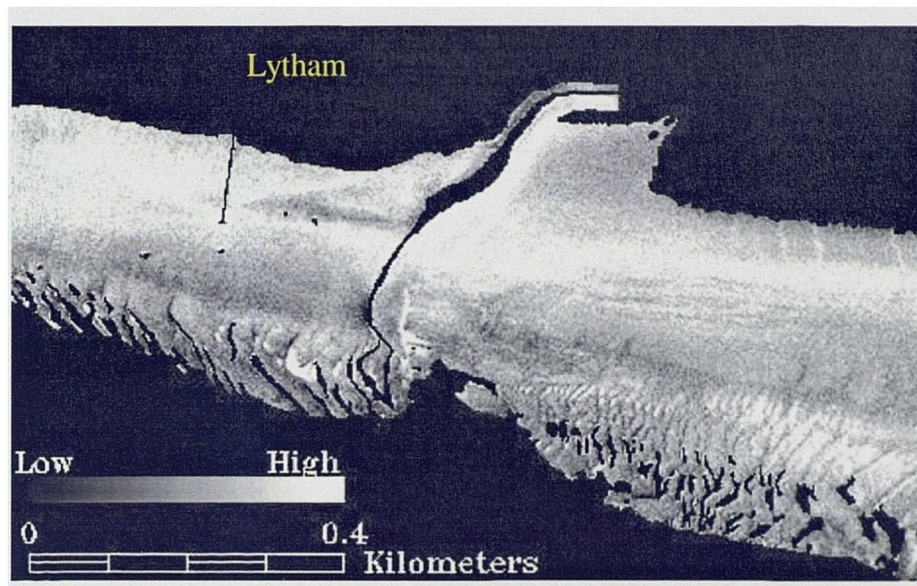
B)
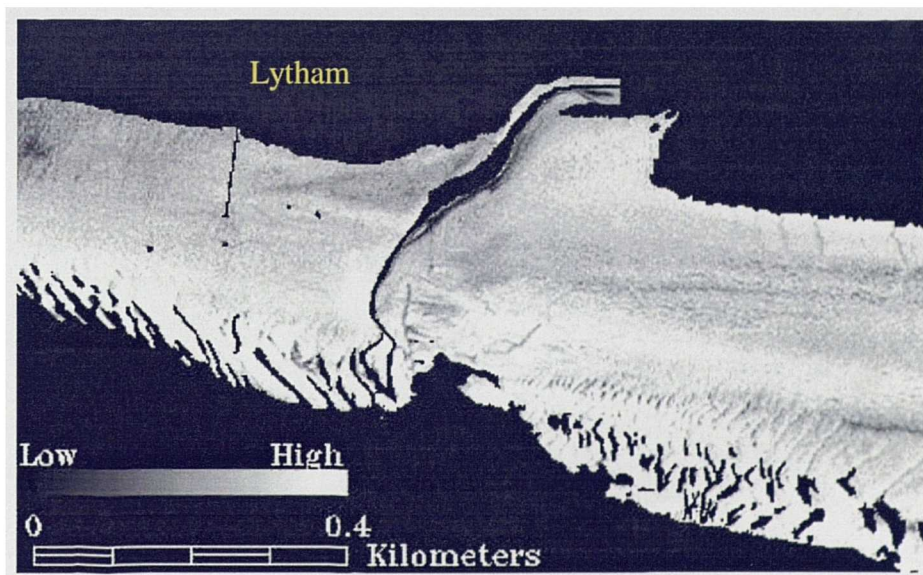
Figure 5.24   The a)Mud and b)Sand Abundance Images Produced by the Linear Unmixing of the 1995 Image Subset
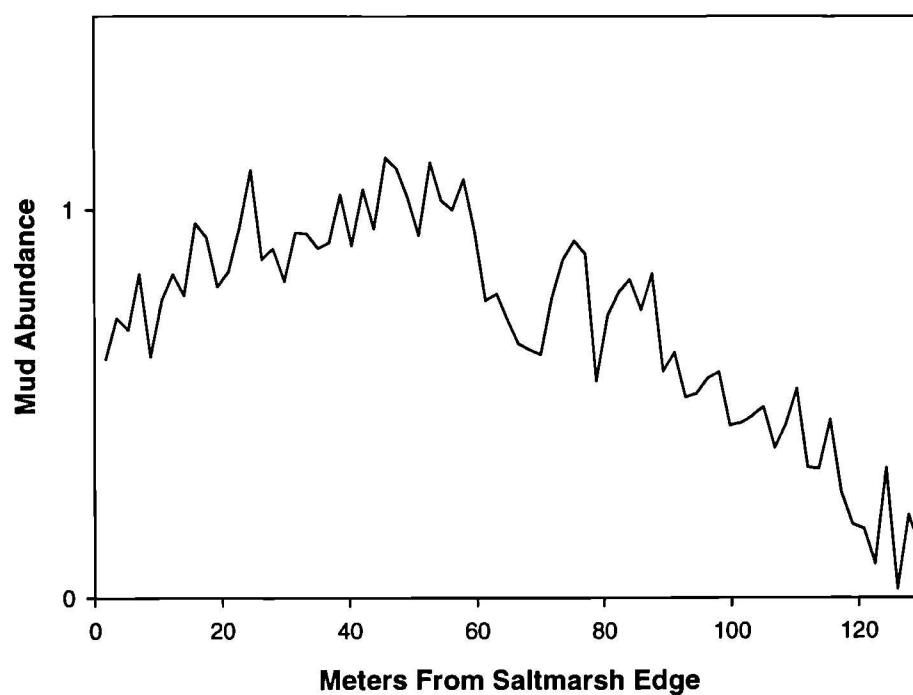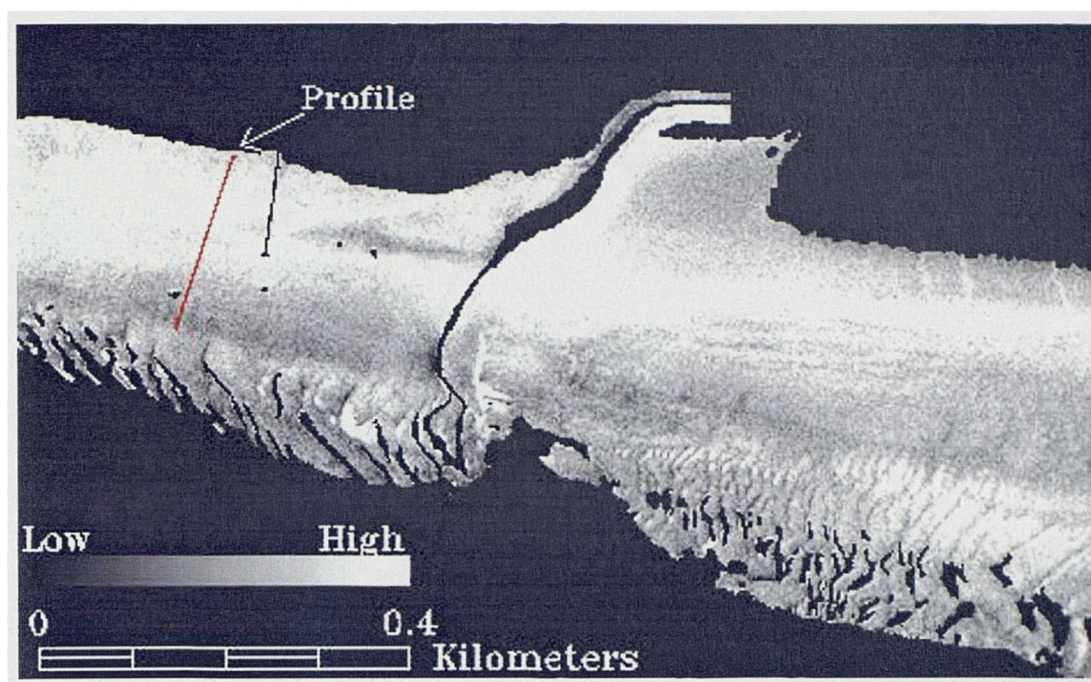
Figure 5.25 Example Mud Abundance Profile from the Saltmarsh Edge to the Main Channel, from the 1995 Image Subset

Intertidal Sand Distribution

In general agreement with the field observations, the sand abundance estimates increase from the saltmarsh edge to the main channel (Figure 5.24b). However, no significant relationship was found between the sand abundance estimates and the sand content of the 1997 samples. When the sand and moisture abundance estimates were combined, the relationship with the sand content of the samples was significantly improved (r^2=0.392, p<0.01).

Intertidal Moisture and Microphytobenthos Distribution

Based on 1995 observations and aerial photographs, the water abundance image appears to accurately represent the distribution of surface and interstitial moisture across the intertidal area (Figure 5.26a). In the microphytobenthos abundance image, the large microphytobenthos mat located west of the saltmarsh creek, which was observed in the 1997 fieldwork, is clearly defined (Figure 5.26b). A band of microphytobenthos is also identifiable in the image, along the central intertidal area east of the main channel.

5.5.4   Intertidal Sediment Variability

Although strong relationships have been observed between the 1997 abundance image estimates and the clay content of the sediment samples, a notable amount of scatter still exists. Preliminary sediment variability experiments (Section 5.2) have demonstrated that a considerable amount of this scatter may be attributed to sediment variability, and sampling and analysis error. In Table 5.5 the inherent variation in sediment grain-size measurements within each 2m^2 quadrat is detailed. Although these factors may not be the sole contributors to the scatter, they have been shown to be potentially significant contributors. Consequently, the relationships between the abundance imagery and the

158

sediment samples, which are used to produce the final clay distribution maps, are possibly the strongest that can be achieved within such an inherently variable environment.

A)

B)
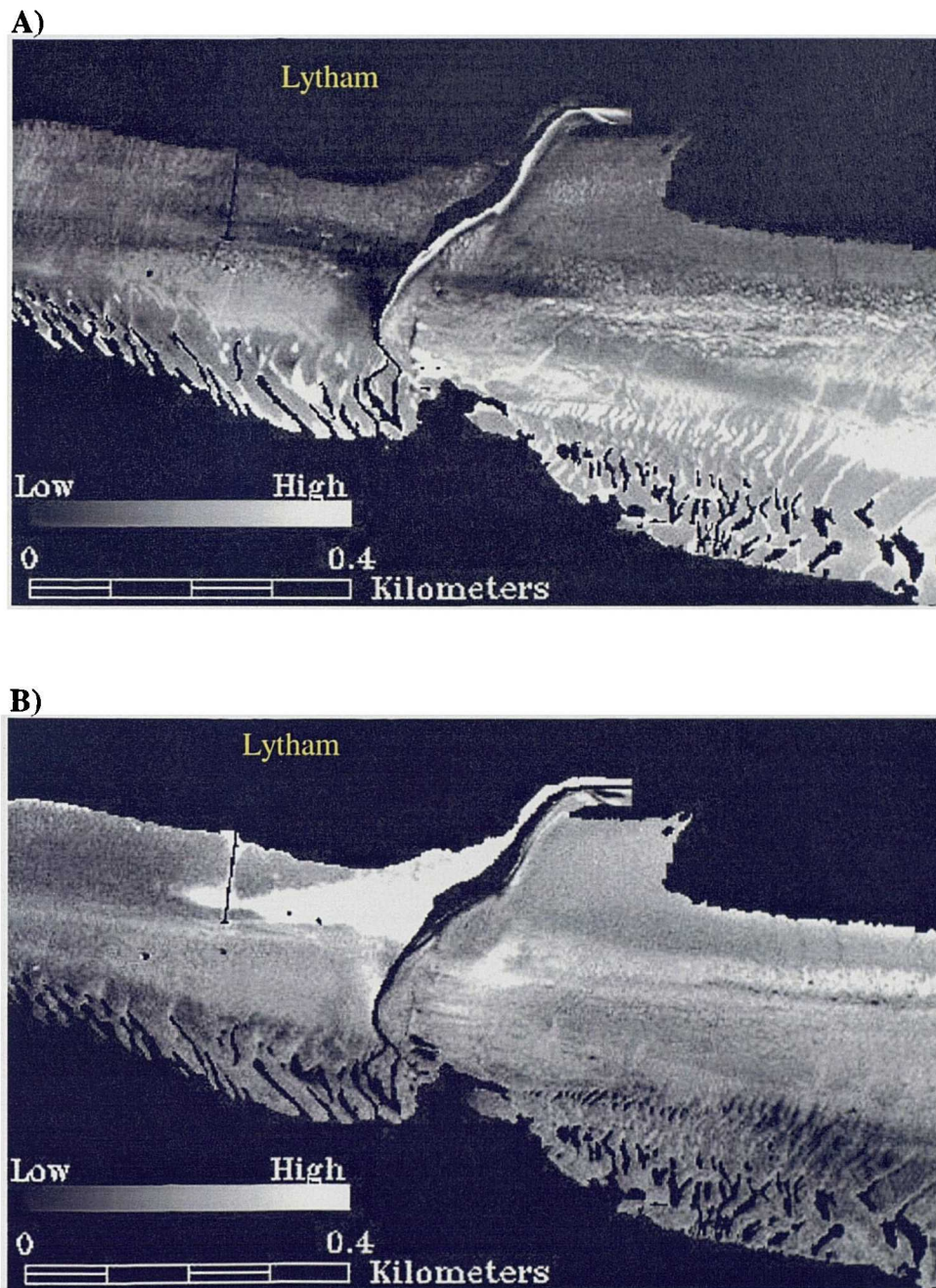
Figure 5.26 The a)Moisture and b)Microphytobenthos Abundance Imagery Produced by the Linear Unmixing of the 1995 Image Subset

Table 5.5 Variation in Surface Percentage Clay Measurements made within 2m^2 Quadrats in the Exposed Intertidal Sediments in the Ribble Estuary

Quadrat	Coefficient of variation (CV%)	Absolute Mean Error (%)
Quadrat 1	20.59	0.52
Quadrat 2	24.71	0.47
Quadrat 3	53.01	0.31

5.5.5 Final Clay Maps of the Ribble Estuary

The final result of this chapter, is a complete map of clay distribution within the intertidal sediments of the Ribble Estuary. This map is based primarily on the mud and microphytobenthos abundance images produced from the 'dry' 1997 ATM imagery (Figure 5.27 & 5.28). This is due to the strong association that exists between the percentage clay content of the sample sites and the combined mud and microphytobenthos abundance estimates (r^2=0.815, p<0.01). The exponential regression equation that defines this relationship was used to convert the two abundance images into a map of percentage clay (Equation 5.2). Similarly, the mud and microphytobenthos abundance imagery produced from the Lytham St Annes image subset were calibrated using 1997 samples to create a clay map of this region (Figure 5.29). The clay distribution maps produced were found to be comparable with what can be identified in the aerial photographs and with *in situ* knowledge of the region.
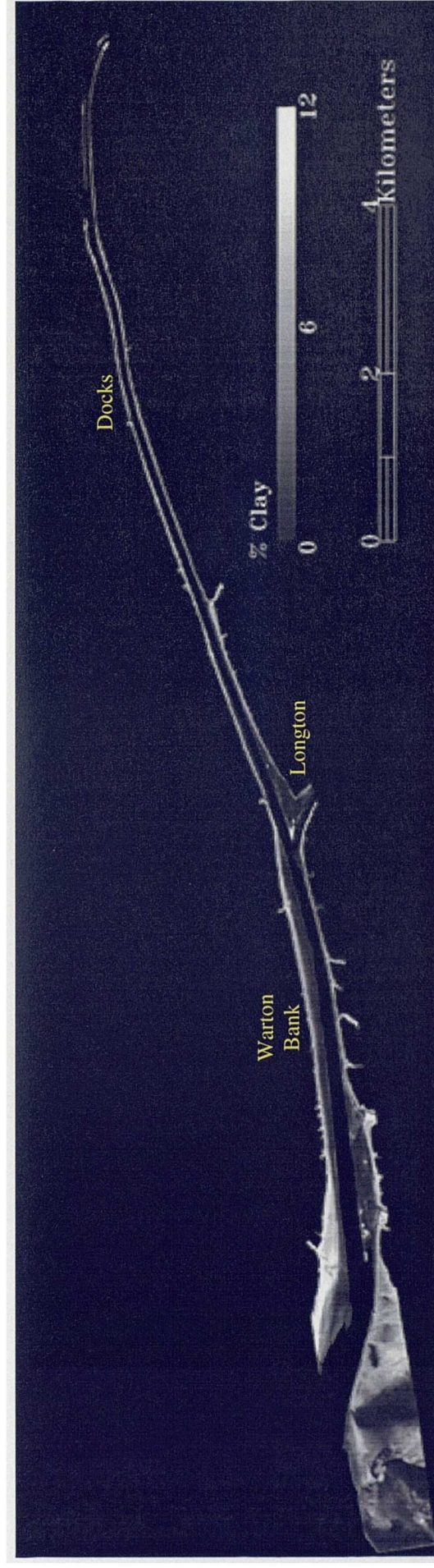
Figure 5.27 Percentage Clay Map Produced from the 'Dry' 1997 Abundance Imagery

161
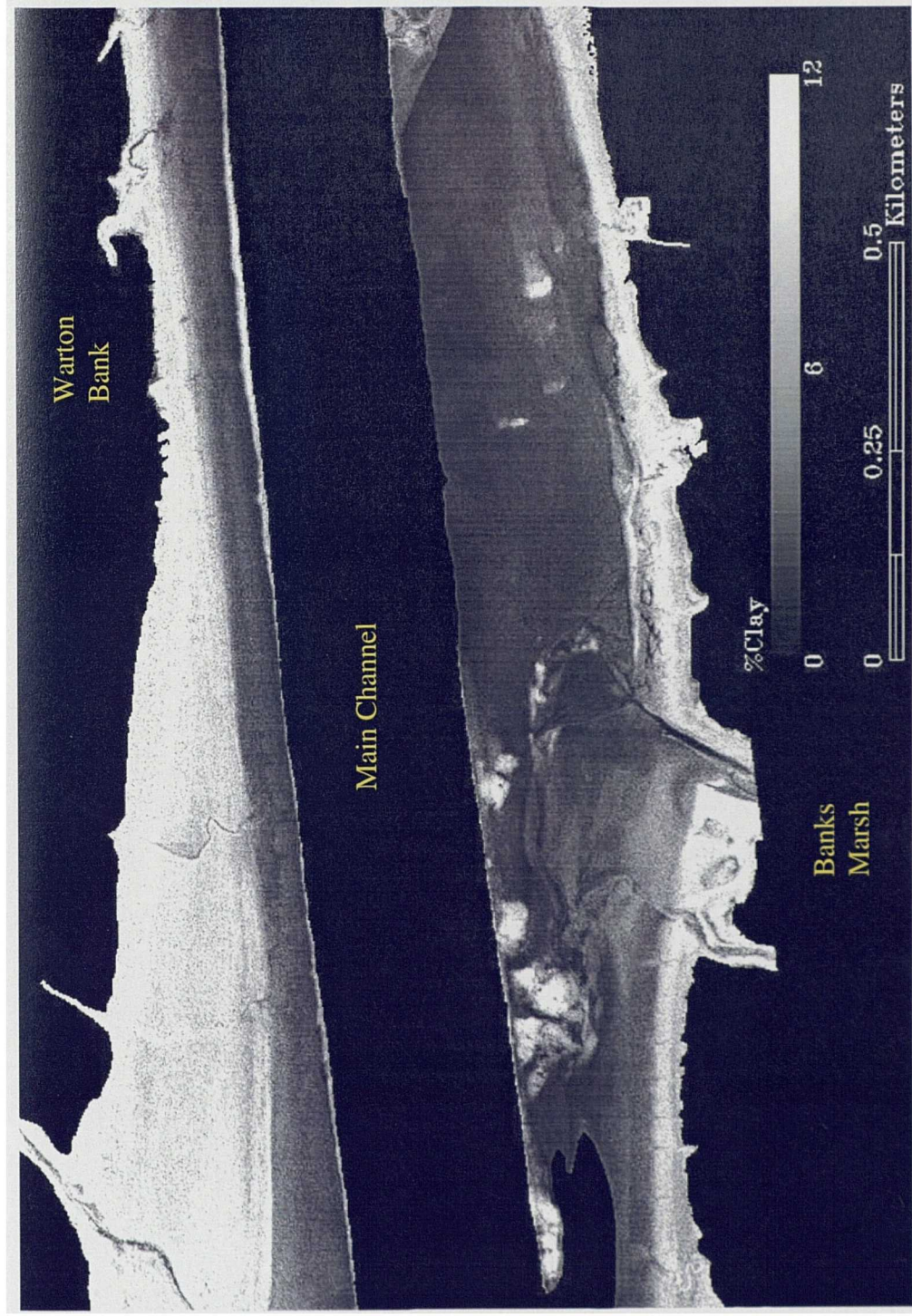
Figure 5.28 Subset of the Percentage Clay Map Produced from the 'Dry' 1997 Abundance Imagery

162
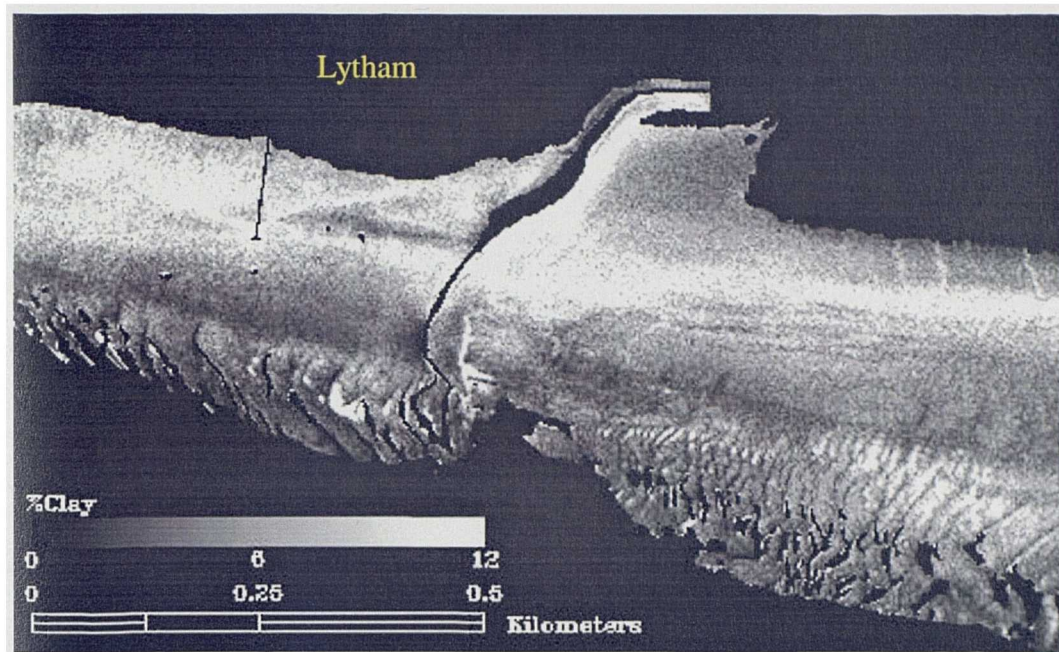
Figure 5.29 Percentage Clay Map Produced from the Lytham St Annes Abundance Imagery

5.6 DISCUSSION

5.6.1 Mapping Intertidal Mud

From low-tide ATM imagery, collected under precise environmental conditions, it is possible to map the mud distribution within the intertidal regions of an estuary. It is suggested that the distribution of the fine-grained sediments within the Ribble Estuary on May 30th is represented in the mud abundance image produced from the 'dry' 1997 ATM image (Figure 5.6). This proposal is based on the strong relationship observed between the actual clay content and the estimated mud abundance of the 1997 sample sites (r^2=0.79). This relationship also supports the earlier assumption that the pure mud pixels are inherently the pixels with the highest clay content. Consequently, this supports the linear unmixing of mud from the imagery as a means of determining the percentage clay content distribution within the intertidal areas.

163

5.6.2 Influence of Interstitial Moisture on Mapping Intertidal Mud

The distribution of mud in the 'wet' 1997 abundance image (Figure 5.18A), is closely correlated with that of the 'dry' 1997 image (Figure 5.6) although the latter is marginally more accurate. This suggests that during the first hour and a half of intertidal exposure, before the collection of the first line of imagery, the sediments lost sufficient moisture to allow the mud distribution to be accurately mapped. The relief of the mudflat areas close to the saltmarsh probably contributed substantially to the loss of moisture in these regions. However, in the more recently exposed flat sand-dominated areas the sediments have less opportunity to lose moisture within the first one and a half hours. This may explain the relatively high moisture abundance estimates of these areas as derived from the 'wet' 1997 imagery (Figure 5.20B). It is suggested that these higher moisture contents contributed to the marginally weaker relationship between the sampled clay contents and the mud abundance estimates derived from the 'wet' 1997 image, in comparison to that of the 'dry' 1997 imagery.

5.6.3 Influence of Interstitial Moisture on Mapping Intertidal Sand

The ability to map sand abundance from ATM imagery is dependent on the moisture content of the sediments and, consequently, on the period of exposure before image collection. This is well demonstrated by the contrasting relationships of the 'wet' 1997 and 'dry' 1997 sand abundance imagery, with the sand content of the 1997 sample sites. During the three hours of sediment exposure between the acquisition of these images, it is suggested that the sediments were able to lose sufficient interstitial moisture to reduce significantly the attenuation of sand's spectral characteristics. This resulted in the map of sand distribution produced from the 'dry' 1997 image (Figure 5.11) being considerably more accurate than that produced from the 'wet' 1997 imagery (Figure 5.20A). It has also been shown that by combining the water

abundance image with the sand abundance image, the ability to estimate percentage sand is improved considerably, especially for the 'wet' subset. This supports the theory that high interstitial moisture levels substantially inhibit the ability to map percentage sand content from ATM imagery.

An alternative explanation for the poor relationship between the 'Wet' 1997 abundance estimates and the actual sand content is that the selected endmember water pixels were not pure. It is possible that the endmember pixels contained a significant sand signal, which resulted in the sand abundance of each pixel being significantly underestimated. However, if this were so, then one would expect the sand and water endmember pixels to be close together in feature space or coplanar/collinear, which they are not (Figure 5.16). Similarly the mean endmember spectra for moisture and sand appear to be substantially different (Figure 5.17). Consequently, it is suggested that the earlier explanation of sand signal attenuation due to higher interstitial moisture contents is more plausible.

5.6.4 Influence of Surface Water on Mapping Intertidal Sediments

Throughout the intertidal regions of the Ribble Estuary, large pools of water and saltmarsh creeks were observed in 1997. These bodies of surface water attenuate the spectral signal of the intertidal sediments to such a degree that they are almost completely masked out (Figure 5.10). Consequently, the mud abundance estimates drop sharply where surface water is present. If more detailed *in situ* knowledge of the surface pools had been available it may have been possible to identify all the surface water directly from the water abundance image. This would then allow suitable corrections to be applied to the affected areas of the abundance

imagery. The overall accuracy of the sediment distribution images would consequently be improved and this in turn would provide a more accurate map of sediment radioactivity.

5.6.5 Influence of Microphytobenthos on Mapping Intertidal Sediments

The ability to estimate the clay content of the sample sites from the 'wet' and 'dry' 1997 abundance imagery is improved significantly when the microphytobenthos abundance is included in the regression equation (Equation 5.2 & 5.4). This implies that the microphytobenthos is causing an underestimation of the mud present, as suggested by some abundance profiles (Figure 5.9 & 5.19). It is suggested that this underestimation is a product of the microphytobenthos cover being thick enough to attenuate the spectral characteristics of the mud underneath. It is therefore valid to compensate for the presence of microphytobenthos, and this is supported by the improvement of the relationship between the image estimates and the clay content of the sample sites. Since the microphytobenthos in this region concentrates on the fine sediments, no significant improvement was made to the relationship between the estimated and actual sand content, when microphytobenthos abundance was included.

5.6.6 Misclassification of Polygonated Mud

In the sand abundance images produced from the 1997 imagery, it was noted that the polygonated mud areas close to the saltmarsh edge were misclassified as areas of high sand abundance (Figure 5.14). Polygonated mud areas were also selected to represent the extremes of the mud endmember in feature space and used in the unmixing of the 1997 imagery. Therefore, although the majority of the polygonated mud was misclassified in the sand abundance imagery, these sediments provide the basis for successfully unmixing mud from the

imagery. The only explanation for this apparent contradiction is that, although these areas have generally got typical low reflectance characteristics, the relatively high reflectance values of these sediments in ATM bandwidths 2 to 4 are more typical of sand than the surrounding wet mud, causing them to be misclassified (Figure 5.5).

5.6.7 Microphytobenthos Distribution Image

It is evident that this project has a number of important implications for future estuarine habitat surveys. The microphytobenthos abundance image, produced from the 'dry' 1997 imagery, has been shown to approximate the distribution and relative abundance of microphytobenthos within the intertidal area of the Ribble Estuary (Figure 5.15b). Consequently, this technique provides a synoptic view of microphytobenthos in the estuary, which is not available from conventional habitat surveys. In future estuarine remote sensing studies, it may be possible to differentiate the species of microphytobenthos present based on their chlorophyll abundance.

The large microphytobenthos mats identified in the image also have a stabilising effect on the underlying radionuclide-rich, fine sediments, reducing the likelihood of resuspension (Sutherland *et al.*, 1998). Consequently, this image could also be used in studies of intertidal sediment resuspension and on the movement of radionuclides. In other words, the microphytobenthos abundance map could be interpreted as a map of radionuclide-associated sediment deposits with enhanced stability.

167

5.6.8 Lytham St. Annes Abundance Imagery

From the 1995 Lytham St. Annes image, poorer relationships were found between the observed and estimated sediment characteristics, than were observed from the 1997 imagery. There is a number of possible explanations for these weaker relationships: *1)* there may be insufficient 'pure' pixels present within the small image window and, consequently, the unmixing process may be based on 'mixed' pixels which bias the end result; *2)* the validation of the 1995 results was based on 1997 samples and if there has been any significant change in the sediment distribution during the two intermediate years the validation accuracy would be affected; *3)* the 1997 sample locations were calculated from compass bearings taken during sampling, rather than the more reliable marker boards used to locate the samples in the 1997 imagery, hence errors in sample location may have influenced the apparent classification accuracy. In conclusion, the apparent reduction in the sediment mapping accuracy may be a product of any one, or a combination of these factors.

5.6.9 Clay Distribution Maps

The clay abundance image, produced from the 1997 'dry' mud abundance image, is an accurate representation of clay distribution within the Ribble Estuary, for May 30th 1997. Excellent correlations between the image abundance estimates and the sample clay content were found (r^2=0.815), with most of the remaining scatter being associated with sampling and analysis errors (Section 5.5.4). The objective of this project is to use this clay distribution map as the basis for Sellafield-derived radionuclide maps of this region. However, this is only one of a range of potential end products that may be derived from the clay distribution image. Sediment grain-size distribution has also got important implications on ecological diversity, habitat location (Goss-Custard and Yates, 1992) and sediment transport dynamics. In short,

whilst this map is only used for one application here, it and the associated image products could potentially be employed in a number of different estuarine studies.

5.7   SUMMARY

An image analysis technique for mapping percentage clay content distribution within the intertidal zones of an estuary at low tide has been presented. This technique was proven effective by the production of accurate maps of intertidal sediment abundance, validated by ground truth data, from raw ATM imagery of the Ribble Estuary. It has been shown that the period of sediment exposure before image collection is fundamental to the accuracy of the final results, supporting the findings from the *in situ* and laboratory reflectance spectroradiometry experiments. Although accurate maps of clay abundance may be created from imagery acquired just one and a half hours after sediment exposure, a more accurate product is produced from imagery collected four and a half hours after exposure. This determinant has been shown to have even more serious implications on the ability to map sand contents within this region.   In addition, the associated abundance map for microphytobenthos, produced by the linear unmixing technique, has been shown to be reliable. Consequently, this technique has also a wide range of potential applications in future ecological studies, as well as estuarine management and radionuclide monitoring studies.

In the next chapter, the conversion of the final clay abundance images to maps of Sellafield-derived radionuclide activities for the Ribble Estuary is described and the results are discussed. In Chapter 7, the image analysis and classification results of this chapter are discussed further, with particular reference to the findings of other studies.

6. CALIBRATION OF IMAGERY TO ACTIVITY UNITS

6.1 INTRODUCTION

The ability to map sediment grain-size distributions, as outlined in Chapter 5, provides a powerful tool in mapping particle reactive pollutants in estuarine environments. Remote sensing of radionuclide distributions in the surface sediments of an intertidal zone is an indirect process, reliant on a series of relationships between reflectance, sediment characteristics and radionuclides. By establishing the relationships between various radionuclide activities and clay content, it is possible to convert a clay abundance map into maps of surface radionuclide distributions. However, these relationships are generally site specific and consequently they have to be defined for each study area.

The Sellafield-derived radionuclides present in the intertidal sediments of the Ribble Estuary are the focus of this study. As described in Section 2.4.4, previous studies of this estuary have demonstrated that strong associations exist between these radionuclides and intertidal sediment clay content (Tyler *et al.*, 1995; Assinder *et al.*, 1997; Brown, 1997). Consequently, it was expected that accurate maps of Sellafield-derived ^{137}Cs and ^{241}Am distribution in the estuarine sediments could be created from the clay abundance images. The relationships between the surface sediment characteristics and Sellafield-derived activities, as observed within this project, are defined in this chapter. In addition, the subsequent radionuclide distribution images produced are described and analysed in terms of estuarine processes, intertidal morphology and microphytobenthos cover.

6.2   1995 AND 1997 SEDIMENT SAMPLE RADIONUCLIDE INVENTORY

6.2.1   Introduction

As detailed in Section 5.2.1, sediment surface scrapings were collected from a number of sites in the Ribble Estuary during the 1995 and 1997 NERC flights and the majority of these samples underwent both gamma and grain-size analysis (Appendix 4). The objective of this work was to, firstly, establish the relationships between the Sellafield-derived radionuclides (primarily ^{137}Cs and ^{241}Am) and clay content and, secondly, to assess the spatial and temporal variability of these associations. Once defined, these relationships would enable the clay abundance maps produced by image analysis and calibration to be converted into maps of surface radionuclide distribution.

6.2.2   Relationship of Intertidal Sediments and Radioactivity

A strong positive relationship between the Sellafield-derived ^{137}Cs and ^{241}Am, and percentage clay content of the Ribble Estuary intertidal sediments was identified both in 1995 and in 1997 (Figures 6.1 and 6.2). Similar, though negative, regression relationships exist between these radionuclides and percentage sand content (Table 6.1). Since these associations are based on samples collected from a number of locations across the whole estuary (e.g. Figure 3.2), they are assumed to be broadly representative of all the Ribble Estuary intertidal sediments. The relationship between percentage clay content and ^{137}Cs is also found to be reasonably stable between 1995 (6.1) and 1997 (6.2).

$$ln^{137}Cs = 2.77 + 1.38(ln\,Clay)\qquad\qquad\textbf{6.1}$$

$$ln^{137}Cs = 2.82 + 1.37(ln\,Clay)\qquad\qquad \mathbf{6.2}$$

In contrast, the ^{241}Am relationship with clay content changed between 1995 (6.3) and 1997 (6.4); however, this change is more likely a product of gamma and grain-size analytical error than any actual temporal change.

$$ln^{241}Am = 2.39 + 1.17(ln\,Clay)\qquad\qquad \mathbf{6.3}$$

$$ln^{241}Am = 1.46 + 1.54(ln\,Clay)\qquad\qquad \mathbf{6.4}$$

To summarise, the relationships between the Sellafield-derived radionuclides and percentage clay described above appear to be both temporally stable and spatially representative of the Ribble Estuary. It is also worth noting that a significant proportion of the scatter observed in the graphs of clay against radionuclide content may be attributed to error introduced by the grain-size analysis of the surface samples (Section 5.5.4). Consequently, the relationships between the radionuclides and clay content may be even stronger than initially inferred from this dataset.

Table 6.1 Regression Analysis Results (r^2) of ^{137}Cs & ^{241}Am Against Percentage Clay, Silt and Sand

	1995		1997		Combined Years	
	^{137}Cs	^{241}Am	^{137}Cs	^{241}Am	^{137}Cs	^{241}Am
% Clay	0.93	0.84	0.93	0.87	0.93	0.84
% Silt	0.83	0.71	0.88	0.86	0.84	0.71
% Sand	0.81	0.79	0.93	0.90	0.83	0.78

A)

B)
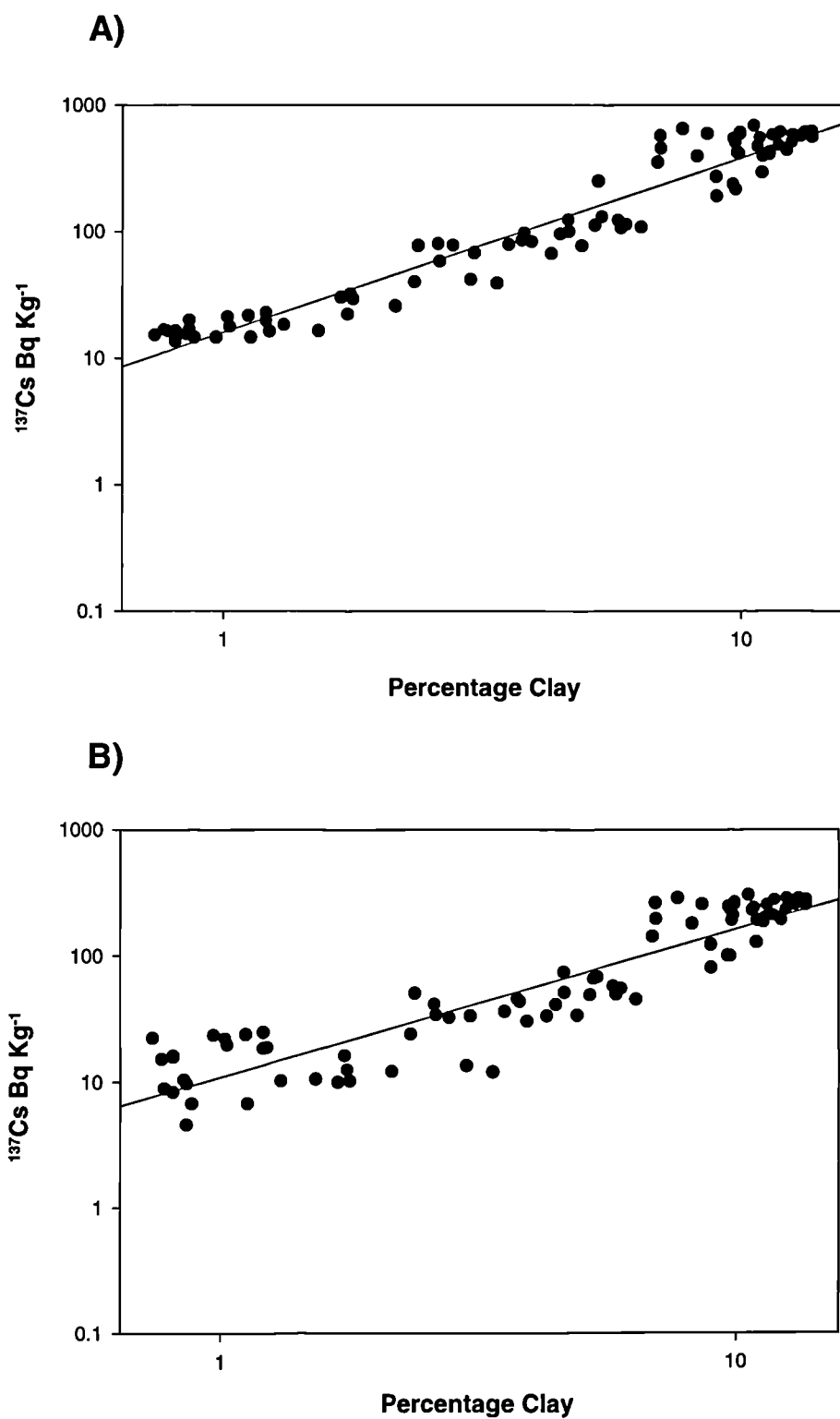
Figure 6.1 Relationship Between ^{137}Cs & ^{241}Am and Percentage Clay of the 1995 Ribble Intertidal Sediment Samples (r^2=0.931 and 0.841 Respectively)

A)

B)
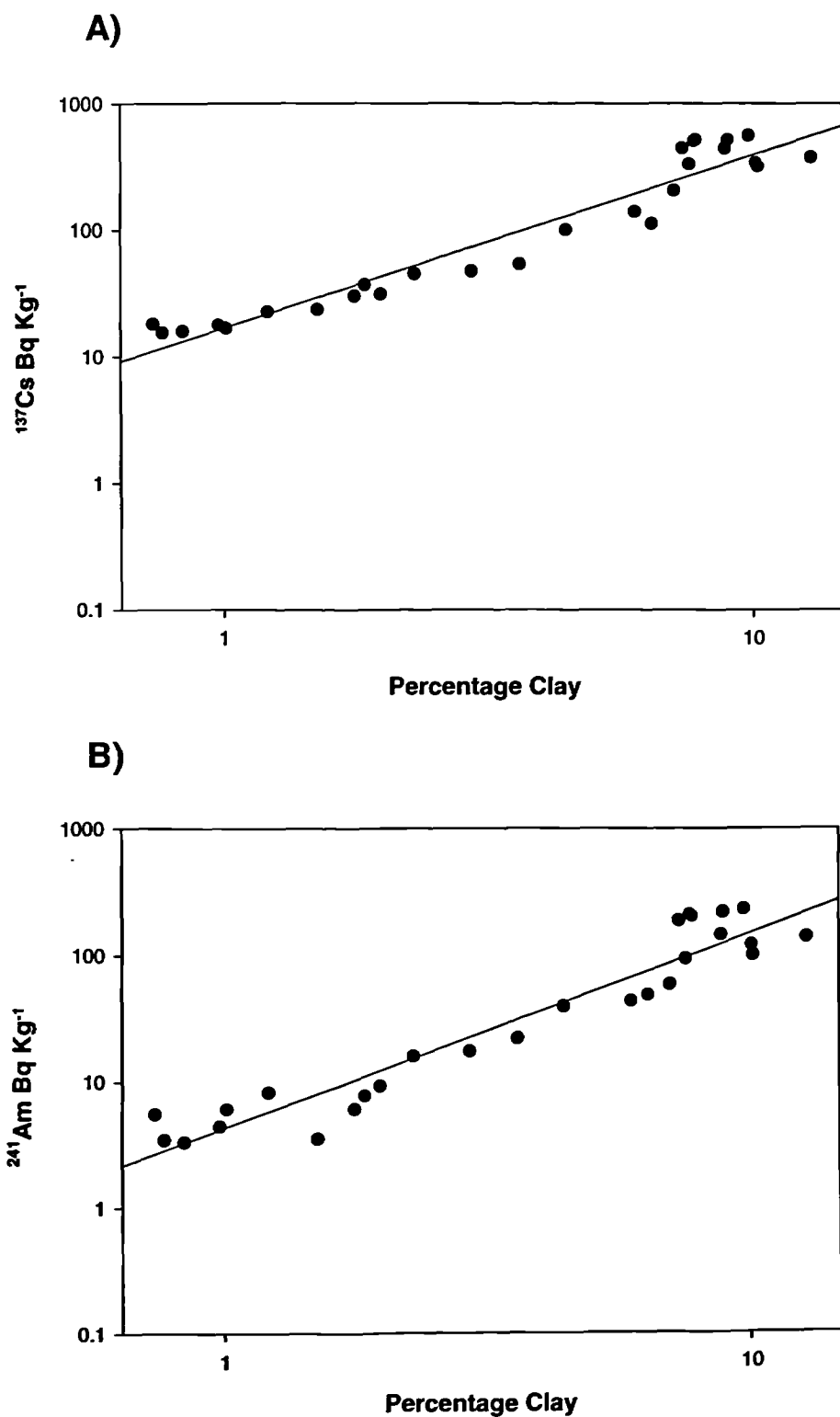
Figure 6.2 Relationship Between ^{137}Cs & ^{241}Am and Percentage Clay of a selection of the 1997 Ribble Intertidal Sediment Samples (r^2=0.927 and 0.869 Respectively)

174

6.3 CALIBRATION OF IMAGERY TO SPECIFIC ACTIVITY (Bq kg^{-1})

6.3.1 Objective

The objective of this section is to convert the clay abundance images, described in the previous chapter, into activity maps of ^{137}Cs and ^{241}Am for the Ribble Estuary intertidal area. The accuracy of the resultant radionuclide maps is firstly assessed by comparison with the actual activities of the sites sampled during image acquisition. Secondly, the estimated activities are compared with samples collected by a recent conventional study of the intertidal sediments of the Ribble Estuary (*i.e.* Brown, 1997). Comparisons with other studies are difficult due to the lack of published detail regarding sampling locations.

6.3.2 Method

Due to the very slight change in the relationship between ^{241}Am and clay content from 1995 to 1997, it was concluded that a combination of both years' gamma analysis results was not suitable for converting the clay abundance maps into radionuclide distribution maps. Instead, the clay abundance image created from the 'dry' 1997 image (Figure 5.27) was calibrated using the relationship between the radionuclides and clay content of the 1997 surface samples (Equation 6.1 & 6.3). Equally, the clay distribution map produced from the 1995 Lytham St Annes image subset (Figure 5.29) was calibrated using the relationship derived from the 1995 surface samples (Equation 6.2 & 6.4).

The ENVI image analysis software was used to calibrate the clay abundance images, producing maps of ^{137}Cs distribution and ^{241}Am distribution within the Ribble Estuary. Comparisons were then made between the radionuclide distribution images and known

175

activity measurements from the Ribble intertidal zone in order to assess the accuracy of the final results.

6.3.3 Results and Discussion

'Dry' 1997 Activity Imagery

Comparison of the estimated and actual activities of the 1997 sample sites confirm that the activity maps created from the 'dry' 1997 image are accurate representations of radionuclide distribution within the intertidal sediments (Figures 6.3 & 6.4). A strong relationship is observed between the actual and the estimated activities for both ^{137}Cs (r^2=0.83, p<0.01) and ^{241}Am (r^2=0.82, p<0.01). When the values are plotted on the same graph, the estimated values are found to parallel the actual activities although there is some slight overestimation (Figures 6.5). It is worth noting, however, that although there is general overestimation, in all cases the actual activity close to the saltmarsh edge is significantly greater than that estimated. This may be a product of misclassification of these sediments in the imagery, possibly due to halite efflorescence in these regions.
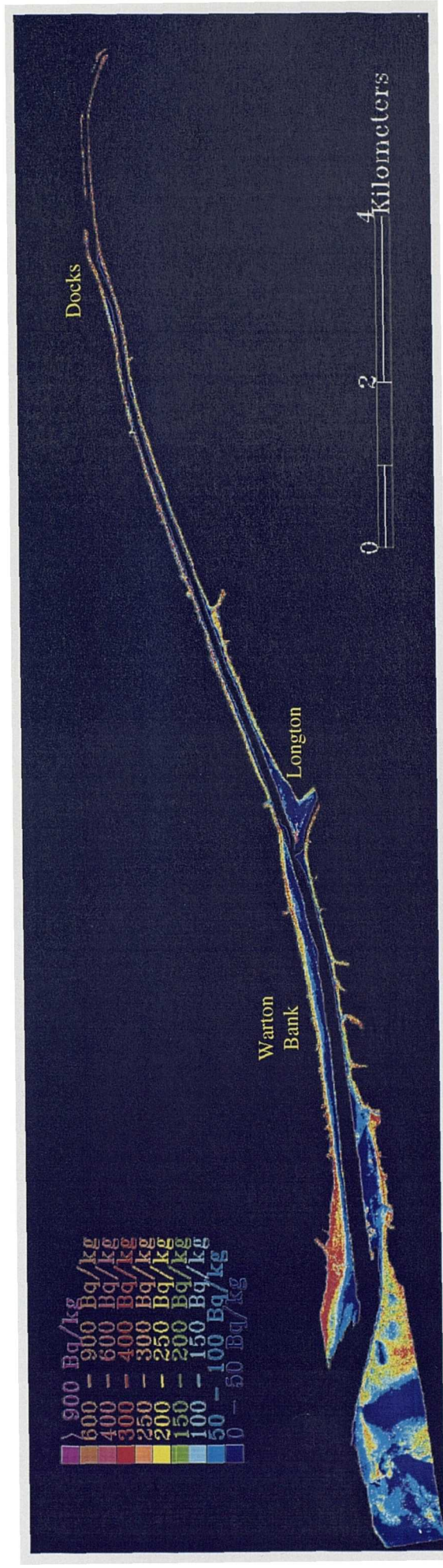
Figure 6.3 ^{137}Cs Distribution Within the Intertidal Sediments of the Ribble Estuary, as Derived from the 'Dry' 1997 Image

177
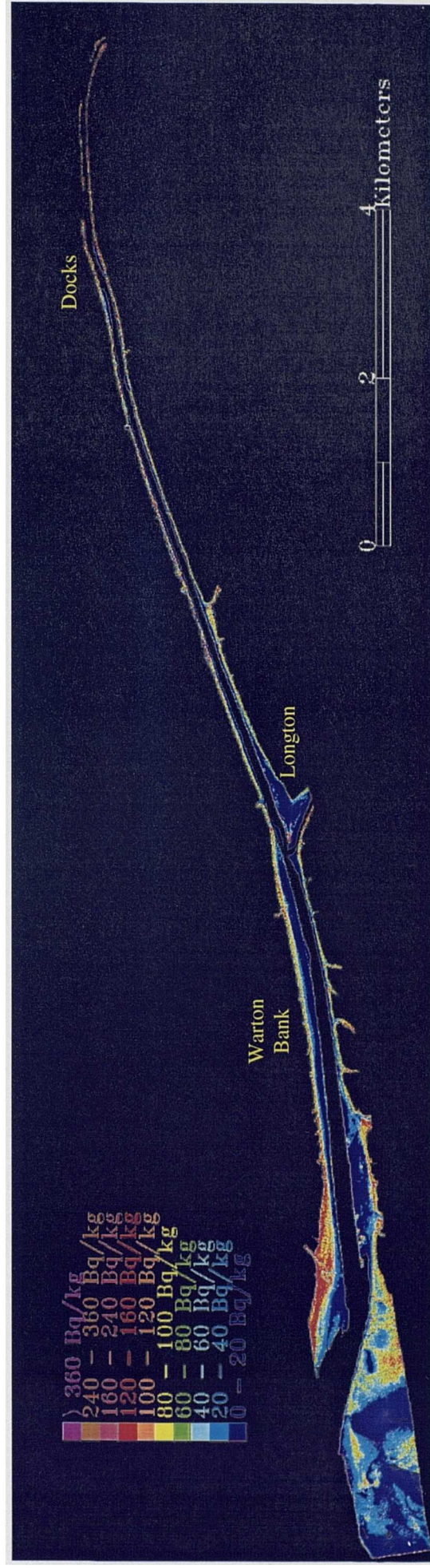
Figure 6.4 ^{241}Am Distribution Within the Intertidal Sediments of the Ribble Estuary, as Derived from the 'Dry' 1997 Image

178
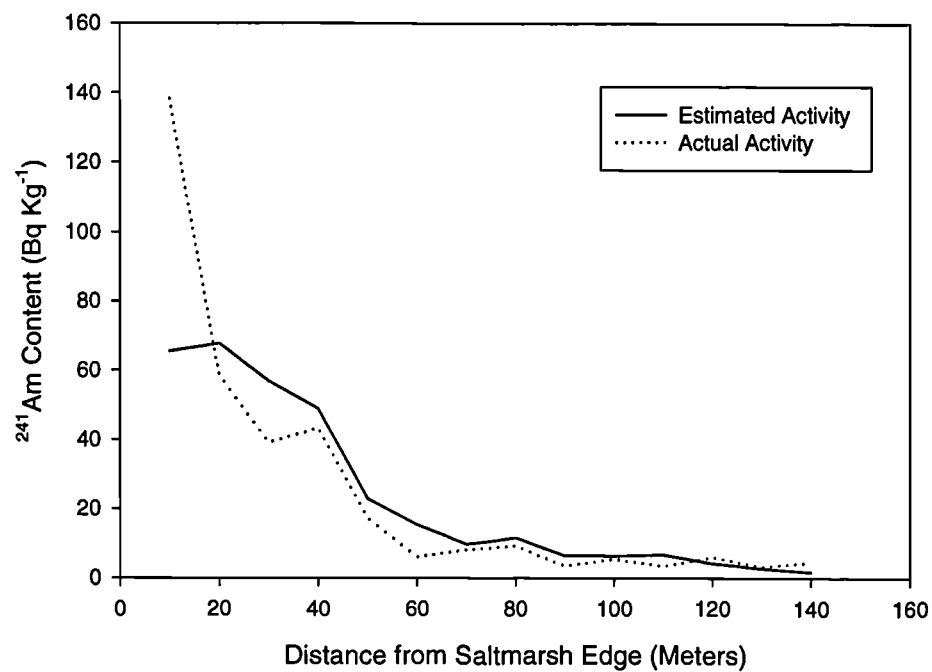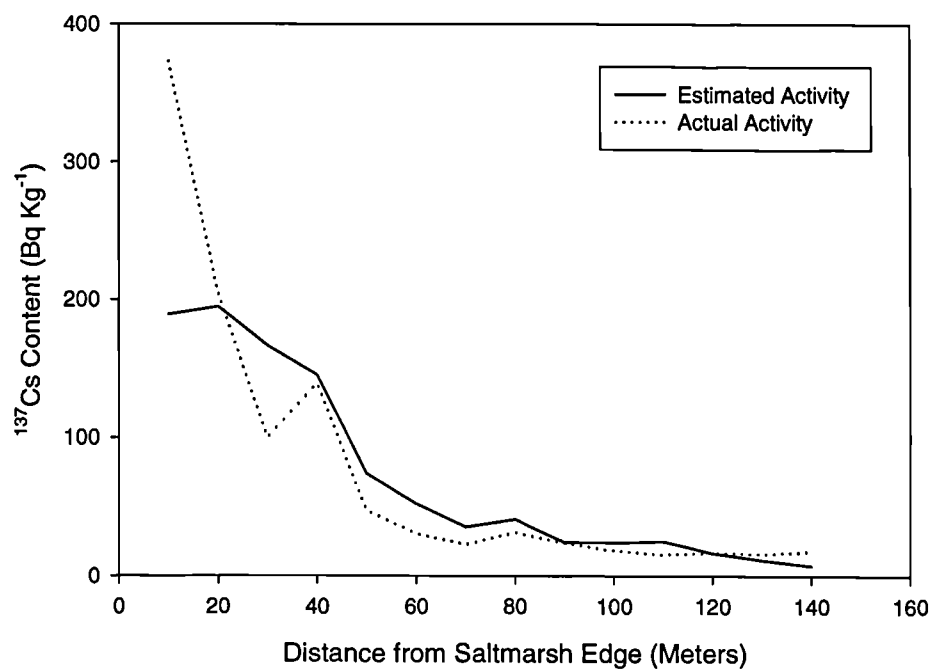
Figure 6.5 Comparison of Estimated and Actual ^{137}Cs & ^{241}Am Activities Along a Sample Transect at Warton Bank (r^2=0.83 and 0.82 Respectively)

Lytham St. Annes Activity Imagery

In contrast, the Lytham St. Annes activity maps are found to be inaccurate representations of the Sellafield-derived radionuclides in the surface sediments of this region (Figure 6.6). No significant relationship was observed between the image estimated activities and the ^{137}Cs (r^2=0.43) and ^{241}Am (r^2=0.45) content of the 1997 sample sites. This may be a product of image misclassification or, more probably, it is a result of using 1997 sample sites to validate 1995 imagery (Section 5.6).
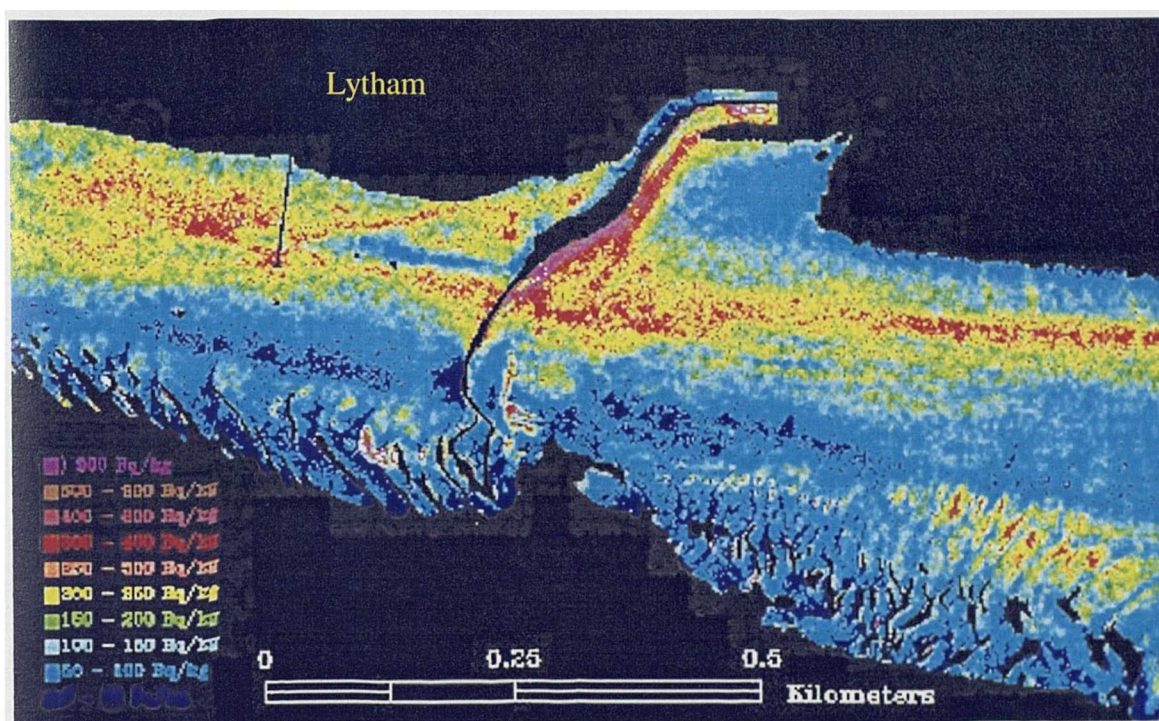
Figure 6.6 ^{137}Cs Distribution Within the Intertidal Sediments of the Lytham St. Annes Intertidal Zone, as Derived from the 1995 Image Subset

Comparisons with Brown's (1997) Results

Nevertheless, any accuracy assessment based on the activities of the 1997 sample sites is inherently biased, as the sediment characteristics of these sites were used to calibrate the initial abundance imagery. Consequently, external sources of information regarding activity levels in the estuary are needed to assess the accuracy of the map. One of the

best external datasets available is that of Brown (1997) who collected monthly (9/6/94 to 14/12/95) surface sediment samples from six locations within the Ribble Estuary (Figure 2.3). Laboratory gamma analysis of these samples demonstrated that the surface intertidal distribution of ^{137}Cs and ^{241}Am is temporally very variable. The best example of this is the ^{137}Cs content of the Penwortham sample site, which had a specific activity of 4.2 Bq kg^{-1} in February 1995 and 729 Bq kg^{-1} in October 1994. To compare results, the approximate locations of the sample sites used in Brown's study (1997) were identified in the ^{137}Cs and ^{241}Am distribution images. An average value for each sample area (approx. 50m^2) was subsequently calculated from the imagery and compared to the surface sample results (Table 6.2 & 6.3). It was found that all the image-derived estimates lay within the range of activities observed at the sample sites, and most of the estimates were comparable to the approximate May/June averages. Whilst this does not completely validate the activity images, it does show that the findings are consistent with the results of other studies.

As a consequence of the temporal variability of the surface activity distributions, observed by Brown (1997) and other studies such as Assinder *et al.* (1997), it is concluded that only samples collected during image acquisition can be used to validate accurately any subsequent activity maps. As briefly stated earlier, this is a possible explanation of the apparent inaccuracy of the Lytham St. Annes activity maps, which were created from a 1995 image and validated using 1997 sample sites. The results from other radionuclide studies may be used, however, to ensure the estimated activities are not beyond the range of expected values for this environment. In addition, these studies provide an understanding of the temporal representativeness of any image-derived radionuclide distribution map.

Table 6.2 Comparison of Surface Sediment ^{137}Cs Activities Measured by Brown (1997) and Average Activity Estimates for the Same Locations Derived from the ^{137}Cs Distribution Map

Sample Location	Surface ^{137}Cs Activities (Brown, 1997)			Average ^{137}Cs Estimated Activities at Sample Locations	
	Minimum	Maximum	May/June Average	^{137}Cs Activity (Bq Kg^{-1})	Standard Deviation
Lytham	60	581	366	178.25	24.45
Nazemouth	358	760	429	480.46	210.87
Docks	185	656	392	465.89	127.76
Warton	197	939	406	263	91.03
Clifton	158	633	298	265.33	66.58
Penwortham*	4.2	729	521	592.33	139.96

Table 6.3 Comparison of Surface Sediment ^{241}Am Activities Measured by Brown (1997) and Average Activity Estimates for the Same Locations Derived from the ^{241}Am Distribution Map

Sample Location	Surface ^{241}Am Activities (Brown, 1997)			Average Estimated Activities at Sample Locations	
	Minimum	Maximum	May/June Average	^{241}Am Activity (Bq Kg^{-1})	Standard Deviation
Lytham	24	243	129	78.61	13.87
Nazemouth	121	315	187	200.88	76.46
Docks	62	259	195	177.56	52.77
Warton	75	366	142	98.21	37.92
Clifton	73	297	102	108.36	42.98
Penwortham*	0	383	288	237.11	63.15

* The actual Penwortham Site sampled by Brown (1997) is not included in the imagery, so an image area close to sample site was used instead.

6.4 TOTAL ^{137}Cs AND ^{241}Am INVENTORIES FOR THE INTERTIDAL AREAS OF THE RIBBLE ESTUARY

6.4.1 Introduction

A number of studies within the Ribble Estuary have attempted to estimate the total intertidal inventories for certain Sellafield-derived radionuclides (Section 2.4.4). However, these estimates are generally dependent on interpolating between isolated cores (*e.g.* Brown, 1997), which potentially introduces substantial spatial errors. In contrast, this project produced total inventory estimates for ^{137}Cs and ^{241}Am from the spatially accurate surface activity images produced from the ATM imagery.

6.4.2 Inventory Assumptions and Calculations

Since no intertidal sediment cores were collected during the 1997 image acquisition these inventory estimates are reliant on broad assumptions regarding sediment depth, sediment density and activity distribution with depth. Based primarily on the work by Brown (1997) it was assumed that the average depth and density of the Ribble Estuary intertidal sediments were 0.6m and 1600kg/m^3 respectively. Within the calculations it was also necessary to assume that the surface activity estimates were representative of the activity distribution with depth.

The inventories were calculated by multiplying the total surface values for the intertidal areas contained within the activity images against the total sediment mass in a pixel area (1.75m x 1.75m) based on the above assumptions. This was calculated for both ^{241}Am and ^{137}Cs.

6.4.3 Total Inventories

From the above calculations it is estimated that 0.62TBq of Sellafield-derived ^{137}Cs and 0.22TBq of ^{241}Am activity exists within 92.1km^2 of the Ribble Estuary intertidal regions. This represents the majority of the total intertidal area of the Ribble Estuary, which is estimated at 106.7km^2 by Buck (1993).

In contrast, for a much smaller intertidal area (7.8km^2) Brown (1997) estimated a ^{137}Cs inventory of 3.115TBq. This suggests that the image-based calculations may be considerably underestimating the total radionuclide inventories of the intertidal regions. The most probable source of error for the image-based inventories is the assumption that the surface activities are representative of activities at depth. In contrast to this assumption, Brown (1997) demonstrated that the Sellafield-derived activities could increase considerably with depth (Table 2.4). In addition, the vertical intertidal sediment profiles produced by Brown (1997) suggest that the surface activities are only representative of the top 5-10cm of intertidal sediment. As a result, it is suggested that a more reliable image-derived inventory may be made for this top layer of intertidal sediment. This is calculated at 0.052TBq of ^{137}Cs and 0.018TBq of ^{241}Am for 92.1km^2 of the Ribble Estuary intertidal regions. It is implied that this represents the total activity present in the top 'erodable' layer of the intertidal sediment.

6.5 DISTRIBUTION OF SURFACE INTERTIDAL RADIOACTIVITY

6.5.1 Introduction

It has been concluded that the activity images are an accurate representation of surface Sellafield-derived radionuclide distribution within the Ribble Estuary for May 30th

1997. The distributions of ^{137}Cs and ^{241}Am in the surface sediments are found to be nearly identical, due to the strong relationship of both with percentage clay content. The aim of this section is to describe the variations of these radionuclide activities across the intertidal areas of the estuary.

6.5.2 Radionuclide Distribution

Inner Estuary

In the inner estuary, from Penwortham to Hutton Sands (Figure 2.1), the distribution of ^{137}Cs and ^{241}Am is very distinctive (Figure 6.7). In broad terms, a narrow strip of higher activity sediments runs parallel to an equally thin strip of low activities on both sides of the main channel. The areas of higher activity (^{137}Cs ~ 330 Bq kg^{-1}, ^{241}Am ~ 120 Bq kg^{-1}) correspond to the sloped mud regions furthest from the main channel. The areas with the lowest radionuclide contents within the inner estuary are the well-washed sands of the exposed sandbanks with average ^{137}Cs and ^{241}Am activities of 15 and 3 Bq kg^{-1} respectively (SD 3495 4290). The highest activities (^{137}Cs ~ 1000 Bq kg^{-1}, ^{241}Am ~ 500 Bq kg^{-1}) are observed within the narrow-sloped intertidal areas near Penwortham (SD 3526 4290) and along the banks of the small channels that join the main channel (e.g. SD 3463 4281). A general decrease in surface activities exists from the east of the inner estuary to the west, although there are intermittent activity increases close to the mouths of small saltmarsh creeks. Polygonated mud regions in the inner estuary have relatively low surface activities in the imagery (^{137}Cs ~ 50 Bq kg^{-1}, ^{241}Am ~ 20 Bq kg^{-1}), though this is likely to be a product of image misclassification (SD 3465 4282).

185
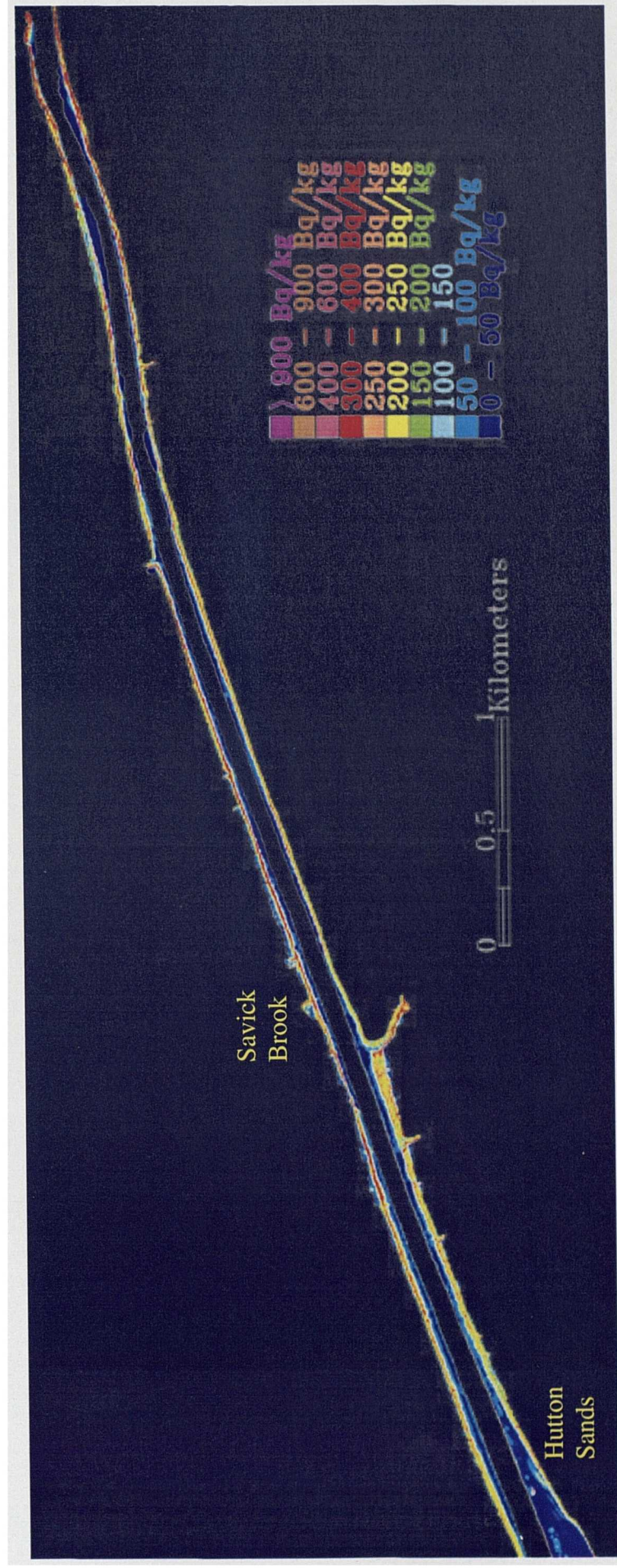
Figure 6.7 The ^{137}Cs Distribution Within the Inner Ribble Estuary, as Determined from the ATM Imagery

Middle Estuary

The radionuclide distribution changes very quickly from the inner estuary to the middle estuary, due primarily to the increased extent of the intertidal zones (Figure 6.8). The sloped mudflat areas close to the saltmarsh edge are still the regions with the greatest surface activities (^{137}Cs ~ 250 Bq kg^{-1}, ^{241}Am ~ 90 Bq kg^{-1}), although these activities are generally much lower in comparison to the inner estuary. The distribution of radionuclides within the middle estuary mudflats is also more closely related to the distribution of creeks. The flat sandy areas are significantly larger in this part of the estuary and, consequently, a more dominant feature in the activity map. As expected, the surface sediments of these regions have low radionuclide contents, with the majority of the ^{137}Cs activities less than 50 Bq kg^{-1}. However small patches of higher activities may be observed within the sand-dominated regions; these are possibly areas of concentrated mud draping (SD 3399 4261). The change in activity from the sloped mudflats to the flat sandy areas is also very distinct in the middle estuary, however a gradation in values is more obvious here in comparison to the inner estuary. The highest activities (^{137}Cs ~ 900 Bq kg^{-1}, ^{241}Am ~ 400 Bq kg^{-1}) are observed within the narrow southern intertidal bank of the Douglas River, that joins the Ribble Estuary at Longton (SD 3435 4265). Although only a small part of the tributary lies within the imagery, these activities indicate that this river is a very important area for future radionuclide monitoring studies. The main sources of error in the imagery are the channel walls and the stone-topped ridges in the estuary, which are misclassified as areas of high activity (e.g. SD 3433 4269). Equally, some small polygonated areas at the edge of the saltmarsh have very unlikely low activity values in comparison to the surrounding mud (e.g. SD 3406 4266). Finally, a large pool of surface water at the tip of the Longton intertidal area (SD 3432 4268) has very high relative activity values (^{137}Cs ~ 1000 Bq
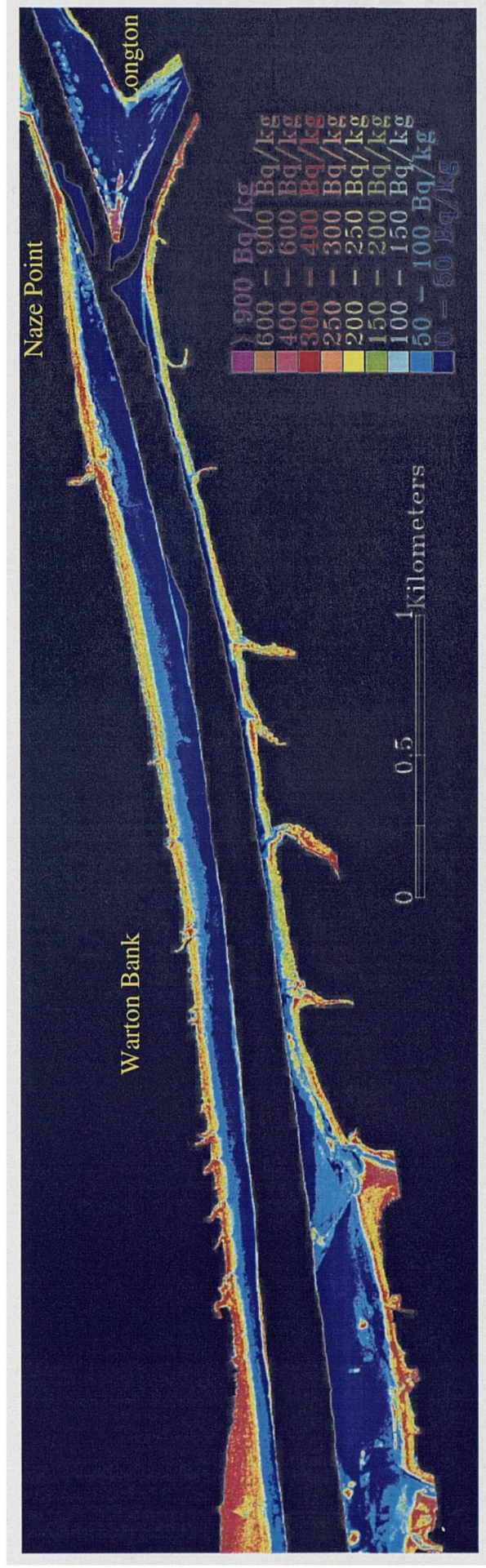
Figure 6.8 The ^{137}Cs Distribution Within the Middle Ribble Estuary, as Determined from the ATM Imagery

188

kg^{-1}, ^{241}Am ~ 500 Bq kg^{-1}). This may be a product of image misclassification, or possibly this area contains a substantial amount of fine sediment, from the nearby Douglas River, which has settled out in the pool as the tide retreated.

Outer Estuary

The outer estuary intertidal area is predominantly made up of large tidal flats that fill the mouth of the Ribble Estuary. Unlike the more easterly parts of the estuary, the intertidal areas north and south of the main channel have very different radionuclide distributions (Figure 6.9 & 6.10). In the north, a large mudflat with relatively high activities (^{137}Cs ~ 250-500 Bq kg^{-1}, ^{241}Am ~ 90-200 Bq kg^{-1}) is located close to the mouth of a large saltmarsh creek (SD 3381 4264). Within this mudflat slightly higher values are found to the west, although the greatest activities (^{137}Cs ~ 1000 Bq kg^{-1}, ^{241}Am ~ 450 Bq kg^{-1}) are observed within the banks of the creek (SD 3383 4266). In contrast, the sand-dominated areas close to the main channel have very low ^{137}Cs activities, on average less than 50 Bq kg^{-1}.
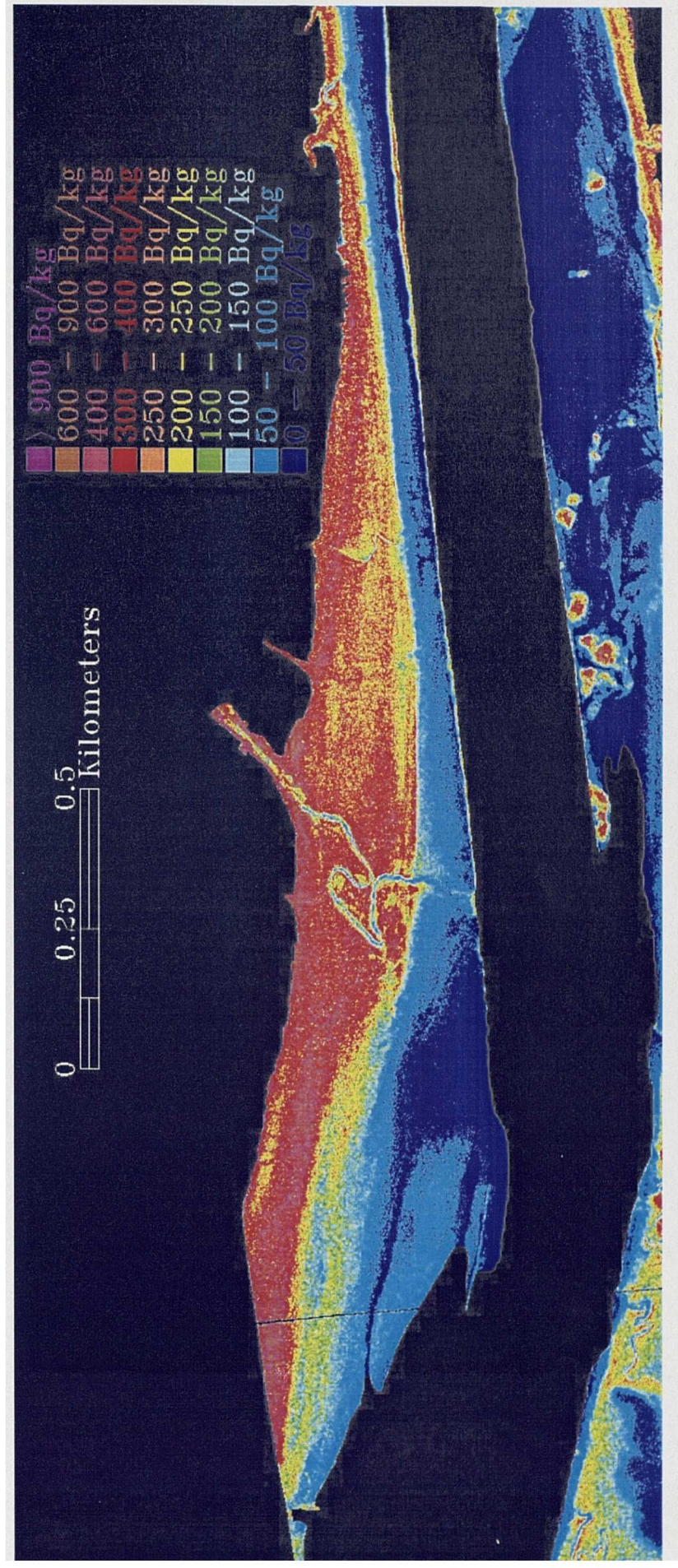
Figure 6.9 The ^{137}Cs Distribution Within the Northern Intertidal Zone of the Outer Estuary, as Determined from the ATM Imagery

190
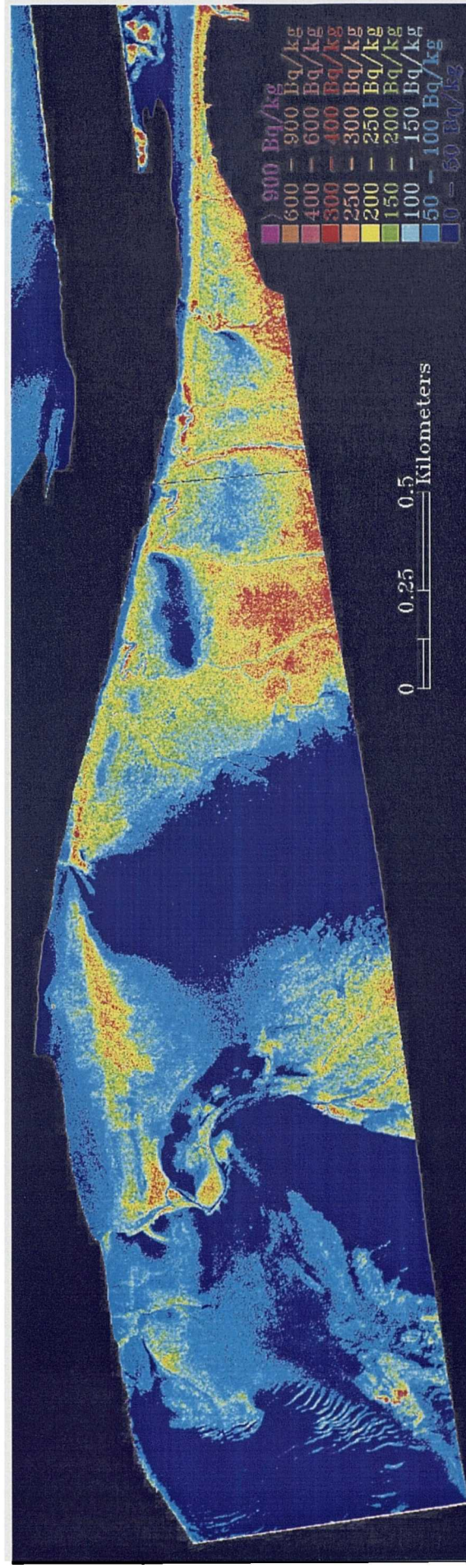
Figure 6.10 The ^{137}Cs Distribution Within the Southern Intertidal Zone of the Outer Estuary, as Determined from the ATM Imagery

191

The distribution of Sellafield-derived radionuclides is completely different in the surface sediments of the southern outer estuary (Figure 6.10). Large sandbanks with low ^{137}Cs activities (~ 50 Bq kg^{-1}) dominate the west, and within these flats small pockets of higher activities (^{137}Cs ~ 250 Bq kg^{-1}, ^{241}Am ~ 90 Bq kg^{-1}) may be observed (SD 3355 4258). To the east, the intertidal area has relatively high surface activities (^{137}Cs ~ 150-400 Bq kg^{-1}, ^{241}Am ~ 50-150 Bq kg^{-1}) with circular central areas (SD 3370 4259) of low activity (^{137}Cs ~ 30 Bq kg^{-1}, ^{241}Am ~ 10 Bq kg^{-1}). The intertidal structure observed in the middle and outer estuary, of a sloped mud-dominated area parallel to a flat sand-dominated area no longer exists in the southern outer estuary. Instead, the distribution of relatively high radionuclide contents is closely related to the position of the saltmarsh creeks that dissect the tidal flats and is consequently more complex.

Lytham St. Annes

The accuracy of the activity maps produced from the Lytham St Annes image subset is uncertain, due to difficulties in validation and calibration (Section 6.3.3). However, a brief description of the estimated radionuclide distribution within these areas is included for completion (Figure 6.6). As expected, the areas close to the main channel have relatively low activities (^{137}Cs ~ 50 Bq kg^{-1}, ^{241}Am ~ 30 Bq kg^{-1}), whilst close to the large saltmarsh creek (SD 3370 4267) an area of relatively high values exists (^{137}Cs ~ 300 Bq kg^{-1}, ^{241}Am ~ 130 Bq kg^{-1}). This area of high activity extends east and west as a narrow band through the centre of the intertidal area. The highest values (^{137}Cs ~ 1100 Bq kg^{-1}, ^{241}Am ~ 400 Bq kg^{-1}) are recorded on the easterly bank of the saltmarsh creek (SD 3369 4266), although some abnormally large values appear near the large sand ridges close to the main channel (SD 3368 4264). These anomalous values may be a product of sediment shadowing caused by the low sun-angle and the height of the sand

mega-ripples in that area. Similarly the sediments covered by dense microphytobenthos mats (SD 3368 4266) have considerably lower activities (^{137}Cs ~ 70 Bq kg^{-1}, ^{241}Am ~ 40 Bq kg^{-1}) than the surrounding mud, suggesting the activities are underestimated in the imagery. Finally, the mud closest to the saltmarsh edge, especially east of the large creek (SD 3372 4267), has relatively low activities (^{137}Cs ~ 90 Bq kg^{-1}, ^{241}Am ~ 50 Bq kg^{-1}). This may be due to misclassification of polygonated mud.

6.6   SOURCES AND SINKS WITHIN THE INTERTIDAL ENVIRONMENT

6.6.1   Introduction

The activity images indicate that the Sellafield-derived radionuclides have a very complex distribution within the surface intertidal sediments of the Ribble Estuary. This distribution has also been shown by earlier studies to be temporally very variable (Brown, 1997; Assinder *et al.*, 1997). Consequently an understanding of the deposition and accretion processes behind the radionuclide distribution is of fundamental importance. In this section, the activity maps are used to identify potential sources and sinks of radionuclides within the Ribble Estuary. In particular, the influence of estuarine morphology and microphytobenthos cover on radionuclide distribution is examined.

6.6.2   Activity Distribution and Intertidal Morphology

Longitudinal Activity Trend

From an in-depth point sampling study of the Ribble Estuary Brown (1997) stated that no longitudinal trend in activities existed. However, examination of the image-derived radionuclide maps reveals a substantial although not linear increase in average intertidal

activities from the mouth of the estuary towards Preston (Figure 6.11). Within this

overall trend there are areas of anomalous values *e.g.* the relatively high surface

radionuclide contents west of Warton Bank (Figure 6.9). Consequently, it is concluded

that a general, although not absolute, longitudinal increase in activities exists from the

mouth of the Ribble Estuary towards Preston, contrary to the findings of Brown (1997).

This implies therefore that point sampling techniques lack the spatial representativeness

to make definitive statements regarding large-scale distributions.
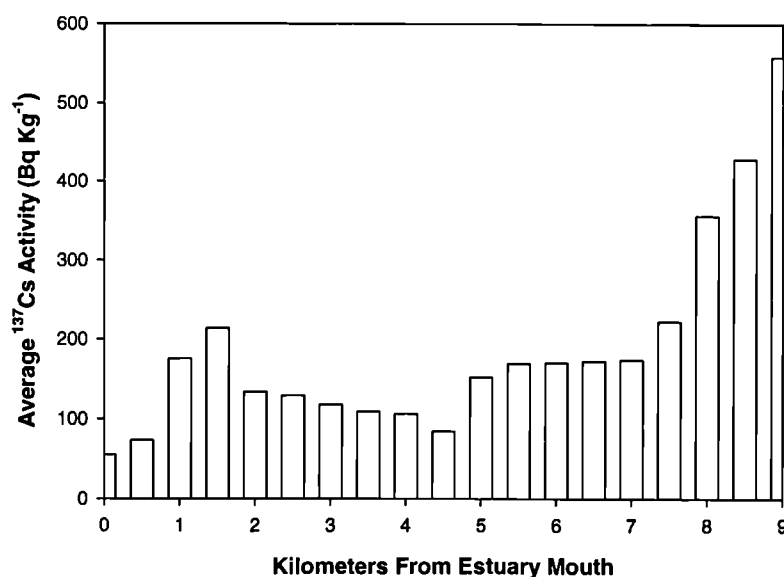
Figure 6.11 Longitudinal Trend in Average Surface [137]Cs Activities from the Mouth of the Ribble Estuary Towards Preston

Proximity to Main Channel

From the activity maps it appears that an important factor behind radionuclide

distribution is the proximity of the surface sediments to the main channel. Throughout

the estuary, excluding some areas to the extreme west, the lowest activities are located

close to the main channel, and the highest are located close to the saltmarsh. The

sediments close to the main channel are submerged and consequently reworked for

longer time periods, resulting in the fine radionuclide-rich sediments remaining in suspension (Section 2.2.3). In contrast, the sediments closest to the saltmarsh are only completely submerged at high-tide, a period of very low water velocities, allowing the fine sediments in the slack water to settle. This is enhanced where the mudflats are sloped rather than flat, as this further reduces the period of inundation of these sediments. As a result, the sloped mudflats close to the saltmarsh edge are acting as a large sink for Sellafield-derived radionuclides in the Ribble Estuary, as observed in the activity images.

Proximity to Saltmarsh Creeks

As stated earlier, within the longitudinal trend in activities surface sediments with anomalous high values are observed. In general this occurs at the interface of the intertidal zone and saltmarsh creeks. An example of this is the extensive area of relatively high radionuclide contents close to the large saltmarsh creek in the north bank of the outer estuary (Figure 6.9). The most plausible explanation for these anomalous activity distributions is that the creeks are resuspending fine radionuclide-rich sediments in the saltmarsh and depositing them as they enter the intertidal environment. Subsequent tidal inundations rework and spread these sediments across the nearby intertidal regions. The suggestion that creeks are acting as radionuclide sources to the estuary is supported by the relatively high activities observed along their banks as they enter the intertidal zone. The influence of the creeks on activity distribution is best observed in the large sand-dominated tidal flats of the outer estuary (SD 3355 4258), where relatively high surface activities are observed close to the banks of the saltmarsh creeks (Figure 6.12). In this area, the creeks are a substantial source of Sellafield-derived radionuclides to a region of otherwise well-worked surface sediment with low

activities. Similarly, it is suggested that the Douglas River is behaving like a large creek, supplying fine radionuclide-rich sediment to the main estuary as the tide retreats (Figure 6.13). This may explain the anomalous high values observed at Naze Point, opposite the mouth of the tributary (SD 3433 4271).
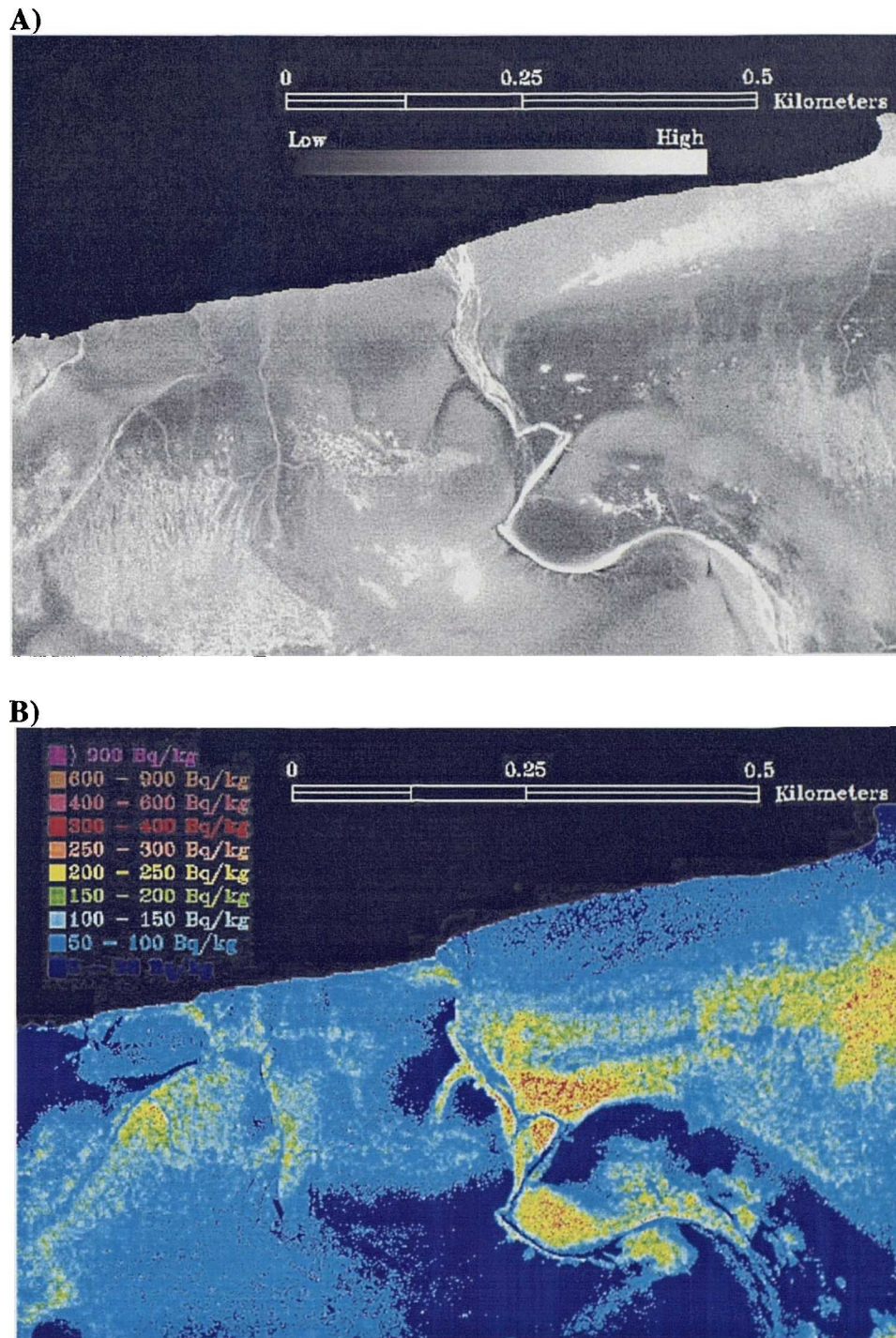
Figure 6.12 Subset of the A)'Dry' 1997 Moisture Abundance Image and B)Outer Estuary Activity Image, Illustrating the Surface Distribution of [137]Cs Relative to a Saltmarsh Creek in the Outer Estuary

196
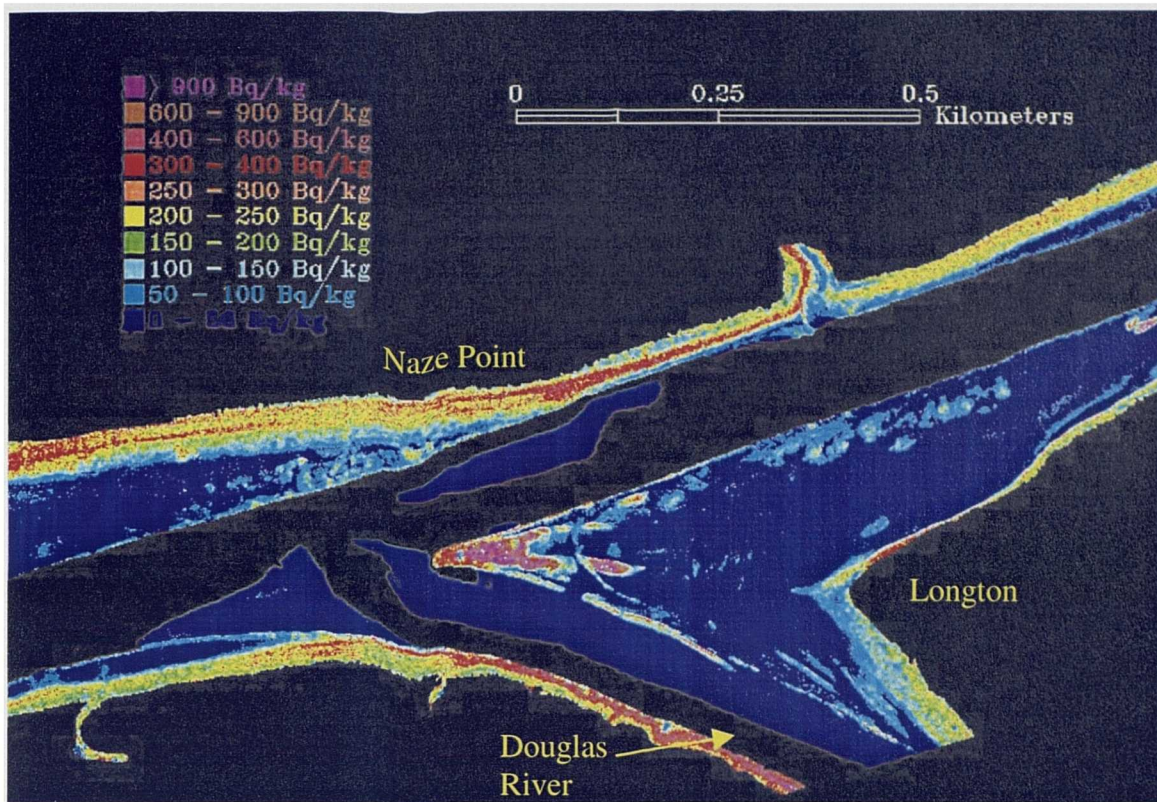
Figure 6.13 – Distribution of ^{137}Cs Activity in the Douglas River Region

6.6.3 Influence of Microphytobenthos Cover on Activity Distribution

Cyanobacteria and diatoms are a common feature in estuarine intertidal environments. They play an important role in the accretion of saltmarshes by stabilising the sediment and building up humus (Section 2.2.3). Surface sediments covered by large microphytobenthos mats are more stable than the surrounding intertidal sediments (Sutherland *et al.*, 1998). Consequently, it is inferred that these areas are acting as stable sinks within the estuary for Sellafield-derived radionuclides. Nevertheless, whilst these surface sediments are relatively stable, subsequent stormy tidal conditions may strip the microphytobenthos mats from the intertidal areas and, consequently, the previous sinks may be changed into sources of elevated activities.

6.6.4 Implication of Findings

The Sellafield-derived radionuclide distribution in the estuary has been shown to be both spatially and temporally complex. On the basis of this, two fundamental conclusions can be drawn which have important implications for future monitoring studies. Firstly, due to the spatial complexity of the activity distribution, *in situ* sediment sampling will inevitably fail to produce radionuclide maps of sufficient spatial detail to incorporate all the localised variations. For example, conventional mapping of the estuary would probably fail to spatially characterise the local and considerable influence of the saltmarsh creeks on the overall activity distribution. Secondly, the activity maps produced in this project depict only the surface radionuclide distribution for the date of image acquisition i.e. May 30th 1997. Consequently, it is impossible to determine how temporally representative the radionuclide estimates are directly from a single image.

These implications suggest that future studies aiming to characterise both the spatial and the temporal variability of surface activities within the Ribble Estuary need to use a series of airborne images collected at regular intervals over a one year period. This would also lead to a better understanding of the fundamental processes behind the surface distribution of radionuclides. The conspicuous limiting factor for such a study would be the availability of suitable cloud-free imagery collected during ideal low-tide conditions.

6.7 SUMMARY

It has been demonstrated that accurate maps of surface Sellafield-derived radionuclide distributions can be created from airborne imagery of an estuary at low tide. This is fundamentally based on the very strong associations between ^{137}Cs & ^{241}Am and percentage clay content, which have been shown to exist in the Ribble Estuary both in 1995 and 1997. From these maps an appreciation of the spatial complexity of the radionuclide distribution has been achieved. Equally, some of the dominant processes behind the activity distribution have been identified, making an important contribution to the understanding of radionuclide source and sink locations within the estuary. Finally, the River Douglas has been identified as an area within the estuary that requires further investigation and general recommendations have been made for future remote sensing campaigns.

In the next chapter, the activity distribution results of this project are discussed further and compared with previous studies. The value of this methodology is also evaluated and possible improvements are outlined.

7. DISCUSSION AND CONCLUSIONS

7.1   INTRODUCTION

A primary objective of many estuarine radionuclide studies is the collection of point samples from which extensive interpretations regarding surface intertidal activity distribution are made (Aston and Stanners, 1982; Assinder *et al.*, 1997; Brown, 1997). However, an estuary is a spatially complex and dynamic environment that is subject to a range of fluvial and marine processes. Consequently, interpolation between isolated point samples introduces gross spatial errors in the characterisation of the elaborate activity distributions. In addition, point sampling is a costly and labour intensive monitoring procedure, which generally incorporates a considerable time interval between sampling and the production of the final results. This approach also experiences considerable problems when sampling dangerous or inaccessible areas, therefore potentially biasing the final results. In conclusion, there is need for an alternative radionuclide monitoring tool, which can provide rapid, inexpensive synoptic coverage on a scale appropriate for geomorphologic investigations.

In an attempt to address the above requirements, this study examined the applicability of airborne remote sensing for mapping surface Sellafield-derived radionuclide distributions in the Ribble Estuary. This chapter examines how successfully that objective has been fulfilled. Initially, the background to the project is summarised and then its results are analysed and placed in the context of previous and complementary research. Subsequently, the limitations of this work and potential improvements to the overall methodology are outlined. A number of potential future applications of this

technique are then proposed and, finally, the main conclusions of this project are extracted and summarised.

7.2 IMPLICATIONS AND CONTRIBUTIONS

7.2.1 Introduction

Airborne remote sensing of surface radionuclide activities is dependent on a number of relationships, each of which had to be defined for the study of the Ribble Estuary. As a result, a number of important conclusions can be made both from the defining of the relationships and the subsequent results. These findings range from the sediment-radionuclide associations to the spectral characteristics of intertidal sediments. They also include an appreciation of the spatial complexity of the surface radionuclide distribution. In this section, these findings are outlined and compared to the results of other studies.

7.2.2 Background

A wide range of conventional radionuclide monitoring studies has been carried out in the estuaries that interface with the Irish Sea (Aston and Stanners, 1981; Assinder *et al.*, 1997; Clifton *et al.*, 1997). The majority of these studies examine the distribution of activity with depth, radionuclide lag times and the relationship of sediment characteristics with various radionuclides. Those studies that look at the surface distribution of activities generally do so on a very large scale *i.e.* interpolating between widely distanced point samples. In the Ribble Estuary, Assinder *et al.* (1997) and Brown (1997) monitored surface intertidal radionuclide distributions using point sampling and broadly identified a number of high activity regions (*e.g.* Penwortham and

201

Savick Brook). Brown (1997) also examined the temporal variability of these surface activities. However, it was evident that the results of these studies were spatially unrepresentative due to the need to interpolate between isolated sample sites. Consequently, neither study adequately defined the spatial distribution of surface radionuclides within the estuary, nor the processes that control the temporal changes in activity.

Remote sensing is an alternative monitoring technique, which allows isolated sample measurements to be placed into a spatial context. Until now, airborne gamma spectrometry was the only remote sensing technique capable of detailed monitoring of intertidal activity distributions (Section 2.6.2). This method was used to survey the activities present in a 20 x 12km rectangular box centred about the Ribble Estuary (Sanderson et al., 1993). However, the spatial resolution of this technique (200-400m) is limited in comparison to the resolution available from airborne sensors such as the Daedalus ATM scanner (1.75m). This caused expansive activity features to be exaggerated and small features, e.g. the intertidal sediments 1km east of Savick Brook, to go undetected by the baseline survey. Consequently, it was evident that ATM imagery may be a more appropriate dataset for identifying and mapping small-scale activity sinks and sources in the estuarine environment. However, radionuclides cannot be directly detected by a multispectral scanner, instead this approach is dependent on a relationship between the surface activities and a spectrally identifiable surface characteristic.

A number of studies at intertidal sites along the Irish Sea coast, including the Ribble Estuary, have recognised very strong relationships between the Sellafield-derived

radionuclides, ^{137}Cs and ^{241}Am, and the grain-size of the intertidal sediment (Aston and Stanners, 1981; Assinder et $al.$, 1985; Assinder et $al.$, 1997; Brown 1997). This is a result of ^{137}Cs and ^{241}Am being preferentially adsorbed onto the clay minerals of the sediment (Section 2.4.2). The spatial and temporal stability of these relationships enables accurate activity estimates to be derived from sediment grain-size measurements. Equally, if remote sensing could be used to create a map of surface grain-size distributions, this could be converted into a map of surface Sellafield-derived activities. Consequently, these relationships provide an indirect valid means of mapping the surface radionuclide distribution through high spatial resolution remote sensing.

A range of remote sensing studies have previously attempted to map intertidal sediment facies with very variable results (Folving, 1984; Bartholdy and Folving, 1986; Doerffer and Murphy; 1989; Jacobsen and Neilson, 1990; Yates et $al.$, 1993). However, all of these studies used satellite rather than airborne data and this introduced a number of substantial problems. Firstly, the spectral range and resolution of some of the satellite data types are too limited to recognise the spectral influences of grain-size. This is very evident in the unsuccessful attempt by Bartholdy and Folving (1986) to map the intertidal flats of the Wadden Sea, Netherlands, using the coarse spectral bands of Landsat MSS data (Table 2.7). Secondly, the spatial resolution of satellite data is too low to characterise sufficiently the very variable sediment distribution within the intertidal regions. This is demonstrated by the coarse sediment classification achieved by Yates et $al.$ (1993) during a study of The Wash, England, using 30m resolution Landsat TM data. Finally, the poor temporal resolution of satellite data increases the difficulty of obtaining cloud-free imagery of an estuary at a particular tidal state. For example, Populas et $al.$ (1995) found that during one five-month period only one of the

203

seven available SPOT images of the Loire Estuary, France, coincided with low-tide conditions. This temporal problem is enhanced when the satellite imagery needs to be collected after a particular period of intertidal exposure. To summarise, the most important conclusion that can be made from these previous studies is that satellite data are not suitable for detailed mapping of intertidal sediment distributions within an estuary. In contrast, airborne remote sensing enables high spatial and spectral resolution data to be collected of a particular environment at short notice. Consequently, this is ideal for estuarine intertidal studies that require cloud-free imagery during specific low-tide conditions.

The results of previous remote sensing studies can also be an aid in the selection of a suitable image classification technique (Cross *et al.*, 1991; Yates *et al.*, 1993; Donoghue *et al.*, 1994; Atkinson *et al.*, 1997; Haguenin *et al.*, 1997). 'Hard' classification techniques define each pixel as a single cover type, this is not suitable for the very variable and gradational intertidal environment. In contrast, 'soft' classifiers allow the intertidal sediments to be mapped on a sub-pixel basis producing individual distribution maps for each cover type. Consequently, these techniques have significantly outperformed 'hard' classifiers when attempting to map intertidal environments (Yates *et al.*, 1993). In particular, Linear Mixture Modelling was identified from previous studies as a 'soft' classifier that performed well in intertidal studies and was suited for use in this project (Section 3.6.1)

In summary, it is evident that a number of substantial conclusions can be drawn from previous studies:

1. Conventional monitoring is generally unsuitable for characterising the spatial complexity of surface radionuclide distributions in an estuary.

2. The spatial resolution of airborne gamma ray surveys is too low for accurate mapping of surface radionuclides in intertidal environments.

3. A need exists for a synoptic tool that can monitor surface radionuclide distributions on a geomorphic scale, allowing sources and sinks within the estuarine environment to be identified.

4. Airborne remote sensing, combined with a sub-pixel classifier such as Linear Mixture Modelling, can potentially satisfy this requirement by providing extensive high spatial resolution (1.75m) maps of intertidal sediment grain-size distribution.

5. Strong relationships exist between the well-mixed Sellafield-derived radionuclides and surface sediment grain-size in the Ribble Estuary. These associations can be used to convert grain-size distribution images into activity maps for the estuary.

6. This is a unique approach to monitoring surface radionuclide concentrations. Consequently, direct comparison with similar studies in other Irish Sea estuaries is difficult.

7.2.3 Spectral Characterisation of Sediments

A strong positive relationship was observed between ATM reflectance and percentage sand content of intertidal sediments (Table 4.3). A similar though negative association was identified between the ATM reflectance and percentage clay content. This supports

the results of earlier reflectance studies, which found an increase in reflectance with grain-size (Irons *et al.*, 1989; Tyler *et al.*, 1995; Bryant *et al.*, 1996). The strongest associations were identified between ATM bandwidths 9 and 10 and sand content (r^2=0.515 & 0.611 respectively), although nearly all the bandwidths had a significant relationship. Based on this, it was concluded that the best estimate of sediment grain-size would be achieved using all ten ATM bandwidths, rather than any smaller selection. This was supported by the results of the spectra PCA analysis (Figure 4.4), which demonstrated that relatively dry coarse and fine sediments were spectrally distinct (Rainey *et al.*, In Press).

Interstitial moisture has been found to have an overwhelming influence on the spectral characteristics of intertidal sediments. When the sediments have relatively high moisture contents the above relationships between reflectance and grain-size are weak or non-existent. The relationship between sand and *in situ* reflectance was improved considerably when moisture was included in the regression equation (Equation 4.1). Laboratory experiments demonstrated that the reflectance of intertidal sand and silt approximate a negative linear relationship with interstitial moisture content (r^2 = 0.96 & 0.92 respectively). In contrast, it has been demonstrated that the reflectance of mud does not change significantly during the loss of the first 75% of moisture content (Figure 4.6). When sand and mud both have high moisture contents, they also have very low reflectance values and, consequently, this explains why *in situ* relationships between reflectance and sand content were only observed after a long period of intertidal exposure to rapid drying conditions.

These findings have very significant implications for the mapping of intertidal sediments through airborne remote sensing (Rainey *et al.*, In Press). In particular, it is evident that the timing of the image acquisition relative to the intertidal exposure is crucial. The limited time period between tidal inundations, combined with the water retention attributes of mud, means it is unlikely that the majority of the mud in the intertidal environment ever loses greater than 75% of its moisture. Consequently, during intertidal exposure to rapid drying conditions the reflectance of sand and silt sediments increases whilst mud remains spectrally stable. Therefore, the spectral contrast between the fine and coarse intertidal sediment increases as long as the sediments are exposed. As a result, the image that is most likely to produce the best sediment distribution map is the one collected after the longest period of exposure. This is in agreement with Folving (1984) who postulated that the best map of the sediment domains within an intertidal zone would be created from a scene acquired during the beginning of the flood when the sediments were at their driest.

It is worth noting that at Warton Bank in 1996, an anomalous strong negative relationship was observed between reflectance and intertidal sand content (Figure 4.2). This is the only occasion that this association was found during this study and it coincided with the sediments being completely saturated immediately after tidal inundation. Consequently, it was concluded that this relationship was not temporally stable and therefore unsuitable as the basis for remote sensing intertidal sediments. This conclusion is supported by the results of Yates *et al.* (1993) who attempted to map the intertidal regions of The Wash using a Landsat TM image. The study was based on the assumption that a negative relationship exists between infrared reflectance and the sand content of sediments covered by a film of water. However this surface film, which

would normally absorb the infrared reflectance, was not present during the image acquisition resulting in the misclassification of the majority of the sandy areas. This is an example of the unsuitability of this association in comparison to the more stable positive relationship between reflectance and sand content when the sediments are relatively dry. This supports the earlier conclusion that the most accurate map of intertidal sediment distribution is likely to be created from an image collected after the longest period of intertidal exposure.

Finally, it is evident from the laboratory experiments that mud has a unique response to drying in comparison to other intertidal sediments. It is suggested that the high $<63\mu m$ component of the intertidal mud contributes to its unique spectral stability during the loss of the first 75% of moisture. In contrast, the intertidal silts and sands have an insignificant $<63\mu m$ component, which may explain their relatively linear spectral response to drying. This suggests that mud is the most spectrally separable surface sediment present in the intertidal environment and therefore possibly the easiest sediment to map from ATM imagery.

7.2.4 Intertidal Sediment Classification

An image acquisition, analysis and classification methodology for mapping intertidal sediment grain-sizes was defined within this project. A very strong relationship was observed between the mud abundance estimates and actual clay content of the 1997 sample sites ($r^2=0.79$). A microphytobenthos abundance image was produced as a by-product of the linear unmixing of the 1997 ATM imagery (Figure 5.24). Where the microphytobenthos abundance was high in the intertidal area, it was observed that the image-derived estimates of mud abundance appeared to be severely underestimated

208

(Figures 5.9 & 5.19). Consequently, it was suggested that the microphytobenthos was in some way attenuating the spectral signature of the mud present. As a result the microphytobenthos abundance values were included in the exponential relationship between the image-derived estimates and the clay content of the sample sites (Equations 5.4 & 5.6). This correction procedure substantially improved the relationship (r^2=0.815), which was subsequently used to produce an accurate map of clay contents within the Ribble Estuary. This calibrated clay distribution image (Figure 5.27) equates to a clay content measurement for each 1.75m square within 92.1km^2 of intertidal sediment. In addition, this study produced an accurate distribution map of intertidal sand abundance and an uncalibrated intertidal moisture abundance image for the Ribble Estuary.

From the analysis and classification of the ATM imagery it has been demonstrated that surface and interstitial moisture contents are limiting factors in the ability to map intertidal sediments. This supports the results of the *in situ* and laboratory reflectance spectroradiometry. Where large pools of surface water exist in the intertidal areas of the 1997 imagery, linear unmixing was incapable of accurately estimating the grain-size of the underlying sediment. This is due to the surface water severely attenuating the spectral characteristics of the sediment (Figure 5.10). Similarly, the least accurate map of percentage clay distribution in the Ribble Estuary (r^2=0.79) was created from the first 1997 ATM image collected after intertidal exposure *i.e.* the 'wet' 1997 image. Although the difference in accuracy is very slight, it is nevertheless attributed to the higher interstitial moisture content of the intertidal sediments during the earlier image acquisition. The influence of interstitial moisture may have been more apparent immediately after tidal exposure when the sediments were saturated compared to one

and a half hours later. Nevertheless, the ability to map intertidal sand content was substantially inhibited by the higher interstitial moisture contents during the 'wet' 1997 image acquisition (Figure 5.21). In conclusion, both the reflectance experiments and the sediment classification results imply that the ability to map intertidal sediments through remote sensing is related to the length of time the intertidal area is exposed to rapid drying conditions before image acquisition.

An advantage of using airborne remote sensing in this study is that it provides a high-resolution synoptic view of intertidal environments. This enables an appreciation of the spatial complexity of the intertidal environment that would be very difficult and expensive to attain through a conventional point-sampling programme. In addition, remote sensing provides detailed sediment information about areas, which are either inaccessible or unsafe to sample by conventional means *e.g.* the large intertidal flats in the outer Ribble Estuary. Consequently this allows a better investigation to be made of the fundamental sediment distribution processes at work in the estuary. Finally, this is not a site-specific technique; instead it can be applied to the majority of estuaries where a detailed map of the intertidal sediment distribution may be required (*e.g.* the Solway Firth, NW England).

The results of this remote sensing study of the Ribble Estuary surpasses the results of any previous intertidal remote sensing study (Folving, 1984; Bartholdy and Folving, 1986; Doerffer and Murphy, 1989; Jacobsen and Neilson, 1990). The most substantial set of results is that by Yates *et al.* (1993) who broadly classified each 30m square within The Wash as either 'sandy' or 'muddy'. In this case, even the use of sophisticated sub-pixel classification techniques such as multiple regression and spectral

mixture modelling failed to provide a more detailed sediment classification. As with the other previous studies, this was primarily due to the poor spectral and spatial resolution of the satellite data. The temporal resolution of most satellite platforms is also highly unsuitable for monitoring estuaries due to the need for cloud-free imagery during low tidal conditions. This unsuitability is enhanced when data is required after a specific period of intertidal exposure to rapid drying conditions, as in this study. Consequently, it can be said that the high spectral and spatial resolution of airborne data combined with its temporal flexibility, is a major advantage when monitoring estuarine intertidal sediments.

7.2.5 Radionuclide Distribution in the Ribble Estuary

The calibrated clay distribution images described in Chapter 5 were used to create activity distribution maps of the Ribble Estuary intertidal area. In agreement with the results of previous studies of the Ribble Estuary (Assinder *et al.* 1997; Brown 1997), strong relationships were identified in 1995 and 1997 between the clay content of the intertidal sediments and the Sellafield-derived radionuclides, ^{137}Cs and ^{241}Am (r^2=0.927 & 0.869 respectively). These relationships were found to be spatially representative for the Ribble Estuary and, consequently, were used to convert the clay distribution imagery into maps of surface radionuclide distributions within the Ribble Estuary (Figures 6.3 & 6.4). These maps are found to portray accurately the activity distribution in the Ribble Estuary on May 30th 1997, providing a detailed understanding of its spatial complexity. With reference to previous studies, it is possible to make a number of significant conclusions regarding surface radionuclide distribution in the Ribble Estuary.

Within a number of Irish Sea estuaries a longitudinal increase in activity may be observed landward from the mouth of the estuary. For example in the Ravenglass Estuary, Aston and Stanners (1982) recognised an increase in radionuclide activities towards the source of the River Irt. In contrast, Brown (1997) suggested that in the Ribble Estuary there is no significant trend in Sellafield-derived activities towards Preston. However, the remotely sensed activity images of the Ribble Estuary demonstrate a general exponential increase in average sediment activities from west to east *i.e.* towards Preston (Figure 6.11). Consequently, it is suggested that the isolated point measurements made by Brown (1997) are not sufficiently spatially representative to recognise the large trends in activity. This is a good example of airborne remote sensing making a considerable contribution to the understanding of surface radionuclide distributions within an estuary.

A number of potential sources of redistributed radionuclides in the Ribble Estuary has been identified by previous studies, primarily Penwortham and Savick Brook (Assinder *et al.*, 1997; Brown 1997; Mudge *et al.*, 1997b). It has been suggested that fine radionuclide-rich sediment accumulate in these upper estuary sites during the periods of low and average-river flow (Mudge *et al.*, 1997b). Subsequent high-river flow, typically in the winter months, then redistributes the surface radionuclides of these regions to the middle and outer estuary intertidal areas. However, this suggested model is found to be too simplistic to explain the complex radionuclide distribution observed in the activity imagery produced by this project. As well as Penwortham and Savick Brook, high activity areas are also identifiable in the middle and outer estuary parts of the imagery, *e.g.* the banks of the Douglas River (^{137}Cs ~ 900 Bq kg^{-1}, ^{241}Am ~ 400 Bq kg^{-1}) and the large saltmarsh creek at Warton Bank (^{137}Cs ~ 1000 Bq kg^{-1}, ^{241}Am ~ 450 Bq kg^{-1}).

This suggests that conventional sampling programmes inadvertently avoid less accessible regions and also fail to identify smaller areas of high activity outside the sampled regions. Consequently, any resulting model of radionuclide redistribution is inherently biased as it is based on a limited dataset.

In contrast to previous conventional studies, this image-based study examined each 1.75m square of sediment within 92.1km^2 of the Ribble Estuary intertidal regions and, consequently, provided a spatially representative map of radionuclide distribution. This is an accurate and unbiased dataset upon which a more complete model of the surface activity redistribution can be created. It is proposed that all the rivers and creeks feeding into the estuary, including the Douglas River (Figure 6.13) and Savick Brook, are acting as sources of radionuclide-rich fine sediment. During high tides or periods of high precipitation a portion of the radionuclide-rich sediment of the surrounding saltmarshes is resuspended and distributed at the interfaces of the intertidal area and the tributaries. This explains the complex distribution of high activity concentrations at the mouths of the small creeks entering into the estuary (Figure 6.9 & 6.12). High-river flow is still thought to be a major factor in the movement of radionuclides from the inner estuary to the outer estuary, however it is not the only process of radionuclide redistribution. Fundamentally, this is an extension of the model defined by Mudge *et al.* (1997b), which, unlike the earlier model, recognises the significant radionuclide contribution made by the complex network of saltmarsh creeks and all the estuarine tributaries.

Previous to this study, the only remotely sensed map of ^{137}Cs distribution within the Ribble Estuary was that produced by an aerial gamma survey in September 1992 (Sanderson *et al.*, 1993). The results of this baseline survey are found to be in broad

agreement with the activity imagery produced from the 1997 ATM data. However, there are a number of fundamental differences, which are attributable to the poor spatial resolution of the gamma survey (200-400m) and its tendency to underestimate small-scale activity features. For example, the baseline survey failed to recognise a ^{137}Cs signal from the narrow intertidal mudbanks between Preston and 1km east of Savick Brook. In contrast, the elevated ^{137}Cs content of this region is identifiable in the high spatial resolution (1.75m) activity images produced from the 1997 ATM data. Such small sources are crucial to the understanding of radionuclide redistribution processes and sea-to-land transfer systems in an estuary. Another handicap of the 1992 baseline survey was its inability to identify low energy radionuclides such as ^{241}Am (59.5 keV). This was not a limitation when using ATM imagery, as it is possible to map any Sellafield-derived particle reactive radionuclide through its strong relationship with sediment grain-size.

Total inventories for the Sellafield-derived radionuclides, ^{137}Cs and ^{241}Am, have been estimated from the activity images produced by this project (Section 6.4). Comparisons with the inventories calculated by Brown (1997) for smaller areas (Table 2.5) and examination of the associated intertidal cores (Table 2.4) suggest that the image-based calculations are substantially underestimating the radionuclides present. This suggests that assuming an average radionuclide distribution with depth (60cm) that is similar to the surface activities is introducing a fundamental error. Nevertheless, the image-based calculations are still spatially more accurate than the sample-based measurements which rely on interpolations between widely distanced cores. Consequently, the total inventories for the top 5cm (the readily 'erodable 'component) of the Ribble Estuary

intertidal sediment (0.052TBq of ^{137}Cs and 0.018TBq of ^{241}Am) are thought to be more reliable.

In conclusion, accurate maps of ^{137}Cs and ^{241}Am distribution within the surface intertidal sediments of an estuary can be produced from ATM imagery collected during the correct conditions. The results are found to be substantially more spatially representative than that produced by conventional sampling programmes or aerial gamma surveys. Consequently, a more mechanistic interpretation can be made regarding the locations of activity sources and sinks, and radionuclide-rich sediment redistribution within estuaries. However, the technique developed by this project has some substantial limitations:

1. Unlike conventional sampling programmes and airborne gamma surveys, suitable ATM imagery can only be collected during cloud-free conditions, constraining the timing and frequency of data collection.

2. This technique can only be applied to exposed intertidal areas. Unlike aerial gamma surveys, it cannot be used to provide any information regarding the radionuclide distribution within estuarine saltmarshes.

3. Only radionuclides that have a strong relationship with sediment grain-size can be mapped by this technique. For example, the Springfields-discharged ^{234}Th could not be mapped, as it is insufficiently mixed with the intertidal sediment *i.e.* it's surface intertidal distribution is not directly related to sediment grain-size throughout the estuary.

4. ATM imagery can only provide data regarding the surface sediments of an estuary. Consequently any subsequent total radionuclide inventory or dose calculations are reliant on average sediment depth and density estimates.

7.3 FUTURE WORK

7.3.1 Introduction

A methodology for accurate mapping of surface radionuclides in estuarine intertidal sediments has been presented and validated for the Ribble Estuary. However, with hindsight a number of potential improvements can be identified, which may increase the accuracy of future results. Similarly, it is possible to identify a number of possible alternative applications for this methodology in the future. In this section, these improvements and future applications are outlined and discussed.

7.3.2 Potential Adaptations of the Methodology

At the beginning of this project, linear mixture modelling was selected as the image classification technique most likely to provide accurate images of sediment distribution from ATM imagery. This was based on a combination of factors including previous performance and the required training data (Section 3.6.1). It was also suspected that when mixture modelling was outperformed by other 'soft' classifiers that it was improperly applied (e.g. Bastin, 1997). The accuracy of the sediment and activity images produced from the Ribble Estuary ATM imagery validates the selected classifier. However, a number of sophisticated sub-pixel classification techniques such as Artificial Neural Networks, fuzzy c-means classification and regression analysis remain to be tested. Consequently, it would have been a useful exercise to compare the results from mixture modelling with that of these alternative techniques. This may have provided some useful insights into the spectral nature of the ATM dataset. Nevertheless, it is still unlikely that the accuracy of the resultant clay distribution images

216

could have been improved substantially considering the inherent variability of the estuarine environment (Section 5.5.4).

The analysis and classification of the ATM imagery has demonstrated that radionuclide-rich surface sediments have a very complex distribution within the intertidal environment of the Ribble Estuary. For example, within the extensive sandflats of the outer estuary small patches of high activity are observed (Figure 6.12). One possible explanation for this is that fine radionuclide-rich sediment from the saltmarsh creeks is settling out in topographic lows in this environment. This theory could be tested if the methodology was adapted to include a vertical dimension within the surface activity maps. For example, if georeferenced *in situ* elevation measurements were made during image acquisition it may be possible to create a digital elevation model (DEM) for the estuary from the colour aerial photographs collected simultaneously by NERC with the ATM imagery. Alternatively, a DEM could be created from airborne LIDAR (LIght Detection and Ranging) data collected on the same day as the ATM imagery. The ATM-derived activity maps could then be draped across the DEM, which would allow the height of the radionuclide-rich areas to be compared to the heights of the surrounding sediments. This is only one of a range of advantages that would come from incorporating a third, vertical dimension to the surface radionuclide maps produced.

Surface water, interstitial moisture and microphytobenthos covers have all been identified as surface sediment characteristics that influence the ability to spectrally identify the grain-size of an intertidal sediment. To accurately quantify these influences in the imagery it is necessary to have a range of concomitant *in situ* measurements of these factors. Inevitably, however, these are also the characteristics that are very

difficult to measure in the field during image acquisition. Consequently, it is recommended that future studies attempt to incorporate into the overall methodology an accurate means of quantifying these limiting factors. This has the potential of both improving the spectral understanding of intertidal environments and enhancing the sediment distribution imagery produced.

In this study, estimates of the total inventories of Sellafield-derived ^{137}Cs and ^{241}Am in the Ribble Estuary intertidal sediments were calculated from the activity imagery (Section 6.4). However, these estimates were based on approximations of depth and density of the intertidal sediment. If the methodology of this project had included the collection of intertidal sediment depth measurements or the manipulation of a DEM for the image area, the accuracy of the total inventories may have been improved. In addition, this depth data could be used to calculate the effective dose of the identified high activity regions to critical groups such as anglers, dog-walkers and bird-watchers. This is especially true for the Ribble Estuary where ^{137}Cs is recognised as the dominant source of gamma radiation (Sanderson *et al.*, 1993; Brown, 1997).

Finally, this project has concentrated on the use of ATM imagery to map intertidal sediments, however there are ranges of alternative present and future datatypes. For example HyMap and DAIS (Digital Airborne Imaging Spectrometer) are hyperspectral airborne sensors that are presently available. These could be used to provide high spatial and spectral resolution data of the intertidal area, potentially allowing a more accurate sediment classification. The data from conventional satellite platforms such as Landsat and SPOT has been proven to be inappropriate for mapping intertidal sediment distributions. However, this may prove not to be the case in the near future due to the

forthcoming launch of a range of platforms (Table 7.1). These will contain instruments capable of providing data with a spatial, spectral and temporal resolution that is far superior to that from previous satellite sensors. Consequently, in the future it may be advantageous to adapt the methodology of this project to include other airborne and satellite datatypes than just ATM imagery.

Table 7.1 A Summary of Forthcoming High-Resolution Satellite Remote Sensing Platforms and Sensors

Sensor and Platform	Launch Date	Spectral Bandwidths	Spatial Resolution	Temporal Resolution
Orbview 3	1999	Pan: 450-900 nm	1m	Less than 3 days
		Blue: 450-520 nm	4m	
		Green: 520-600 nm	4m	
		Red: 625-695 nm	4m	
		Near-IR: 760-900 nm	4m	
Orbview 4	2000	Pan: 450-900 nm	1m	Less than 3 days
		Blue: 450-520 nm	4m	
		Green: 520-600 nm	4m	
		Red: 625-695 nm	4m	
		Near-IR: 760-900 nm	4m	
		Hyperspectral: 450-2500 nm (200 Channels)	8m	
Quickbird	1999	Pan: 450 to 900 nm	1m	1 to 5 days depending on latitude
		Blue: 450 to 520 nm	4m	
		Green: 520 to 600 nm	4m	
		Red: 630 to 690 nm	4m	
		Near-IR: 760 to 890 nm	4m	
SPOT-5	2002	Pan: 610-680	5m	26 days
		1: 500-590 nm	10m	
		2: 610-680 nm	10m	
		3: 790-890 nm	10m	
		4: 1580-1750 nm	20m	
EO-1 (Hyperion)	1999	Hyperspectral 400-2500 nm		Variable
		220 bands with a 10 nm resolution	30m	

7.3.3 Potential Future Applications

It has already been demonstrated that important conclusions regarding sediment redistribution can be made directly from the ATM-based activity images. A future objective would be to build on this work through a range of contrasting remote sensing approaches. Primarily, this would involve the use of multidate imagery as a means of accurately quantifying the temporal variability of the activity distributions. In addition, this would demonstrate the respective influence of tidal regimes and seasonal conditions on radionuclide distribution. A second approach would involve the manipulation of flood-tide imagery to identify the actual marine processes responsible for redistribution. This would be an extension of the valuable parallel investigations being carried out by Atkin (In Prep.) into the movement of suspended sediments within the Ribble Estuary. The last source of information would come from intertidal microphytobenthos abundance maps created from the multidate low-tide imagery. These would allow inferences regarding the relative stability of the radionuclide-bearing intertidal sediments to be made (Sutherland *et al.*, 1998). In summary, this multi-approach investigation would provide a range of remotely sensed products for the interpretation of the redistribution processes at work within the Ribble Estuary.

Although beyond the primary objectives of this project, the potential of the image collection, analysis and classification methodology of this project for future estuarine habitat surveys has become apparent. The sediment distribution imagery produced by this project could easily be adapted into habitat suitability maps for a range of intertidal fauna and flora that are sensitive to the grain-size of their environments. This includes macrobenthos such as mussel beds and green algae, and birds such as the Redshank and Dunlin (Goss-Custard and Yates, 1992). In addition, it may be possible to extract more

information from the CASI data, and possibly the ATM imagery, regarding the intertidal microphytobenthos cover. For example it may be possible to classify broadly the various species of diatom or cyanobacteria present, on the basis of the relative abundance of chlorophyll a and b. Similar studies of microphytic crusts in desert environments have been able to recognise the spectral absorption features associated with the different chlorophyll types (O'Neill, 1994; Bajjouk et al., 1996).

It may also be possible to adapt the methodology of this project to map alternative radionuclides to the Sellafield-derived ^{137}Cs and ^{241}Am. For example, another potentially identifiable activity is the Sellafield-discharged Pu, which has associations with both grain-size and the organic content of intertidal sediments. By mapping microphytobenthos cover, an understanding of the spatial distribution of organics in the surface intertidal sediments may be achieved. Consequently, the Pu distribution could be investigated using both sediment grain-size and microphytobenthos abundance images produced from ATM data.

Finally, this project has concentrated on the Ribble Estuary. However, associations between Sellafield-derived radionuclides and intertidal sediment grain-size have also been observed in a range of other Irish Sea estuaries, e.g. the Ravenglass Estuary (Aston and Stanners, 1982). Consequently, airborne remote sensing could be used to provide high resolution spatially representative maps of the surface radionuclide distributions within a range of estuaries in the future. This is particularly important for estuaries like the Solway Firth, which has extensive and often inaccessible intertidal areas. The subsequent results would provide a substantial insight into the contrasting radionuclide

redistribution processes at work in the Irish Sea. In addition, the importance of estuaries as sinks for Sellafield-derived radionuclides would be highlighted.

7.4   FINAL CONCLUSIONS

Within environmental radioactivity a need has been identified for a synoptic tool which can provide high resolution spatially representative maps of surface radionuclide distributions. The results of conventional sampling programmes and aerial gamma surveys are found to be too spatially coarse to allow the activity distributions to be interpreted on a geomorphic scale. This inhibits the identification of sinks and sources within the estuarine environment.

This project has successfully addressed these needs by developing and validating an airborne remote sensing technique that can provide very accurate estimates of the surface activities within each 1.75m square of intertidal sediment present in an estuary. This technique was used to accurately map the Sellafield-derived activities present within $92.1km^2$ of exposed intertidal sediment in the Ribble Estuary. This enabled a previously unattainable appreciation of the complex radionuclide distributions within the Ribble Estuary, which highlighted the need for a high resolution synoptic monitoring tool. As a result substantial conclusions regarding the locations of activity sinks and sources, and the radionuclide redistribution processes were made.

From the development of this unique and innovative remote sensing technique a number of conclusions were made, which are fundamental to the understanding of intertidal radioactivity, reflectance and remote sensing:

1. The Sellafield-derived ^{137}Cs and ^{241}Am have a very complex distribution within the surface intertidal flats of the Ribble Estuary. This is partially attributed to the radionuclide redistribution performed by saltmarsh creeks that interface with the intertidal environment.

2. Strong associations exist in the Ribble Estuary between the Sellafield-derived ^{137}Cs and ^{241}Am, and the clay content of the intertidal sediments. These relationships are spatially stable and have not changed significantly between 1995 and 1997.

3. Significant relationships exist between *in situ* ATM-simulated reflectance and the grain-size characteristics of intertidal sediment that has been exposed for a period of time to strong drying conditions. These relationships are sensitive to moisture, which attenuates the spectral characteristics of the sediment grain-size.

4. Mud and sand are distinct spectral endmembers within Daedalus ATM imagery of exposed intertidal surface sediments collected after a lengthy period of exposure. Consequently, linear mixture modelling can be used to accurately map the sub-pixel abundance of these endmembers within the intertidal areas of the imagery.

5. Image-derived intertidal clay distribution images can be converted into accurate representations of surface Sellafield-derived radionuclides. As a result, important conclusions can be made regarding the activity distributions within an estuarine environment.

The future of the radionuclide monitoring technique developed by this project is likely to lie in its application to other Irish Sea estuaries that are also acting as sinks for Sellafield-derived radionuclides. In addition, airborne remote sensing may be used to monitor a larger suite of radionuclides that also have an association with sediment grain-size. Equally, the availability of high spectral and spatial resolution satellite imagery will allow a range of similar environments to be investigated rapidly and inexpensively.

To summarise this project has demonstrated that airborne remote sensing can be used to provide high resolution quantitative information that surpasses the capabilities of conventional techniques. It is the potential speed, cost-effectiveness and spatial representativeness that makes remote sensing an attractive tool for future estuarine radionuclide investigations.

REFERENCES

Anderson, R.R., 1973, Wetlands mapping in New Jersey. *Photogrammetric Engineering and Remote Sensing*, 39, 353-358.

Asrar, G., (Ed.), 1989, Theory and Applications of Optical Remote Sensing. Chichester: Wiley.

Assinder, D.J., Kelly, M. and Aston, S.R., 1985, Tidal variations in dissolved and particulate phase radionuclide activities in the Esk Estuary, England, and their distribution coefficients and particulate activity fractions. *J. Environ. Radioactivity*, 2, 1-22.

Assinder, D.J., Mudge, S.M. and Bourne, G.S., 1997, Radiological assessment of the Ribble Estuary - I. Distribution of radionuclides in surface sediments. *J. Environ Radioactivity*, 36, 1, 1-19.

Aston, S.R. and Stanners, D.A., 1981, Plutonium occurrence and phase distribution in sediments of the Wyre Estuary, Northwest England. *Marine Pollution Bulletin*, 12, 9, 308-314.

Aston, S.R. and Stanners, D.A., 1982, Gamma emitting fission products in surface sediments of the Ravenglass Estuary. *Marine Pollution Bulletin*, 31, 4, 135-138.

Atkin, P., In Prep, The potential of airborne remote sensing as a tool to assess the transport of radionuclide bearing suspended sediments in the Ribble Estuary, Lancashire, UK. Unpublished PhD Thesis, University of Stirling, Stirling, UK.

Atkinson, P.M., Cutler, M.E.J. and Lewis, H., 1997, Mapping sub-pixel proportional land cover with AVHRR imagery. *Int. J. Remote Sensing*, 18, 4, 917-935.

Bajjouk, T., Guillaumont, B. and Populus, J., 1996, Application of airborne imaging spectrometry system data to intertidal seaweed classification and mapping. *Hydrobiologia*, 326/327, 463-471.

Bartholdy, J. and Folving, S., 1986, Sediment classification and surface type mapping in the Danish Wadden Sea by remote sensing. *Netherlands Journal of Sea Research*, 20, 4, 337-345.

Bastin, L., 1997, Comparison of fuzzy c-means classification, linear mixture modelling and MLC probabilities as tools for unmixing coarse pixels. *Int. J. Remote Sensing*, 18, 17, 3629-3648.

Bierwirth, P.N., 1990, Mineral mapping and vegetation removal via data-calibrated pixel unmixing, using multispectral images. *Int. J. Remote Sensing*, 11, 11, 1999-2017.

Boardman, J.W., 1989, Inversion of imaging spectrometry data using singular value decomposition. In *Proceedings of IGARSS '89 12th Canadian Symposium on Remote Sensing*, 4, 2069-2072.

225

Boardman, J.W., Kruse, F.A. and Green, R.O., 1995, Mapping target signatures via partial unmixing of AVIRIS data. *Fifth JPL Airborne Earth science Workshop, JPL Publication*, **95**, 1, 23–26.

Bowden, K.F., 1980, Physical factors: salinity, temperature, circulation, and mixing processes. In *Chemistry and Biogeochemistry of Estuaries*, eds. Olausson E., and Cato I.. John Wiley and Sons Ltd, 37-70.

Brown, J., 1997, The behaviour of radionuclides in the Ribble Estuary, NW England. Unpublished PhD Thesis, University of Reading, UK.

Bryant, R.G., 1996, Validated linear mixture modelling of Landsat TM data for mapping evaporite minerals on a playa surface: methods and applications. *Int. J. Remote Sensing*, **17**, 2, 315-330.

Bryant, R.G., Tyler A., Gilvear D., McDonald P., Teasdale I., and Ferrier, G., 1996, A preliminary investigation into the VNIR spectral characteristics of inter-tidal estuarine sediments. *Int. J. Remote Sensing*, **17**, 405-412.

Buck, A.L., 1993, An inventory of UK estuaries. Volume 3. North-west Britain. Peterborough, Joint Nature Conservation Committee.

Burton, D.J., West, J.R., Horsington, R.W., and Randle, K., 1995, Modelling transport processes in the Ribble Estuary. *Environmental International*, **21**, 2, 131-141.

Busby, R., McCartney, M and McDonald, P. (1997), Technetium-99 concentration factors in Cumbrian Seafood. In *Proceedings of International Symposium on Radionuclides in the Oceans (RADOC 96), 7-11 October 1996, Cherbourg, France, Radioprotection*, **32**, 311 - 316.

Chavez, P.S., 1988, An improved dark-object subtraction technique for atmospheric scattering correction of multispectral data. *Remote Sensing of Environment*, **24**, 459-479.

Clifton, J., McDonald, P., Plater, A. and Oldfield, F., 1997, Relationship between radionuclide content and textural properties in Irish Sea intertidal sediments. *Water, Air and Soil Pollution*, **99**, 209-216.

Conel, J.E., Green, R.O., Vane, G., Bruegge, C.J. and Alley, R.E., 1987, Airborne Imaging Spectrometer-2: Radiometric spectral characteristics and comparison of ways to compensate for the atmosphere. In *Proceedings of SPIE*, **834**, 140-157.

Collins, M. and Pattiaratchi, C., 1984, Identification of suspended sediment in coastal waters using airborne thematic mapper data. *Int. J. Remote Sensing*, **5**, 4, 635-657.

Cook, G.T., MacKenzie, A.B., McDonald, P. and Jones, S.R., 1997, Remobilization of Sellafield-derived radionuclides and transport from the North-east Irish Sea. *J. Environ Radioactivity*, **35**, 3, 227-241.

Cracknell, A.P., MacFarlane, N., McMillan, K., Charlton, J.A., McManus, J., and Ulbricht, K.A., 1982, Remote sensing in Scotland using data received from satellites. A study of the Tay Estuary region using Landsat multispectral scanning imagery. *Int. J. Remote Sensing*, **3**, 2, 113-137.

Cross, A.M., Settle, J.J., Drake, N.A. and Paivinen, R.T.M., 1991, Subpixel measurement of tropical forest cover using AVHRR data. *Int. J. Remote Sensing*, **12**, 5, 1119-1129.

Doerffer, R. and Murphy, D., 1989, Factor analysis and classification of remotely sensed data for monitoring tidal flats. *Helgolander Meeresunters*, **43**, 275-293.

Donoghue, D.N.M. and Shennan, I., 1987, A preliminary assessment of Landsat TM imagery for mapping vegetation and sediment distribution in The Wash estuary. *Int. J. Remote Sensing*, **8**, 7, 1101-1108.

Donoghue, D.N.M., Reid Thomas, D.C. and Zong, Y., 1994, Mapping and monitoring the intertidal zone of the east coast using remote sensing techniques and a coastal monitoring GIS. *Marine Technology Society*, **28**, 2, 19-29.

Drake, N.A., 1995, Reflectance spectra of evaporite minerals (400-2500nm): applications for remote sensing. *Int. J. Remote Sensing*, **16**, 14, 2555-2571.

Dyer, K.R., 1998, The typology of intertidal mudflats. In *Sedimentary Processes in the Intertidal Zone*, eds. Black, K.S., Paterson, D.M. & Cramp, A.. Geological Society, London, Special Publications, **139**, 11-24.

Fairbridge, R.W., 1980, The estuary: its definition and geodynamic cycle. In *Chemistry and Biogeochemistry of Estuaries*, eds. Olausson, E. and Cato I.. John Wiley and Sons Ltd, 1-35.

Ferrier, G., 1995, Evaluation of apparent surface reflectance estimation methodologies. *Int. J. Remote Sensing*, **16**, 12, 2291-2297.

Ferrier, G. and Anderson, J.M., 1996, The application of remote sensing data in the study of effluent dispersal in the Tay Estuary, Scotland. *Int. J. Remote Sensing*, **17**, 18, 3541-3566.

Ferrier, G. and Anderson, J.M., 1997, A multi-disciplinary study of frontal systems in the Tay Estuary, Scotland. *Estuarine Coastal and Shelf Science*, **45**, 3, 317-336

Fitzpatrick, F., 1990, Remotely sensed sedimentology of Plymouth Sound. In *Proceedings of the Annual Conference of the Ussher Society, January 1990*, **7**, 3, 289-294.

Folving, S., 1984, The Danish Wadden Sea: thematic mapping by means of remote sensing. *Folia Geographica Danica*, **15**, 1-56.

Francis, C.W. and Brinkley, F.S., 1976, Preferential absorbtion of Cs(137) to micaceous minerals in contaminated freshwater sediment. *Nature*, **260**, 511-513.

Fraser, R.S. Ferrare, R.A., Kaufman, Y.J., Markham, B.L. and Mattoo, S., 1992, Algorithm for atmospheric corrections of aircraft and satellite imagery. *Int. J. Remote Sensing*, **13**, 3, 541-557.

Gilabert, M.A., Conese, C. and Maselli, F., 1994, An atmospheric correction method for the automatic retrieval of surface reflectances from TM images. *Int. J. Remote Sensing*, **15**, 10, 2065-2086.

Gonima, L., 1993, Simple algorithm for the atmospheric correction of reflectance images. *Int. J. Remote Sensing*, **14**, 6, 1179-1187.

Goss-Custard, J.D. and Yates, M.G., 1992, Towards predicting the effect of salt-marsh reclamation on feeding bird numbers on the Wash. *Journal of Applied Ecology*, **29**, 330-340.

Green, A.A., Berman, M., Switzer, P. and Graig, M.D., 1988, A transformation for ordering multispectral data in terms of image quality with implications for noise removal. *IEEE Transactions on Geoscience and Remote Sensing*, **26**, 1, 65-74.

Haguenin, R.L., Karaska, M.A., Blaricom, D.V. and Jensen, J.R., 1997, Subpixel classification of Bald Cypress and Tupelo Gum trees in Thematic Mapper imagery. *Photogrammetric Engineering and Remote Sensing*, **63**, 6, 717-725.

Harris, A.R. and Mason, I.M., 1992, An extension to the split-window technique giving improved atmospheric correction and total water vapour. *Int. J. Remote Sensing*, **13**, 5, 881-892.

Hird, A.B. and Rimmer, D.L., 1995, Total caesium-fixing potentials of acid organic soils. *J. Environ Radioactivity*, **26**, 103-118.

HMIPa, 1994, A survey of radioactivity in the Ribble Estuary: Activity concentrations and estuarine dynamics. Her Majesty's Inspectorate of pollution, Environment Series Report No.1.

HMIPb, 1994, A survey of radioactivity in the Ribble Estuary : Radiological assessment. Her Majesty's Inspectorate of pollution, Environment Series Report No.2.

Hook, S.J., 1990, Laboratory spectra of alteration mineral mixtures in the short wave infrared: significance for mineral identification with airborne spectrometers. In *Proceedings of the 9th Earsel Symposium*, 531-536.

Hudson, S.J., Moore, G.F., Bale, A.J., Dyer, K.R. and Aiken, J., 1994, An operational approach to determining suspended sediment distributions in the Humber Estuary by airborne multi-spectral imagery. In *Proceedings of the First International Airborne Remote Sensing Conference and Exhibition, Strasbourg, France, 11-15 September, 1994, 465-474.*

Hunt, G.R. and Salisbury, J.W., 1970, Visible and Near-Infrared Spectra of Minerals and Rocks: II. Silicate minerals. *Modern Geology*, **1**, 283-300.

Hunt, G.R. and Salisbury, J.W., 1971, Visible and Near-Infrared Spectra of Minerals and Rocks: II. Carbonates. *Modern Geology*, **2**, 23-30.

Hunt, G.J. and Kershaw, P.J., 1990, Remobilisation of artificial radionuclides from the sediment of the Irish Sea. *J. Radiol. Prot.*, **10**, 2, 147-151.

Hunt, G.J., 1997, Radiation doses to critical groups since the early 1950's due to discharges of liquid radioactive waste from Sellafield. *Health Physics*, **72**, 558-567.

Hurtado, E., Vidal, A., Caselles, V., 1996, Comparison of two atmospheric correction methods for Landsat TM thermal band. *Int. J. Remote Sensing*, **17**, 2, 237-247.

IAEA, 1985, Sediment K_ds and concentration factors for radionuclides in the marine environment. *Technical Reports Series* No. 247, International Atomic Energy Agency, Vienna.

Irons, J.R., Weismiller, R.A. and Petersen, G.W., (1989), Soil Reflectance. In *The Theory and Applications of Remote Sensing*, ed. Arsar, G., Chichester: Wiley, 66-106.

Jacobsen, N.K., and Nielson, T.S., 1990, Remote sensing and geo-ecological studies of the Danish Wadden Sea. Classification and mapping of landscape elements in a tidal area by means of remote sensing, SPOT images : a preliminary report. 69-75.

Jones, D.G., Miller, J.M. and Roberts, P.D., 1984, The distribution of Cs(137) in surface intertidal sediments from the Solway Firth. *Marine Pollution Bulletin*, **15**, 5, 187-194.

Jones, D.G., Roberts, P.D. and Miller, J.M., 1988, The distribution of gamma emitting radionuclides in surface subtidal sediments near the Sellafield plant. *Estuarine, Coastal and Shelf Science*, **27** 143-161.

Kalluri, S.N.V. and Dubayah, R.O., 1995, Comparison of atmospheric correction models for thermal bands of the advanced very high resolution radiometer over FIFE. *Journal of Geophysical Research*, **100**, D12, 25411-25418.

Karnelli, A. and Tsoar, H., 1995, Spectral reflectance of biogenic crust developed in desert dune sand along the Israel-Egypt border. *Int. J. Remote Sensing*, **16**, 2, 369-374.

Khorram, S., 1982, Remote Sensing of salinity in the San Francisco Bay delta. *Remote Sensing of Environment*, **12**, 15-22.

Knoll, G.F., 1989, Radiation Detection and Measurement, 2nd Edition. New York: John Wiley and Sons.

Kruse, F.A., Lefkoff, A.B., Boardman, J.W., Heidebrecht, K.B., Shapiro, A.T., Basloon, P.J. and Goetz, A.F.H., 1993, The spectral image processing system (SIPS) - interactive visualization and analysis of imaging spectrometer data. *Remote Sensing of Environment*, **44**, 145-163.

Lavery, P., Pattiaratchi, C., Wyllie, A. and Hick, P., 1993, Water quality monitoring in estuarine waters using the Landsat Thematic Mapper. *Remote Sensing of Environment*, **46**, 3, 268-280.

Leu, D.J., 1977, Visible and near-infrared reflectance of beach sands: A study on the spectral reflectance/grain size relationship. *Remote Sensing of Environment*, **6**, 169-182.

Livens, F.R. and Baxter, M.S., 1988, Particle size and radionuclide levels in some West Cumbrian soils. *The Science of the Total Environment*, **70**, 1-17.

Lyons, M.G., 1997, The dynamics of suspended sediment transport in the Ribble estuary. *Water, Air and Soil Pollution*, **99**, 141-148.

MacKenzie, A.B., Scott, R.D. and Williams, T.M., 1987, Mechanisms for northwards dispersal of Sellafield Waste. *Nature*, **329**, 42-45.

MacKenzie, A.B., Scott, R.D., Allan, R.L., Ben Shaban, Y.A., Cook, G.T., and Pulford, I.D., 1994, Sediment radionuclide profiles: Implications for mechanisms of Sellafield waste dispersal in the Irish Sea. *J. Environ. Radioactivity*, **23**, 39-69.

Mamas, C.V.J., Earwaker, L.G., Sokhi, R.S., Randle, K., Beresford-Hartwell, P.R. and West, J.R., 1995, An estimation of sediment rates along the Ribble estuary, Lancashire, UK, based on radiocaesium profiles preserved in intertidal sediments. *Environmental International*, **21**, 2, 151-165.

Marsh, S.H., 1993, Discrimination between sulphate, carbonate and hydrosilicate minerals using Landsat Thematic Mapper data. *Proceedings of the Ninth Thematic Conference on Geologic Remote Sensing, Pasadena, California, USA, 8-11 February 1993*, 677-685.

McCartney, M., Kershaw, P.J., Allington, D.J., Young, A.K. and Turner, D., 1992, Industrial sources of naturally occurring radionuclides in the eastern Irish Sea. *Radiation Protection Dosimetry*, **45**, 1/4, 711-714.

McDonald, P., Cook, G.T. and Baxter, M.S., 1991, Natural and artificial radionuclides in coastal regions of the UK. In *Radionuclides in the study of marine processes*, ed. Kershaw, P.J., Elsevier, 329–339.

McDonald, P., Cook, G.T. and MacKenzie, A.B., 1993, The dispersal of radionuclides in the Irish Sea. In *Heavy Metals in the Environment*, eds. Allan R.J., Nriagu, J.O. CEP Consultants Ltd Publishers, 239 - 242.

McDonald, P. and Jones, S. R., 1997, The biogeochemistry of radionuclides in intertidal sediments. In *Biogeochemistry of Intertidal Sediments*, eds. Jickells, T.D. and Rae, J.E., Cambridge Environmental Chemistry Series, **9**, 152 - 172.

McKay, W.A. and Pattenden, N.J., 1993, The behaviour of plutonium and americium in the shoreline waters of the Irish Sea: A review of Harwell studies in the 1980s. *J. Environ. Radioactivity*, **18**, 99-132.

McLusky, D.S., 1989, The Estuarine Ecosystem, 2nd Ed. New York: Chapman and Hall.

Mehta, A.J., 1989, On estuarine cohesive sediment suspension behaviour. *Journal of Geophysical Research-Oceans*, **94**, c10, 14303-14314.

Milovich, J.A., Frulla, L.A. and Gagliardini, D.A., 1995, Environment contribution to the atmospheric correction for Landsat-MSS images. *Int. J. Remote Sensing*, **16**, 14, 2515-2537.

Mudge, S.M., Bourne, G.S. and Assinder, D.J., 1997a, Radiological assessment of the Ribble Estuary - II. Beta and gamma dose rates and doses to critical groups. *J. Environ. Radioactivity*, **36**, 1, 21-41.

Mudge, S.M., Assinder, D.J. and Bourne, G.S., 1997b, Radiological assessment of the Ribble Estuary - III. Redistribution of radionuclides. *J. Environ. Radioactivity*, **36**, 1, 43-67.

Nature Conservancy Council Report, 1981, Acquatic estuarine habitats and estuarine habitats.

Nicodemus, F.E., Richmond, J.C. and Hsia, J.J., 1977, Geometrical considerations and nomenclature for reflectance. *National Bureau of Standards Monograph* **160**, U.S. Department of Commerce.

Nicodemus, F.E., 1982, Reflectance nomenclature and directional reflectance and emissivity. *Applied Optics*, **9**, 6, 1474-1475.

Nieke, B., Condal, A., Berthon, J.F., Bellehumeur, C., Legendre, L., Morin, S., Therriault, J.C., Giroud, C. and Dick, R., 1995, Depth resolved detection of oceanographic variables in the St. Lawrence Estuary using a laser fluorosensor: instrument characteristics and first results. *Int. J. Remote Sensing*, **16**, 8, 1503-1522.

O'Neill, A.L., 1994, Reflectance spectra of microphytic soil crusts in semi-arid Australia. *Int. J. Remote Sensing*, **15**, 3, 675-681.

Pardue, J.H., Delaune, R.D., Patrick, W.H. and Whitcomb, J.H., 1989, Effect of redox potential on fixation of Cs(137) in lake sediment. *Health Physics*, **57**, 5, 781-789.

Pinker, R.T. and Karnelli, A., 1995, Characteristic spectral reflectance of a semi-arid environment. *Int. J. Remote Sensing*, **16**, 7, 1341-1363.

Postma, H., 1980, Sediment transport and sedimentation. In *Chemistry and Biogeochemistry of Estuaries*, eds E. Olausson, and I. Cato. John Wiley and Sons Ltd, pp 153-186.

Populus, J., Moreau, F., Coquelet, D. and Xavier, J.P., 1995, An assessment of environmental sensitivity to marine pollutions : solutions with remote sensing and Geographical Information Systems (GIS). *Int. J. Remote Sensing*, 16, 1, 3-15.

Price, J.C., 1995, Examples of high resolution visible to near-infrared reflectance spectra and a standardized collection for remote sensing studies. *Int. J. Remote Sensing*, 16, 6, 993-1000.

Rainey, M.P., Tyler, A.N., Bryant, R., Gilvear, D., and McDonald, P., (In Press) The influence of surface and interstitial moisture on the spectral characteristics of intertidal sediments: Implication for airborne image acquisition and processing. *Int. J. Remote Sensing*

Ramasamy, S.M., Venkatasbrumania, V. and Anbazhagan, S., 1993, Reflectance spectra of minerals and their discrimination using Thematic Mapper, IRS and SPOT multispectral data. *Int. J. Remote Sensing*, 14, 16, 2935-2970.

Roberts, D.A., Yamaguchi, Y. and Lyon, R.J.P., 1985, Calibration of airborne imaging spectrometer data to percent reflectance using field spectral measurements. In *Proceedings of the Nineteenth International Symposium on Remote Sensing of Environment, Ann Arbor, Michigan, October 21-25, 679-688*.

Robinson, B.F. and Biehl, L.L., 1979, Calibration procedures for measurement of reflectance factor in remote sensing field research. *Measurements of Optical Relations*, 196, 16-26.

Sanderson, D.C.W., Allyson, J.D., Tyler, A.N. and Murphy, S., 1993, An aerial gamma ray survey of Springfields and the Ribble Estuary in September 1992. Scottish Universities research and Reactor Centre Aerial Survey Report to British Nuclear Fuels PLC.

Sanderson, D.C.W., Allyson, J.D., Tyler, A.N. and Scott, E.M., 1995, Environmental applications of airborne gamma spectrometry. In *Proceedings of the IAEA Technical Committee Meeting*, Vienna, 9-12 November, 1993, 71-91.

Settle, J.J. and Drake, N.A., 1993, Linear mixing and the estimation of ground cover proportions. *Int. J. Remote Sensing*, 14, 6, 1159-1177.

Singh, S.M., 1994, Parameterization of a single scattering atmospheric correction algorithm using 5S code. *Int. J. Remote Sensing*, 15, 1, 191-196.

Singer, R.B. and McCord, T.B., 1979, Mars: Large scale mixing of bright and dark surface materials and implications for analysis of spectral reflectance. In *Proceedings of Lunar Planet Sci. Conf. 10th*, 1835-1848.

Smith, M.O., Johnson, P.E. and Adams, J.B., 1985, Quantitative determination of mineral types and abundances from reflectance spectra using Principle Component Analysis. In *Proceedings of Lunar Planet Sci. Conf. 15th*, **2**, 797-804.

Stanners, D.A. and Aston, R.S., 1981, Cs(134), Cs(137), Ru(106): Cs(137) ratios in intertidal sediments from the Cumbria and Lancashire coasts, England. *Estuarine, Coastal and Shelf Science*, **13**, 409-417.

Steffensen, D.A. and McGregor, F.E., 1976, The application of aerial photography to estuarine ecology. *Aquatic Biology*, **2**, 3-11.

Sutherland, T.F., Amos, C.L., and Grant, J., 1998, The erosion threshold of biotic sediments: a comparison of methods. In Black, K.S., Paterson, D.M. & Cramp, A. (eds) *Sedimentary Processes in the Intertidal Zone*. Geological Society, London, Special Publications, **139**, 295-307.

Tanré, D., Deroo, C., Duhaut, P., Herman, M. and Morcrette, J.J., 1990, Description of a computer code to simulate the satellite signal in the solar spectrum : the 5S code. *Int. J. Remote Sensing*, **11**, 4, 659-668.

Thomson, A.G., Fuller, R.M., Sparks, T.H., Yates, M.G., and Eastwood, J.A., 1998, Ground and airborne radiometry over intertidal surfaces: waveband selection for cover classification. *Int. J. Remote Sensing*, **19**, 6, 1189-1205.

Tyler, A.N., Bryant, R., Gilvear, D., McDonald, P., Teasdale, I., Brown, J. and Ferrier, G., 1995, The spectral characterisation of radionuclide bearing sediments in the Ribble estuary. In *Proceedings of the 21st Annual Conference of the Remote Sensing Society*, 433-440.

Tyler, A.N., Sanderson, D.C.W., Scott, E.M. and Allyson, J.D., 1996, Accounting for spatial variability and fields of view in environmental gamma ray spectrometry. *J. Environ. Radioactivity*, **33**, 3, 213-235.

Van den Bosch, J.M. and Alley, R.E., 1991, Comparison of two atmospheric correction models for a vegetated airborne visible/infrared imaging spectrometer (AVIRIS) scene. In *Proceedings of the 5th International Colloquium - Physical Measurements and Signatures in Remote Sensing, Courchevel, France, 14-18 January 1991*, 567-574.

Van der Meer, F., 1995, Spectral unmixing of Landsat Thematic Mapper data. *Int. J. Remote Sensing*, **16**, 16, 3189-3194.

Van der Meer, F., 1997, Mineral mapping and Landsat thematic mapper image classification using spectral unmixing. *Geocarto International*, **12**, 3, 27-40.

Wilson, A.K., 1995, NERC scientific services airborne remote sensing faculty user guide handbook, Version 1.0. NERC Publication.

Wilson, A.K., Mockeridge, W. and White, S., 1996, The NERC airborne remote sensing facility, development and implementation of the integrated data system. In *Proceedings of 22nd Annual Conference of the Remote Sensing Society, Durham, 11-14 September,* 263-270.

Yates, M.G., Jones, A.R., McGrorty, S. and Goss-custard, J.D., 1993, The use of satellite imagery to determine the distribution of intertidal surafce sediments of The Wash, England. *Estuarine, Coastal and Shelf Science,* **36**, 333-334.

Zagolski, F. and Gastellu-Etchegorry, J.P., 1995, Atmospheric corrections of AVIRIS images with a procedure based on the inversion of the S5 model. *Int. J. Remote Sensing,* **16**, 16, 3115-3146.

Zhang, M., Ustin, S.L., Rejmankova, E. and Sanderson, E.W., 1997, Monitoring Pacific Coast saltmarshes using remote sensing. *Ecological Applications,* **7**, 3, 1039-1053.

APPENDICES

APPENDIX 1

REFSPEC command line for the conversion of each of the replicate target spectra into absolute reflectance

refspec [-a d h] [r] [-o] target reference panel output

where 'target' and 'panel' are the names of the raw binary format target and reference files respectively; panel is the name of an ASCII-format panel calibration file; output is the name of the text file to be created.

-a   specifies that both header and spectrum data will be converted,
-d   specifies that only spectrum data will be converted,
-h   specifies that only header data will be converted (default),
-r   convert only every second channel,
-o   allows the output file to overwrite pre-existing files but not any of the input files

APPENDIX 2

Filter function files ATM 1- ATM 10 were provided by NERC EPFS. These ASCII format files are multiplied individually against each spectra. The resultant values are totaled for each band and normalized by multiplying by 100.

APPENDIX 3

Command lines for a) the geocorrection of the raw ATM files (.hdf) and b) the subsequent conversion to generic binary (.bil) format.

a) Basic GCORR Command line for ATM data

gcorr -1 input.hdf -3 output.hdf -p 1.75 1.75

- This is a basic level 1 to level 3 conversion, with no DEM details, or line and band selection.

b) EXHDF commands

exhdf [-BS or -B output.***] -h input.hdf

- Converts input file to either a BSEQ or a BIL binary output file

APPENDIX 4

Gamma Ray Spectrometry and Grain-size Analysis Results – 1995 Samples

SAMPLE NAME	Cs-137 Activity (Bq kg^{-1})	Am-241 Activity (Bq kg^{-1})	% Clay	% Silt	% Sand
Longton 01 03	66.400	33.500	4.300	40.590	55.120
Longton 02 01	541.000	246.000	9.670	71.580	18.750
Longton 02 02	190.000	80.600	8.960	55.980	35.050
Longton 02 03	19.600	18.600	1.210	3.640	95.150
Longton 02 04	14.300	16.100	0.810	1.980	97.210
Longton 03 01	550.000	240.000	10.870	77.430	11.700
Longton 03 02	472.000	229.000	10.750	72.710	16.540
Longton 03 03	39.800	24.000	2.340	15.900	81.760
Longton 04 01	237.000	100.000	9.630	59.080	31.290
Longton 04 02	38.800	12.000	3.380	31.470	65.150
Longton 04 03	41.400	13.500	3.010	23.250	73.740
Longton 05 02	295.000	128.000	10.980	66.090	22.940
Longton 06 01	95.400	41.100	4.480	34.490	61.030
Longton 06 02	76.500	33.800	4.930	34.200	60.870
Longton 06 03	21.600	23.900	1.120	4.000	94.880
Longton 06 05	13.500	8.350	0.810	1.880	97.310
Longton 07 01	113.000	54.900	6.000	43.360	50.650
Longton 07 03	58.000	34.100	2.620	21.220	76.160
Longton 07 04	19.800	4.570	0.860	2.450	96.690
Longton 08 001	18.300	10.200	1.310	6.660	92.030
Longton 08 01	249.000	65.800	5.310	40.400	54.290
Longton 08 003	108.000	45.200	6.410	41.340	52.250
Longton 08 02 (50m)	16.400	10.500	1.530	10.370	88.100
Longton 08 02 (60m)	14.500	23.600	0.970	3.960	95.070
Longton 08 03 (80m)	17.700	19.800	1.030	4.020	94.960
Longton 08 03 (90m)	14.530	6.760	1.130	5.020	93.850
Longton 08 04 (120m)	22.200	16.300	1.740	10.250	88.010
Longton 08 04 (110m)	14.500	6.760	0.880	2.420	96.700
Longton 08 05	16.300	18.900	1.230	5.410	93.360
Longton 01 01	571.000	256.000	13.030	76.400	10.570
Longton Trans2	22.700	24.900	1.210	5.260	93.520
Penwortham 1	393.000	179.000	8.220	75.840	15.940
Penwortham 2	396.000	192.000	11.010	71.230	17.760
BNFL Output 1 1	610.000	286.000	13.260	67.400	19.340
BNFL Output 1 2	512.000	234.000	12.510	76.210	11.280
BNFL Output 1 3	111.000	49.000	5.220	42.160	52.620
BNFL Output 1 4	25.700	12.100	2.150	13.880	83.970
BNFL Output 2 1	651.000	286.000	7.710	46.560	45.730
BNFL Output 2 2	430.000	200.000	11.370	73.700	14.930
BNFL Output 2 3	216.000	99.700	9.750	45.530	44.720
BNFL Output 2 4	30.000	10.000	1.690	10.360	87.950

Warton 0001-000	580.000	253.000	11.500	69.420	19.080
Warton 0006-001	621.000	280.000	13.670	77.170	9.160
Warton 0013-001	452.000	195.000	7.000	75.150	17.850
Warton 0018-002	352.000	142.000	6.900	65.110	27.990
Warton 0023-002	67.300	33.500	3.060	22.200	74.740
Warton 0032-003	122.000	74.300	4.640	31.040	64.320
Warton 0037-004	16.400	8.870	0.780	1.300	97.930
Warton 0042-004	15.200	22.300	0.740	1.000	98.260
Warton 0047-005	106.000	49.400	5.870	46.500	47.630
Warton 0053-005	77.200	32.500	2.780	24.240	72.980
Warton 0061-006	122.000	57.200	5.790	38.910	55.290
Warton 0066-007	561.000	255.000	13.680	78.460	7.860
Warton 0071-007	589.000	264.000	9.950	61.540	28.510
Warton 0076-008	568.000	260.000	6.980	48.760	44.260
Warton 2 Scrape	608.000	257.000	9.950	81.280	8.770
Warton 3 Scrape	421.000	192.000	9.830	75.200	14.970
Warton 4 Scrape	84.800	45.600	3.770	30.320	65.910
Warton 5 Scrape	78.300	36.300	3.560	28.790	67.650
Warton 6 Scrape	96.800	43.600	3.810	29.100	67.090
Warton 7 Scrape	79.400	41.300	2.600	19.220	78.190
Warton 8 Scrape	21.000	22.100	1.020	2.630	96.350
Warton 9 Scrape	16.800	9.720	0.860	1.960	97.180
Warton 10 Scrap	16.400	15.800	0.810	1.530	97.660
Warton 11 Scrap	15.400	10.400	0.850	1.860	97.290
Warton 12 Scrap	16.700	15.200	0.770	1.200	98.040
Warton 13 Scrap	29.200	10.200	1.780	8.910	89.310
Warton 14 Scrap	76.900	50.400	2.380	16.920	80.700
Warton 15 Scrap	82.600	30.400	3.940	27.590	68.470
Warton 16 Scrap	99.200	51.400	4.650	38.280	57.070
Warton 17 Scrap	409.000	186.000	11.330	75.310	13.360
Warton 18 Scarp	609.000	277.000	11.910	68.430	19.660

Gamma Ray Spectrometry and Grain-size Analysis Results – 1997 Samples

SAMPLE NAME	Cs-137 Activity (Bq kg^{-1})	Am-241 Activity (Bq kg^{-1})	% Clay	% Silt	% Sand
WA1	372.91	138.21	12.82	65.71	21.46
WA2	204.49	58.44	7.05	54.24	38.7
WA3	100.18	39.09	4.41	32.11	63.48
WA4	139.68	43.26	5.95	43.71	50.34
WA5	46.97	17.26	2.92	23.23	73.85
WA6	30.22	6.04	1.76	10.72	87.52
WA7	22.69	8.20	1.21	5.28	93.51
WA8	31.16	9.19	1.97	15.4	82.64
WA9	23.59	3.52	1.5	8.13	90.37
WA10	18.11	5.51	0.74	1.52	97.73
WA11	15.46	3.45	0.77	1.95	97.28
WA12	16.76	5.98	1.01	4.18	94.81

237

WA13	15.87	3.33	0.84	2.94	96.22
WA14	17.70	4.40	0.98	4.65	94.37
DA_01	318.02	99.90	10.14	72.49	17.37
DA_02	334.95	119.35	10.07	74.17	15.76
DA_03	440.26	144.10	8.81	73.63	17.56
DA_04	330.55	93.01	7.55	73.16	19.29
DB_01	517.78	218.34	8.91	76.34	14.76
DB_02	513.39	201.93	7.75	82.56	9.69
DB_03	501.89	207.05	7.69	79.75	12.56
LSA1_1	554.16	228.62	9.76	78.13	12.11
LSA5_1	441.12	185.01	7.33	72.53	20.13
LSA10_1	112.21	48.13	6.4	51.1	42.5
LSA15_1	53.36	21.84	3.6	29.54	66.86
LSA20_1	36.70	7.77	1.84	15.39	82.78
LSA22_1	45.06	15.85	2.28	14.38	83.34